THREE-DIMENSIONAL SIMULATION OF LASER GAS-ASSISTED CUTTING: JET IMPINGEMENT CONSIDERATIONS

BY

Omar Ahmad Melhem

A Dissertation Presented to the

DEANSHIP OF GRADUATE STUDIES

KING FAHD UNIVERSITY OF PETROLEUM & MINERALS

DHAHRAN, SAUDI ARABIA

In Partial Fulfillment of the
Requirements for the Degree of

DOCTOR OF PHILOSOPHY

In

MECHANICAL ENGINEERING

February 2010

KING FAHD UNIVERSITY OF PETROLEUM & MINERALS
DHAHRAN 31261, SAUDI ARABIA

DEANSHIP OF GRADUATE STUDIES

This dissertation, written by **OMAR AHMAD MELHEM** under the direction of his dissertation advisor and approved by his dissertation committee, has been presented to and accepted by the Dean of Graduate Studies, in partial fulfillment of the requirements for the degree of **DOCTOR OF PHILOSOPHY IN MECHANICAL ENGINEERING**.

Dissertation Committee

Prof. Bekir S. Yilbas
Dissertation Advisor

Dr. Shahzada Z. Shuja
Member

Prof. Ahmet Z. Sahin
Member

Dr. Amro Al-Qutub
Department Chairman

Prof. Habib Abualhamayel
Member

Dr. Salam A. Zummo
Dean of Graduate Studies

Prof. Eiazuddin Zaman
Member

31/1/10
Date

عمادة الدراسات العليا
DEANSHIP OF GRADUATE STUDIES

TO MY PARENTS FOR UNDERTAKING MORE THAN ANYONE CAN HANDLE

TO MY WIFE, AHMAD, SUMAYYAH, AND HASAN FOR THE TIMES I WAS ABSENT

ACKNOWLEDGMENT

In the Name of ALLAH, the Most Gracious, the Most Merciful; all the praises and thanks are due to ALLAH and peace and blessings are upon Muhammad, the Messenger of ALLAH and the last of the Prophets. *"And keep your duty to Him, fear Him Who has aided you with all (good things) that you know"* (QURAN, V.26:132).

Acknowledgement is due to King Fahd University of Petroleum & Minerals for giving me the opportunity to pursue my PhD research.

I express my deepest appreciation and gratitude to my advisor Professor Bekir S. Yilbas for his guidance, support, and understanding over the past five years. I also thank Dr. Shahzada Shuja for his aid in this research and for the fruitful discussions. I wish also to thank Professors Ahmet Sahin, Habib Abualhamayel, and Fiazuddin Zaman for accepting to be in my dissertation committee and for taking the time to review my dissertation.

I want to thank the Chairman of the Mechanical Engineering department for help in academic and administrative matters. I wish also to extend my appreciation to all faculty members who taught and helped me and whom I worked with. Special thanks are due to Doctors Rached Ben-Mansour and Esmail Mokheimer for all the valuable discussions and their ideal care.

I also thank Professor Nesreen Ghaddar, Dr. Kamel Abou-Ghali, Dr. Issam Lakkis, and Dr. Alan Shihadeh of the American University of Beirut for their tutoring and advice.

My thanks go to all my friends at KFUPM and especially to Saad Ben Mansour for his patience during endless stream of discussions.

No words can express my gratitude to my father, mother, my aunt, my wife, my uncle, and my brothers Nidal, Ali, Dr. Hisham, and especially Hasan for their ultimate devotion, sacrifices, and support. I thank my wife and children Ahmad, Sumayyah and Hasan and apologize for any shortening.

TABLE OF CONTENTS

Page
DEDICATION……....iii
ACKNOWLEDGEMENT……..iv
TABLE OF CONTENTS……v
LIST OF TABLES……...viii
LIST OF FIGURES……...ix
ABSTRACT……..xv
ABSTRACT (Arabic)……...xvi

CHAPTER 1 1
INTRODUCTION 1
1.1 BACKGROUND 2
1.1.1 LASER APPLICATIONS 3
1.1.2 THE LASER MATERIAL INTERACTION PROCESS 3
1.1.2.1 Thermal Damage..... 3
1.1.2.2 Mechanical Damage..... 4
1.2 LASER CUTTING 5
1.2.1 FORMS OF LASER CUTTING..... 7
1.2.1.1 Fusion Cutting..... 7
1.2.1.2 Sublimation Cutting 7
1.2.1.3 Photochemical Ablation..... 7
1.2.2 PROCESS DESCRIPTION AND CHARACTERIZATION 8
1.2.2.1 Physical Phenomena 9
1.2.2.2 Kerf Geometry and Melt Flow Characteristics..... 12
1.2.3 ASSISTING GAS FUNCTIONS..... 13
1.2.4 CUTTING QUALITY 14
1.2.4.1 Striations of the Cut Surface 14
1.2.4.2 Dross Formation..... 14
1.2.5 MATERIAL CONSIDERATIONS 15
1.2.6 ADVANTAGES 16
1.3 JET IMPINGEMENT 19
1.3.1 JET IMPINGEMENT FLOW CONFIGURATIONS..... 19
1.3.2 DESIGN PARAMETERS 22
1.4 NUMERICAL MODELING CONSIDERATIONS..... 22
1.4.1 TURBULENCE MODELING IN COMPUTATIONAL FLUID DYNAMICS 23
1.4.2 TURBULENCE MODELING OPTIONS IN FLUENT 24
1.4.3 CLOSURE 28
1.5 SCOPE AND OBJECTIVES..... 30
1.5.1 GEOMETRICAL AND MATHEMATICAL MODELING 30

1.5.2 VALIDATION OF THE TURBULENCE MODEL 31
1.5.3 IDENTIFYING AND STUDYING MAJOR PARAMETERS 32
1.5.4 DISSERTATION CONTRIBUTION 33
1.6 DISSERTATION ORGANIZATION 33

CHAPTER 2 34
LITERATURE REVIEW 34
2.1 LASER CUTTING 34
2.1.1 EXPERIMENTAL STUDIES 35
2.1.2 MODELING STUDIES 37
2.2 JET IMPINGEMENT 42
2.2.1 EXPERIMENTAL STUDIES 43
2.2.2 NUMERICAL STUDIES 51
2.2.2.1 Round/Axisymmetric Jets 51
2.2.2.2 Slot/Rectangular Jets 58
2.3 CONCLUSIONS 63

CHAPTER 3 64
NUMERICAL MODELING 64
3.1 MODELING OF GAS JET ASSISTED LASER CUTTING – FLOW EQUATIONS AND TURBULENCE MODELS 64
3.1.1 PRELUDE 64
3.1.2 MATHEMATICAL MODELING 65
3.1.3 TURBULENCE MODELING 68
3.1.3.1 Transport Equations for the RNG k-ε model 68
3.1.3.2 Near-Wall Turbulence Modeling 72
3.2 COMPUTATIONAL DOMAIN 78
3.2.1 COMPUTATIONAL DOMAIN GEOMETRY 78
3.2.2 BOUNDARY CONDITIONS 83
3.2.2.1 Flow Boundary Conditions 83
3.2.2.2 Solid Boundary Conditions 84
3.2.2.3 Solid Fluid Interface Boundary Conditions 85
3.2.2.4 Variable Properties 85
3.3 GRID DETAILS AND CONSIDERATIONS 87
3.4 NUMERICAL SCHEME 91
3.4.1 THE GENERAL DIFFERENTIAL EQUATION 91
3.4.2 The Finite Volume Method 94
3.4.2.1 Discretization 94
3.4.2.2 Calculation of the Flow Field 98
3.4.2.3 Under-Relaxation 104
3.4.2.4 Convergence 104
3.5 SIMULATIONS 106

CHAPTER 4 107

NUMERICAL CODE AND MODEL VERIFICATION 107
4.1 INTRODUCTION 107
4.2 CASE STUDY 108
4.3 GRID INDEPENDENCE STUDY 117

CHAPTER 5 122
RESULTS AND DISCUSSION 122
5.1 Effect of Averaged Jet Velocity at Nozzle Exit on Heat Transfer Rates and Skin Friction 124
5.2 Effect of the Kerf Wedge Angle on Heat Transfer Rates and Skin Friction 143
5.3 Effect of Kerf Thickness on Heat Transfer Rates and Skin Friction 201
5.4 Effect of the Standoff Distance on Heat Transfer Rates and Skin Friction 261
5.5 Effect of Averaged Jet Velocity, Kerf Wedge Angle, Kerf Depth, and Standoff Distance on Exiting Mass Flow Rate Ratio, Average Nusselt Number, and Average Skin Friction 278

CHAPTER 6 284
CONCLUSIONS AND RECOMMENDATIONS 284
6.1 EFFECTS OF AVERAGED JET VELOCITY 285
6.2 EFFECTS OF KERF WEDGE ANGLE 286
6.3 EFFECTS OF KERF THICKNESS 287
6.4 EFFECTS OF STANDOFF DISTANCE 288
6.5 CLOSURE 289

APPENDIX A 291
NOMENCLATURE 294
BIBLIOGRAPHY 298
VITA 310

LIST OF TABLES

Table Page

TABLE 1.1 Comparison of Thermal Cutting Processes 18

TABLE 3.1 Geometric Parameters and Average Jet Velocities Considered in Simulations 82
TABLE 3.2 Nitrogen Thermo-Physical Properties Used in Simulations 86
TABLE 3.3 Dependent Variables and the Associated Diffusion Coefficients and Source Terms for the Governing Conservation Equations 93

TABLE 4.1 Comparison of Average Nusselt Numbers for the Three Cases Under Consideration 116

TABLE A.1……..291

LIST OF FIGURES

Figure Page

Figure 1.1 Schematic of laser cutting process [3]……...6
Figure 1.2 Schematic representation of core factors in laser materials processing [1]…..11
Figure 3.1 Schematic diagram of the impinging jet flow configuration used in the simulations 80
Figure 3.2 Solid material (kerf shaded in blue and kerf side wall shaded in black)..... 81
Figure 3.3 Sample computational grid used in the simulations 89
Figure 3.4 Computational grid in the kerf region for two kerf wedge angles 90
Figure 3.5 Three-dimensional cell with center node P and neighboring nodes..... 95
Figure 3.6 Overview of the segregated solution method [15] 103

Figure 4.1 Schematic of the experimental setup used by Sagot et al. [20] 110
Figure 4.2 Computational domain and insert showing close-up view of the grids in the nozzle exit and impingement regions 114
Figure 4.3 Grid independence test for velocity magnitude along centerline 119
Figure 4.4 Grid independence test for temperature distribution along centerline 120
Figure 4.5 Grid independence test for Nusselt number distribution along normalized kerf wall thickness at the location where Nusselt number approximately attained highest values 121

Figure 5.1 Kerf regions for two kerf wedge angles 123
Figure 5.2 Normalized velocity magnitude for one averaged jet velocity (30 m/s) and two kerf wedge angles (0° and 4°)..... 125
Figure 5.3 Normalized velocity magnitude for one averaged jet velocity (60 m/s) and two kerf wedge angles (0° and 4°)..... 126
Figure 5.4 Normalized temperature for one averaged jet velocity (30 m/s) and two kerf wedge angles (0° and 4°) 128
Figure 5.5 Normalized temperature for one averaged jet velocity (60 m/s) and two kerf wedge angles (0° and 4°) 129
Figure 5.6 Pressure Coefficient for one averaged jet velocity (30 m/s) and two kerf wedge angles (0° and 4°)..... 131
Figure 5.7 Pressure Coefficient for one averaged jet velocity (60 m/s) and two kerf wedge angles (0° and 4°)..... 132
Figure 5.8 Velocity magnitude along laser beam axis for different averaged jet velocities kerf wedge angles of 0° and 4° 135
Figure 5.9 Pressure variation along laser beam axis for different averaged jet velocities kerf wedge angles of 0° and 4° 136

Figure 5.10 Temperature variation along laser beam axis for different averaged jet velocities kerf wedge angles of 0° and 4° 137
Figure 5.11 Nusselt number distribution along the normalized kerf wall thickness for different averaged jet velocities at nozzle exit and kerf wedge angles of 0° and 4° 141
Figure 5.12 Skin friction distribution along the normalized kerf wall thickness for different averaged jet velocities at nozzle exit and kerf wedge angles of 0° and 4° 142
Figure 5.13 Normalized velocity magnitude (V/V_j) for jet averaged velocity of 30 m/s, kerf thickness of 0.5 mm, and kerf wedge angles of 0° and 2° 145
Figure 5.14 Normalized velocity magnitude (V/V_j) for jet averaged velocity of 30 m/s, kerf thickness of 0.5 mm, and kerf wedge angles of 4° and 6° 146
Figure 5.15 Normalized velocity magnitude (V/V_j) for jet averaged velocity of 60 m/s, kerf thickness of 0.5 mm, and kerf wedge angles of 0° and 2° 148
Figure 5.16 Normalized velocity magnitude (V/V_j) for jet averaged velocity of 60 m/s, kerf thickness of 0.5 mm, and kerf wedge angles of 4° and 6° 149
Figure 5.17 Normalized velocity magnitude (V/V_j) for jet averaged velocity of 30 m/s, kerf thickness of 1.0 mm, and kerf wedge angles of 0° and 2° 150
Figure 5.18 Normalized velocity magnitude (V/V_j) for jet averaged velocity of 30 m/s, kerf thickness of 1.0 mm, and kerf wedge angles of 4° and 6° 151
Figure 5.19 Normalized velocity magnitude (V/V_j) for jet averaged velocity of 60 m/s, kerf thickness of 1.0 mm, and kerf wedge angles of 0° and 2° 152
Figure 5.20 Normalized velocity magnitude (V/V_j) for jet averaged velocity of 60 m/s, kerf thickness of 1.0 mm, and kerf wedge angles of 4° and 6° 153
Figure 5.21 Pressure coefficient in the symmetry plane for jet averaged velocity of 30 m/s, kerf thickness of 0.5 mm, and kerf wedge angles of 0° and 2° 154
Figure 5.22 Pressure coefficient in the symmetry plane for jet averaged velocity of 30 m/s, kerf thickness of 0.5 mm, and kerf wedge angles of 4° and 6° 155
Figure 5.23 Pressure coefficient in the symmetry plane for jet averaged velocity of 60 m/s, kerf thickness of 0.5 mm, and kerf wedge angles of 0° and 2°. 156
Figure 5.24 Pressure coefficient in the symmetry plane for jet averaged velocity of 60 m/s, kerf thickness of 0.5 mm, and kerf wedge angles of 4° and 6°. 157
Figure 5.25 Pressure coefficient in the symmetry plane for jet averaged velocity of 30 m/s, kerf thickness of 1.0 mm, and kerf wedge angles of 0° and 2° 160
Figure 5.26 Pressure coefficient in the symmetry plane for jet averaged velocity of 30 m/s, kerf thickness of 1.0 mm, and kerf wedge angles of 4° and 6° 161
Figure 5.27 Pressure coefficient in the symmetry plane for jet averaged velocity of 60 m/s, kerf thickness of 1.0 mm, and kerf wedge angles of 0° and 2° 162
Figure 5.28 Pressure coefficient in the symmetry plane for jet averaged velocity of 60 m/s, kerf thickness of 1.0 mm, and kerf wedge angles of 4° and 6° 163
Figure 5.29 Normalized temperature (T/T_j) in the symmetry plane for jet averaged velocity of 30 m/s, kerf thickness of 0.5 mm, and kerf wedge angles of 0° and 2° 164
Figure 5.30 Normalized temperature (T/T_j) in the symmetry plane for jet averaged velocity of 30 m/s, kerf thickness of 0.5 mm, and kerf wedge angles of 4° and 6° 165
Figure 5.31 Normalized temperature (T/T_j) in the symmetry plane for jet averaged velocity of 60 m/s, kerf thickness of 0.5 mm, and kerf wedge angles of 0° and 2° 166

Figure 5.32 temperature (T/T_j) in the symmetry plane for jet averaged velocity of 60 m/s, kerf thickness of 0.5 mm, and kerf wedge angles of 4° and 6° 167
Figure 5.33 Normalized temperature (T/T_j) in the symmetry plane for jet averaged velocity of 30 m/s, kerf thickness of 1.0 mm, and kerf wedge angles of 0° and 2° 169
Figure 5.34 Normalized temperature (T/T_j) in the symmetry plane for jet averaged velocity of 30 m/s, kerf thickness of 1.0 mm, and kerf wedge angles of 4° and 6° 170
Figure 5.35 Normalized temperature (T/T_j) in the symmetry plane for jet averaged velocity of 60 m/s, kerf thickness of 1.0 mm, and kerf wedge angles of 0° and 2° 171
Figure 5.36 Normalized temperature (T/T_j) in the symmetry plane for jet averaged velocity of 60 m/s, kerf thickness of 1.0 mm, and kerf wedge angles of 4° and 6° 172
Figure 5.37 Velocity magnitude along laser beam axis for two different averaged jet velocities, kerf thickness of 0.5 mm, and four kerf wedge angles..... 175
Figure 5.38 Velocity magnitude along laser beam axis for two different averaged jet velocities, kerf thickness of 1.0 mm, and four kerf wedge angles..... 176
Figure 5.39 Pressure distribution along laser beam axis for two different averaged jet velocities, kerf thickness of 0.5 mm, and four kerf wedge angles..... 178
Figure 5.40 Pressure distribution along laser beam axis for two different averaged jet velocities, kerf thickness of 1.0 mm, and four kerf wedge angles..... 179
Figure 5.41 Temperature distribution along laser beam axis for two different averaged jet velocities, kerf thickness of 0.5 mm, and four kerf wedge angles..... 181
Figure 5.42 Temperature distribution along laser beam axis for two different averaged jet velocities, kerf thickness of 1.0 mm, and four kerf wedge angles..... 182
Figure 5.43 Nusselt number distribution at five locations along the kerf wall for kerf thickness = 0.5 mm, averaged jet velocity = 30 m/s, and four kerf wedge angles 184
Figure 5.44 Nusselt number distribution at five locations along the kerf wall for kerf thickness = 0.5 mm, averaged jet velocity = 60 m/s, and four kerf wedge angles 186
Figure 5.45 Nusselt number distribution at five locations along the kerf wall for kerf thickness = 1.0 mm, averaged jet velocity = 30 m/s, and four kerf wedge angles 187
Figure 5.46 Nusselt number distribution at five locations along the kerf wall for kerf thickness = 1.0 mm, averaged jet velocity = 60 m/s, and four kerf wedge angles 188
Figure 5.47 Nusselt number distribution at location B (x = -0.000125, z = 0.000075 m) along kerf wall for kerf thickness = 0.5 mm, two averaged jet velocities, and four kerf wedge angles..... 191
Figure 5.48 Nusselt number distribution at location B (x = -0.000125, z = 0.000075 m) along kerf wall for kerf thickness = 1.0 mm, two averaged jet velocities, and four kerf wedge angles..... 192
Figure 5.49 Skin Friction distribution at five locations along the kerf wall for kerf thickness = 0.5 mm, averaged jet velocity = 30 m/s, and four kerf wedge angles 193
Figure 5.50 Skin Friction distribution at five locations along the kerf wall for kerf thickness = 0.5 mm, averaged jet velocity = 60 m/s, and four kerf wedge angles 195
Figure 5.51 Skin Friction distribution at five locations along the kerf wall for kerf thickness = 1.0 mm, averaged jet velocity = 30 m/s, and four kerf wedge angles 196
Figure 5.52 Skin Friction distribution at five locations along the kerf wall for kerf thickness = 1.0 mm, averaged jet velocity = 60 m/s, and four kerf wedge angles 197

Figure 5.53 Skin friction distribution at location B (x = -0.000125, z = 0.000075 m) along kerf wall for kerf thickness = 0.5 mm, two averaged jet velocities, and four kerf wedge angles 199
Figure 5.54 Skin friction distribution at location B (x = -0.000125, z = 0.000075 m) along kerf wall for kerf thickness = 1.0 mm, two averaged jet velocities, and four kerf wedge angles 200
Figure 5.55 Normalized velocity magnitude (V/V_j) for jet averaged velocity of 30 m/s, kerf thickness of 0.5 and 1.0 mm, and kerf wedge angle of 0°..... 202
Figure 5.56 Normalized velocity magnitude (V/V_j) for jet averaged velocity of 30 m/s, kerf thickness of 1.5 and 2.0 mm, and kerf wedge angle of 0°..... 203
Figure 5.57 Normalized velocity magnitude (V/V_j) for jet averaged velocity of 60 m/s, kerf thickness of 0.5 and 1.0 mm, and kerf wedge angle of 0°..... 206
Figure 5.58 Normalized velocity magnitude (V/V_j) for jet averaged velocity of 60 m/s, kerf thickness of 1.5 and 2.0 mm, and kerf wedge angle of 0°..... 207
Figure 5.59 Normalized velocity magnitude (V/V_j) for jet averaged velocity of 30 m/s, kerf thickness of 0.5 and 1.0 mm, and kerf wedge angle of 4°..... 208
Figure 5.60 Normalized velocity magnitude (V/V_j) for jet averaged velocity of 30 m/s, kerf thickness of 1.5 mm, and kerf wedge angle of 4° 209
Figure 5.61 Normalized velocity magnitude (V/V_j) for jet averaged velocity of 60 m/s, kerf thickness of 0.5 and 1.0 mm, and kerf wedge angle of 4°..... 210
Figure 5.62 Normalized velocity magnitude (V/V_j) for jet averaged velocity of 60 m/s, kerf thickness of 1.5 mm, and kerf wedge angles of 4°..... 211
Figure 5.63 Pressure coefficient in the symmetry plane for jet averaged velocity of 30 m/s, kerf thickness of 0.5 and 1.0 mm, and kerf wedge angle of 0°..... 212
Figure 5.64 Pressure coefficient in the symmetry plane for jet averaged velocity of 30 m/s, kerf thickness of 1.5 and 2.0 mm, and kerf wedge angle of 0°..... 213
Figure 5.65 Pressure coefficient in the symmetry plane for jet averaged velocity of 60 m/s, kerf thickness of 0.5 and 1.0 mm, and kerf wedge angle of 0°..... 214
Figure 5.66 Pressure coefficient in the symmetry plane for jet averaged velocity of 60 m/s, kerf thickness of 1.5 and 2.0 mm, and kerf wedge angle of 0°..... 215
Figure 5.67 Pressure coefficient in the symmetry plane for jet averaged velocity of 30 m/s, kerf thickness of 0.5 and 1.0 mm, and kerf wedge angle of 4°..... 217
Figure 5.68 Pressure coefficient in the symmetry plane for jet averaged velocity of 30 m/s, kerf thickness of 1.5 mm, and kerf wedge angle of 4° 218
Figure 5.69 Pressure coefficient in the symmetry plane for jet averaged velocity of 60 m/s, kerf thickness of 0.5 and 1.0 mm, and kerf wedge angle of 4°..... 219
Figure 5.70 Pressure coefficient in the symmetry plane for jet averaged velocity of 60 m/s, kerf thickness of 1.5 mm, and kerf wedge angle of 4° 220
Figure 5.71 Normalized temperature (T/T_j) in the symmetry plane for jet averaged velocity of 30 m/s, kerf thickness of 0.5 and 1.0 mm, and kerf wedge angle of 0°..... 223
Figure 5.72 Normalized temperature (T/T_j) in the symmetry plane for jet averaged velocity of 30 m/s, kerf thickness of 1.5 and 2.0 mm, and kerf wedge angle of 0°..... 224
Figure 5.73 Normalized temperature (T/T_j) in the symmetry plane for jet averaged velocity of 60 m/s, kerf thickness of 0.5 and 1.0 mm, and kerf wedge angles of 0° 225

Figure 5.74 Normalized temperature (T/T_j) in the symmetry plane for jet averaged velocity of 60 m/s, kerf thickness of 1.5 and 2.0 mm, and kerf wedge angle of 0°..... 226
Figure 5.75 Normalized temperature (T/T_j) in the symmetry plane for jet averaged velocity of 30 m/s, kerf thickness of 0.5 and 1.0 mm, and kerf wedge angle of 4°..... 227
Figure 5.76 Normalized temperature (T/T_j) in the symmetry plane for jet averaged velocity of 30 m/s, kerf thickness of 1.5 mm, and kerf wedge angle of 4° 228
Figure 5.77 Normalized temperature (T/T_j) in the symmetry plane for jet averaged velocity of 60 m/s, kerf thickness of 0.5 and 1.0 mm, and kerf wedge angles of 4° 229
Figure 5.78 Normalized temperature (T/T_j) in the symmetry plane for jet averaged velocity of 60 m/s, kerf thickness of 1.5 mm, and kerf wedge angles of 4°..... 230
Figure 5.79 Velocity magnitude along laser beam axis for two different averaged jet velocities, kerf thickness of 0.5, 1.0, 1.5, and 2.0 mm, and kerf wedge angle = 0° 233
Figure 5.80 Velocity magnitude along laser beam axis for two different averaged jet velocities, kerf thickness of 0.5, 1.0, and 1.5 mm, and kerf wedge angle = 4° 234
Figure 5.81 Pressure distribution along laser beam axis for two different averaged jet velocities, kerf thickness of 0.5, 1.0, 1.5, and 2.0 mm, and kerf wedge angle = 0° 237
Figure 5.82 Pressure distribution along laser beam axis for two different averaged jet velocities, kerf thickness of 0.5, 1.0, and 1.5 mm, and kerf wedge angle = 4° 238
Figure 5.83 Temperature distribution along laser beam axis for two different averaged jet velocities, kerf thickness of 0.5, 1.0, 1.5, and 2.0 mm, and kerf wedge angle = 0° 240
Figure 5.84 Temperature distribution along laser beam axis for two different averaged jet velocities, kerf thickness of 0.5, 1.0, and 1.5 mm, and kerf wedge angle = 4° 241
Figure 5.85 Nusselt number distribution at five locations along the kerf wall for kerf thickness = 0.5, 1.0, 1.5, and 2.0 mm, averaged jet velocity = 30 m/s, and kerf wedge angle = 0° 244
Figure 5.86 Nusselt number distribution at five locations along the kerf wall for kerf thickness = 0.5, 1.0, 1.5, and 2.0 mm, averaged jet velocity = 60 m/s, and kerf wedge angle = 0° 245
Figure 5.87 Nusselt number distribution at five locations along the kerf wall for kerf thickness = 0.5, 1.0, and 1.5 mm, averaged jet velocity = 30 m/s, and kerf wedge angle = 4° 246
Figure 5.88 Nusselt number distribution at five locations along the kerf wall for kerf thickness = 0.5, 1.0, and 1.5 mm, averaged jet velocity = 60 m/s, and kerf wedge angle = 4° 247
Figure 5.89 Nusselt number distribution at location B (x = -0.000125, z = 0.000075 m) along kerf wall for kerf thickness = 0.5, 1.0, 1.5, and 2.0 mm, two averaged jet velocities, and kerf wedge angle = 0° 250
Figure 5.90 Nusselt number distribution at location B (x = -0.000125, z = 0.000075 m) along kerf wall for kerf thickness = 0.5, 1.0, and 1.5 mm, two averaged jet velocities, and kerf wedge angles = 4°..... 251
Figure 5.91 Skin friction distribution at five locations along the kerf wall for kerf thickness = 0.5, 1.0, 1.5, and 2.0 mm, averaged jet velocity = 30 m/s, and kerf wedge angle = 0° 254

Figure 5.92 Skin friction distribution at five locations along the kerf wall for kerf thickness = 0.5, 1.0, 1.5, and 2.0 mm, averaged jet velocity = 60 m/s, and kerf wedge angle = 0° 255
Figure 5.93 Skin friction distribution at five locations along the kerf wall for kerf thickness = 0.5, 1.0, and 1.5 mm, averaged jet velocity = 30 m/s, and kerf wedge angle = 4° 256
Figure 5.94 Skin friction distribution at five locations along the kerf wall for kerf thickness = 0.5, 1.0, and 1.5 mm, averaged jet velocity = 60 m/s, and kerf wedge angle = 4° 257
Figure 5.95 Skin friction distribution at location B (x = -0.000125, z = 0.000075 m) along kerf wall for kerf thickness = 0.5, 1.0, 1.5, and 2.0 mm, two averaged jet velocities, and kerf wedge angle = 0° 259
Figure 5.96 Skin friction distribution at location B (x = -0.000125, z = 0.000075 m) along kerf wall for kerf thickness = 0.5, 1.0, and 1.5 mm, two averaged jet velocities, and kerf wedge angle = 4° 260
Figure 5.97 Normalized velocity magnitude (V/V_j) for jet averaged velocity of 30 m/s, kerf thickness of 2.0 mm, kerf wedge angles of 0°, and dimensionless standoff distances of 2.2 and 3.0 262
Figure 5.98 Normalized velocity magnitude (V/V_j) for jet averaged velocity of 60 m/s, kerf thickness of 2.0 mm, kerf wedge angles of 0°, and dimensionless standoff distances of 2.2 and 3.0 263
Figure 5.99 Pressure coefficient for jet averaged velocity of 30 m/s, kerf thickness of 2.0 mm, kerf wedge angles of 0°, and dimensionless standoff distances of 2.2 and 3.0 265
Figure 5.100 Pressure coefficient for jet averaged velocity of 60 m/s, kerf thickness of 2.0 mm, kerf wedge angles of 0°, and dimensionless standoff distances of 2.2 and 3.0 266
Figure 5.101 Normalized temperature (T/T_j) for jet averaged velocity of 30 m/s, kerf thickness of 2.0 mm, kerf wedge angles of 0°, and dimensionless standoff distances of 2.2 and 3.0 268
Figure 5.102 Normalized temperature (T/T_j) for jet averaged velocity of 60 m/s, kerf thickness of 2.0 mm, kerf wedge angles of 0°, and dimensionless standoff distances of 2.2 and 3.0 269
Figure 5.103 Velocity magnitude along laser beam axis for two different averaged jet velocities, kerf thickness of 2.0 mm, and two dimensionless standoff distances 271
Figure 5.104 Pressure distribution along laser beam axis for two different averaged jet velocities, kerf thickness of 2.0 mm, and two dimensionless standoff distances 273
Figure 5.105 Temperature distribution along laser beam axis for two different averaged jet velocities, kerf thickness of 2.0 mm, and two dimensionless standoff distances 274
Figure 5.106 Nusselt number distribution along the normalized kerf wall thickness for two different averaged jet velocities at nozzle exit and two dimensionless standoff distances 276
Figure 5.107 Skin Friction distribution along the normalized kerf wall thickness for two different averaged jet velocities at nozzle exit and two dimensionless standoff distances 277

DISSERTATION ABSTRACT

NAME: OMAR AHMAD MELHEM
TITLE: THREE-DIMENSIONAL SIMULATION OF LASER GAS-ASSISTED CUTTING: JET IMPINGEMENT CONSIDERATIONS
MAJOR: MECHANICAL ENGINEERING – THERMAL/FLUID SCIENCES
DATE: FEBRUARY 2010

A major laser machining operation is laser gas-assisted cutting, in which an impinging gas jet enhances heat transfer along the cut edges and serves in ejecting the phase-changed material from the kerf formed during the cutting process. Therefore, understanding and efficiently designing the process requires deep investigation into the impinging gas jet flow structure and the thermal effects occurring at the laser interaction zone. Numerical modeling of the process gives insight into the physical processes involved and provides a resources-efficient tool for parametric studies.

In this study, three-dimensional numerical simulations are conducted to study the fluid flow and heat transfer phenomena of nitrogen gas jet emerging from a conical convergent nozzle and impinging onto a laser produced kerf. The model incorporates the three-dimensionality associated with the laser cut kerf, of which no consideration is found in the open literature. The renormalization group (RNG) k-ε model with enhanced wall treatment is employed to account for turbulence. A finite-volume approach is utilized to discretize the governing equations and FLUENT 6.2.16 is utilized to conduct the simulations.

The study incorporates four averaged jet velocities at nozzle exit, two dimensionless standoff distances, four different kerf depths, and different kerf wall wedge angles. The flow field, local Nusselt number and skin friction distribution, mass flow rate factor, average Nusselt number at the kerf wall surface, and average skin friction at kerf wall surface are computed and analyzed.

It is found that the averaged jet velocity and kerf wedge angle have a major effect on local and average parameters being quantified. The effect of kerf depth is important but less pronounced. Moreover, the standoff distance is found to have a significant effect on the average Nusselt number and average skin friction. The results obtained are expected to be valuable in identifying effects of the key parameters on the flow and heat transfer phenomena associated with jet impingement in laser cutting process.

ملخص بحث

درجة الدكتوراة في الفلسفة

الاسم: عمر أحمد ملحم

عنوان الأُطروحة: محاكاة ثلاثيّة الأبعاد لعمليّة القطع بواسطة الليزر والمُعزّزة بالغاز المُساعِد: دراسة ظواهر دَهم المِنفَث الغازيّ

التخصّص: الهندسة الميكانيكيّة – علوم الموائع والحرارة

تاريخ التخرّج: فبراير ٢٠١٠

تُعتبر عمليّة القطع بواسطة الليزر والمُعزّزة بالغاز المُساعِد من أهمّ عمليّات التصنيع بواسطة الليزر، حيث يقوم المِنفث الغازيّ الداهم بتحسين الانتقال الحراري على طول الأطراف المقطوعة. ويقوم المِنفث الغازيّ أيضاً بعمليّة طرد المادّةِ المُحوّلةِ الطورِ من الثّلمِ الناشئِ عن القطع بواسطة الليزر. ولذلك كانت دراسة تركيب انسياب المِنفث الغازيّ ودراسة الآثار الحرارية الناتجة عنه عند نطاق التآثرِ بالليزر عنصراً أساسيّاً في فهم وفي تصميم عمليّة القطع بواسطة الليزر بكفاءة. ولمّا كانت النمذجة الرقميّة تؤدّي إلى زيادة التبصّر في الجوانب الفيزيائيّة لعمليّة القطع، ولمّا كانت تشكّلُ أداةً عالية الكفاءة للدراسات البارمتريّة، تمّ اعتماد النمذجة الرقمية لدراسة آثار المِنفث الغازيّ في هذه الأُطروحة.

تمّ في هذه الدراسة إجراء محاكاة رقميّة ثلاثيّة الأبعاد لدراسة ظواهرِ الانسياب والانتقال الحراري لمِنفثِ غاز النيتروجين المُنبثقِ من فُوّهةٍ مخروطيّة مُخصّرة والداهم على الثّلمِ الناشئِ عن الليزر. ويُدمِج النموذج طبيعة الثّلم الثلاثيّة الأبعاد حيث أنّه لم يتمّ العثور على اعتبارٍ مماثلٍ لهذه الخاصيّة في الأبحاث المنشورة. كما أنّه تمّ استعمال نموذج RNG مع المعالجة المُطوّرة للأسطح لحساب الاضطراب الدُوّاميّ. ومن ثمّ تمّ استعمال طريقة الحجم المحدود لتمييز المعادلات، وبرنامج FLUENT ٦.٢.١٦ لإجراء المُحاكاة الحسابيّة.

وتعتبر هذه الدراسة أربع قِيَمٍ لِمُعدّل سرعة الغاز على مخرج الفُوّهة، وقيمتين للمسافة اللابعديّة بين مخرج الفُوّهة والسطح المُعالج، وأربع قيم مختلفة لعُمق الثّلم، بالاضافة إلى قِيمٍ مختلفة لزاوية سطح الثّلم. ومن ثمّ تمّ حساب وتحليل حقلي الانسياب والانتقال الحراري بالإضافة إلى معدّل رقم Nusselt ومُعدّل الاحتكاك على سطح الثّلم وعامل نسبة الانسياب.

وأظهرت النتائج الأثر الكبير لكل من مُعدّل سرعة الغاز وزاوية سطح الثّلم في تغيير حقلي الانسياب والانتقال الحراريّ، في حين كان أثر عمق الثّلم ملحوظاً ولكن أقلّ أهميّة. أما بالنسبة للمسافة اللابعديّة بين مخرج الفُوّهة والسطح المُعالج فكان أثرها على مُعدّلات القِيم أكثرَ منه أهميّة على القِيمِ المحليّة. ويُتوقّع أن تكون النتائج الحاليّة بالغة الأهميّة في تحديد آثار العوامل الأساسية على ظواهرِ الانسياب والانتقال الحراري المُتعلّقة بالمِنفث الغازيّ الداهم على السطح المُعالج بواسطة الليزر.

CHAPTER 1

INTRODUCTION

Advanced machining processes are quite demanding and constitute critical areas of focus for research in the discipline of materials science and manufacturing. Lasers are considered to be the state-of-the-art machining tools for advanced manufacturing systems due their machining favorable characteristics. Laser machining applications have become an integral part of the aerospace, power generation, electronic, sheet-metal forming and other industries. However, in laser machining operations, the physical processes are complicated in nature and this requires deep understanding of the involved processes in order to ensure improved end-product quality. A major laser machining operation is laser gas-assisted cutting, in which an impinging gas jet plays the major role in the material removal process. Laser cutting process incorporates several thermo-mechanical phenomena several of which are effects of the impinging gas jet. Therefore, understanding and efficiently designing the process requires deep investigation into the impinging gas jet flow structure and the thermal effects occurring at the laser interaction zone. Considering the many processes and parameters involved, and the complexity of the fluid dynamic structure of jet impingement flows, a comprehensive experimental study of the cutting process is rather complex and expensive. In addition, experimental studies may not show a fixed pattern in different operating ranges, which makes it

difficult to achieve a comprehensive characterization of process behavior. Therefore, experimental studies need to be supplemented with numerical studies that should receive considerable attention in order to optimize the laser machining process and reduce the experimental time and cost.

1.1 BACKGROUND

"LASER" is an acronym for "light amplification by stimulated emission of radiation". Although the laser is normally considered to be a light source, it is also a form of energy that can be a useful source of intense heat when concentrated by focusing. In the context of machining operations, laser can be defined as a "machine tool" that produces a beam of light with several unique characteristics that make it favorable and efficient for materials processing. A laser beam is a coherent and amplified beam of electromagnetic radiation with wavelengths ranging from 0.2 to 500 μm; that is, from x-ray, through ultraviolet and visible, to infrared radiation. The beam is also characterized by its high directionality, high power density, and high focusing capability. The beam can also be manipulated with optical components to perform a variety of operations simultaneously, or switched between locations for sequential processing. Moreover, lasers are characterized by their precision, low cost, localized processing, and high speed of operation. Thus, lasers are considered to be the state-of-the-art machining tools for advanced manufacturing.

1.1.1 LASER APPLICATIONS

Applications of lasers in materials processing have been evolving since the development of the laser in 1960. The early applications focused on processes such as welding, machining, surface modification, and heat treatment. Newer processes that have evolved over the years include laser forming, shock peening, micromachining, and nanoprocessing. Laser machining applications have become an integral part of several industries such as the aerospace, power generation, electronic, and sheet-metal forming industries. Among various material processes using high power lasers, laser beam cutting has been the most established and accepted technology in industry for many years [1]. Laser cutting constitutes more than 60% of the total of all laser applications, covering around 85-90% of the technical market for high power lasers [1]. Laser processing dominates the market for industrial laser applications, with “metal sheet cutting more important than metal sheet welding and marking, as well as other applications that are not yet widespread" [1].

1.1.2 THE LASER MATERIAL INTERACTION PROCESS

Interaction of laser with materials usually leads to two types of damage, thermal and mechanical damage. Details of the two types of damage are provided by Kar and Mazumder [2].

1.1.2.1 Thermal Damage

Lasers are able to produce high energy concentrations because of their monochromatic, coherent, and low divergence properties compared to an ordinary light source. As a result,

they can be used to heat, melt and vaporize most materials. When laser light is focused on the surface of a solid target, a fraction of the laser energy is absorbed by the target material. This heats up the material to generate a heat-affected zone (HAZ) where the microstructure of the target material may alter. Also, such localized heating can produce an enormous amount of thermal stress to cause fracture in the material if the thermal stress exceeds the fracture strength of the material. As the irradiation continues, the target material may sublimate for very high laser intensity on the order of 10^9 W/cm^2 and short pulse duration on the order of 10 ns. This phenomenon can be called sublimation damage. On the other hand, if the laser intensity is low (on the order of 10^5 W/cm^2 or less) and the pulse duration is several milliseconds melting dominates. However, both melting and vaporization occur for laser intensity of the order of 10^7 W/cm^2 and pulses lasting several hundred microseconds leading to thermal damage of the material which can be classified as evaporative damage.

1.1.2.2 Mechanical Damage

Besides what is mentioned in the previous paragraph of fracture resulting in the material due to thermal stress, mechanical damage can also be caused to the target material with shock waves generated during laser-materials interaction. The shock waves are produced due to the recoil pressure of the vapor generated during rapid vaporization. Also, continuous exposure of the vapor to the laser beam may lead to the formation of plasma which, in turn, can interact with the laser beam to generate shock waves.

1.2 LASER CUTTING

Laser cutting is a thermal separation process widely used in shaping and contour cutting of sheet and plate stock in a wide variety of materials. In laser cutting, the focused laser beam is directed onto the surface of the workpiece to rapidly heat it up, resulting in melting and/or vaporization, depending on the beam intensity and workpiece material (Figure 1.1). The molten metal and/or vapor is then blown away using an assist gas. Cut surfaces are roughly parallel and straight edged. The diverging nature of the beam results in slight tapering. The workpiece thickness that can be cut with parallel sides is determined by the depth of focus[1] [3]. Plates that are thicker than the depth of focus normally result in tapered surfaces [3]. Furthermore, for effective removal of material from the cutting zone, the ratio of workpiece thickness to kerf width needs to be less than 20:1 for most metals, and less than 40:1 for ceramics [3]. The kerf is the slot or opening created by the cutting process.

[1] The depth of focus of a focusing system is the distance over which the workpiece can be moved from the original focal point without a significant change in the focused beam radius. A long depth of focus is good for laser cutting, where parallel-sided cuts are needed.

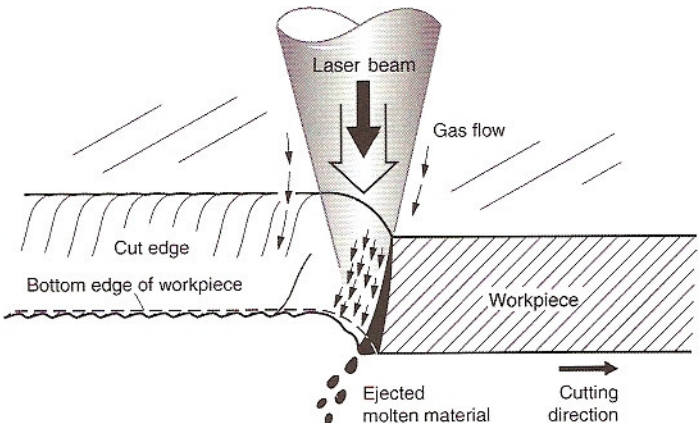

Figure 1.1 Schematic of the Laser Cutting Process [3]

1.2.1 FORMS OF LASER CUTTING

Laser cutting can occur in one of three forms: fusion cutting, sublimation cutting, and photochemical ablation.

1.2.1.1 Fusion Cutting

Fusion cutting involves melting of the base material, which is then ejected using a high-pressure assisting gas. This gas may be inert, in which case the energy for melting is provided entirely by the laser beam. It may also be oxygen (or air), which reacts with the base metal thus providing additional exothermic energy to enhance the process. A major problem of this form is the formation of striations (valleys and peaks that run along the thickness) on the cut surface and dross (molten material that clings to and solidifies on the underside of the cut edge as burr) at the lower cut edge.

1.2.1.2 Sublimation Cutting

Sublimation cutting involves vaporizing the base material along the cutting seam, which is often achieved using a pulsed beam and an inert gas jet coaxial with the beam to blow away the produced vapor. It is limited to thin sections since more energy is required per unit volume of material as compared to fusion cutting. However, it has the advantage of resulting in a narrower kerf width and a better surface quality.

1.2.1.3 Photochemical Ablation

Photochemical ablation involves generating little heat used in cutting organic materials, ceramics or difficult-to-cut materials. The material absorbs the laser beam's energy in a very thin layer near the surface (of the order of submicrons). This causes an almost

instantaneous ablative decomposition of the irradiated area (about 20 ns duration). It usually results in well defined cut edges, with minimum thermal damage to the surrounding area.

1.2.2 PROCESS DESCRIPTION AND CHARACTERIZATION

A laser beam is directed via a focusing lens onto the workpiece. A nozzle assembly, usually integral with the focusing assembly and coaxial with the beam, is used for directing the assist gas to the workpiece (Figure 1.1). Relative motion occurs between the laser beam and the workpiece.

The laser beam with high intensity creates a cutting front at which absorption of the beam takes place. The generated heat then diffuses into the surrounding material. The upstream material close to the laser beam melts and forms the melt film. The material in front of the beam may partly evaporate. The process gas is at high pressure in the nozzle and creates an under-expanded transonic gas jet that transfers momentum to the melt film. Consequently, the melt is vertically accelerated and ejected at the bottom of the kerf. Due to the quasi-stationary removal of molten material a cut kerf is formed so dividing the workpiece into two pieces.

In the initial stages of the process, the entire beam and gas jet hit the workpiece surface. However, once the process is initiated, a kerf is formed, and only a portion of the gas and laser beam impinges on the top surface of the workpiece directly ahead of the kerf. The remaining portion of the beam propagates downward into the kerf, and is partly absorbed at the front end of the kerf (erosion front), which is slightly inclined to the vertical.

Principal parameters that affect the laser cutting process include the following:

1. Beam characteristics.
2. Location of focal point relative to the workpiece surface.
3. Laser beam power.
4. Traverse (cutting) speed.
5. Assisting gas type and flow.

Beam characteristics, such as beam mode, stability, polarization, beam form, and focal position are important parameters to consider when optimizing cutting quality and kerf width. Beam power controls the maximum thickness that can be cut and/or speed at which it can be cut. Traverse speed depends on power such that the maximum speed that can be achieved for a given laser power decreases with increasing thickness of the workpiece. Corresponding to a workpiece thickness there is an upper and a lower limit for the traverse speed. Beyond the upper limit, cutting is incomplete. Below the lower limit, self-burning occurs, which often widens the kerf and produces rough surface. More information about these four parameters can be found in several references [3, 4, and 5]. The assisting gas flow parameter will be discussed in details in a following section because it is a core subject of this thesis.

1.2.2.1 Physical Phenomena

Physical phenomena taking place during laser cutting process are depicted in Figure 1.2 and described by Gross [1]. Considering the momentum transfer in the melt, the main driving forces are assist gas pressure, recoil pressure from the evaporating melt, surface tension, advection, Navier–Stokes stresses, Marangoni forces (due to the temperature-

dependent surface tension), viscous forcing of the melt by means of the assist gas jet, and gravity. At relatively low intensities the mass transfer is dominated by the advection of melt. A further contributor is evaporation which increases with temperature and decreases with ambient pressure. The energy transfer in the melt is described by considering advection, evaporation, radiation sink, a source representing the laser beam and convective heat transfer into the gas jet into account. Conduction increases with temperature when a temperature-dependent thermal conductivity is assumed. In the solid phase the energy transfer is described by considering a sink for solid-melt phase changes, radiation losses and conduction/convection.

Understanding the process thus requires studying the various phenomena incorporated. These include transmission, absorption, and reflection of radiant energy; conduction, convection, and radiation of thermal energy; temperature-dependent material properties; moving boundaries; melting; fluid flow; vaporization and gas dynamics.

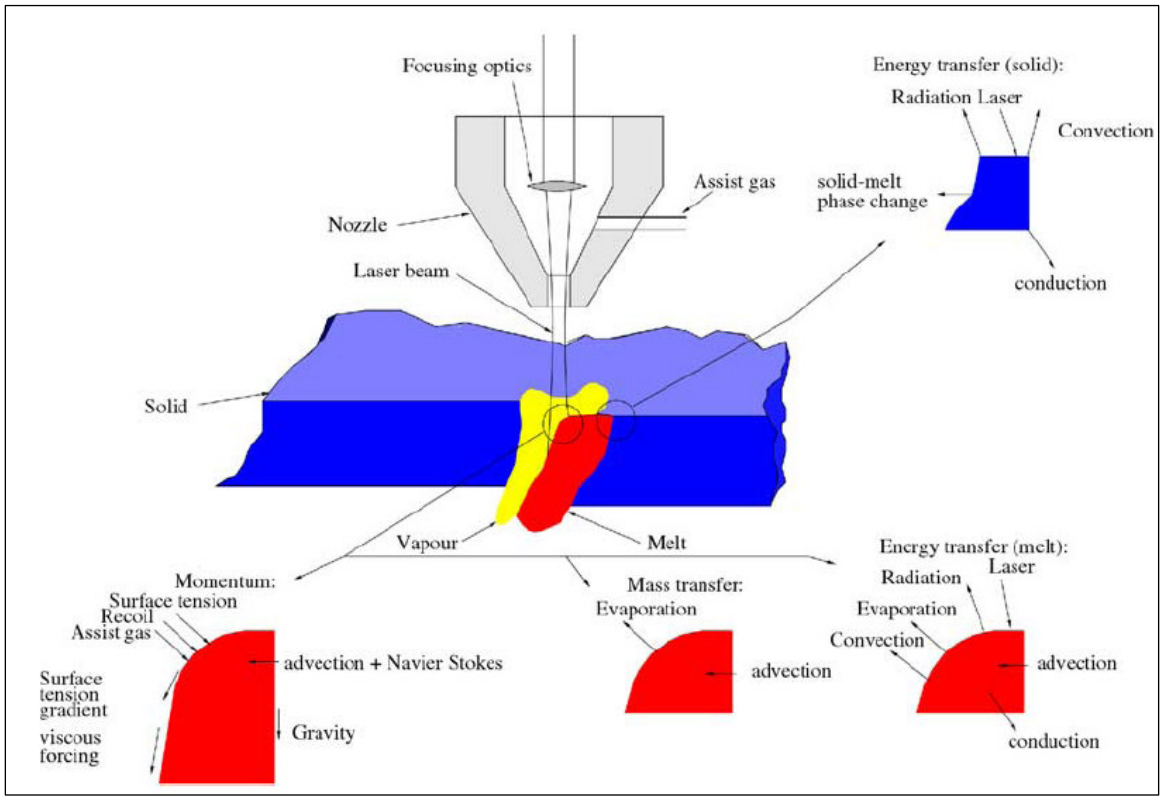
Focusing optics
Energy transfer (solid):
Radiation Laser
Convection
Assist gas
solid-melt
phase change
Nozzle
Laser beam
conduction
Solid
Vapour
Melt
Energy transfer (melt):
Laser
Radiation
Momentum:
Surface tension
Recoil
Assist gas
Mass transfer:
Evaporation
Evaporation
Convection
advection + Navier Stokes
advection
advection
Surface
tension
gradient
viscous
forcing
Gravity
conduction

1.2.2.2 Kerf Geometry and Melt Flow Characteristics

The kerf geometry resembles a half-conical surface with decreasing width from the top to the bottom of the sheet. For high beam intensities, the cutting front is almost vertical. For typical cutting conditions, the inclination of the cutting front to the vertical may increase to an inclination of 3° – 5° toward the bottom of the workpiece [3]. Kerf width obtained is related to the cutting speed such that narrower kerfs are produced at higher speeds. Consequently, the melt film thickness can become greater than the half-width of the kerf [6]. This is also due to the fact that increasing cutting speed determines an increase in the melt film thickness.

The molten material is removed by the gas jet with great efficiency, and usually a molten layer of certain thickness remains on the cutting front. There are two different forces acting on the molten material: the pressure gradient of the gas flow and the shear stress due to friction between the gas flow and the surface of the molten layer. These two forces are of the same order of magnitude in laser cutting. However, one of the two forces can be dominant. The flow profiles generated in the cases of either dominant shear stress or dominant pressure gradient differ essentially. The melt flow is shear stress driven if the cutting speed is low, the material is not too thick, and/ or the gas jet is intense. With increasing gas jet flow velocity, the molten layer thickness is decreasing because the removal is more efficient. On the other hand, with increasing cutting speed, the molten layer thickness is increasing since more molten material is produced/ unit time in the cutting kerf. Shear stress driven flow is more stable than the pressure gradient flow. A more stable melt flow is expected to cause diminished surface roughness [7]. On the

other hand, instabilities occurring for a pressure gradient controlled melt removal may result in ripple formation on the cutting surface [7].

1.2.3 ASSISTING GAS FUNCTIONS

The assisting gas used in laser cutting performs one or more of the following functions:

- Facilitates ejection of the phase-changed material through the backside of the workpiece. The impinging jet exerts the mechanical force required to drag away the melt/vapor from the cut zone. An effective removal of the molten layer leads to better cut quality.
- Enhances heat transfer. An assisting gas protects the cutting section from high temperatures through its shielding effect generated by forced convection. This effect is desirable when combustible materials are being processed. Moreover, it can reduce thermal deformation of processed materials.
- Acts as a heat source which results in an exothermic reaction that aids in cutting and improves process efficiency. A reactive gas, such as oxygen, enhances the oxidation process to provide additional exothermic energy that aids the cutting process. This is desirable when thick-section metals are being processed and also when higher cutting speeds are required.
- Protects the lens from spatter.

Common gases used include oxygen, air, inert gases, and nitrogen. Oxygen or air is used where exothermic reaction while cutting is desirable. In addition to the exothermic reaction that results, the use of oxygen assist in cutting also reduces the viscosity and surface tension for some metals, making it easier for the molten metal to flow. The flow

structure around the substrate significantly affects the material removal rate, the cutting depth, and the surface finish of the cutting front.

1.2.4 CUTTING QUALITY

Surface striations and dross formation are the most significant quality factors in laser cutting operations.

1.2.4.1 Striations of the Cut Surface

The surfaces cut using a laser beam normally have a nearly periodic striation pattern that results in a surface roughness. Striation formation is associated with the melt flow on the kerf walls. Primary causes of striations are:

1. Fluctuations in the laser power.
2. Fluctuations in the gas flow.
3. Hydrodynamics of the molten metal flow.
4. Vibrations in the motion unit.

1.2.4.2 Dross Formation

Dross is essentially material that clings to the lower edge of the workpiece, and appears as solidified drops after laser cutting. Dross attachment to the cut walls results from incomplete expelling of the melt from the bottom of the kerf by the impinging flow system. This takes the form of small metal droplets formed at the onset of the melt leaves the cutting kerf. Dross formation depends on the surface tension and viscosity of the molten material. The higher the surface tension or viscosity, the greater the tendency to form dross, since that prevents smooth flowing of the molten material out of the kerf.

1.2.5 MATERIAL CONSIDERATIONS

Laser can be used for cutting metals such as plain carbon steels, galvanized steel, stainless steels, alloy and tool steels, aluminum and its alloys, copper and its alloys, titanium and its alloys, and nickel and its alloys. It can also be used for cutting nonmetals such as polymers, composites, quartz, glass, ceramics, textiles, fabrics, wood, paper, and cardboard. The effectiveness of laser in processing a given material depends on material properties such as absorptivity at the given wavelength, reflectivity, thermal conductivity, melting point, boiling point, heat of reaction, and surface tension of the molten material.

Oxygen-assisted cutting is commonly used for cutting metals, which results in higher cutting speeds when compared to the inert gas cutting commonly used for nonmetals. Care should be exercised to establish balance between energy input and material output from the cut zone. An imbalance between the two factors will on one hand lead to material overheating and damaging and on the other hand to ineffective material removing. The process speed controls the energy input to the cutting zone at any particular point along the cut line. The effect of exceeding the maximum speed is similar to that of reducing laser power. Both lead to incomplete cutting because the cutting reaction cannot penetrate to the bottom of the sheet.

Laser cutting offers a number of advantages in cutting of nonmetals over conventional methods, which include a narrow high-precision kerf, ability to cut materials of any hardness, and small heat-affected zone. The share of nonmetals roughly accounts for 70% of the stock of the stock of materials cut with industrial lasers. The high absorptivity enables the laser beam to effectively couple to the target and to afford a large cutting depth.

The mechanism of shielding: The formation of erosion plume is often associated with laser cutting of materials that tend to evaporate rapidly. This erosion plume shields the target surface, absorbs the laser energy, and reduces the heat input rate. The mechanism of shielding differs between metals and nonmetals. In the interaction with metals, the beam of a 10^5 to 10^7 W/cm^2 power density initiates an optical breakdown in the vapor medium and the plasma plume so formed shields the target surface. On the other hand, the same power density is delivered to a nonmetal target causes the flow of vaporized material to carry out solid particles which tend to shield the target to a greater extent.

1.2.6 ADVANTAGES

The laser cutting process excels over competing technologies in several advantages:

1. It is a non-contact process which means that there is no tool force. Consequently, this reduces the restrictions on material positioning under the beam. That is, complex fixtures are unnecessary to hold workpiece. Moreover, it eliminates the phenomena of tool wear, tool breakage, and mechanical material breakage commonly encountered during conventional machining processes.
2. The small size of the focused beam results in very narrow kerf width (typically 0.05 to 1.0 mm) which permits carrying detailed work with minimum material loss.
3. The total heat input required for laser cutting is relatively small. This results in a small heat-affected zone size, of the order of 0.1 mm. Also, thermal distortion is generally avoided. Although laser cutting is a thermal process, the actual area

heated by the laser is very small and the thermal input to the bulk of the material is very low. Thus, there is very little damage to the base material. There is also very little residual stress and distortion.

4. Process cutting velocities are high compared to other cutting methods. With similar machined surface finish quality, the cutting speed for laser was 6 to 10 times higher than that of water jet [8].
5. Laser cutting process is independent of work piece mechanical properties and could thus be used to cut nearly all known materials whether very soft (highly deformable) or very hard (difficult to cut).
6. The process can be easily and fully automated.
7. The process is characterized by high degree of flexibility and low level of noise.
8. It results in cut edges that are square, and not rounded, as occurs in many other thermal cutting processes.
9. The process is characterized by high accuracy, and superior edge quality.

Because of these characteristics, "*laser beam cutting is superior to any cutting method conventional or non-conventional*" [1]. presents data comparing laser, oxyacetylene, and plasma-arc cutting processes with respect to kerf size and heat affected zone for low-carbon steel [3]. When compared to electrical discharge machining (EDM), laser cutting is performed at much higher speeds. EDM results in better accuracy, smaller kerf width, and smaller heat-affected zone size than laser cutting. However, the advantages with respect to these parameters are only slight [3].

TABLE 1.1 Comparison of Thermal Cutting Processes

	Laser	Oxy-Fuel	Plasma-Arc
Kerf size	0.3 mm	0.9 mm	3.2 mm
HAZ	0.05 mm	0.6 mm	0.4 mm

1.3 JET IMPINGEMENT

The previous discussion highlights the importance of the impinging gas jet in the laser cutting process. Laser serves as the heat source and the assisting gas jet serves as the material removing agent. The assisting gas jet emerges from the nozzle and impinges onto the cut kerf, whose side wall is at elevated temperature, typically the substrate melting temperature. The flow structure developed within the kerf region influences the heat transfer rates and skin friction in the irradiated region. Therefore, a brief description of the general flow and heat transfer phenomena associated with impinging jets is essential for discussions that will follow in subsequent chapters.

Jet impingement flows of various configurations are commonly used in numerous industrial applications such as drying of fabrics and films, cooling of turbine airfoils and high power density electronic components, tempering of glass, and processing of materials, because of their highly superior heat and mass transfer characteristics compared to those obtained in other flows.

1.3.1 JET IMPINGEMENT FLOW CONFIGURATIONS

Jet impingement heat transfer configurations may be grouped into two categories: free-surface jet impingement and submerged jet impingement. Free-surface jet impingement involves a jet of liquid discharging into an ambient gas and impinging on the target surface. With the submerged jet, the fluid is discharged into stagnant fluid of the same type. The flow phenomena in the two cases differ, and there are corresponding differences in the heat transfer characteristics of the two configurations. In the free-surface liquid jet negligibly small shear stress exists at the jet/gas interface. Consequently,

in the absence of significant gravitational acceleration, the nozzle exit velocity is preserved, virtually unchanged, until impingement occurs. Heat transfer from the targeted surface is, therefore, usually not greatly affected by changes in the nozzle-to-surface separation distance. The submerged jet configuration is characterized by a shear layer between the jet and the quiescent ambient fluid. For jet Reynolds numbers, Re_j (based on nozzle diameter), exceeding 1000, the shear layer is turbulent [9]. With increasing distance form the nozzle, momentum exchange between the jet and the ambient causes the free boundary of the jet or shear layer to broaden by entraining ambient fluid, while the potential core, in which the fluid velocity is unaffected by the shear layer, shrinks and eventually disappears. The length of the potential core varies with Re_j, achieving a value of 20 nozzle diameters at $Re_j = 1000$ and diminishing sharply thereafter to a minimum of approximately 5 nozzle diameters for Reynolds numbers in the range $3500 \leq Re_j \leq 5500$ [9]. With further increases in Reynolds number, the length of the potential core gradually increases to a maximum of approximately seven nozzle diameters [9]. In comparison to free-surface jets, submerged jet impingement heat transfer is more sensitive to the nozzle-to-surface separation distance, especially if the target surface is beyond the end of the potential core.

The flow field of a submerged plane or axisymmetric impinging jet can be divided into three separate regions: (1) the free jet region, (2) the impingement or stagnation flow region, and (3) the wall jet region. The free jet region is the region of the flow over which conditions are unaffected by the impingement surface. Depending on the nozzle-to-surface spacing the free jet region may display one or more of the following three characteristic regions: (1) potential core, (2) developing flow, and (3) developed

flow region. Downstream of the potential core the velocity profile is non-uniform over the entire jet cross section and the center velocity decreases with increasing distance from the nozzle exit. The impingement region is characterized by an increased static pressure as a result of the sharp decrease in mean axial velocity. The flow then deflects and starts to accelerate along the impingement surface. Then, accelerating flow in the stagnation zone is transformed to a decelerating wall jet due to entrainment of zero momentum ambient fluid. This applies to situations of normal impingement. For oblique impingement, it might be difficult to define the stagnation point. In certain conditions when the impingement surface is in motion, no stagnation point or region may exist.

One can define four characteristic jet patterns for circular free jets [10]:

1. Dissipated laminar jet, $Re_j < 300$
2. Fully laminar jet, $300 < Re_j < 1000$
3. Transition or semiturbulent jet, $1000 < Re_j < 3000$
4. Fully turbulent jet, $Re_j > 3000$

One can regard slot jets with $Re_j > 2000$ as turbulent. As mentioned above, the shear layer of submerged jets with Re_j exceeding 1000 can be considered turbulent [9]. In general, whether an originally laminar free jet is still laminar before impact depends on many factors such as Re_j, the velocity profile at the nozzle exit, the nozzle-to-surface spacing, whether the jet is confined or not, etc. [10]. All these factors affect the level of mixing at the outer jet boundaries which determines how fast the laminar jet transforms into a turbulent one.

1.3.2 DESIGN PARAMETERS

A large number of geometric and flow parameters is involved in the effective design of an impinging jet system for a given thermal application. Some important parameters are jet type, jet configuration, jet pressure, jet Reynolds number, nozzle design, nozzle-to-impinged surface spacing (standoff distance), material thickness, surface motion, angle of impingement, large temperature differences between the jet and the impingement surface, etc. The effects of these variables need to be characterized for better understanding of the effect on fluid flow and heat transfer and better design of the impingement flow system. In view of this complexity, experimental studies need to be supplemented by numerical investigations so as to obtain a satisfactory solution to the problem through extrapolation, interpolation, or even true prediction of complex impingement transport phenomena.

Although extensive research has been done on the subject over the past three decades, impinging jet flow and heat transfer remain an active area of research for both experimental and computational aspects because of the inherently complex fluid and heat flow characteristics.

1.4 NUMERICAL MODELING CONSIDERATIONS

In general cutting conditions, a turbulent gas jet impinges on the workpiece surface and penetrates into a narrow cut kerf whose side wall is maintained at a high temperature, which can be approximated by the melting temperature of the substrate material. A turbulent flow obeys the Navier-Stokes equations. Needless to say, there is no general analytical solution to this “formidable set of equations” [11]. Solving the Navier-Stokes equations for a turbulent flow is impossible because the equations are elliptic, non-linear,

and coupled (pressure-velocity, temperature-velocity). The flow is three dimensional, chaotic, diffusive, dissipative, intermittent, and most important possesses and infinite number of scales. One of the solutions is to reduce the number of scales by using the Reynolds decomposition. This decomposition will yield a set of equations governing the average flow field called Reynolds Averaged Navier Stokes Equations (RANS).

Thus, description of the flow field generated and the heat transfer effects associated requires solution of the Reynolds-averaged Navier-Stokes equations and the energy equation. Averaging of the Navier-Stokes equations results in additional unknown variables: the Reynolds stresses and the scalar transport terms. Detailed description of the Reynolds-averaged equations will be provided in chapter 3. Turbulence models are needed to predict and close the system of RANS equations and to determine these unknown variables in terms of known quantities.

1.4.1 TURBULENCE MODELING IN COMPUTATIONAL FLUID DYNAMICS

Turbulence modeling is a key element in Computational Fluid Dynamics (CFD) and the turbulence model equations pose special numerical difficulties that must be properly handled in order to obtain reliable numerical solutions [12].

With recent developments in computational fluid dynamics (CFD) packages, use of commercial CFD software has been proven to be a powerful tool in numerically experimenting with turbulence flow in general and various impinging jet problems in particular [13, 14]. One of the well-established CFD codes that is based on the finite volume method is FLUENT [15].

FLUENT is a state-of-the-art computer program for modeling fluid flow and heat transfer in complex geometries on a wide variety of grids. FLUENT provides complete mesh flexibility, solving flow problems with structured or unstructured meshes that can be generated about complex geometries with relative ease. Both single-block and multi-block structured meshes are acceptable, as well as hybrid meshes containing quadrilateral and triangular cells for two-dimensional models or hexahedral, tetrahedral, pyramid, and wedge cells for three-dimensional models. FLUENT is written in the C computer language and makes full use of the flexibility and power offered by the language.

1.4.2 TURBULENCE MODELING OPTIONS IN FLUENT

FLUENT provides the following choices of turbulence models to resolve turbulent flows:

I. Reynolds-averaging models

1. Spalart-Allmaras model
2. k-ε models
    a. Standard k-ε model
    b. Renormalization-group (RNG) k-ε model
    c. Realizable k-ε model
3. k-ω models
    a. Standard k-ω model
    b. Shear-stress transport (SST) k-ω model
4. v^2-f model
5. Reynolds stress model (RSM)

II. Filtering models

1. Large eddy simulation (LES) model

2. Detached eddy simulation (DES) model

Our choice of the turbulence model and its details will based on considerations such as physics encompassed in the flow, the established practice for the class of problems under which our problem falls, the desired level of details to be resolved, and the amount of time available for the simulations.

The first set of models are the closure models for the Reynolds-averaged Navier-Stokes (RANS) equations that govern the transport of the averaged flow quantities, with the whole range of turbulence scales being modeled. This type of modeling reduces the required computational effort, and is widely adopted for practical engineering applications. LES modeling is based on the filtered Navier-Stokes equations where large eddies are explicitly computed in a time-dependent simulation. Filtering is essentially a mathematical manipulation of the exact Navier-Stokes equations to remove eddies that are smaller than the size of the filter. Large computer resources are usually required to accurately resolve the energy-containing turbulent eddies in both space and time domains, which become severe in near-wall regions where the scales to be resolved become increasingly smaller. The DES forms a coupling between the LES and RANS modeling. Two separate regions are created in the flow domain: LES based region, which is normally associated with the high-Re core turbulent region where large turbulence scales play a dominant role and RANS based region, which is normally close to the wall where viscous effects prevail. The application of DES, however, may still require significant CPU resources. Taking into consideration that this work may represent a first step

towards modeling three-dimensional jet impingement in laser cutting applications, the LES and DES are excluded in the present investigation.

The Spalart-Allmaras model, the k-ε models, and the k-ω models use the Boussinesq hypothesis to relate the Reynolds stresses to the mean velocity gradients and close the RANS equations. In Cartesian tensor notation form the Boussinesq hypothesis can be written as:

$$-\rho\overline{u_i^{'}u_j^{'}} = \mu_t\left(\frac{\partial u_i}{\partial x_j} + \frac{\partial u_j}{\partial x_i}\right) - \frac{2}{3}\rho k\delta_{ij}$$

where μ_t is the turbulent viscosity. The disadvantage of this hypothesis is that it assumes μ_t is an siotropic scalar quantity, which is not strictly true. The other approach embodied in the RSM is to solve transport equations for each of the terms in the Reynolds stress tensor and an additional scale-determining equation. This means seven additional transport equations must be solved in 3D. Although the RSM is the most elaborate model that FLUENT provides, it might not always yield results that are clearly superior to the simpler models in all classes of flows [15]. In many cases, one can rely on models based on the Boussinesq hypothesis and avoid the additional computational expense of the RSM. However, in cases where anisotropy of turbulence has a dominant effect on the mean flow such as swirling flows and stress-driven secondary flows, the RSM is clearly superior.

The Spalart-Allmaras model is a relatively simple one-equation model that solves an additional modeled transport equation for the kinematic eddy (turbulent) viscosity. This model is a low-Reynolds-number model, requiring the viscous-affected region to be properly resolved. In FLUENT, however, this model has been implemented to use wall

functions when the mesh resolution is not sufficiently fine. However, it is still relatively new, and no claim is made on its suitability to all types of complex engineering flows [15]. Also, one-equation models are often unable to rapidly accommodate changes in length scale.

The standard k- ε model and its variants, the RNG k-ε and the realizable k-ε model, are the simplest "complete models" of turbulence. Each is a two-equation model in which the solution of two separate transport equations allows the turbulent velocity and length scales to be independently determined. The standard k-ε model is a semi-empirical model. The RNG k-ε model, derived using a statistical technique, is similar in form to the standard k-ε model, but includes the following refinements [15]:

- The RNG model has an additional term in its ε equation that significantly improves the accuracy for rapidly strained flows.
- The effect of swirl on turbulence is included in the RNG model, enhancing accuracy for swirling flows.
- The RNG theory provides an analytical formula for turbulent Prandtl numbers, while the standard model uses user-specified, constant values.
- While the standard model is a high Reynolds number model, the RNG theory provides an analytically derived differential formula for effective viscosity that accounts for low Reynolds number effects. Effective use of this feature, however, depends on an appropriate treatment of the near-wall region.

These features make the RNG k-ε model more accurate and reliable for a wider class of flows than the standard k-ε model. The Realizable k-ε model is relatively recent development and differs from the standard k- ε in two important ways:

- The realizable model contains a new formulation for the turbulent viscosity.
- A new transport equation for the dissipation rate has been derived from an exact equation for the transport of the mean-square vorticity fluctuation.

Both the realizable and RNG models have shown substantial improvements over the standard k- ε model where the flow features include strong streamline curvature, vortices and rotation [15].

The standard k-ω model in FLUENT is based on the Wilcox k-ω model, which incorporates modifications for low-Reynolds-number effects, compressibility, and shear flow spreading [15]. The shear-stress transport (SST) k-ω model is developed to effectively blend the robust and accurate formulation of the k-ω model in the near-wall region with the free-stream independence of the k-ε model in the far field.

The v^2-f model is similar to the standard k- ε model, but incorporates near-wall turbulence anisotropy and non-local pressure-strain effects. It is somewhat new addition in FLUENT and, its application in numerical heat transfer is not well documented. No further details about this model will follow.

1.4.3 CLOSURE

Many researchers simulated the turbulent impinging jet using different turbulence models. The standard k-ε model or its variations have been predominantly the models of choice by researchers to simulate turbulent impinging jets [14]. A brief reference to these studies will be made in this introductory chapter as a partial justification of our choice of the turbulence model for the present simulations. More details can be found in Chapter 2.

Morris et al. [16] used FLUENT to solve the thermal and flow fields due to a normally impinging, axisymmetric, confined, and submerged liquid jet on a square heat source. The authors indicated that the high degree of recirculation outside the stagnation region may be better predicted with relatively newer models such as the RNG k-ε model. Chen et al. [17] used the RNG k-ε turbulence model to model the interaction of a supersonic, turbulent axisymmetric jet with the workpiece in the context of laser machining. Experimental measurements obtained by the authors were found to match and hence validate the simulations. Shi et al. [18] simulated a single semiconfined turbulent slot jet impinging normally on a flat plate using the commercial finite volume code FLUENT 5.0. The authors explicitly stated based on their experience that "the RNG k-ε model is better suited than the standard k-ε model for simulating flow with high rates of strain (e.g. at the impingement point)". Ramezanpour et al. [19] applied two re-normalization group (RNG) k-ε and the basic Reynolds stress models by using enhanced wall treatment for near wall turbulent modeling to compute local Nusselt numbers due to inclined turbulent impinging jet discharged from a slot nozzle on a plate. They uniquely achieved a successful comparison with experimental data in locating the exact peak of the local Nusselt number on impinging plate by changing Reynolds number, nozzle height to nozzle hydraulic diameter ratio, and inclination angle.

This brief review of few of the successful applications of the RNG k-ε model in modeling turbulent impinging jet motivates the author towards choosing the RNG k-ε model to be used in the present simulations of the impinging gas jet effects in the context of laser cutting. Another reason for this motivation is the turbulence modeling options

available in FLUENT and the range of applicability and computational cost associated with each as described in section 1.4.2.

1.5 SCOPE AND OBJECTIVES

In laser gas-assisted cutting, a gas jet impinges on the workpiece surface and penetrates into a narrow laser-cut kerf. The gas jet plays the major role in the material removal process. Moreover, the assisting gas protects the cutting front from high temperatures through its shielding effect generated by forced convection. Therefore, the fluid structure in the kerf and the associated heat transfer rates from the kerf wall are major quality control factors. However, it is the small scale of operation in time and space which makes in situ measurements of the process variables so difficult and costly. Therefore, numerical modeling of the physical processes, which is the objective of the present study, can yield much insight into the complex phenomena occurring in the kerf region.

1.5.1 GEOMETRICAL AND MATHEMATICAL MODELING

The current effort aims at examining the gas jet effects by carrying out numerical simulations for a geometry that closely mimics the real laser cutting situation. The effects of several gas-jet related processing parameters are examined.

In order to achieve the abovementioned aim, a three-dimensional geometry which captures most of the significant flow features is presented. A conical convergent nozzle, which delivers the assisting gas jet, is incorporated because details of the flow at the nozzle exit are unavailable. By including the nozzle, we can apply a mass flow rate boundary condition which will be based on real cutting situations at the nozzle inlet. The

laser heating effect is modeled by assuming the kerf wall temperature to be close to the substrate melting temperature. Most important of all, the three-dimensionality of the kerf region is to be considered in the geometrical model. The flow domain is mapped onto a computational domain through constructing a **structured** grid.

In normal cutting situation, the compressible gas jet is of turbulent nature. Therefore, the flow and heat transfer fields are governed by the three-dimensional Favre-averaged Navier-Stokes and energy equations. Closure to the governing set of equations is established through the RNG k-ε model. The governing equations are solved numerically using the finite volume approach with the aid of the commercial CFD code FLUENT. Details of the flow field and heat transfer effects are extracted and examined. Chapter 3 includes full details on the geometrical and mathematical models and on the solution methodology.

1.5.2 VALIDATION OF THE TURBULENCE MODEL

Use of commercial CFD packages in general and use of FLUENT in particular has been proven to be a useful tool in numerically experimenting with various impinging jet problems [13, 16]. Moreover, several studies have showed through numerical simulations and experimental validations that the RNG k-ε model is suitable for simulating jet impingement flows and flows with high rates of strain (e.g. at the impingement point) [14, 19].

FLUENT will be used in the present study to model the fluid flow and heat transfer effects due to a turbulent jet impinging onto a laser cut kerf, using the RNG k-ε model. Moreover, the enhanced wall treatment will be employed to model the near wall

region. Therefore validation of the CFD solver is a must. No experimental work is available in the open literature which reports on the fluid flow in the three-dimensional kerf region and the associated heat transfer rates from the kerf wall. However, numerous data on local and average heat transfer rates in two-dimensional configurations are reported in the literature.

To validate the CFD solver, a complex test case for which reliable experimental data exists is used [20]. The test case will be described in detail in chapter 4 of this study. The test case considered should be able to demonstrate the ability of the selected turbulence model in describing the jet development, its impact, and the development in the flow that takes place downstream the impact/stagnation point.

1.5.3 IDENTIFYING AND STUDYING MAJOR PARAMETERS

Several parameters have been identified as important factors in studying jet impingement problems (see sections 1.2.2 and 1.3.2). This study considers nitrogen as the assisting gas. Compressibility effects are modeled using the ideal gas law. Moreover, properties are assumed to be temperature dependent for both the solid and fluid phases. This work presents results of simulation of the fluid flow and heat transfer behavior in impinging jet onto a cutting laser cut kerf using the RNG k-ϵ model. The modeling studies are carried out for four different mass flow rates at the nozzle inlet. Also, four different value of the material or kerf wall thickness are incorporated in the simulations, to examine the effect of the kerf wall thickness on the flow field in the kerf region and on the heat transfer rates from the kerf wall. Moreover, the effect of the kerf wedge angle is investigate by varying the kerf wedge angle from 0° to a maximum, whose value is constrained by the kerf wall

thickness and the kerf width or radius that is maintained at a constant value in the present study. Furthermore, the study is extended to include the effect of the nozzle-kerf surface separation (standoff) distance. Two values of the dimensionless standoff distance are incorporated in the present investigation.

A full record of the solution parameters considered in this work is presented in chapter 3. Selected results of the flow field variables, wall skin friction, and Nusselt number distributions are presented in chapter 5.

1.5.4 DISSERTATION CONTRIBUTION

According to the knowledge of the author, the present work will present the first numerical computations of flow variables and heat transfer rates associated with turbulent gas jet impinging onto a three dimensional laser cut kerf, whose wall is maintained at high temperature. The results obtained are expected to be valuable in identifying effects of the key parameters on the flow filed and heat transfer effects in laser gas-assisted cutting processes.

1.6 DISSERTATION ORGANIZATION

The present chapter has provided background material found to be essential for understanding following discussions. Chapter 2 will provide literature review of relevant work found in the open literature over the period 1987 up to present. Chapter 3 will be dedicated to mathematical modeling and problem definition. Chapter 4 will provide the validation of turbulence model and numerical solver. Chapter 5 will present the results and discussions. Chapter 6 will present conclusions and directions of future research.

CHAPTER 2

LITERATURE REVIEW

2.1 LASER CUTTING

Lot of work has been done to understand the laser cutting process in order to monitor and improve end-product quality. Researchers in the field have adopted approaches including theoretical studies, experimental investigations and/or numerical simulations.

One recent review of laser beam machining was made by Dubey and Yadava [21]. They reviewed research work in the area of laser beam machining, including laser cutting. They reported about several experimental and theoretical studies and examined critically several modeling and optimization techniques for the determination of optimum laser beam cutting condition. The concluded that researchers tried to optimize the laser beam cutting process through experiment based, analytical, and artificial intelligence based modeling and optimization techniques. However, modeling and optimization of laser beam cutting with multi-objective, and with hybrid approach were nonexistent in literature. It was also concluded that the two extreme application areas such as machining of thick materials and machining of micro-parts required considerable research work.

Gross [22] presented an almost comprehensive record of the literature concerning the modeling of laser cutting since the year 1980 up to 2009. Gross noted that most of the

available work uses some sort of simplification the choice of which was guided by the preference of the investigators who often find themselves in the situation where they had to fit their model to the computational resources at hand, thus sacrificing detail. Gross emphasized the need for comprehensive and non-biased simulation.

Research carried out in the area of laser cutting can be classified into experimental studies and modeling studies. Experimental studies on laser cutting show the effect of process input parameters such as laser power, type and pressure of assisting gas, cutting material thickness and its composition, cutting speed and mode of operation (continuous or pulsed mode) on quality or process performance. The quality characteristics of interest are material removal rate, kerf width, surface quality (striation formation, dross adhesion), and metallurgical characteristics (recast layer, oxidized layer, heat affected zone). On the other hand modeling studies are scientific ways to study system behavior and get better understanding of this complex process. Models can be divided in three categories: experimental or empirical models, analytical models, and artificial intelligence based models [21]. Analytical models are mathematical models based on basic laws and principles and can be divided in three categories: exact solution based model, numerical solution based model, and stochastic solution based model.

2.1.1 EXPERIMENTAL STUDIES

Chen [23] examined the kerf width obtained during CO_2 laser cutting of 3 mm thick mild steel sheet for three different assisting gases at high pressure: oxygen, nitrogen, and argon at high pressure. It was found that the cutting quality of inert laser cutting could be improved significantly by using high cutting gas pressure. He showed that an acceptable

quality cutting region did not exist for pure oxygen pressure of 10 bar within specified laser power and cutting speed range because of the side-burning effect that always appeared on the top of the cut surface. The author concluded that whilst oxygen cutting was the best, nitrogen and argon may be used. Air, however, was inferior to these gases as an assistant gas.

Wang et al. [24] examined CO_2 laser cutting coated steel sheets. They found that decreasing power and increasing feed rate generally lead to a decrease in heat affected zone (HAZ). It was also observed that increasing oxygen pressure increased the HAZ.

O'Neill and Gabzdyl [25] conducted an experimental and theoretical analysis to study a newly proposed process termed the laser-assisted oxygen process for cutting thick steel sections. They demonstrated that dross-free deep section cuts were possible at an incident power level of 1 KW provided that the gas jet impingement area was greater than the ignition temperature of the steel.

Karatas et al. [26] examined the influence of laser beam waist position relative to the work piece surface and the work piece thickness on the striation formation. It was found that beam waist position had significant effect on the kerf size. It was also found that the kerf width reduced to minimum when the focus setting is kept on the workpiece surface for thin sheets (1.5 mm) and inside the workpiece for thicker sheets (3.5 mm) during hot rolled and pickled steel cutting. They also reported that stria width and depth increased with increasing work piece thickness. Moreover, thermal stresses well above the yielding limit of the substrate material were reached in the resolidified material because of the non-uniform flow and cooling rates of molten metal across the kerf surface.

2.1.2 MODELING STUDIES

Vicanek et al. [7] presented a mathematical dynamic model for the melt ejection by a gas jet in laser cutting. The thickness of the molten layer and its velocity of flow were obtained as functions of the cutting speed, gas stream velocity and the viscosities and densities of the melt and the gas. They performed a stability analysis which showed that instabilities occur for a pressure gradient controlled melt removal (see section 1.2.2.2). These instabilities were then correlated with ripple formation on the cutting surface.

Vicanek and Simon [27] theoretically investigated the forces exerted by inert gas jet on the molten layer formed on the cutting front in laser cutting. It was reported that the two driving forces acting on the melt, the one being due to pressure gradient and the other due to shear stress were of the same order of magnitude. It was also found that both forces were increasing with increasing gas velocity. Both forces were also increasing with increasing angle of inclination of the cutting front. Finally, the cooling of the melt due to the gas jet was shown to be negligible compared to the incident laser beam power.

Farooq and Kar [28] presented a model of melt removal during laser materials processing to investigate the effect of assist gas pressure on the material removal rate. Melt depth, cut depth, and kerf width were modeled. The cut depth was found to reach a constant value beyond a critical pressure. It was also found that the cutting speed decreased when the assist gas pressure exceeds a critical value if the kerf dimensions were smaller than the nozzle dimensions leading to shock formation above the substrate surface.

Kaplan [29] presented an analytical model of laser beam cutting of metals both for reactive and inert assisting gases. It was found that the kerf width decreased with

increasing cutting speed due to heat conduction, whereas cutting front angle and absorption together with thickness, speed and temperature of the melt film all increased. In laser oxygen cutting all molten metal reacted at low speeds and self-burning can appear. However, with increasing speed the laser beam absorption became more important and the diffusion limited oxide layer became much thinner than the growing total melt film.

Schulz et al. [30] investigated the dynamical behavior of the laser beam fusion cutting process of metals. A model was obtained which described the shape of the evolving cutting kerf and the melt flow. The nonlinear response of the dynamical system on modulated laser beam power and on accelerated movement of the laser beam axis were identified as typical dynamical properties of the process, which were important for technical applications like contour cutting. It was found that surface tension effects had negligible contributions at the cutting front but might become dominant at the lower edge of the cutting front, where the molten material separated from the solid material.

Tani et al. [6] developed an analytical model for the evaluation of the melt film geometry in laser cutting of steels. The film thickness and velocity were determined as a function of the kerf depth, for both reactive and non-reactive process gases. Two criteria were then adopted to predict the quality of the laser cutting operation as far as dross formation is concerned: the first was based on a minimum acceptable value of the ejection speed of the melt from the bottom of the kerf, the second on the occlusion of the kerf itself due to an excess of molten material in the boundary layer at the kerf width. The authors then demonstrated a relationship between the occurrence of dross adhesion and

the different mechanisms predicted for such a phenomenon: unsatisfactory ejection speed of the melt film from the bottom of the kerf and occlusion of the kerf.

Yilbas [31] examined different aspects of gas assisted laser cutting and developed a kerf width model using scaling laws for oxygen-assisted laser cutting of mild steel. Contribution of high temperature oxidation reaction was accommodated in the analysis. It was determined that kerf width reduced with increasing laser beam scanning speed and increases with increasing laser output power. It was also observed that the cut quality improved as laser beam scanning velocity increased provided that beyond the limit cutting ceased. Also, first law efficiency of the process improved as laser beam scanning speed and work piece thickness increased. Kerf width results at low cutting speeds were validated against experimental results obtained by the author.

Tani et al. [32] presented a 3D analytical model to analyze striation and dross formation. Through considering mass, force, and energy balances, the model evaluated the geometry of the cutting front, and the geometry and temperature fields of the melt film. It was found that the transition of the melt from a free flow to a constricted flow at high process speed can explain the characteristic two-slope pattern of striation, in proximity of the occlusion of the kerf. Also, at high speeds, narrow kerfs were produced, so that melt film thickness became greater than kerf half-width. The mechanics of dross adhesion were also discussed, by introducing the kinetic energy of the melt film and relating it to the local temperature.

Yilbas and Abdul Aleem [33] used lump parameter analysis to study dross ejection during laser cutting of metallic substrate and formulate melt thickness in the cutting section. They reported that increasing laser power enhanced the thickness of the

liquid layer formed during the cutting process, while increasing assisting gas jet velocity lowered liquid layer thickness. Spherical droplets were formed whose predicted size agreed well with experimental results obtained by the authors from a CO_2 laser cutting experiment.

Yilbas [34] investigated the effect of laser cutting parameters, in particular laser output power, cutting speed, and oxygen assisting gas pressure, on end product quality of thick mild steel sheets. He formulated the thermal efficiency of the cutting process, liquid layer thickness and specific energy required for the cutting. He conducted factorial analysis and experimental tests to identify the significant effects of the parameters and their first order interactions on the cut quality. It was also observed that the coupling effects of oxygen pressure and laser power and that of oxygen pressure and cutting speed and that of laser power and cutting speed influenced the percentage of kerf size variation significantly. Thermal efficiency improved at low power intensities and high cutting speeds, provided that once the power intensity was reduced below threshold deep melting occurred at the work piece surface and replaced through cutting.

The interaction of a supersonic, turbulent axisymmetric jet with the workpiece was studied by Chen et al. [17] through simulating the influence of processing parameters on the shock structure of the gas flow. Both numerical modeling and experimental validation were performed. Predictions of the pressure, mass flow rate as well as the shear force at the machining front were made. Also, effects of gas pressure and nozzle standoff distance on structure of the supersonic shock pattern were studied. It was found that the interaction of the oblique incident shock with the normal standoff shock contributed to a large reduction in the total pressure at the machining front. The

associated reduction in flow rate, fluctuations in the pressure gradient and shear force at the machining front could reduce the material removal capability of the gas jet and possibly result in a poorer surface finish.

Mai and Lin [35] numerically simulated the flow structure of a supersonic impinging jet from a straight nozzle for laser cutting of a substrate with varying inclined angles. The numerical results were in good agreement with the experimental flow visualization they performed. It was demonstrated that shock waves were generated in the jet streams due to the extreme change of pressure and density of the flow at the nozzle outlet. Shock waves reflected from the wall of the inclined substrate resulting in an axisymmetric pressure distribution. Their results demonstrated a steep pressure gradient along the wall of the substrate when the inclined angle was large which consequently implied a strong variation of wall shear force in inclined plate cutting.

Gross [1] presented a numerical analysis for the laser cutting process using a three-dimensional fully coupled model highly minimizing simplifications. His model considered the physical phenomena depicted in figure 1.1 (Chapter 1) and thus presented to be the most comprehensive model available to the date of his research. For the first time in research, energy exchange from the work piece to the gas jet had been considered. Further, no assumptions were made about either the kerf geometry or its dimensionality. However, the assist gas was modeled assuming a non-viscous ideal gas and neglecting the turbulent nature of the jet flow. I assume this reduced from the presented model comprehensiveness. He concluded that gas flow pattern was intrinsically three-dimensional and reduction in model dimension simplification was inadequate for the investigation of the complete process. It was stated that to that date “only” qualitative

interpretations can be made because the available computer hardware can not perform three-dimensional simulations of laser materials processing at the necessary detail and at reasonable cost.

Schulz et al. [36] performed simulation studies of the laser cutting process. The cutting process was first described with a spatial three-dimensional Free Boundary Problem for the motion of one phase boundary in order to reproduce details of the ripples evolving at the cut surface. The model was then improved to include the melt flow phenomenon using two phase problem formulation. The dynamic model predicted modulation frequency for the laser power that leaded to almost suppression of adherent dross in contour cutting. The model was further improved to analyze the gas flow phenomenon and study the interaction of the gas flow with the condensed phase.

2.2 JET IMPINGEMENT

Considerable research work has been done to investigate the flow field structure of impinging jets and the heat transfer effects. Researchers have investigated different aspects of the phenomenon theoretically, experimentally, and numerically. Reviewing these studies is essential to our problem which involves a gas jet emerging from the nozzle and impinging onto a laser irradiated work piece surface. Extensive studies covering several aspects of turbulent impinging jets have been reviewed by several authors.

Polat et al. [10] presented an extensive literature review of the developments in the numerical prediction of impingement transport processes and of the pertaining studies prior to 1989. Computational results pertinent to selected configurations were analyzed.

They indicated that prediction of flow, heat, and mass transfer under a single, semi-confined turbulent jet might be employed as a good test for new turbulence models. Areas of further studies in light of the state of the art in modeling impingement flows were highlighted.

2.2.1 EXPERIMENTAL STUDIES

Baughn and Shimizu [37] considered a single circular turbulent air jet at ambient temperature impinging on a flat stationary surface with uniform heat flux. A long pipe of diameter D was used to ensure fully developed flow at the jet exit, which was at a distance Z from the impinged surface. Distribution of Nusselt number along the surface was determined for different values of Z/D (Z/D = 2, 6, 10, 14) at a Reynolds number of 23,750. The maximum stagnation point heat transfer was found to occur at a Z/D of approximately 6.

A turbulent jet impinging orthogonally onto a large plane surface was considered by Cooper et al. [38] to provide data suitable for assessing the adequacy of turbulence models at predicting impinging and related shear flows. A fully developed flow was reached at the exit plane of the jet – a feature which would help in using the data for turbulence-model evaluation. A companion numerical study [66] confirmed that the group of flows considered by the authors did indeed serve as a powerful discriminator between models.

Mohanty and Tawfek [39] experimentally measured heat transfer rates from an isothermal plate due to a normal round impinging air jet. Different diameter circular nozzles were considered and nozzle to plate distance ratio was varied. It was found that

the heat transfer rate decayed exponentially with radial distance from the highest value at the impingement point. Stagnation Nusselt number was found to increase with increasing Reynolds number. The stagnation Nusselt number also increased with increasing nozzle diameter but increased at a slower rate with increasing Reynolds number.

Womac et al. [9] experimentally measured heat transfer between small square heat sources and circular impinging liquid jets for both the *free-surface* and *submerged* jet configurations. It was observed that under submerged jet conditions, the heat transfer coefficient was influenced by the location of the heater relative to the potential core of the jet. The heat transfer coefficient varied weakly with the separation distance S for S/D ≤ 4 (d is nozzle diameter), while much stronger variations existed for greater values of S/D. Two new correlations, one for each of the considered configurations, for the average Nusselt number were developed over parameter ranges applicable to the cooling of microelectronic chips.

Huang and El-Genk [40] experimentally investigated the heat transfer rates for a uniformly heated flat plate impinged by a circular air jet. Their results showed that the maximum stagnation Nusselt number occurred for certain nozzle exit-to-plate spacing and that the average Nusselt number was a strong function of both nozzle exit-to-plate spacing and radial distance from stagnation point. Their results also led to a correlation for the average Nusselt number in terms of *Re* and *Pr*.

Lytle and Webb [41] conducted an experiment to investigate the flow structure and heat transfer of air jet impingement at nozzle-plate spacings of less than one nozzle diameter. They determined a stagnation point minimum and an inner and outer peak in the local heat transfer. They obtained a correlation for Nu which revealed that stagnation

point heat transfer coefficients increased significantly for decreasing nozzle-plate spacings.

Elison and Webb [42] investigated heat transfer to liquid jets impinging normally on a constant heat flux surface. Free-surface and submerged impinging liquid jets in the initially laminar, transitional, and turbulent flow regimes (at the nozzle exit) were considered. They determined correlations for *Nu* corresponding to different flow regimes. For the fully turbulent jet, the free surface configuration data showed little dependence on nozzle-to plate spacing. By contrast, the submerged jet data exhibited the usual potential core behavior for turbulent flow.

Bizzak and Chyu [43] calculated the local heat transfer coefficient about the stagnation point due to jet impingement onto flat surfaces. Their results were in excellent agreement with theoretical and pertinent empirical data. The experiments were performed to test a thermal imaging system for transient two-dimensional surface temperature measurement, suitable for use in calculating local heat transfer rates.

Wolf et al. [44] experimentally investigated the flow structure of a free-surface, planar jet of water impinging normally on a uniformly heated surface. They measured the mean velocity and turbulence intensity within the jet and the velocity gradient along the impingement surface. They found that the mean velocity profile across the jet width was uniform, and independent of exit condition, distance from nozzle exit, and *Re*. They also indicated that the lateral profiles of the turbulence intensity became more homogeneous with streamwise distance, and that the velocity gradient along the impingement surface was almost insensitive to *Re*.

Wolf et al. [45] used the flow structures identified in the previous paper and presented their effects on local heat transfer. Correlations were developed for both the onset of transition to turbulence and the dimensionless convection coefficient at the stagnation point. The effect of streamwise turbulence intensity on the convection coefficient was shown to scale approximately as the one-quarter power.

Garimella and Rice [46] experimentally investigated flow structure and heat transfer from a small square heat source to a normally impinging, axisymmetric, and submerged liquid jet in confined and unconfined configurations. Their results showed that for a given flow and nozzle exit-to-plate spacing, smaller nozzles produce higher heat transfer coefficients. Secondary peaks in the local heat transfer coefficient observed were more pronounced at the smaller (confined) spacing and larger nozzle diameter for a given Reynolds number, and shifted radially outward from the stagnation point as the spacing increased. The secondary-peak magnitude increased with Reynolds number, and was higher than the stagnation value in some instances. They proposed correlations for the stagnation point and area-averaged heat transfer coefficients.

Lee *et al*. [47] determined the heat transfer coefficient due to axisymmetric air jet impingement on a flat plate with constant heat flux. A fully developed turbulent velocity profile was assumed. They indicated that the stagnation point Nusselt number Nu_{stag} is nearly independent of nozzle exit-to-plate spacing below a certain value of this spacing and below a certain range of *Re* values. They also derived correlations for the variation of Nu_{stag} with Re for different nozzle-to-plate distances. They have also shown that over a certain range of *Re* the local *Nu* decreases monotonically from its maximum value at the stagnation point.

The effects of nozzle diameter on heat transfer and fluid flow for a round turbulent jet impinging on a flat plate surface were investigated by Lee et al. [48]. A fully developed velocity profile was reached at the nozzle exit, and a uniform heat flux boundary was created at the plate surface. Results showed that the local Nusselt numbers in the stagnation point region increased with the increasing nozzle diameter. This may be attributed to an increase in the jet momentum and turbulence intensity level with the larger nozzle diameter, which resulted in the heat transfer augmentation. However, the effect of the nozzle diameter on the local Nusselt numbers at the wall jet region was negligibly small. This may be attributed to the fact that the impinging jet flow characteristics were almost lost in the process of the re-development of the boundary layer after the jet impinges on the plate.

Fenot et al. [49] experimentally studied heat transfer between a flat plate and a single round high temperature impinging jet. It was shown that Nusselt number distributions will not depend on the jet injection temperature up to 140 ˚C if the adiabatic wall temperature was used as the reference temperature.

Dano et al. [50] experimentally studied the effect of the nozzle geometry on the flow and heat transfer characteristics of confined jet array impingement with cross flow. An isothermal surface and a uniform heat flux boundary conditions at the impinging surface were presented. Circular and cusped ellipse nozzle geometries were studied. It was observed that the flow development from the cusped ellipse nozzle affected the wall region flow more than the circular nozzle, as influenced by the cross-flow interactions. They found that cusped ellipse jets increased the heat transfer from the impingement

plate with uniform heat flux at high *Re*. The authors recommended that more detailed three-dimensional studies should be carried out.

The nonlinear flow and heat transfer characteristics for a slot jet impinging on a slightly curved concave surface were investigated by Eren et al. [51]. Constant heat flux was applied to the surface to obtain impingement cooling by air jet at ambient temperature. New correlations for local, stagnation point, and average Nusselt numbers as function of jet Reynolds number and dimensionless circumferential distance were obtained.

San and Shiao [52] studied the effects of jet plate size and plate spacing in the heat transfer characteristics for a confined circular air jet vertically impinging on a constant surface heat flux flat plate. The jet after impingement was restricted to flow in two opposite directions. It was found that the stagnation Nusselt number increased with Re, but decreased with an increase of the jet plat width-to-jet diameter ratio and jet plate length-to-jet diameter ration. It was also found that the stagnation Nusselt number decreased as plate spacing-to-jet diameter ratio. This was attributed to the increase in the mixing length between the jet and recirculation flow.

Zhou and Ma [53] experimentally investigated the radial heat transfer behaviors of impinging submerged circular jets. They obtained correlations for the local heat transfer rates at given radial locations and different nozzle-to-plate spacings. They indicated that the exponent of jet Reynolds number of *Nu~Re* expression implied a flow pattern of the working fluid regardless of jet type.

Yuan et al [54] considered heat transfer of swirling and conventional CO_2-air submerged jet impingement. It was revealed that the swirling of the jet improved the

radial uniformity of the heat transfer significantly. The heat transfer deteriorated in the stagnation region but got enhanced in the wall jet region. In addition, the swirling jet enhanced the heat transfer in terms of the mean Nusselt number in a larger area.

O'Donovan and Murray [55, 56] performed a two part investigation of heat transfer distributions from a heated flat surface subject to an axially symmetric impinging air jet. It was shown that at low nozzle to impingement surface spacing the mean heat transfer distribution in the radial direction exhibited secondary peaks. These peaks were reported by several investigators and attributed, in general, to an abrupt increase in turbulence in the wall jet boundary layer. It was also shown that the magnitude of the secondary peak in the Nusselt number distribution was influenced more by velocity fluctuations normal to the surface than by fluctuations parallel to the surface. It was shown in the second part that vortices that roll-up naturally in the shear layer of the free jet moved upon impingement along the wall jet before being broken down. These vortices were eventually broken down and the turbulence level within the wall jet increased significantly, which in turn increased the heat transfer, leading to a secondary peak in the heat transfer distribution. It was also shown that vortices that impinged at later stages in their development were weaker and therefore induced smaller velocity fluctuations normal to the surface. This did not enhance the heat transfer in the wall jet to the same extent as stronger vortices did.

Zhou and Lee [57] investigated the fluid flow and heat transfer characteristics of air jet exiting a sharp-edged rectangular nozzle and impinging on a heated flat plate. Results showed that the jet Reynolds number and nozzle-to-plate spacing had a significant influence on heat transfer behaviors of impinging jet.

The flow field topology of a confined turbulent slot submerged air jet impinging normally on a moving flat surface was investigated by Senter and Solliec [58]. Measurements of the mean velocities and turbulent quantities were presented in the main characteristic regions of the jet: the potential core, the intermediate zone, and the impinging zone. The flow field patterns at a given surface-to-jet velocity ratio were independent of the jet Reynolds number in the range investigated. However, it was found that the surface-to-jet velocity ratio appeared as the influencing parameter on the flow field topology, independently of the Reynolds number in the studied range.

The effects of concave hemi-spherical surface with an inclined angle on the local heat transfer from a turbulent round impinging jet were studied by Lee et al. [59]. Correlations of the stagnation point Nusselt number in terms of Reynolds number, jet-to-surface distance ratio, and dimensionless surface angle were presented. It was found that the displacement in the upstream direction of the maximum Nusselt number from the stagnation point increased with increasing surface angle or decreasing nozzle-to-surface distance. The maximum displacement under the experimental conditions was found to be 0.7 times of the jet nozzle diameter.

Measurements of the local heat transfer coefficients on a hemispherical convex surface with a round oblique impinging jet were made by Lim et al. [60]. It was found that the Nusselt number at the stagnation point decreased as that jet angle increased and had the maximum value for a certain nozzle-to-surface distance. Secondary maxima were reported in the x-axis and y-axis Nusselt number distributions. The displacement of the maximum Nusselt number from the stagnation point was observed to increase as the jet

angle increased or the nozzle-to-surface distance decreased. The ratio of the maximum Nusselt number to the stagnation Nusselt number increased as the jet angle increased.

The behavior of the assisting gas inside a simulating laser cut kerf for a supersonic and a conical nozzle tip were studied by Man et al. [61]. It was found that under a gas pressure of 7 bar, the gas jet from a conical nozzle tip expands radially and the jet momentum deteriorates rapidly inside the kerf. The behavior of the jet was strongly influenced by the stand-off distance and thickness of the workpiece. On the other hand, the gas jet from a supersonic nozzle had tidy boundary and uniform distribution of pressure and thrust inside the cut kerf. The sensitivity to the stand-off distance and the workpiece thickness of the supersonic nozzle were much less as compared with the conical nozzle.

2.2.2 NUMERICAL STUDIES

2.2.2.1 Round/Axisymmetric Jets

Morris and Garimella [13] computationally investigated the flow fields in the orifice and the confinement region of a normally impinging, axisymmetric, confined, and submerged liquid jet. FLUENT was used to solve the flow fields using the RNG k-ε model. The predicted separation and reattachment region of the flow at the entrance of the orifice were in excellent agreement with visualizations in the literature. The pressure drop across an orifice was predicted to within ±5% of published experimental data. The predicted toroidal recirculation patterns in the confinement region of the impinging jet were in qualitative agreement with flow visualizations.

The local heat transfer coefficient distribution on a square heat source due to a normally impinging, axisymmetric, confined, and submerged liquid jet was computationally investigated by Morris et al. [16]. FLUENT was used to solve the thermal and flow fields using the standard high-Reynolds number k-ε turbulence model. The predicted stagnation and average heat transfer coefficients agreed with experiments to within a maximum deviation of 16 and 20 percent. Overpredictions in stagnation and average heat transfer coefficients are indicated and attributed to near wall treatment and the turbulent Prandtl number variation in the wall region. The importance of near wall treatment and the turbulent Prandtl number variation in the wall region in predicting the stagnation as well as the average heat transfer coefficients was indicated.

Amano and Brandt [62] considered turbulent submerged axisymmetric incompressible jets impinging on a flat plate and flowing into an axisymmetric cavity. They employed a hybrid finite-difference method with the k-ε turbulence model to account for turbulence. They indicated that the use of the k-ε turbulence model resulted in good predictions of the velocity, pressure and skin friction distributions and that the near-wall models for the kinetic energy and turbulent shear stress gave good predictions of the skin friction coefficients.

Wang et al. [63] and Wang et al. [64] performed an analytical study of the heat transfer between an axisymmetrical free impinging jet and a solid flat surface with non-uniform wall temperature or wall heat flux. In the first paper, both the exact energy equation and the boundary layer energy equation were solved asymptotically in the vicinity of the stagnation point. Results showed that the nonuniformity of wall temperature or wall heat flux has a considerable effect on the stagnation point Nusselt

number. Increasing the wall temperature or wall heat flux with the radial distance reduced the stagnation point Nusselt number while decreasing the wall temperature or wall heat flux with the radial distance enhanced the heat transfer at the stagnation point. In the second paper, the authors investigated the heat transfer in the boundary layer region. The solution was matched with that for the stagnation region obtained in the first paper so that the Nusselt number throughout the stagnation region and the boundary layer region was obtained. It was shown that the Nusselt number for increasing wall temperature or wall heat flux could be considerably higher than that for constant wall temperature or wall heat flux outside the stagnation region.

Bejan [65] performed thermodynamic integral analysis of two-dimensional turbulent jet. It was shown that even when the temperature difference between the nozzle fluid and the reservoir fluid was zero, the jet region was nonisothermal. Also, the natural shape of the velocity and temperature profiles of the jet was one that minimizes the total entropy generation rate.

Craft et al. [66] performed an assessment of four turbulence models: one k-ε eddy viscosity model and three second moment closures of the Reynolds averaged Navier-Stokes equations. All schemes used a low-Reynolds-number k-ε model across the near-wall semi-viscous sublayer. The models were applied to the numerical prediction of the dynamic and thermal characteristics of the near-impingement region of the turbulent impinging jets discharged from a circular pipe measured by Baughn and Shimizu [37] and Cooper at al. [38]. The numerical predictions indicated that the k-ε model and one of the Reynolds stress models lead to far too large values of turbulence near the stagnation point. This excessive energy in turn induced much too high heat transfer coefficients and

turbulent mixing with the ambient fluid. The other two second-moment closures, adopting new schemes for accounting for the wall's effect on pressure fluctuations, did much better though one of them was clearly superior in accounting for the effects of the height of the jet discharge above the plate. However, none of the schemes was entirely successful in predicting the effects of Reynolds number. The authors attributed this failure to the two-equation eddy viscosity scheme adopted in all case to span the near-wall sublayer rather that the outer layer models on which their study focused.

Lasher and Taulbee [67] performed an evaluation of individual components of Reynolds stress turbulence models by considering turbulent round jet. Emphasis was made on linear and nonlinear pressure-strain models. Predictions using the linear models were generally as good as those obtained using nonlinear models, indicating that nonlinear models may not be necessary for engineering accuracy for this flow.

Hosseinalipour and Mujumdar [68] numerically studied turbulent flow and heat transfer in a confined single impinging jet (IJ) and opposing jet (OJ) configuration. The performance of five low-Reynolds number k-ε models and the standard high-Reynolds number k-ε model were evaluated with respect to the degree of agreement with experimental measurements. They reported that the low Reynolds number k-ε model predicted the heat transfer characteristics more accurately than the corresponding high Reynolds number k-ε model. They reported that increasing the jet Re caused a flatter Nu distribution along the channel walls, which is favorable for electronic cooling applications. They concluded that higher-order closure models were needed for more reasonable predictions in the stagnation region.

Dianat et al. [69] considered circular and two-dimensional jets impinging orthogonally on a solid flat surface. The k-ε turbulence model and a version of a second-moment Reynolds stress closure, modified to include the effect of pressure reflections form a solid surface were used as the basis of predictions of the resulting flow field. The results, in general, confirmed the superiority of the Reynolds stress transport equation model for predicting mean and fluctuating velocities within the stagnation and wall jet regions of the impinging flows. In particular, modifications to the second-moment closure to account for the influence of the surface in distorting the fluctuating pressure field away from the wall successfully predicted the damping of normal-to-wall velocity fluctuations throughout the impinging flows. In contrast, results derived from the eddy-viscosity-based approach significantly overpredicted the latter velocities, particularly in the stagnation region, and, as a consequence (in part), mean and fluctuating velocities throughout the flow were not predicted accurately.

Ashforth-Frost and Jambunathan [70] applied the standard k-ε model of turbulence in conjunction with the logarithmic law of the wall to study flow structure and heat transfer for a fully developed turbulent axisymmetric jet impinging on a flat plate within a semi-confined space. They found that the k-ε turbulence model reasonably predicted the jet impingement flow trends; however, careful thought has to be given to the near-wall predictions of the model. The wall jet heat transfer where isotropy prevails was predicted to within 20% of experimental values. However, the stagnation point Nu is overpredicted by about 300%. The authors attributed this directly to the turbulence model and inapplicability of the wall function.

Shuja and Yilbas [71] considered laser-assisted heating of a workpiece moving at constant speed. The three-dimensional model for the impinging gas jet was studied with the low-Reynolds number k-ε model. It was found that the surface temperature rise was influenced significantly by the workpiece speed. The peak values of surface temperature moved towards the direction of workpiece motion as the workpiece speed increased. Also, it was indicated that the cooling of the surface due to gas jet impingement was more pronounced towards the edge of the heated spot.

The entropy generation rate in the flow field due to jet emanating from an annular nozzle and impinging onto a flat plate was examined by Shuja et al. [72]. Entropy generation rate due to heat transfer and fluid friction was formulated and the resulting entropy equations solved numerically. It was found that volumetric entropy generation rate increased at nozzle exit due to velocity distribution of flow emerging from the nozzle and complex flow structure generated in the vicinity of the nozzle exit. Entropy generation rate also increased in the region of flat plate surface due to radial jet development from the stagnation zone. It was also determined that nozzle geometry had significant effect on entropy generation rate, such that increasing nozzle outer cone angle enhanced the entropy generation rate, particularly due to fluid friction.

Yilbas et al. [73] conducted a numerical study using a control volume approach of jet impingement onto a conical cavity with elevated wall temperature due to laser heating. Two dimensional forms of the Navier-Stokes equation for compressible flow and the energy equation were considered. The Reynolds stress turbulence model was used to account for turbulence. It was found that the influence of cavity depth on the flow field was considerable. Also, it was found that the stagnation region moved into the cavity as

the depth increased. Moreover, it was found that the Nusselt number increased gradually in the radial direction towards the cavity exit for deep cavities.

Shuja et al. [74] presented a study of jet impingement onto a conical cavity from an annular nozzle. The study was two dimensional and the Reynolds stress turbulence model was used to account for turbulence. It was found that increasing cavity depth and reducing both the nozzle outer cone angle and the average jet velocity at the nozzle exit enhanced the size of the stagnation zone in the cavity. It was also found increasing nozzle outer angle and jet velocity enhanced heat transfer rates and skin friction. Moreover, it was found that that the location of the maximum heat transfer coefficient moved further into the cavity with increasing nozzle angle.

Shuja et al. [75] presented a numerical analysis to investigate the influence of nozzle geometric configurations, cavity diameter and depth on the flow structure of impinging air jet emerging from a conical nozzle and heat transfer rates from the cavity created during laser gas-assisted processing. They reported that the frictional drag due to the impinging jet was minimal for the small diameter cavity, and the opposite is true for the large diameter cavity. The also found that for deep cavities the heat transfer coefficient increased towards the cavity edge.

Shuja et al. [76] studied the effects of jet emerging from an annular nozzle and impinging onto a cylindrical cavity with elevated wall temperature thus resembling laser-produced cavity. It was found that jet velocity had a significant effect on the heat transfer rates and skin friction. The effect was even more pronounced with increasing cavity depths.

A numerical simulation of flow emerging from a combination of annular and conical nozzles and impinging onto a cylindrical cavity at elevated wall temperature was performed by Shuja et al. [77]. The flow considered was axisymmetric. Turbulence was modeled by considering the Reynolds Stress Turbulence model. It was found that the Nusselt number attained high values in the neighborhood of the stagnation zone at the cavity bottom surface, with the effect more pronounced for the deeper cavity. It was also observed that the wall shear stress attained slightly higher values for shallow cavity as compared to the deep cavity, and that it reduced significantly at the cavity bottom and increases when the radial acceleration enhanced the rate of fluid strain in the cavity wall.

Shuja et al. [78] numerically predicted the heat transfer rates and skin friction at the surface of a tapered hole wall with elevated temperature and onto which gas jet impingement occurs. The effect of the hole wall velocity resembling the molten flow occurring from the hole wall as in laser processing applications was examined. It was found that the Nusselt number and skin friction at the hole wall in the regions of the hole inlet and exit attained high values. The influence of the wall velocity on the Nusselt number and skin friction was found not to be very significant.

2.2.2.2 Slot/Rectangular Jets

Shi et al. [14] simulated a single semiconfined turbulent slot jet impinging normally on a flat plate using the commercial finite volume code FLUENT 5.0. They studied the effects of turbulence models, near wall functions, jet turbulence, jet Reynolds number, as well as the thermal boundary condition type at the target surface. The standard k-ε model and the RSM were employed in the study. Both models slightly overpredicted the Nusselt

number distributions under some conditions. This was reported to be partially due to use of standard wall functions as compared to use of nonequilibrium wall functions. However, the qualitative trends compared very well with the experimental trend. They indicated that predictions for small nozzle-to-target spacing call for further improvement in the simulation. It was also found that standard k-ε was not successful in predicting the secondary flow patterns, which occur for small nozzle-to-target spacings, whereas the RSM could predict a secondary peak, albeit at a different distance than the experimental value.

Shi et al. [18] numerically examined the effect of fluid thermal properties on impinging jet heat transfer under a semi-confined turbulent slot jet. They reported that *Nu* increased with increasing Pr in over the range of 0.7-71. Their results indicated that gases with similar *Pr* yielded similar values of *Nu*, but different values of the surface heat transfer coefficient. They also deduced correlations for stagnation and average Nusselt numbers in terms of *Pr*.

The standard k-ε turbulence model in conjunction with the logarithmic law of the wall was applied by Lei et al. [79] to the prediction of a fully-developed turbulent impinging slot jet within semi-confined space. The model yielded reasonable good predictions of the mean velocity. However, the fluctuating velocity was poorly predicted. The authors attributed the poor predictions to the turbulence model and the application of the wall functions.

Cziela et al. [80] determined Nusselt number distributions for impinging jet flow of an array of slot nozzles with large-eddy simulation (LES) using a dynamic sub-grid stress model and the direct numerical simulation (DNS). Good agreement was established

between LES using a logarithmic law of the wall and the DNS. It was found that the velocity profile at the feed tube exit strongly influenced the maximum heat transfer at the stagnation point.

Hattori and Nagano [81] conducted direct numerical simulations of confined plane turbulent impinging jet at low nozzle-plate spacing with heat transfer. They conducted DNS under 3 different impingement distance H to inlet channel width D ratios (H/D = 2, 1, 0.5). Their DNS results showed that the Nusselt number increased with a decrease in H. Also, Nusselt number in the case with the highest distance decreased monotonously in the wall-jet development direction. In the other two cases the second peak of Nusselt number was clearly observed away from the stagnation point, due to the increase in wall-normal turbulence intensities in the region away from the stagnation point. Also, the skin friction coefficient in the case of the lowest spacing had a second peak similar to the heat transfer rate.

Laminar mixed convective cooling of a constant heat flux surface by confined slot jet impingement was studied by Sahoo and Sharif [82]. Two-dimensional numerical simulation for a wide range of domain aspect ratio, jet exit Reynolds number, and Richardson number was performed by the authors. It was observed that for a given domain aspect ratio and Richardson number, the average Nusselt number at the heat flux surface increased with increasing jet exit Reynolds number. The overall Nusselt number at the hot plate did not change significantly with Richardson number for the range of jet exit Reynolds number considered (100 – 500). At low Reynolds (Re = 30), the effect of Richardson number variation was significant.

Li et al. [83] investigated the flow field of a 2-D laminar confined impinging slot jet. Two different flow patterns or two different numerical solutions that coexist in some range of geometric and flow parameters were shown: a curved flow pattern and a straight flow pattern. Boundary conditions at the channel exit exerted minor changes on the flow. The authors indicated that the flow patterns significantly affected the heat transfer for the downstream half of the target surface and that awareness of the consequence of this variation in heat transfer should be exercised when similar arrangement is used to cool a heated surface. Flow visualizations of the two flow patterns indicated agreement with numerical predictions.

Dagtekin and Oztop [84] studied heat transfer due to double impinging vertical slot jets onto an isothermal wall for laminar flow regime. It was found that the thermal boundary layer on the bottom wall became thinner with the increase of Reynolds number to enhance heat transfer. As jet-bottom wall spacing was increased peak Nusselt number at the stagnation point decreased resulting in lower heat transfer rate. Also, as the jet Reynolds number ratio (Re_2/Re_1) decreased mean Nusselt number value increased.

Chen et al. [85] theoretically studied heat transfer from horizontal surfaces with arbitrary heat flux due to laminar free-surface liquid slot jet impingement. The thermal and hydraulic boundary layers of laminar flow were divided into four regions of flow along heat transfer surfaces including a stagnation zone and three wall jet zones, from which general expressions of heat transfer coefficients were obtained.

Ramezanpour et al. [19] conducted a numerical study using finite volume code FLUENT to investigate heat transfer in turbulent , unconfined, submerged, and inclined impinging jet discharged from a slot nozzle on a plate. They found that in inclined

impinging jet the location of the maximum Nusselt number moved to the uphill side of the plate by movement of stagnation point to the uphill side. This movement increased by increasing nozzle height to nozzle hydraulic diameter ratio (H/D) and by decreasing of Reynolds number and inclination angle.

Patel and Roy [86] considered an array of two rectangular jets impinging on an inclined surface. Heat transfer process in the domain was investigated by using the finite volume based commercial code FLUENT. The three-dimensional computational model was analyzed with the RNG k-ε model. The Nusselt number distribution on the inside of the inclined surface was obtained for several jet Reynolds numbers. Closed and open boundary conditions were considered. It was found that heat transfer was maximum through the shear layer formed near the jet attachment stagnation region. It was also reported that turbulence and wall shear force were higher in the shear layer region and highest at stagnation point.

Rasipuram and Nasr [87] numerically studied heat transfer between an inclined impingement surface and an air jet issued from one, two, or three rectangular openings or two circular openings. They found that the configuration with one rectangular opening had the highest overall heat transfer coefficient. However, the configuration with three rectangular openings could result with an average heat transfer comparable to that of the one opening but for a much lower flow rate.

The flow field due to a turbulent impinging jet over a moving surface, emanating from a rectangular slot nozzle was computed by Chattopadhyay and Saha [88] using large eddy simulation technique. It was observed that, while the turbulent kinetic energy increases with increasing velocity of the impinging surface, production rate of turbulence

initially increases with increasing surface velocity and then comes down. Also, heat transfer from the plate initially increases with non-dimensional surface velocity and then comes down.

2.3 CONCLUSIONS

Numerous studies have been reported in the literature on the subjects of laser cutting and jet impingement over the past four decades. However, no research has been found in the open literature which describes three dimensional modeling of the impinging jet effects in relation to the three dimensional kerf generated during the laser cutting process. Due to the complexity of the fluid dynamic structure of impinging jets that are mostly turbulent except at very low Reynolds numbers, several simplifications are employed in attempts to their understanding. Available models when they exist are either simplified two-dimensional models or consider different geometric configurations or do not make assumptions about either the kerf geometry or its dimensionality. Model order reduction when considering the laser cutting process are not acceptable if comprehensive understanding of gas jet work-piece interactions is needed [1]. This is true especially if kerf geometry formed is to be considered.

CHAPTER 3

NUMERICAL MODELING

3.1 MODELING OF GAS JET ASSISTED LASER CUTTING – FLOW EQUATIONS AND TURBULENCE MODELS

3.1.1 PRELUDE

In general cutting conditions, a gas jet exits the nozzle at ambient temperature and impinges on the workpiece surface and penetrates into a narrow cut kerf whose side wall is maintained at 1500 k to simulate the laser cutting process. Turbulent mixing of the assisting gas stream with the surrounding air occurs. The mixing zone is increasing downstream until finally, at a distance of several nozzle diameters, the whole gas jet becomes turbulent [7, 27]. Disregarding small velocities of flow, it is found that the jet becomes completely turbulent at a short distance from the point of discharge, which can be a nozzle or orifice [89]. Therefore, the flow will mainly be of a **compressible** and **turbulent** nature.

A jet impingement system results in a flow field that is often steady unless an internal geometrical feature of the arrangement or external means like forced pulsation or

periodic interruption of the jet impingement is used to generate unsteadiness [90]. In laser gas-assisted processing, impinging jet flow conditions are generally **steady**.

3.1.2 MATHEMATICAL MODELING

Steady flow conditions will be considered in the analysis that must accommodate the compressibility effect and variable properties. The flow field due to jet impingement will be simulated using the three-dimensional forms of the continuity and Reynolds-averaged Navier-Stokes equations for compressible flow, commonly referred to as Favre-Averaged Transport Equations. These equations can be written as [91 and 92]:

(i) Continuity equation

$$div(\overline{\rho}\underline{\tilde{U}}) = 0 \tag{3.1}$$

(ii) Reynolds equations

$$\begin{aligned}
div(\overline{\rho}\tilde{U}\underline{\tilde{U}}) &= -\frac{\partial \overline{P}}{\partial x} + div(\mu grad\tilde{U}) + \left[-\frac{\partial(\overline{\rho u'' u''})}{\partial x} - \frac{\partial(\overline{\rho u'' v''})}{\partial y} - \frac{\partial(\overline{\rho u'' w''})}{\partial z} \right] + S_{Mx} \\
div(\overline{\rho}\tilde{V}\underline{\tilde{U}}) &= -\frac{\partial \overline{P}}{\partial y} + div(\mu grad\tilde{V}) + \left[-\frac{\partial(\overline{\rho u'' v''})}{\partial x} - \frac{\partial(\overline{\rho v'' v''})}{\partial y} - \frac{\partial(\overline{\rho v'' w''})}{\partial z} \right] + S_{My} \\
div(\overline{\rho}\tilde{W}\underline{\tilde{U}}) &= -\frac{\partial \overline{P}}{\partial z} + div(\mu grad\tilde{W}) + \left[-\frac{\partial(\overline{\rho u'' w''})}{\partial x} - \frac{\partial(\overline{\rho v'' w''})}{\partial y} - \frac{\partial(\overline{\rho w'' w''})}{\partial z} \right] + S_{Mz}
\end{aligned} \tag{3.2}$$

(iii) Scalar transport equation (φ represents any scalar quantity such as energy)

$$div(\overline{\rho}\tilde{\Phi}\underline{\tilde{U}}) = div(\Gamma_{\Phi} grad\tilde{\Phi}) + \left[-\frac{\partial(\overline{\rho u'' \varphi''})}{\partial x} - \frac{\partial(\overline{\rho v'' \varphi''})}{\partial y} - \frac{\partial(\overline{\rho w'' \varphi''})}{\partial z} \right] + S_{\Phi} \tag{3.3}$$

where the over-bar indicates a conventional Reynolds-averaged or time-averaged variable, the under-bar indicates a vector quantity, and the tilde indicates a density-weighted or Favre-averaged variable. Γ_Φ is a relevant diffusion coefficient.

Consequently we can write the energy equation with temperature as the independent variable as:

$$div(\overline{\rho} c_p \underline{\tilde{U}} \tilde{T}) = div(\lambda grad \tilde{T}) + \left[-\frac{\partial c_p \overline{(\rho u'' \theta'')}}{\partial x} - \frac{\partial c_p \overline{(\rho v'' \theta'')}}{\partial y} - \frac{\partial c_p \overline{(\rho w'' \theta'')}}{\partial z} \right] + S_T \qquad (3.4)$$

It should be noted that the fluid thermal conductivity λ can be expressed as $\lambda = c_p \alpha \mu$ where α is the inverse Prandtl number.

Equations 3.1 – 3.4 are convenient for treatment of compressible flows where density fluctuations due to turbulence exist. Equations 3.1 – 3.4 are derived from the original governing equations in Cartesian coordinates by defining a density averaged variable according to:

$\tilde{f} = \overline{\rho f} / \overline{\rho}$, f is generalized variable which can be any of the velocity components and thermal variables. It is significantly important to note that fluid properties, including density, and pressure are treated using conventional Reynolds or time averaging. Moreover, fluctuations in viscosity and other properties have been neglected [91, 92]. Before substituting into the conservation equations fluctuating quantities are defined according to:

$$f = \tilde{f} + f'' \qquad (3.5)$$

where the double prime denotes fluctuations in Favre-averaging. Note that the doubly primed fluctuations are significantly different from the single primed fluctuations in time-averaging (see [92]).

Pressure, temperature, and density are related by the equation of state:

$$\overline{P} = \overline{\rho} R \tilde{T} \tag{3.6}$$

The Favre averaging operation on the momentum equations yields six additional unknowns in the Favre-averaged momentum equations (Equations 3.2): the Favre-Averaged Reynolds stresses $-\overline{\rho u''^2}, -\overline{\rho v''^2}, -\overline{\rho w''^2}, -\overline{\rho u'' v''}, -\overline{\rho u'' w''}, -\overline{\rho v'' w''}$. Similarly, the Favre-averaged energy equation shows extra terms containing $\overline{\rho u'' \theta''}, \overline{\rho v'' \theta''}, \overline{\rho w'' \theta''}$. The Reynolds stresses are related to the mean rates of deformation through Boussinesq hypothesis [12], which proposes an analogy between these stresses and viscous stresses in laminar flows (see section 1.4):

$$-\overline{\rho u_i'' u_j''} = \mu_t \left(\frac{\partial \tilde{U}_i}{\partial x_j} + \frac{\partial \tilde{U}_j}{\partial x_i}\right) - \frac{2}{3}\left(\mu_t \frac{\partial \tilde{U}_k}{\partial x_k} + \overline{\rho} k\right)\delta_{ij} \tag{3.7}$$

using the suffix notation, where μ_t is eddy viscosity. By analogy turbulent transport of a scalar is taken to be proportional to the gradient of the mean value of the transported quantity. Consequently, for turbulent transports in the energy equation can be expressed as as:

$$-\overline{\rho u_i'' \theta''} = \alpha_t \mu_t \frac{\partial \tilde{T}}{\partial x_i} \tag{3.8}$$

where α_t is the inverse Prandtl number.

3.1.3 TURBULENCE MODELING

3.1.3.1 Transport Equations for the RNG k-ε model

FLUENT offers ten turbulence models to evaluate $\overline{u_i' u_j'}$ and $\overline{u_i' \theta'}$ for the closure of equations 3.1 – 3.4. These models are described in the introductory chapter. The RNG k-ε model will be used in this work for modeling the Reynolds transports in averaged form of Navier-Stokes equations. The RNG-based *k-ε* turbulence model is derived from the instantaneous Navier-Stokes equations, using a mathematical technique called "renormalization group" methods. The analytical derivation results in the following transport equations for the turbulence kinetic energy, k, and its rate of dissipation, ε in steady state [12, 15, and 91]:

$$div(\overline{\rho} k \underline{\tilde{U}}) = div(\alpha_k \mu_{eff}\, grad k) + G_k - \overline{\rho}\varepsilon - Y_M \tag{3.9}$$

$$div(\overline{\rho} \varepsilon \underline{\tilde{U}}) = div(\alpha_\varepsilon \mu_{eff}\, grad \varepsilon) + C_{1\varepsilon} \frac{\varepsilon}{k}(G_k) - C^*_{2\varepsilon} \overline{\rho} \frac{\varepsilon^2}{k} \tag{3.10}$$

where

α_k is the inverse effective Prandtl number for k,

$\alpha\varepsilon$ is the inverse effective Prandtl number for ε,

$\mu eff = \mu + \mu_t$ is the effective viscosity,

G_k the generation of turbulence kinetic energy due to the mean velocity gradients,

Y_M is the dilatation dissipation term, and is used to account for compressibility effects on turbulence

$C_{1\varepsilon} = 1.42$ is a constant,

and $C_{2\varepsilon}^{*}$ is a modified constant with respect to what is used in the standard *k-ε* model and its significance will be discussed shortly.

The above equations assume steady state, neglect generation of turbulence due to buoyancy and the corresponding contribution to the production of ε, and neglect other source terms. The term on the left hand side of each equation represents the transport of k or ε by convection. The first term on the right hand side is the transport of k or ε by diffusion. The second term on the right hand side is the rate of generation of k or ε. The third term on the right hand side is the rate of destruction of k or ε.

Modeling the effective viscosity

The scale elimination procedure in RNG theory results in a differential equation for turbulent viscosity [15]:

$$d\left(\frac{\overline{\rho}^{2}k}{\sqrt{\varepsilon\mu}}\right)=1.72\frac{\hat{v}}{\sqrt{\hat{v}^{3}-1+C_{v}}}d\hat{v} \tag{3.11}$$

where $\hat{v}=\mu_{eff}/\mu$ and $C_v \approx 100$.

Equation 3.11 is integrated to obtain an accurate description of how the effective turbulent transport varies with the effective Reynolds number (or eddy scale), allowing the model to better handle **low-Reynolds-number** and near wall flows. It is important to note that in the **high-Reynolds-number limit**, equation 3.11 gives

$$\mu_{eff}=\mu_{t}=\overline{\rho}C_{\mu}\frac{k^{2}}{\varepsilon} \tag{3.12}$$

With C_μ = 0.0845 [91], derived using RNG theory. Then equation 3.9 and 3.10 are modified accordingly. It is interesting to not that this value of C_μ is very close to the empirically-determined value of 0.09 used in the standard k-ε model.

Calculating the inverse effective Prandtl numbers

The inverse effective Prandtl numbers, α_k and $\alpha\varepsilon$, are computed using the following formula derived analytically by the RNG theory [15]:

$$\left|\frac{\alpha - 1.3929}{\alpha_0 - 1.3929}\right|^{0.6321} \left|\frac{\alpha + 2.3929}{\alpha_0 + 2.3929}\right|^{0.3679} = \frac{\mu}{\mu_{eff}} \tag{3.13}$$

Where α_0 = 1.0. In the high-Reynolds-number limit, $\alpha_k = \alpha\varepsilon \approx 1.393$ [91].

Calculating the parameter $C^*_{2\varepsilon}$

$C^*_{2\varepsilon}$ is calculated from the following equation (FLUENT 2005):

$$C^*_{2\varepsilon} \equiv C_{2\varepsilon} + \frac{C_\mu \eta^3 (1 - \eta/\eta_0)}{1 + \beta\eta^3} \tag{3.14}$$

where $C_{2\varepsilon}$ = 1.68, β = 0.012, η_0 = 4.38, and $\eta = Sk/\varepsilon$ with S = strain rate = $\sqrt{2S_{ij}S_{ji}}$, (Sij is defined in equation 3.17 below) [15].

The main difference between the standard and RNG k-ε models lies in modified constant, $C^*_{2\varepsilon}$. In the low-strain region ($\eta < \eta_0$), the effect of equation 3.14 is to increase $C_{2\varepsilon}$ and the results for weakly to moderately strained flows are comparable to the standard k-ε model. In the high strain region ($\eta > \eta_0$), equation 3.14 leads to a reduction of $C_{2\varepsilon}$. The smaller destruction of ε augments ε, reducing k and, eventually, the effective viscosity. This improves the prediction of heat transfer in the impinging (high-strain) region by the

RNG *k-ε* model compared to the standard *k-ε* model that overestimates the kinetic energy and heat transfer rate in the impinging region [19].

Modeling Turbulent Production

G_k represents the generation of turbulence kinetic energy due to the mean velocity gradients and is calculated using the following definition:

$$G_k = \tau_{ij} \cdot S_{ij} \tag{3.15}$$

The Favre-averaged Reynolds stresses tensor τ_{ij} is defined by Wilcox [12] as follows:

$$\tau_{ij} = \frac{-\overline{\rho u_i'' u_j''}}{\overline{\rho}} \tag{3.16}$$

and the Favre-averaged strain-rate tensor is defined as [12]:

$$S_{ij} = \frac{1}{2}\left(\frac{\partial \tilde{U}_i}{\partial x_j} + \frac{\partial \tilde{U}_j}{\partial x_i}\right) \tag{3.17}$$

Modeling the effect of compressibility on turbulence

Y_M is the dilatation dissipation term and represents the contribution of the fluctuating dilatation in compressible turbulence to the overall dissipation rate. This term is modeled according to [15]:

$$Y_M = 2\rho\varepsilon M_t^2 \tag{3.18}$$

where Mt is the turbulent Mach number, defined as

$$M_t = \sqrt{\frac{k}{a^2}} \tag{3.19}$$

where $a \equiv \sqrt{\gamma R \tilde{T}}$ is the speed of sound.

Convective Heat Transfer Modeling

Turbulent heat transport is modeled in FLUENT using the concept of Reynolds' analogy to turbulent momentum heat transfer. The modeled energy equation is given in FLUENT User's Guide [15] where an effective thermal conductivity is defined for for the RNG *k-ε* model as:

$$\lambda_{eff} = \alpha c_p \mu_{eff} \tag{3.20}$$

where α, the inverse Prandtl number, is calculated from equation 3.13, but with $\alpha_0 = \lambda/\mu c_p$. λ and c_p are the thermal conductivity and specific heat of the gas into consideration and are temperature dependent in our study. The fact that α varies with μ/μ_{eff} is an advantage of the RNG *k-ε* model over other *k-ε* models. It is consistent with experimental evidence indicating that the turbulent Prandtl number varies with the molecular Prandtl number and turbulence [15]. Equation 3.13 allows heat transfer to be calculated in low-Reynolds-number regions. Equation 3.13 smoothly predicts the variation of effective Prandtl number from the molecular value in the viscosity-dominated region to the fully turbulent value in the fully turbulent regions of the flow [15].

3.1.3.2 Near-Wall Turbulence Modeling

Wall-bounded turbulent flows are affected in many ways by the presence of the wall. The mean velocity field is affected through the no-slip condition that has to be satisfied at the wall. In the region very close to the wall, the tangential velocity fluctuations are reduced by viscous damping, while the normal fluctuations are reduced by kinematic blocking. Toward the outer part of the near wall region, however, turbulence is rapidly strengthened by the production of turbulence kinetic energy due to large gradients in

mean velocity. Furthermore, walls are the main source of mean vorticity and turbulence. Moreover, momentum and other scalar transports occur most vigorously in the near-wall region because it is in that region that solution variables have large gradients. Thus, accurate near-wall modeling is vital to successful numerical solutions. The k-ε models and the RSM are primarily valid for turbulent core flows. Consideration therefore needs to be given as to how make these models suitable for wall-bounded flows.

Traditionally, there are two approaches to modeling the near-wall region. In one approach "wall functions" are used to link the inner viscosity-affected region between the wall and the fully-turbulent region. In other words, the wall functions link the solution variables at the near-wall cells and the corresponding quantities on the wall. This eliminates the need to resolve the inner region. In the other approach, turbulence models are modified to account for the inner viscosity-affected region. Hence, the inner region has to be resolved with a mesh all the way to the wall.

FLUENT offers two choices of wall function approaches:

- Standard wall functions
- Non-equilibrium wall functions

Details and formulations related to the wall function approach can be found in the FLUENT user's guide. The standard wall functions work reasonably well for wall-bounded flows except in situations when the near-wall flows are subjected to severe pressure gradients, and when the flows are in strong non-equilibrium. In such flows improvements can be obtained, particularly in the prediction of wall shear and heat transfer, by using the non-equilibrium wall functions. The wall function approach becomes less reliable when the flow conditions depart much from the ideal conditions

underlying the wall functions [15]. Examples of such departure are pervasive low-Reynolds-number or near-wall effects (e.g., flow through a small gap or highly viscous, low-velocity fluid flow) and situation of high three-dimensionality in the near-wall region. Several studies, some of which are referred to in the chapter on literature review, applied the RNG *k-ε* model with the wall function approach to simulate jet impingement problems. However, these studies reported poor prediction of the Nusselt number on the impinging area [19]. Since the problem being considered involves a gas jet impinging on workpiece surface and penetrating into narrow cut three-dimensional kerf, we must employ the near-wall modeling approach combined with adequate mesh resolution in the near-wall region for success of simulations. FLUENT provides for such situations the enhanced wall treatment, which can be used with the RNG *k-ε* models.

Enhanced Wall Treatment

Enhanced wall treatment is a near-wall modeling method that solves the turbulence sublayer instead of using function to set and simulate turbulence behavior near the wall [19]. In this method, the momentum and k equations for the inner region are solved and eddy viscosity as well as dissipation rate are obtained algebraically. In the inner region, the eddy viscosity and dissipation rate are calculated based on a blending function whose output near the wall leads to the algebraic values of a one-equation turbulence model and in boundaries of the outer region leads to the values of the turbulence model applied in the outer region (RNG k-ε model) [15]. **Enhanced wall treatment option presented by FLUENT combines a two-layer model with enhanced wall functions.**

Two-layer model for enhanced wall treatment

The two-layer approach is an integral part of the enhanced wall treatment and is used to specify both ε and the turbulent viscosity in the near-wall cells. In this approach, the whole domain is subdivided into a viscosity-affected region that is completely resolved all the way to the viscous sublayer and a fully-turbulent region. The demarcation of the two regions is determined by a wall-distance-based, turbulent Reynolds number, Re_y, defined as

$$\mathrm{Re}_y \equiv \frac{\rho y \sqrt{k}}{\mu} \tag{3.21}$$

Where

y = normal distance from the wall at the cell centers.

In the fully turbulent region ($Re_y > Re_y^*$; $Re_y^* = 200$), the RNG k-ε model is employed. Whereas, in the viscosity-affected near-wall region ($Re_y < Re_y^*$), the one-equation model is employed [15]. In the one-equation model, the momentum and the k equations remain as described in section 3.1.3.1 above. However, the turbulent viscosity is computed from (FLUENT, 2005)

$$\mu_{t,2layer} = \rho C_\mu l_\mu \sqrt{k} \tag{3.22}$$

Where the length scale that appears in the above equation is computed from

$$l_\mu = y c_l (1 - e^{-\mathrm{Re}_y / A_\mu}) \tag{3.23}$$

The two-layer formulation for turbulent viscosity described above is used as a part of the enhanced wall treatment, in which the two-layer definition is smoothly blended with the high-Reynolds-number μ_t definition from the outer region

$$\mu_{t,enh} = \lambda_\varepsilon \mu_t + (1-\lambda_\varepsilon)\mu_{t,2layer} \tag{3.24}$$

where μ_t is the high-Reynolds-number viscosity defined in section 3.1.3.1. A blending function, λ_ε, is defined in such a way that it is equal to unity far from walls and is zero very near to walls. The blending function chosen is

$$\lambda_\varepsilon = \frac{1}{2}\left[1+\tanh\left(\frac{\mathrm{Re}_y - \mathrm{Re}_y^*}{A}\right)\right] \tag{3.25}$$

with

$$A = \frac{\left|\Delta \mathrm{Re}_y\right|}{\tanh(0.98)} \tag{3.26}$$

Typically, $\Delta\mathrm{Re}_y$ would be assigned a value that is between 5% and 20% of Re_y^*. The main purpose of the blending function λ_ε is to prevent solution convergence from being impeded when the *k-ε* solution in the outer layer does not match with the two-layer formulation. The ε field is computed from

$$\varepsilon = \frac{k^{3/2}}{l_\varepsilon} \tag{3.27}$$

The length scales that appear in equation 3.27 are again computed from

$$l_\varepsilon = y c_l (1 - e^{-\mathrm{Re}_y / A_\varepsilon}) \tag{3.28}$$

FLUENT uses a procedure for the *ε* specification that is similar to the μ_t blending in order to ensure a smooth transition between the algebraically-specified *ε* in the inner region an the ε obtained from solution of the transport equation in the outer region.

The constants in the length scale formulas, equations 3.23 and 3.28, are given by:

$$c_l = 0.4187 C_\mu^{-3/4}, A_\mu = 70, A_\varepsilon = 2c_l$$

If the near-wall mesh is fine enough to be able to resolve the laminar sublayer, then the enhanced wall treatment will be identical to the two-layer model described above. For capturing a laminar viscous sublayer, the non-dimensional wall coordinate y^+ given by equation 3.29 is recommended to be equal to 1 at the wall adjacent cells [19]. **A higher y^+ is acceptable as long as it is well inside the viscous sublayer ($y^+ < 5$) [15].**

The restriction that the near-wall mesh must be sufficiently fine everywhere might impose too large a computational requirement. To achieve the goal of having a near-wall modeling approach that will possess the accuracy of the standard two-layer approach for fine near-wall meshes and that at the same time, will not significantly reduce accuracy for coarse meshes (usually referred to as wall-function meshes) FLUENT combines the two-layer model with enhanced wall functions described below [15].

$$y^+ = \frac{\rho C_{\mu,wall}^{1/4} k^{1/2} y}{\mu} \tag{3.29}$$

With y being the distance from the wall, k turbulence kinetic energy, $C_{\mu,wall} = 0.09$, ρ density, and μ viscosity [19].

Enhanced Wall Functions

FLUENT uses a blending function suggested by Kader (1981) to formulate the law-of-the-wall as a single wall law for the entire wall region, thus blending linear (laminar) and logarithmic (turbulent) laws-of-the-wall [15]:

$$u^+ = e^{\Gamma} u_{lam}^+ + e^{1/\Gamma} u_{turb}^+ \tag{3.30}$$

$$\frac{du^+}{dy^+} = e^{\Gamma} \frac{du_{lam}^+}{dy^+} + e^{1/\Gamma} \frac{du_{turb}^+}{dy^+}) \tag{3.31}$$

Where the blending function is given by:

$$\Gamma = -\frac{a(y^+)^4}{1+by^+} \tag{3.32}$$

where a = 0.01 and b = 5.

The enhanced wall functions are developed by smoothly blending an enhanced turbulent wall law with the laminar wall law. The enhanced turbulent law-of-the wall for compressible flow with heat transfer and pressure gradients has been derived by combining the approaches of White and Cristoph (1971) and Huang et al. (1993) [15]. For details about the laminar law-of-the-wall and the turbulent law-of-the-wall and on how u^+_{lam} and u^+_{turb} are computed refer to FLUENT user guide.

Similarly, temperature near the wall is obtained by blending the laminar linear sublayer and turbulence logarithmic laws according to the method of Kader (1981) [15]:

$$T^+ = e^{\Pi} T^+_{lam} + e^{1/\Pi} T^+_{turb} \tag{3.33}$$

where

$$\Pi = -\frac{a(\Pr y^+)^4}{1+b\Pr^3 y^+} \tag{3.34}$$

Where Pr is the molecular Prandtl number, and the coefficients a and b are as defined in equation 3.32.

3.2 COMPUTATIONAL DOMAIN

3.2.1 COMPUTATIONAL DOMAIN GEOMETRY

A schematic diagram of the impinging jet flow configuration is shown in Figure 3.1. For clarity another figure (Figure 3.2) is included to show the solid substrate material

including the kerf produced during the laser cutting process. Because of plane symmetry, simulation of only a half-domain is adequate for fully characterizing the flow.

The three-dimensional computational domain consists of the nozzle inlet, conical convergent nozzle, confining nozzle surface (C), impinging jet domain, solid domain, laser-cut kerf, kerf outlet, and exiting fluid region. The impinging jet is studied by varying the average jet velocity at the nozzle exit, varying the nozzle-to-kerf surface spacing, changing the kerf thickness, and changing the cutting front inclination. The desired average jet velocity at the nozzle exit is obtained through specifying the mass flow rate at the nozzle inlet. The mass flow rates used in this study will be based on actual laser cutting applications. Four different average jet velocities will be considered in this study. The spacing between the nozzle exit and the kerf top onto which the gas jet is impinging is commonly referred to as the standoff distance, H. Two different values of H will be considered. Four different values of the kerf thickness are considered in this study. There corresponds to each wall thickness a set of cutting front inclinations. In this study, the cutting front inclination will be referred to as the kerf wedge angle α. The kerf geometry and thickness impose a constraint on the maximum kerf wedge angle that can be accommodated in this study (Table 3.1). Table 3.1 summarizes the geometric parameters and average jet velocities at nozzle exit considered in the simulations.

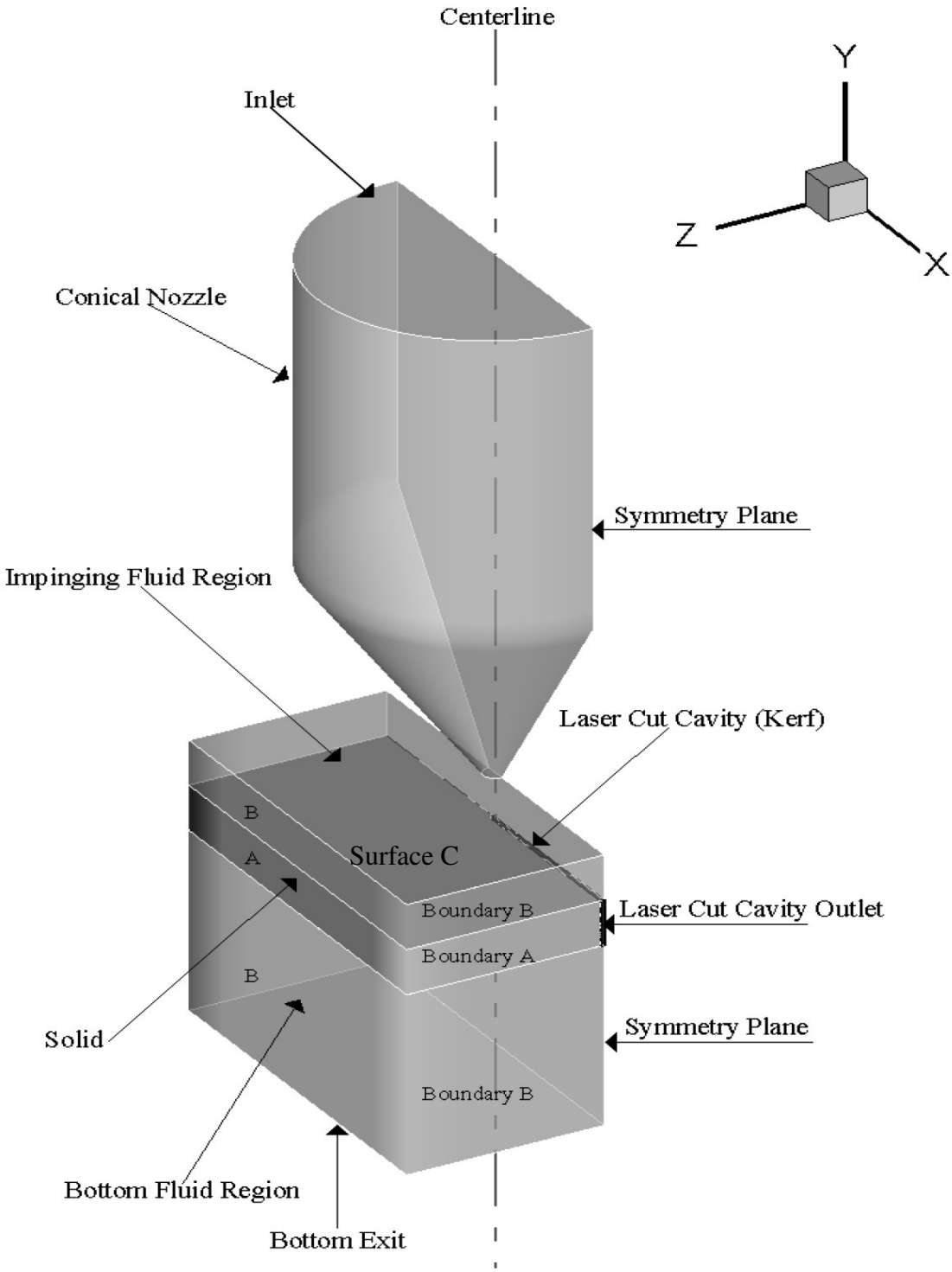

Figure 3.1 Schematic diagram of the impinging jet flow configuration used in the simulations

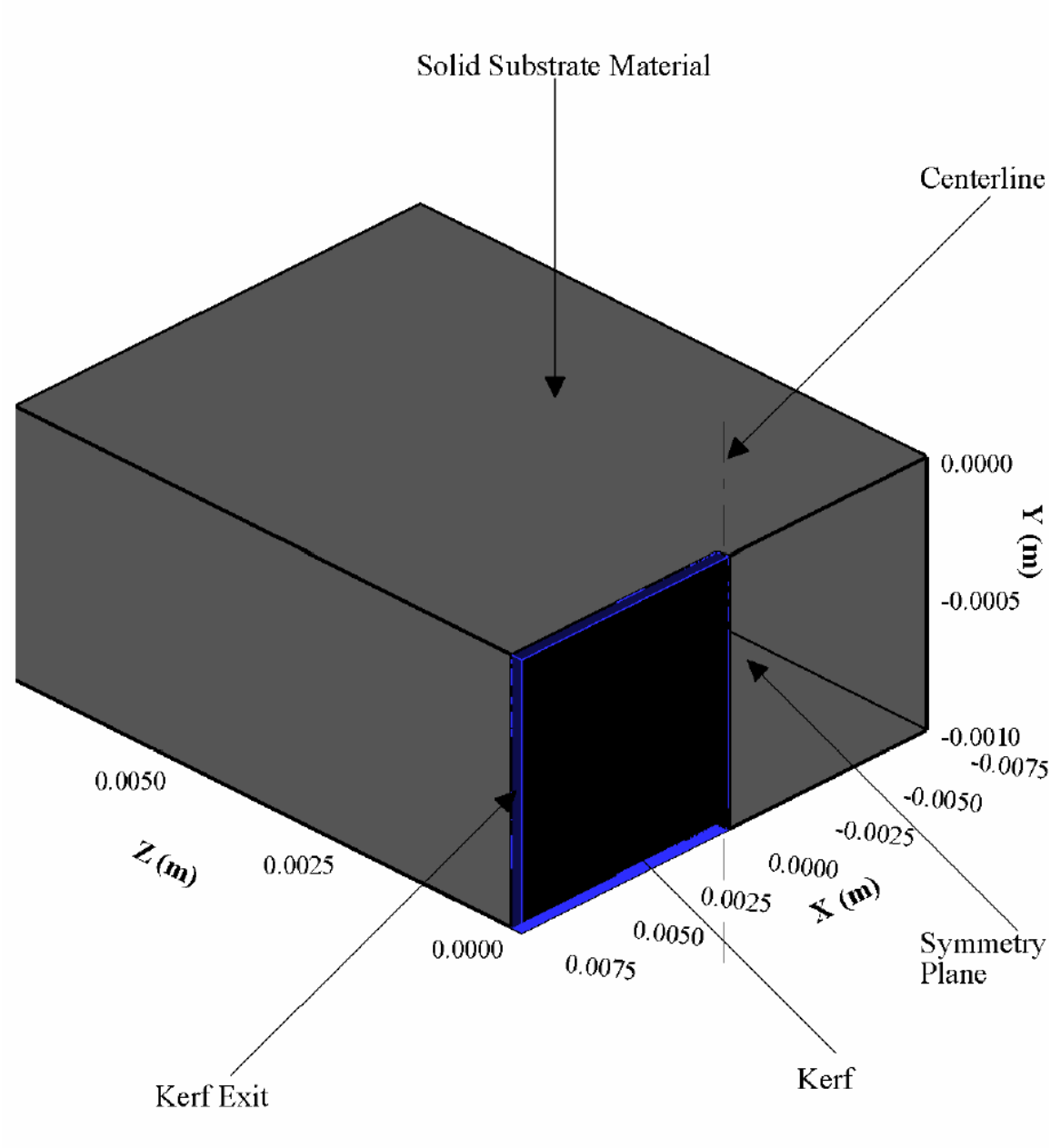

Figure 3.2 Solid material (kerf shaded in blue and kerf side wall shaded in black)

TABLE 3.1 Geometric Parameters and Average Jet Velocities Considered in Simulations

Kerf Wall Thickness	Standoff Distance (H/D)	Kerf Wedge Angle (α)	Average Jet Velocity (V_j)
0.0005 m	2.2	0°	30 m/s
		2°	40 m/s
	3.0	4°	50 m/s
0.0010 m	2.2	0°	30 m/s
		2°	40 m/s
	3.0	4°	50 m/s
0.0015 m	2.2	0°	30 m/s
		2°	40 m/s
	3.0	4°	50 m/s
0.0020 m	2.2	0°	30 m/s
		2°	40 m/s
	3.0		50 m/s

The origin of the (x, y, z) coordinate system is at the kerf surface. The total nozzle length is 0.023 m with the length of the converging section being 0.00965 m. The nozzle inlet and outlet diameters are 0.013 m and 0.0009 m respectively. The kerf radius considered in the above geometry is 0.00015 m. Therefore, the kerf width is 0.0003 m. The kerf region is extended along the x-direction to a distance of 0.0075 m so that the outlet boundary condition does not affect the flow and heat transfer. Similarly, the exiting flow region below the kerf is extended to a distance of 5 times the kerf wall thickness along the negative y-direction.

3.2.2 BOUNDARY CONDITIONS

3.2.2.1 Flow Boundary Conditions

- *Inlet:* The boundary conditions for temperature and the mass flow rate at the nozzle inlet are introduced. A constant mass flow rate is imposed at the nozzle inlet since the flow is compressible and the exact velocity profile at nozzle exit is unknown. Exploratory computations of axisymmetric, confined and submerged liquid jet performed by Morris et al. [16] showed that the turbulence intensity at the inlet had a negligible effect on the exit profile. Shi et al. [18] also reported that turbulent intensity at the boundary is expected to have negligible effect on the impingement heat transfer. Because, turbulence intensity at inlet is unknown, FLUENT default values are used. The dissipation rate is calculated from the hydraulic diameter associated with an established flow condition. Four values for the mass flow rate are used, which correspond to the four average velocities at nozzle exit (Table 3.1). They are: 2.34×10^{-5}, 3.12×10^{-5}, 3.90×10^{-5}, and 4.68×10^{-5}

Kg/s. Temperature is set to 300 K. The selection of the values of temperature and mass flow rate is due to the similar values used in the laser gas assisted processing.

- *Nozzle Wall:* A no-slip boundary condition is imposed along the nozzle wall. Therefore, the boundary condition for velocity is $\tilde{U}_i = 0$. The wall temperature is set to 300 K.
- *Confinement Surface (C):* No-slip and constant temperature (300 K) boundary conditions are applied at the nozzle confinement surface.
- *Laser Cut Kerf Outlet:* A constant static pressure boundary condition was applied at the kerf outlet.
- *Kerf Wall:* No-slip boundary condition is imposed at the kerf wall.
- *Outlet Condition:* A constant static pressure boundary condition was applied at the outlet boundaries (B) shown in figure 3.1.

3.2.2.2 Solid Boundary Conditions

- *Kerf Wall:* A constant temperature boundary condition was imposed at the kerf wall. The kerf wall temperature is kept at 1500 K, which is almost the melting temperature of the substrate material steel, to simulate actual laser cutting conditions.
- *Convective Boundary Condition:* The solid material transfers heat from its sides to the ambient fluid by convection. This is denoted as boundary (A) in figure 3.1. A heat transfer coefficient for still air (h = 10 W/m^2K) and a free stream temperature of 300 K are assumed.

3.2.2.3 Solid Fluid Interface Boundary Conditions

Coupling of conduction within the solid and convection within the fluid is applied at the solid fluid interface. This implies continuity of heat flux and temperature that can be expressed mathematically as:

$$\tilde{T}_{w,solid} = \tilde{T}_{w,gas}$$

$$k_{solid} \frac{\partial \tilde{T}_{w,solid}}{\partial x} = k_{gas} \frac{\partial \tilde{T}_{w,gas}}{\partial x}$$

The solid has two interfaces with the fluid. The top part of the solid has an interface with the impinging fluid region. The bottom part of the solid has an interface with the region containing the fluid exiting through the kerf. Radiation effects are neglected.

3.2.2.4 Variable Properties

Nitrogen is employed as an inert assisting gas jet. The density of nitrogen varies according to the ideal gas law (Equation of State, 3.6) depending on the local pressure and temperature; while the specific heat, dynamic viscosity and thermal conductivity are considered to be a function of temperature only. Table 3.2 gives the Nitrogen gas properties used in the simulations. The density of steel is constant; while its specific heat capacity and thermal conductivity vary with temperature according to the following correlations [8]:

$$k = 64.102 - 0.04803T + 1.518 \times 10^{-5} T^2$$

$$c_p = 24.558 + 1.223T - 3.7693 \times 10^{-4} T^2$$

TABLE 3.2 Nitrogen Thermo-Physical Properties Used in Simulations

Temperature (K)	c_p (kJ/kg·K)	$\mu \cdot 10^7$ (N· s/m^2)	$k \cdot 10^3$ (W/m· K)
300	1.041	178.2	25.9
350	1.042	200.0	29.3
400	1.045	220.4	32.7
450	1.050	239.6	35.8
500	1.056	257.7	38.9
550	1.065	274.7	41.7
600	1.075	290.8	44.6
700	1.098	321.0	49.9
800	1.22	349.1	54.8
900	1.146	375.3	59.7
1000	1.167	399.9	64.7
1100	1.187	423.2	70.0
1200	1.204	445.3	75.8
1300	1.219	466.2	81.0
1400	1.232	486.2	86.7
1500	1.243	505.2	91.8

3.3 GRID DETAILS AND CONSIDERATIONS

The geometrical domain is modeled in Gambit 2.1.6 using a bottom-up approach. A structured and conformal grid is then constructed, where edge meshing is used to assure high-quality elements. Hexahedral cells are used over the computational domain. Although the mesh employed is structured, it should be emphasized that in the current version (FLUENT 6.2.16) FLUENT uses an *unstructured* solver [15]. Therefore, it uses internal data structures to assign an order to the cells, faces, and grid points in a mesh and to maintain contact between adjacent cells [15]. Moreover, it does not require i,j,k indexing to locate neighboring cells and does not force an overall structure or topology on the grid [15].

The computer program FLUENT used for the present simulation can handle non-uniform grid spacing. Figure 3.3 shows the basic computational grid used in the simulations for kerf wall thickness = 2 mm and kerf wedge angle = 0°. Along the Y-axis, uniform grid spacing is used in the straight part of the nozzle. Whereas, in the converging part of the nozzle grid spacing decreases towards the nozzle exit such that a fine grid is allocated in the region of the nozzle exit. A fine uniform grid is created in the impinging fluid region along Y-axis above the kerf surface. In the solid and kerf region, a find grid is allocated provided that the grid points' density decreases towards the kerf exit along the negative y-axis and so in the bottom fluid region below the kerf exit. Moreover, fine grid is allocated in the vicinity of the centerline grid spacing increases at locations away from the centerline along both the x-axis and z-axis directions, with the grid size growing factor adjusted to 1.2 or 1.3. Figure 3.4 shows the three dimensional grid constructed in

the kerf region for two kerf wall wedge angles: 0° and 4°. In each direction fine grid spacing near the gas jet impinging point and the kerf wall is allocated.

Considering the case for which kerf wall thickness = 2 mm and nozzle-kerf surface spacing = 2 mm, the number of grid points used in the simulations for nozzle and kerf including the solid part in x, y, and z directions is 26×68×26 and 41×54×41, respectively. Moreover, the number of grid points used in the spacing between the nozzle exit and the kerf surface in x, y, and z directions is 41×134×41. The number of grid points used in the spacing between the kerf exit and bottom outer boundary in x, y, and z directions is 41×52×41. Modifications in the abovementioned grid size and description have been applied when determined necessary as the physical domain geometry have been changed. As a reminder, changes have been applied to the following geometric parameters: standoff distance, kerf wall thickness, and kerf wall wedge angle. Accordingly, slight modifications have been necessary in order to maintain grid quality as far as smoothness and cells' aspect ratios are concerned. Grid independence tests have been performed. Details concerning the grid independence tests are provided in Chapter 4: Numerical Code and Turbulence Model verification.

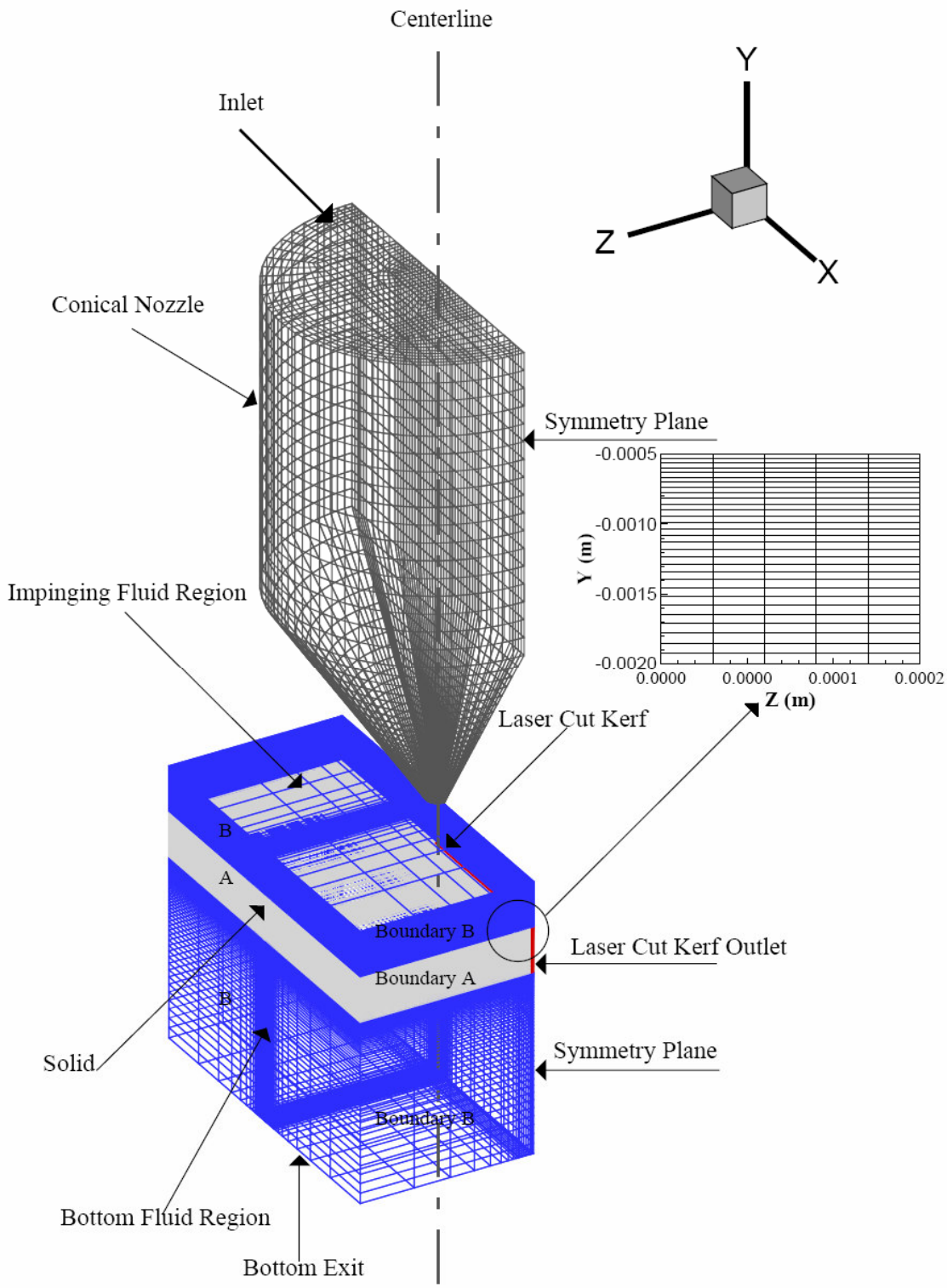

Figure 3.3 Sample computational grid used in the simulations

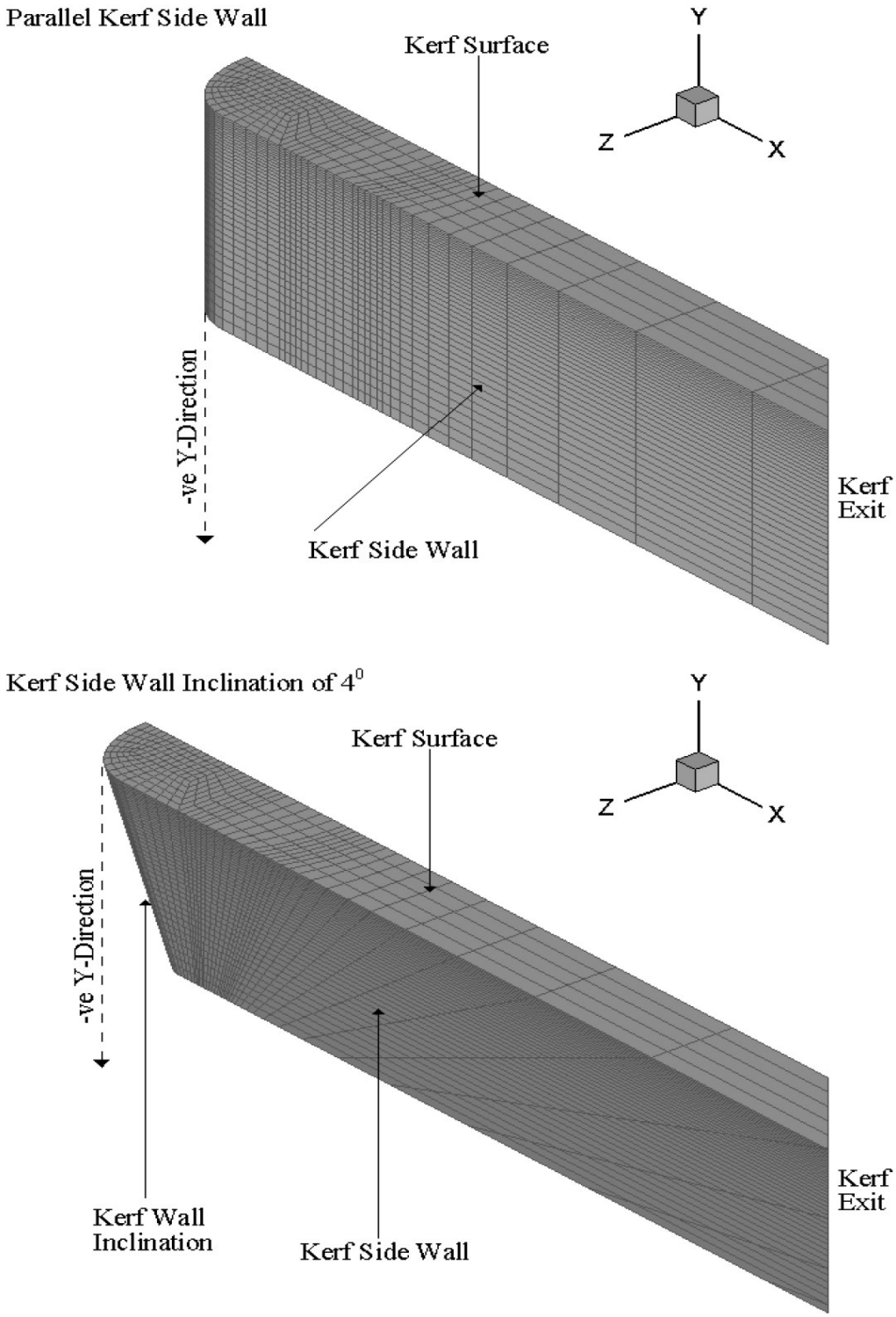

Figure 3.4 Computational grid in the kerf region for two kerf wedge angles

3.4 NUMERICAL SCHEME

3.4.1 THE GENERAL DIFFERENTIAL EQUATION

A close investigation of the differential conservation equations governing the flow field and heat transfer (Equations 3.1 – 3.4) and the transport of turbulent quantities (3.9 – 3.10) indicates that all the dependent variables of interest seem to obey a generalized conservation principle. If the dependent variable here is denoted by ϕ, the general differential equation for steady state can be written as [94]

$$div(\overline{\rho}\underline{\tilde{U}}\phi) = div(\Gamma_\phi grad\phi) + S_\phi \tag{3.35}$$

It should be reemphasized that the under-bar indicates a vector quantity. Γ_ϕ is the diffusion coefficient and S_ϕ is the source term. It should be noted that the above partial differential equation is non-linear and elliptic. The following table lists the dependent variables and the associated Γ_ϕ and S_ϕ terms for the governing conservation equations RNG turbulence model transport equation for k and its rate of dissipation ε. Note that the tilde is removed from the general variable in the above general equation. However, it should be always kept in mind that the favre-averaging indicated by the tilde is applicable where suitable.

The general variable parameters, diffusion coefficient, and source terms in Table 3.3 are determined by direct comparison to equations 3.1 – 3.4 and equations 3.9 and 3.10. Note that $\tilde{U},\tilde{V},\tilde{W}$ represent the Favre-averaged (denoted by the tilde) components of the Favre-averaged velocity vector. $\tilde{T}$ is the Favre-averaged temperature field. The momentum and energy diffusion coefficients in the second column are defined taking

into consideration the Reynolds Favre-averaged transport terms defined in equations 3.7 and 3.8. In this regards, reference should be made to Versteeg and Malalasekera [91] about the treatment and definition of the momentum and energy source terms in column three. The turbulence parameters diffusion coefficients and source terms in the second and third columns are defined based on direct comparison with equations 3.9 and 3.10.

TABLE 3.3 Dependent Variables and the Associated Diffusion Coefficients and Source Terms for the Governing Conservation Equations

Conservation of	σ	Γ_σ	S_σ
Mass	1	0	0
x momentum	$\tilde{U}$	μ_{eff}	$-\frac{\partial P}{\partial x}+S_{Mx}$
y momentum	$\tilde{V}$	μ_{eff}	$-\frac{\partial P}{\partial y}+S_{My}$
z momentum	$\tilde{W}$	μ_{eff}	$-\frac{\partial P}{\partial z}+S_{Mz}$
Temperature	$\tilde{T}$	λ_{eff}	S_T
Turbulent Kinetic Energy	K	$\alpha_k \mu_{eff}$	$G_k-\rho\varepsilon-Y_M$
Dissipation Rate	E	$\alpha_\varepsilon \mu_{eff}$	$C_{1\varepsilon}\frac{\varepsilon}{k}(G_k)-C^*_{2\varepsilon}\rho\frac{\varepsilon^2}{k}$

3.4.2 The Finite Volume Method

A finite-volume-based approach is used to solve the flow, energy, and turbulence equations. The finite-volume-based approach consists off

- Division of the domain into discrete non-overlapping control volumes such that there is one control volume surrounding each grid point.
- Integration of the governing differential equations over the individual control volumes to construct algebraic discretization equations for the discrete dependent variables. Thus algebraic equations are obtained for the values of the dependent variables (velocity, pressure, temperature, etc.) at the grid points.
- Linearization of the discretized equations and solution of the resultant linear equation system to yield updated values of the dependent variables.

3.4.2.1 Discretization

The flow domain is overlaid with a computational grid. Computational grid center points or nodes denote the locations at which all variables, with the exception of velocities, are calculated. The latter are computed at locations midway between the pressures which drive them. Thus the normal velocity components are directly available at the control-volume faces, where they are needed for the calculation of mass flow rates. A node P with surrounding control volume and neighboring nodes in three dimensions is shown in the following figure. The nodes of a typical grid cluster are labeled as P and its six nearest neighbors: N, S, E, W, T, and B.

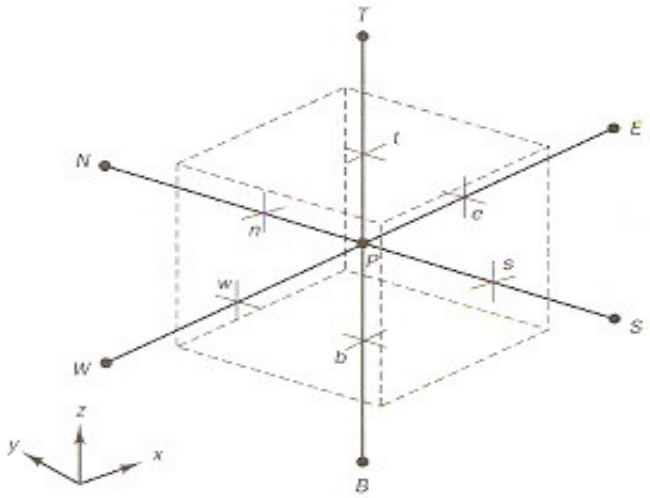

Figure 3.5 Three-dimensional cell with center node P and neighboring nodes

The discretization equations are obtained by integrating equation 3.35 over a three-dimensional control volume. With reference to the control volume for a node P, integration yields:

$$\int_{CV} div(\overline{\rho}\underline{\tilde{U}}\phi)dV = \int_{CV} div(\Gamma_{\phi} grad\phi)dV + \int_{CV} S_{\phi} dV \tag{3.36}$$

Applying Gauss's divergence theorem, equation 3.31 can be written as:

$$\int_{A} \vec{n} \cdot (\overline{\rho}\underline{\tilde{U}}\phi)dA = \int_{A} \vec{n} \cdot (\Gamma_{\phi} grad\phi)dA + \int_{CV} S_{\phi} dV \tag{3.37}$$

It is important to note that the above integration is performed on every three-dimensional cell in the computational domain. The volume element is designated by CV and the surface element by A in the limits of integration in equations 3.36 and 3.37. The limits of integration are such that the surface A completely encloses the volume CV. The vector $\vec{n}$ is the unit vector normal to the surface A, being defined as positive when pointing outward from the enclosed volume CV.

Integration of the general partial differential equation lead to a statement of the conservation of a fluid property for a finite size control volume. Equation 3.37 can interpreted as:

Net rate of decrease of ϕ due to convection across the control volume boundaries	=	Net rate of increase of ϕ due to diffusion across the control volume boundaries	+	Net rate of creation of ϕ inside the control volume

The direct interpretation of the general equation makes the finite volume method easy to understand in physical terms.

The central difference scheme is applied to discretize the diffusion term and the first order upwind scheme is employed to discretize the convection term. Details about deriving the discretization algebraic equation can be found in [91, 94]. The final discretization equation will be presented in this work. Expressing the source term in linear form ($S_\phi = S_c + S_p\phi_p$), the discretization equation for three dimensions can be written as:

$$a_p\phi_p = a_E\phi_E + a_W\phi_W + a_N\phi_N + a_S\phi_S + a_T\phi_T + a_B\phi_B + b$$

where

$$\begin{aligned}
a_E &= D_e + \|-F_e, 0\| \\
a_W &= D_w + \|-F_w, 0\| \\
a_N &= D_n + \|-F_n, 0\| \\
a_S &= D_s + \|-F_s, 0\| \\
a_T &= D_t + \|-F_t, 0\| \\
a_B &= D_b + \|-F_b, 0\| \\
b &= S_c \Delta x \Delta y \Delta z \\
a_p &= a_E + a_W + a_N + a_S + a_T + a_B - S_p \Delta x \Delta y \Delta z
\end{aligned} \tag{3.38}$$

Note that the capital subscript letters E, W, N, S, T, and B denote the neighbor grid points. E denotes the east side; i.e., the positive x direction, while W stands for the west or the negative x direction. N denotes the north side; i.e., the positive y direction, while S stands for the south or the negative y direction. T denotes the top side; i.e., the positive z direction, while B stands for the bottom or the negative z direction. The small subscript letters e, w, n, s, t, and b denote the control volume faces in the respective directions. D is the diffusion conductance defined as: $D = \frac{\Gamma}{\delta x}$ and F indicates the strength of convection strength or flow defined as: $F = \rho U$. It is useful at this point to define Peclet number Pe

as the ratio of F and D. The notation $\|A, B\|$ is used to denote the greater of A and B. The flow rates and conductances are defined as:

$$
\begin{aligned}
F_e &= (\rho U)_e \Delta y \Delta z, D_e = \frac{\Gamma_e \Delta y \Delta z}{(\delta x)_e} \\
F_w &= (\rho U)_w \Delta y \Delta z, D_w = \frac{\Gamma_w \Delta y \Delta z}{(\delta x)_w} \\
F_n &= (\rho V)_n \Delta z \Delta x, D_n = \frac{\Gamma_n \Delta z \Delta x}{(\delta y)_n} \\
F_s &= (\rho V)_s \Delta z \Delta x, D_s = \frac{\Gamma_s \Delta z \Delta x}{(\delta y)_s} \\
F_t &= (\rho W)_t \Delta x \Delta y, D_t = \frac{\Gamma_t \Delta x \Delta y}{(\delta z)_t} \\
F_b &= (\rho W)_b \Delta x \Delta y, D_b = \frac{\Gamma_b \Delta x \Delta y}{(\delta z)_b}
\end{aligned}
\tag{3.39}
$$

$\Delta x, \Delta y, and \Delta z$ denote control volume dimensions, while $\delta x, \delta y, and \delta z$ denote separations between nodes. Equations of the form (3.38 and 3.39) are written for each variable (see table) at every cell in the computational domain. Cells adjacent to the boundary are dealt with separately, by the boundary conditions, so that a uniform approach can be made in matching the boundary conditions to the interior for all ϕ variables and all flow conditions.

3.4.2.2 Calculation of the Flow Field

The pressure gradient forms a part of the source term for a momentum equation. However, there is no obvious equation for obtaining pressure. The pressure field is indirectly specified via the continuity equation. When the correct pressure field is substituted into the momentum equations, the resulting velocity field satisfies the continuity equation. Therefore two problems exist: 1) determining the pressure field and

2) satisfying continuity. The two problems are overcome by adjusting the pressure field so as to satisfy continuity.

Scalar variables, such as pressure, density, temperature etc., are evaluated at nodal points. However, if velocities and pressures are both defined at the control volume nodes, the influence of pressure is not properly represented in the discretised momentum equations. Therefore, a staggered grid arrangement is used in which the velocity components are calculated on staggered grids centered around the cell faces. A staggered grid arrangement generates velocities at exactly the locations where they are required for the scalar transport – convection-diffusion – computations. Hence, no interpolation is needed to calculate velocities at the cell faces.

FLUENT [15] uses momentum-weighted averaging of the face value of velocity, employing weighting factors based on the a_p coefficient from discrete momentum equation. Using this procedure, the face flux J_f may be written as:

$$J_f = \hat{J}_f + d_f (p_{c0} - p_{c1}) \tag{3.40}$$

where $p_{c0} and p_{c1}$ are the pressures within the two cells on either side of the face, and $\hat{J}_f$ contains the influence of velocities in these cells. The term d_f is a function of $\overline{a_p}$, the average of the momentum equation a_p coefficients for the cells on either side of face f. Pressure-velocity coupling is achieved by using equation 3.39 to derive an equation for pressure from the discrete continuity equation. FLUENT provides the option to choose among four pressure-velocity coupling algorithms [15]. In this work, the **SIMPLE** (Semi-Implicit Method for Pressure-Linked Equations) algorithm will be employed. This algorithm employs an iterative process to convergence. The mathematical development

of this procedure focuses on providing a pressure link between continuity and momentum. Full details of the SIMPLE algorithm are provided by [91, 94]. Brief details on executing the SIMPLE algorithm in FLUENT [15] are provided below.

The SIMPLE algorithm uses a relationship between velocity and pressure corrections to enforce mass conservation and to obtain the pressure field. An initial guess of the pressure is required at each grid point. If the momentum equation is solved with a guessed pressure field p^*, the resulting face flux J_f^* computed from equation 3.39

$$J_f^* = \hat{J}_f^* + d_f (p_{c0}^* - p_{c1}^*) \tag{3.41}$$

does not satisfy the continuity equation. Consequently, a correction J_f' is added to the face flux J_f^* so that the corrected face flux, J_f

$$J_f = J_f^* + J_f' \tag{3.42}$$

satisfies the continuity equation. The SIMPLE algorithm postulates that J_f' be written as

$$J_f' = d_f (p_{c0}' - p_{c1}') \tag{3.43}$$

where p' is the cell pressure correction. The SIMPLE algorithm substitutes the flux correction equations (Equations 3.41 and 3.42) into the discrete continuity equation to obtain a discrete equation for the pressure p' correction in the cell:

$$a_p p' = \sum_{nb} a_{nb} p_{nb}' + b \tag{3.44}$$

The subscript (nb) refers to neighbor cells and the source term b is the net flow rate into the cell:

$$b = \sum_{f}^{N_{faces}} J_f^* A_f \tag{3.45}$$

A_f is the face area. Once a solution of the pressure correction equation (Equation 3.43) is obtained, the cell pressure and the face flux are corrected using:

$$p = p^* + \alpha_p p' \tag{3.46}$$

$$J_f = J_f^* + d_f (p'_{c0} - p'_{c1}) \tag{3.47}$$

Here α_p is the under-relaxation factor for pressure.

The solution for the discretization equations proceeds through iterations by repeating the following steps:

1. Provide an initial guess of the solution flow field variables, including pressure.
2. Solve the dicretised momentum equations using the guessed pressure field and compute resulting fluxes using equation 3.41.
3. Solve the pressure correction equation 3.45.
4. Calculate the corrected pressure and face fluxes using equations 3.46 and 3.47.
5. Solve the dicretization equation (3.38) for all dependent variables.
6. Set the newly computed values of the variables as improved estimates and return to step 1.
7. Repeat steps 1 through 6 until convergence.

The segregated algorithm, illustrated in Figure 3.5, is chosen in FLUENT to solve the governing equations. Using this approach, the governing equations are solved sequentially (i.e. segregated from one another). In this approach, each discrete governing equation is linearized implicitly with respect to that equation's dependent variable. This will result in a system of linear equations with one equation for each cell in the domain. Because implicit linearization is employed, each unknown will appear in more than one

equation in the system, and these equations must be solved simultaneously to give the unknown quantities. A point implicit (Gauss-Seidel) linear equation solver [95] is used in conjunction with an algebraic multigrid (AMG) method [15] to solve the resultant scalar system of equations for the dependent variable in each cell.

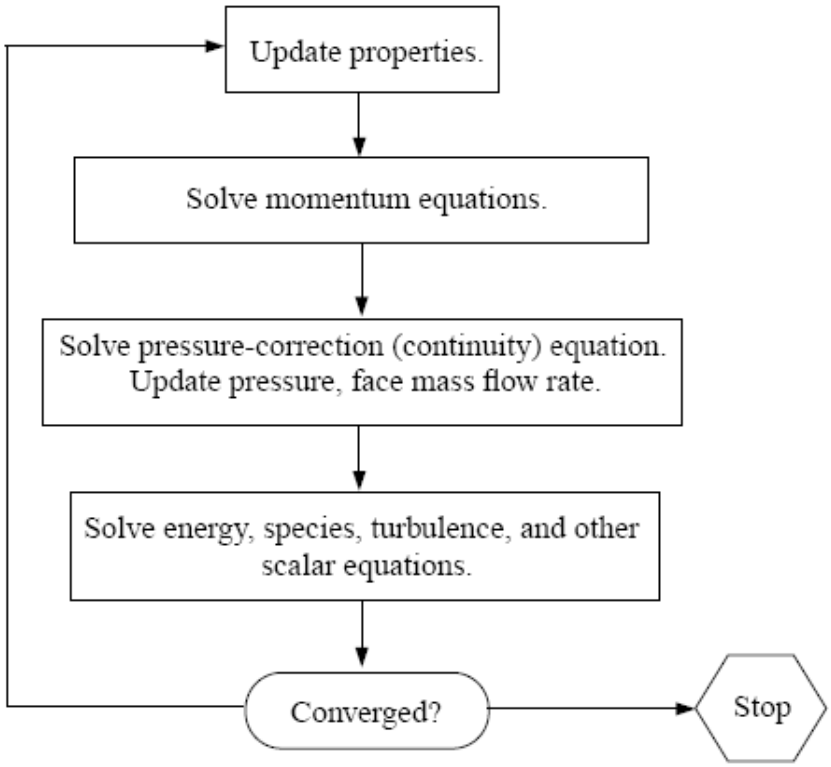

Figure 3.6 Overview of the segregated solution method [15]

In summary, the general discretization equation is linearized to produce a system of equations for each of the dependent variables. A segregated and implicit solver is utilized to solve the flow, energy, and turbulence equations. For the pressure-velocity coupling SIMPLE algorithm is used while standard pressure discretization is applied [15]. The momentum, energy, and turbulence equations are discretized using the first order upwind scheme. The segregated approach solves for a single variable field (ϕ) by considering all cells at the same time to yield an updated field for that variable. It then solves for the next variable field by again considering all cells at the same time, and so on until convergence is reached.

3.4.2.3 Under-Relaxation

Because of the nonlinearity of the equation set being solved by FLUENT, it is necessary to control the change of ϕ. This is typically achieved by under-relaxation, which reduces the change of ϕ produced during iteration. In a simple form the under-relxation can be expressed as:

$$\phi = \phi_{old} + \alpha \Delta \phi \tag{3.48}$$

The under-relaxation factors used in the simulations for pressure, momentum, k, ε, and energy are 0.3, 0.8, 0.8, 0.8, and 0.8 respectively. The under-relaxation factors density and turbulent viscosity are set to 1.0. In some cases, where the kerf wedge angle increased, the solution demanded further under-relaxation for momentum and energy.

3.4.2.4 Convergence

The convergence criterion adopted in this work requires that the scaled residuals decrease to 10^{-6} for all equations. Scaled residuals are defined by FLUENT as follows [15]:

Rewriting equation 3.38 as:

$$a_p \phi_p = \sum_{nb} a_{nb} \phi_{nb} + b \tag{3.49}$$

FLUENT defines an "unscaled" residual as follows:

$$R^{\phi} = \sum_{cellsP} \left| \sum_{nb} a_{nb} \phi_{nb} + b - a_p \phi_p \right| \tag{3.50}$$

R^{ϕ} is the imbalance in equation 3.49 summed over all the computational cells P. FLUENT [15] scales the residual using a scaling factor representative of the flow rate of ϕ through the domain. This "scaled" residual is defined as:

$$R^{\phi} = \frac{\sum_{cellsP} \left| \sum_{nb} a_{nb} \phi_{nb} + b - a_p \phi_p \right|}{\sum_{cellsP} \left| a_p \phi_p \right|} \tag{3.51}$$

For the continuity equation, the unscaled residual is defined as:

$$R^{c} = \sum_{cellP} \left| \mathrm{M} \right| \tag{3.52}$$

where M is the rate of mass creation in cell P. The scaled residual for the continuity equation is then defined as:

$$R^{\phi}_{continuity} = \frac{R^{c}_{iterationN}}{R^{c}_{iteration5}} \tag{3.53}$$

The denominator is the largest absolute value of the continuity residual in the first five iterations.

The solution will stop automatically when each variable meets its specified convergence criterion: $R^{\phi} \leq 10^{-6}$.

Another criterion used for monitoring convergence in this study is monitoring the surface heat flux integral on the kerf wall. This is of importance especially in cases where the

residuals decay to some small value (close to 10^{-6}) and then level out. This occurs in simulation for which the kerf wedge angle ≥ 4°. In other words, when the heat flux integral stops changing iterations are stopped and the solution is considered as converged solution.

3.5 SIMULATIONS

Considering the range of parameters investigated in this work (Table 3.1) the total of number of cases that were studied is 104 cases. FLUENT version 6.2.16 was used for the simulations. Typically, 10,000 – 12,000 iterations were necessary to procure convergence, on an eight processor Dell Precision PWS490, E5320@1.86 GHZ, 8.00 GB RAM. Results will be presented in Chapter 5 of this dissertation.

CHAPTER 4

NUMERICAL CODE AND MODEL VERIFICATION

4.1 INTRODUCTION

The heat transfer simulations of turbulent jet flow configuration are quite complex. Indeed, the selected turbulence model has to be able to describe the jet development, its impact, and the laminar/turbulent transition which takes place. It has been mentioned in the introductory chapter and it is emphasized in this section that commercial CFD software has been proven to be a powerful tool in numerically experimenting with turbulence flow in general and various impinging jet problems in particular [13, 14]. Moreover, several studies [16-19] have indicated that the RNG k-ε is well suited for modeling turbulence in jet impingement problems and even can depict several phenomena better than other known turbulence models [18,19].

A recent study performed by Sharif and Mothe [95] aimed at evaluating the performance of several turbulence models in the prediction of convective heat transfer due to slot jet impingement onto flat and concave cylindrical surfaces. Models considered were (1) the standard k-ε model, (2) the RNG k-ε model, (3) the realizable k-ε model, (4) the SST k-ω model, and (5) Large Reynolds number stress transport model. Various near-wall treatments were incorporated. FLUENT was used to perform the computations. It

was found that when the impingement surface was outside the potential core of the jet, most of the turbulence models predicted reasonably accurate thermal data. It was also found that when the impingement surface was within the potential core of the jet, the turbulence models grossly overpredicted the Nusselt number in the impingement region, but in the wall jet region the Nusselt number prediction was fairly accurate. The authors reported that the RNG k-ε model with the enhanced wall treatment and the SST k-ω model predicted the Nusselt number distribution better than the other models for the flat plate as well as the concave surface impingement cases. Moreover, the RNG k-ε model was superior to the SST k-ω model in predictions of hydrodynamic data. The Reynolds stress model did not show any distinctive advantage over the other eddy viscosity models.

4.2 CASE STUDY

Gas-to-wall heat transfer configuration for a round air jet impinging on a circular flat plate has been investigated in a recent experimental study by Sagot et al. [20]. The experimental setup used by the authors is shown schematically in figure 4.1. The radius of the impacted circular plate is R = 24 mm. The jet enters into a PMMA cylindrical vessel with a thickness of 3 mm, height of 200 mm and an inner diameter D_v = 154 mm. The enclosure/plate radius ratio is 3.2 which minimizes any possible jet confinement effects. The enclosure gas outlet consists in a 33 mm diameter tube located on the top of the enclosure. The large values of the enclosure diameter and height make it possible to consider the impinging flow as ***axi-symmetric*** [20]. The average temperature inside the vessel is close to the ambient temperature and the low conductivity plastic enclosure is glass wool insulated to minimize heat losses. The enclosure can be modeled as ***adiabatic***

under test conditions. The gas flows through a long thermally insulated pipe with a large inner diameter (17 mm) in order to obtain a fully developed flow at the nozzle inlet. The nozzle restriction geometry accelerates the flow, thus generating a flat velocity profile. The nozzle diameter used in this study D = 4.8 mm; thus, R/D = 5. The nozzle has constant thickness e = 2 mm, with a chamfer thickness x = 1 mm. The nozzle-to-plate distance is fixed such that H/D = 2. The jet Reynolds number Re_j is fixed by adjusting the gas flow rate.

$$\mathrm{Re}_j = \frac{4\dot{m}_g}{\mu_g \pi D} \tag{4.1}$$

The jet temperature T_j is fixed. A fixed and uniform temperature T_w = 277 K is maintained on the impingement plate.

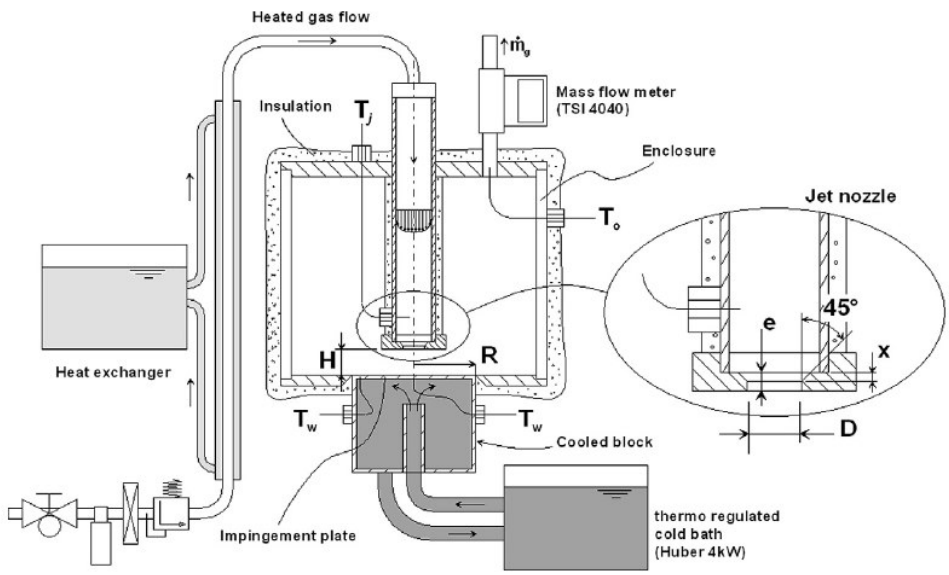

Figure 4.1 Schematic of the experimental setup used by Sagot et al. [20]

A 2D axi-symmetric analysis of fluid flow and heat transfer is carried out using finite-volume based CFD software FLUENT 6.2.16. Dimensions used for the simulation are those defined previously and shown on Figure 4.1. The geometry of the nozzle and its supporting tube, which are described above are taken into account in the grid construction. Structured mesh is generated in GAMBIT 2.1.6 using the bottom-up approach (Figure 4.2). The boundary conditions taken into account in simulations are:

- Conjugate heat transfer is assumed at the enclosure inner wall and nozzle inner and outer wall. This type of boundary condition is termed boundary condition of fourth kind and associated mathematical expressions are given in Chapter 3. Whereas, the enclosure outer wall is assumed to be at ambient temperature.
- The impingement plate is maintained at $T_w = 277$ K.
- No-slip velocity boundary condition is imposed on all walls.
- The inlet condition is an imposed mass flow rate, with a flow rate adjusted according to the prescribed Reynolds number, with an imposed temperature.
- The turbulence intensity has been fixed at a constant value of 4%, and the dissipation rate is calculated from the hydraulic diameter associated with an established flow condition.
- Because of the axi-symmetric 2D chosen configuration, the 33 mm diameter outlet has been represented by an annular slot of equivalent section ($\pi(r_0^2 - r_i^2) = \pi r_{tube}^2$), with a prescribed pressure condition.

The simulated flow is governed by compressible form (Favre-averaged) of the Reynolds-averaged Navier-Stokes (RANS) equations and by the additional equations describing the transport of other scalar properties (see Chapter 3), neglecting viscous dissipation in the

energy transport equation [20]. The numerical method applied is described in full details in Chapter 3. The grid used in the computations is shown in figure 4.2. Simulations are carried out for the following three cases determined by inlet boundary conditions:

1. $T_j = 313$ K, $Re_j = 15000$
2. $T_j = 323$ K, $Re_j = 23000$
3. $T_j = 333$ K, $Re_j = 30000$

The authors of the research paper being examined explicitly defined Reynolds number used in their study. However, during the experiments the gas jet temperature T_j was fixed between 313 and 338 K depending on the Reynolds number [20], without giving clear information about the exact jet temperature. Therefore, the temperatures given above are associated with the respective jet Reynolds number based on the present author's judgment. This has to be taken into consideration when discussing the results obtained. The local heat flux q'' distribution along the circular plate with the imposed temperature is determined using FLUENT. The local heat flux q'' may be expressed as

$$q'' = h(T_j - T_w) \tag{4.2}$$

where h is the local convection coefficient;

T_w is the fixed wall temperature;

and T_j is the jet temperature.

T_j and T_w constitute two fixed reference temperatures for computing the wall/gas heat transfer coefficient. The corresponding local Nusselt number Nu for impinging jet configuration can be defined as follows with the characteristic length being the nozzle hydraulic diameter [92, 20]:

$$Nu = hD/\lambda_g \tag{4.3}$$

where D is nozzle diameter and λ_g is thermal conductivity of the gas.

The total heat transfer rate Q may be obtained by integrating the local flux over the entire three dimensional surface of the kerf side wall. That is,

$$Q = \int_{A_s} q'' dA_s \tag{4.4}$$

The average convective wall heat transfer coefficient is consequently defined as:

$$\bar{h} = \frac{1}{A_s} \frac{Q}{T_j - T_w} \tag{4.5}$$

where A_s is the surface area of the circular plate.

The corresponding average Nusselt number as:

$$\overline{Nu} = \frac{\bar{h}D}{\lambda_g} \tag{4.6}$$

Similarly, the wall shear stress can be determined. The skin friction C_f can be defined as:

$$C_f = \frac{\tau_w}{(1/2)\rho V_j^2} \tag{4.7}$$

where τ_w is the wall shear stress;

ρ is the fluid density;

V_j is the jet velocity magnitude.

The wall shear stress can be integrated over the surface area. The average wall shear stress will be given as: $\bar{\tau}_w = \frac{1}{A_s} \int_{A_s} \tau_w dA_s$ (4.8)

The average skin friction is then given as:

$$\bar{C}_f = \frac{\bar{\tau}_w}{(1/2)\rho V_j^2} \tag{4.9}$$

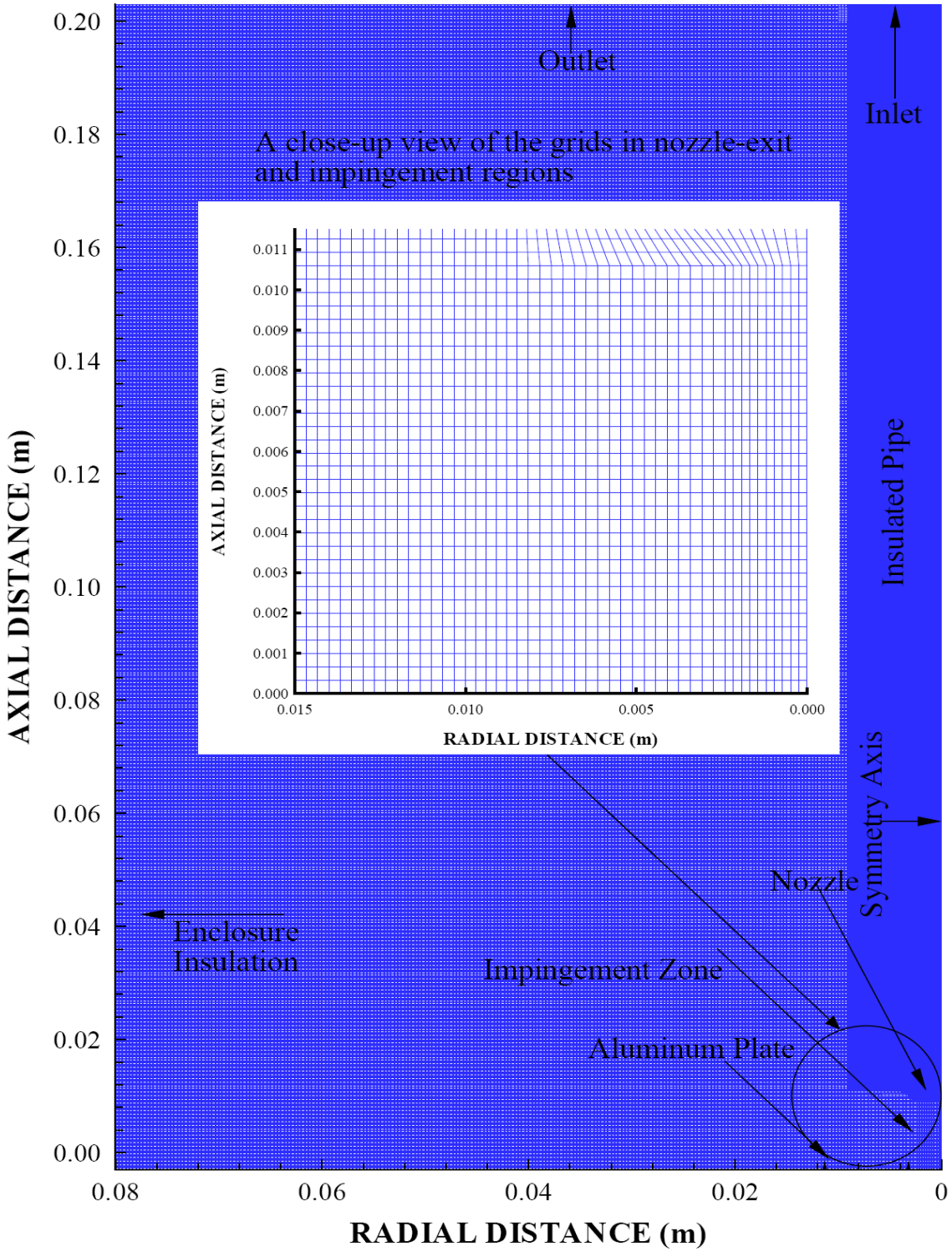

Figure 4.2 Computational domain and insert showing close-up view of the grids in the nozzle exit and impingement regions

Table 4.1 compares the average Nusselt number for the three cases listed above to the average value obtained with the correlation derived by Sagot et al [20]. Computed local Nusselt number distribution has approximately the same trend of variation as the distribution determine by Sagot et al. [20]. Moreover, the computed average Nusselt numbers compare reasonably well to the values reported by Sagot et al. [20]. Considering that all experimental results are subject to some uncertainty, which is rarely quantitatively reported by the authors, and an inadequate description of flow and temperature conditions, and considering the approximation of the data reported by Sagot et al. [20] made by the present author, the agreement between simulation and experimental data is quite encouraging.

TABLE 4.1 Comparison of Average Nusselt Numbers for the Three Cases Under Consideration

	Average Nu (Sagot et al. (2008)	Average Nu (Present Study)	Deviation
Case 1	48	52.58	9.5%
Case 2	67.5	73.82	9.5%
Case 3	90	84.29	6.3%

4.3 GRID INDEPENDENCE STUDY

Considering the case for which kerf wall thickness = 2 mm and nozzle-kerf surface spacing = 2 mm, the number of grid points used in the simulations for nozzle and kerf including the solid part in *x*, *y*, and *z* directions is 26×68×26 and 41×54×41, respectively. Moreover, the number of grid points used in the spacing between the nozzle exit and the kerf surface in x, y, and z directions is 41×134×41. The number of grid points used in the spacing between the kerf exit and bottom outer boundary in x, y, and z directions is 41×52×41. Reference will be made to this grid in the following discussion by the number of grid points in the kerf including the solid section; i.e., 41×54×41. Two additional computational grids are considered in this study. For the first grid, the number of grid points in the kerf including the solid section is 33×49×33. In other words, the number of grid points along the x-axis and z-axis is reduced by 20%. Whereas, the number of grid points along the y-axis is reduced by 10%. This reduction is applied overall the computational domain. For the second grid, the number of grid points in the kerf including the solid section is 49×59×49. In other words, the number of grid points along the x-axis and z-axis is increased by 20%. Whereas, the number of grid points along the y-axis is increased by 10%. This increase is applied overall the computational domain. The simulation will be conducted for averaged jet velocity at nozzle exit = 60 m/s.

Figure 4.4 shows the grid independence test for velocity distribution along centerline. It should be noted that the location y = 0.0 m corresponds to kerf surface or inlet and that the location y = -0.002 m corresponds to kerf bottom exit. It may be

observed that for 41×54×41 grid points the velocity magnitude is almost in agreement with velocity magnitude for the other two grids with a maximum deviation of about 2%.

Figure 4.5 shows the grid independence test for temperature distribution along centerline. It may be observed that temperature distribution in kerf region is exactly matching for the three grids considered. Figure 4.6 shows the grid independence test for Nusselt number distribution at maximum location along normalized kerf thickness. The kerf wall thickness is normalized with the maximum thickness; i.e., normalized kerf wall thickness = 0 represents the kerf inlet and normalized kerf wall thickness = -1 is the kerf exit. The curves are plotted at a location (x = -0.000125 m; z = 0.000075 m) where the Nusselt number almost attained the highest value. It may be observed that for 41×54×41 grid points the Nusselt number distribution is almost in agreement with Nusselt number distribution for the grid with less density with a maximum deviation of about 5%. It may also be observed that for 41×54×41 grid points the Nusselt number distribution is almost in agreement with Nusselt number distribution for the grid with higher density with a maximum deviation of about 3.5%.

Based on the above grid independence study results and taking into consideration that the present study is three dimensional in nature, the grid 41×54×41 has yielded grid independent results. Therefore similar grid density distribution will be adopted in the simulations in accordance with configuration geometric parameters.

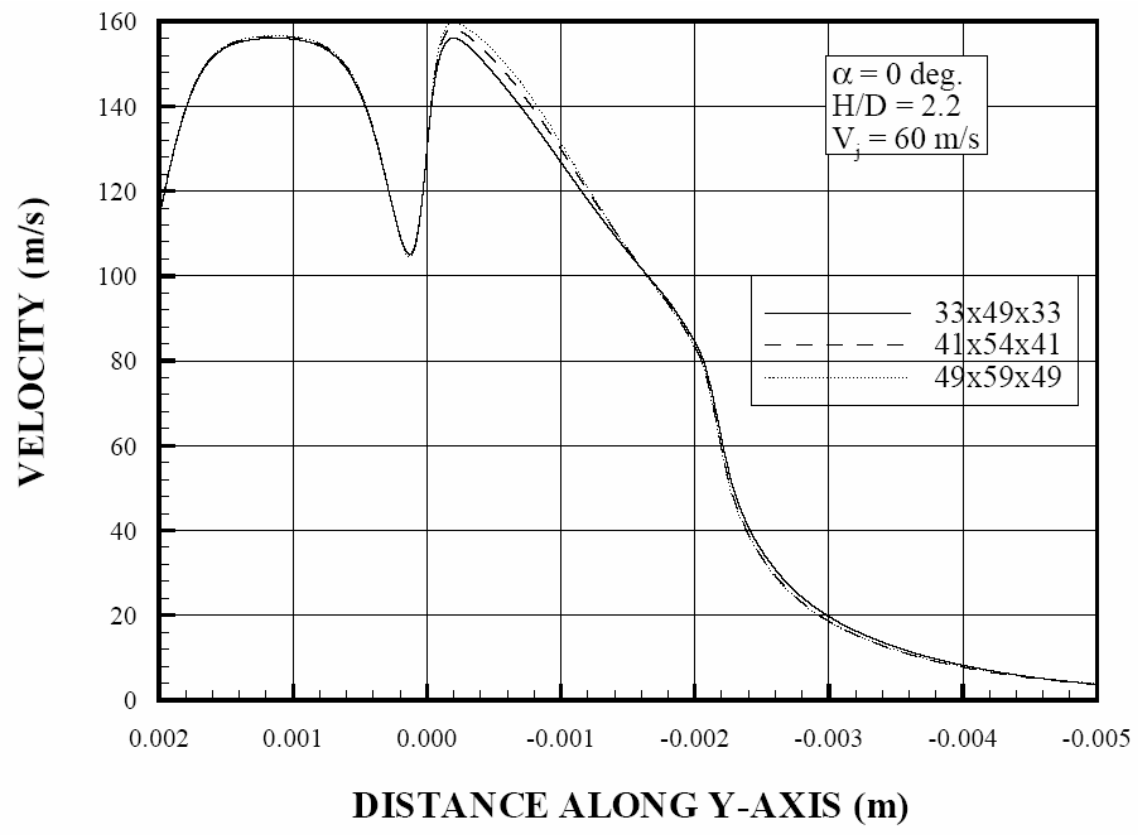

Figure 4.3 Grid independence test for velocity magnitude along centerline

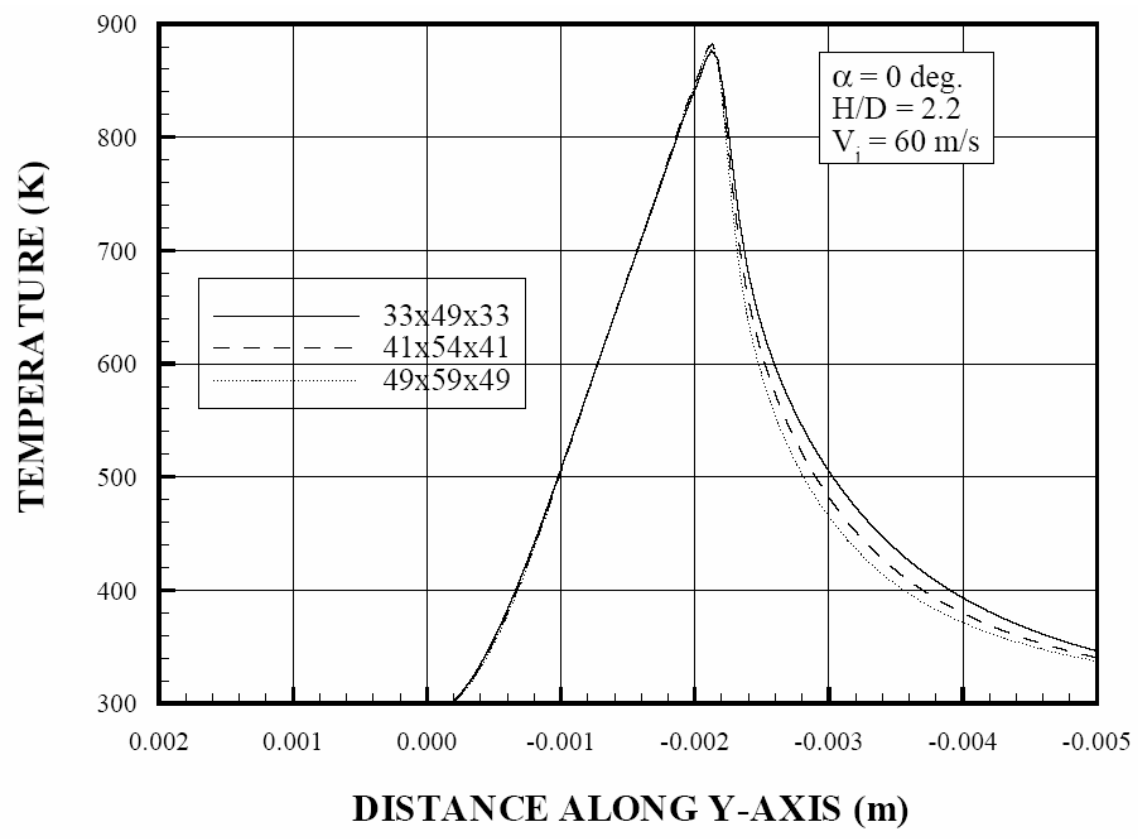

Figure 4.4 Grid independence test for temperature distribution along centerline

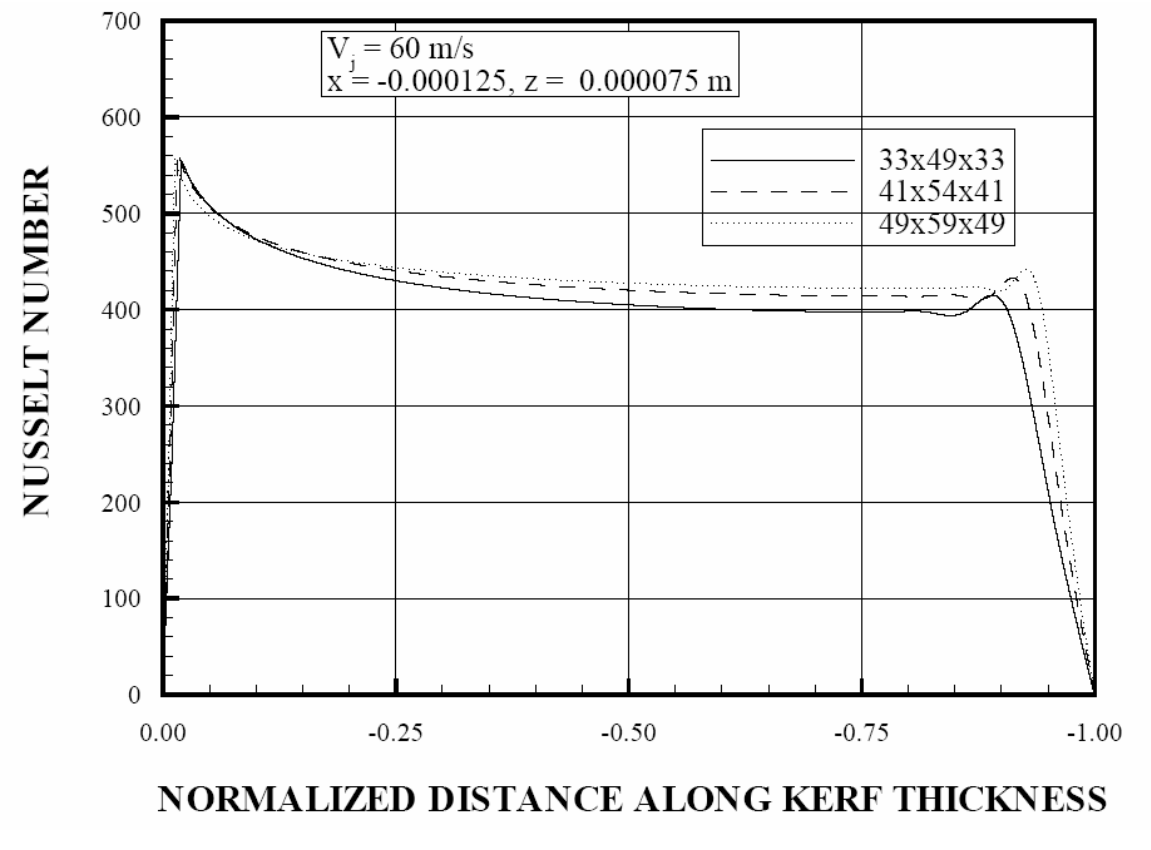

Figure 4.5 Grid independence test for Nusselt number distribution along normalized kerf wall thickness at the location where Nusselt number approximately attained highest values

CHAPTER 5

RESULTS AND DISCUSSION

In the present study, jet emerging from a conical convergent nozzle and impinging onto the kerf surface is investigated in relation to the laser cutting process. Heat transfer rates from the kerf wall and the skin friction along the kerf surface are important for quality cutting. The flow field in the kerf, the heat transfer rates from the kerf wall, and the skin friction along the kerf surface are computed for various average jet velocities at nozzle exit, two different standoff distances, four different kerf thicknesses (depths), and four kerf wall wedge angles. The kerf wall temperature is kept at 1500 K to resemble the laser cutting process. The heat transfer rates from the kerf surface and the skin friction are predicted using the three-dimensional model while accommodating the control volume approach. Figure 5.1 shows two kerf geometries considered in this study. The grey curved surface is the kerf wall maintained at 1500 K and blue plane parallel to y-axis is kerf symmetry plane. Reference to this figure is made in the following discussion when deemed necessary. The reader is also advised to refer back to figures 3.1, 3.2, 3.3, and 3.4 in Chapter 3.

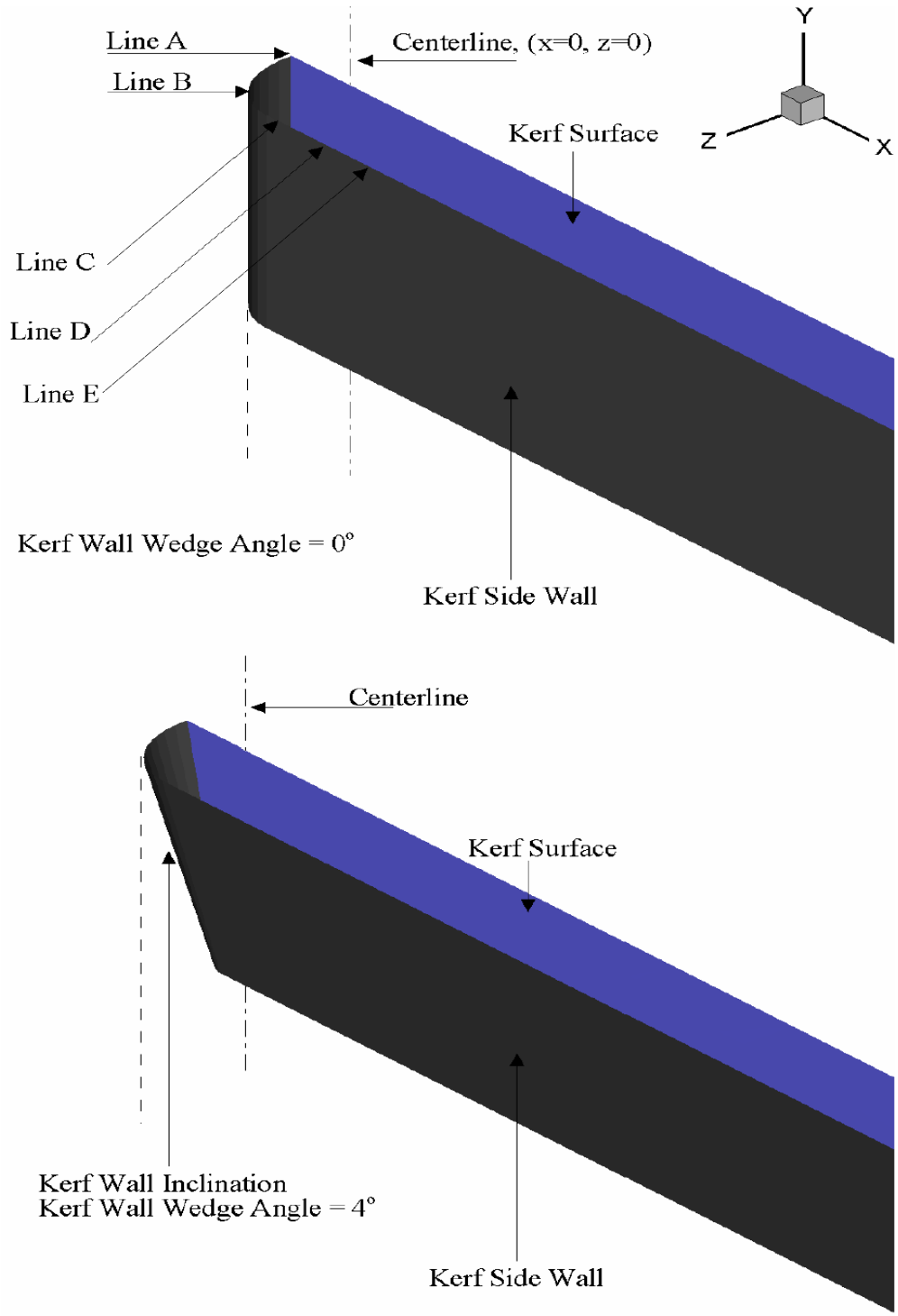

Figure 5.1 Kerf regions for two kerf wedge angles

5.1 Effect of Averaged Jet Velocity at Nozzle Exit on Heat Transfer Rates and Skin Friction

The effects of jet velocity on the heat transfer rates and the skin friction are considered in this section. For this purpose, kerf thickness of 1.0 mm is considered. Two corresponding kerf wedge angles (0° and 4°) and two averaged jet velocities at the nozzle exit (30 m/s and 60 m/s) are accommodated.

Figures 5.2 and 5.3 show normalized velocity contours (V/V_j, V_j is the averaged jet velocity at the nozzle exit) for two different averaged jet velocities and two kerf wedge angles. It should be noted that since the geometric configuration of the jet impingement onto a kerf has plane symmetry, the normalized velocity contours were shown in the symmetry plane. In general, jet expands radially in the region of the kerf surface, provided that the expansion of the impinging jet in the region close to surface of the kerf (Figures 5.2 and 5.3) is more pronounced. The radial acceleration of the jet along the kerf surface results in the formation of the radial jet. In this case, streamline curvature formed becomes sharp in the region of the jet outer boundary due to bending of the impinging jet. The sharp forming of the impinging flow and the radial expansion result in small circulation cell at the tip of the edge of the kerf surface. This situation is true for all gas jet velocities and the kerf wedge angles incorporated in the present study. Moreover, flow spilling at the edge of the kerf surface contributes to the formation of the small circulation cell. However, a large circulation cell is developed in the neighborhood of the outer region of the impinging jet above the kerf top (open) surface. Formation of large circulation is associated with the shear flow in the outer surface of the impinging jet and the loss of momentum of the radially developing jet due to presence of kerf open surface.

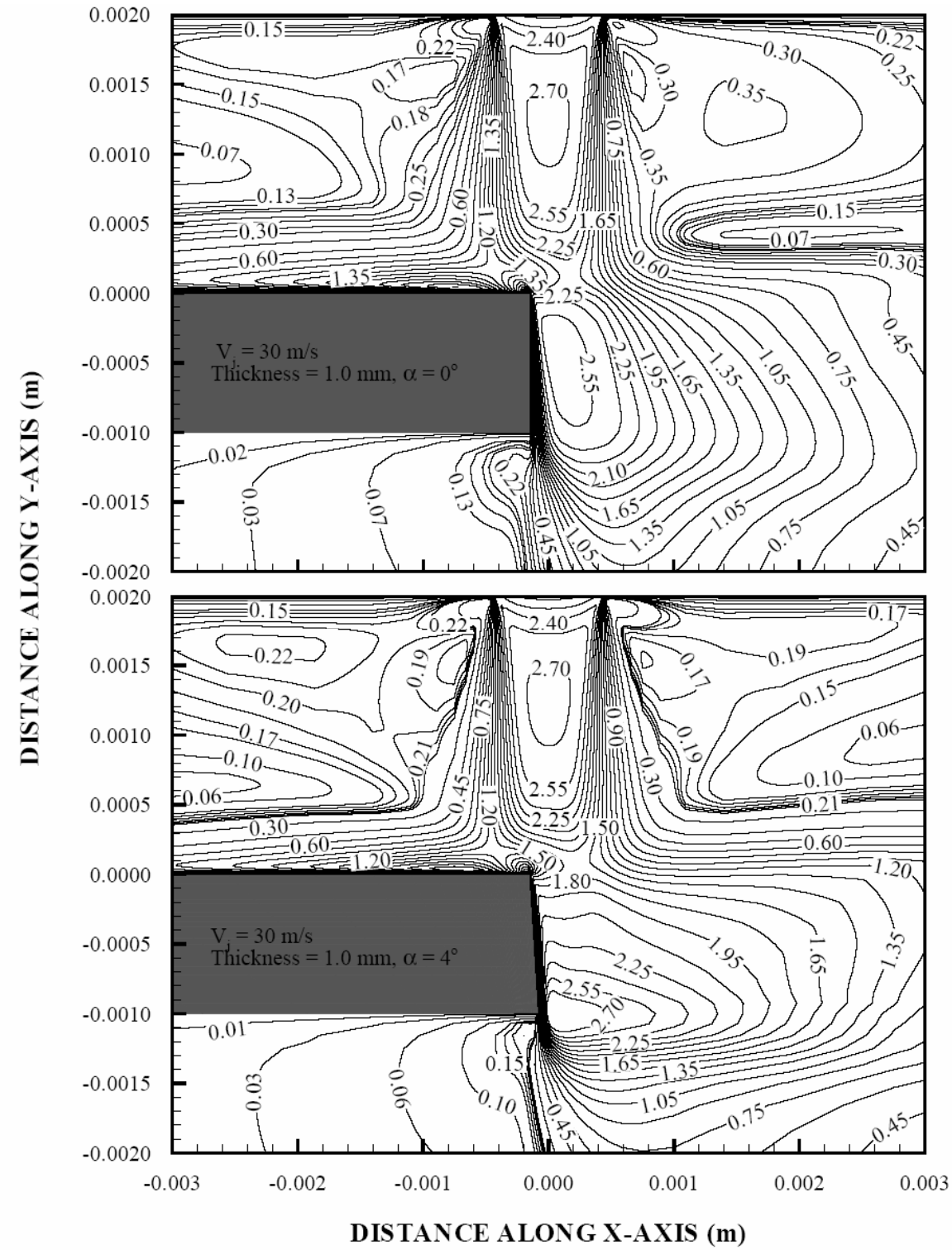

Figure 5.2 Normalized velocity magnitude for one averaged jet velocity (30 m/s) and two kerf wedge angles (0° and 4°)

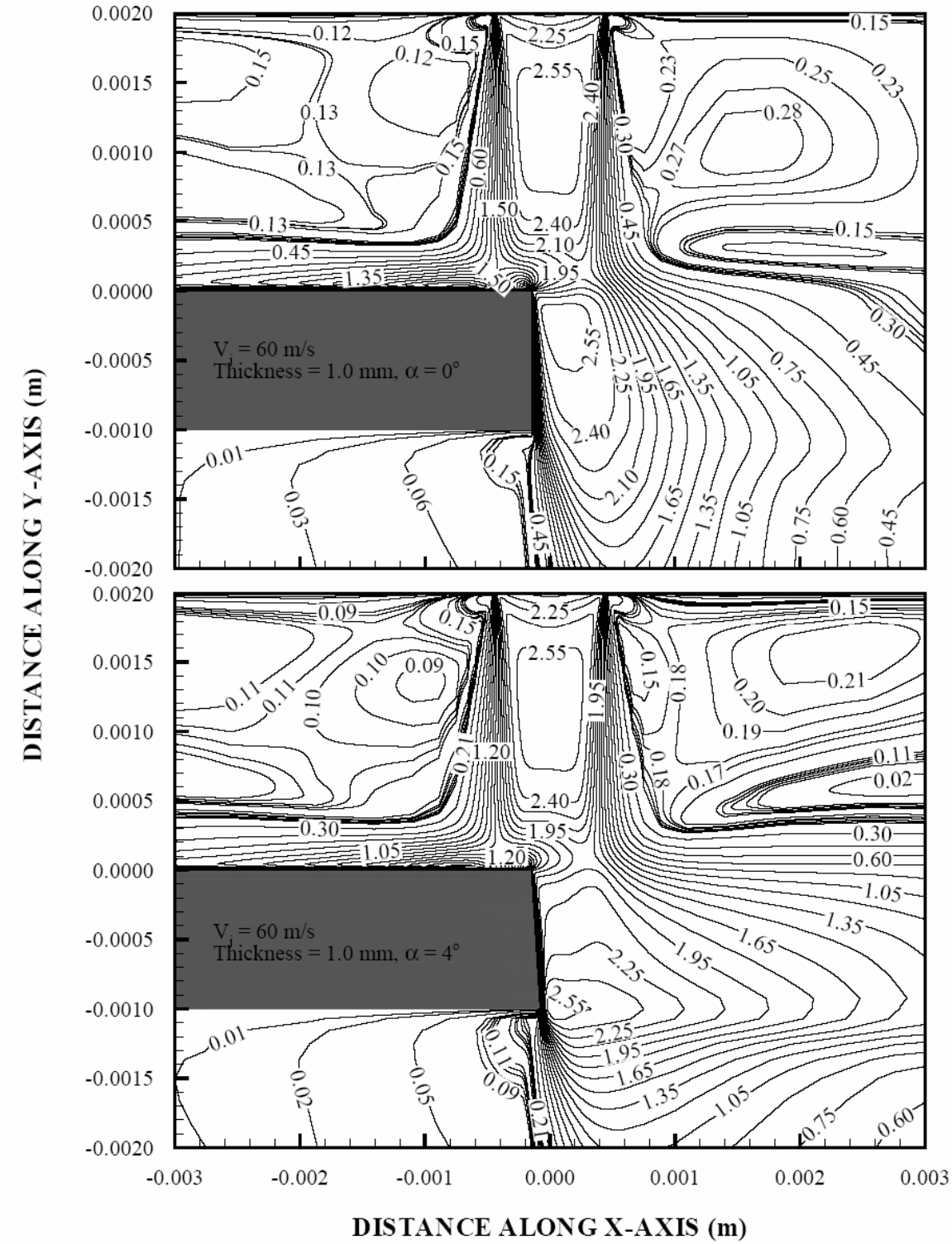

Figure 5.3 Normalized velocity magnitude for one averaged jet velocity (60 m/s) and two kerf wedge angles (0° and 4°)

However, by increasing the kerf wedge angle, the location and size of the circulation cell are modified. In this case, the circulation cell is shifted away from the kerf surface region. In addition, increasing the kerf wedge angle influences the streamline curvature of the impinging jet and flow spilling along the kerf surface, which enhances the radial momentum of the flow while forming a circulation cell along the solid surface next to the kerf edge. It should be noted that increasing kerf wedge angle partially blocks the flow inside the kerf enhancing the blockage effect of the impinging flow. Radial acceleration of the flow results in the region close to the kerf side wall because of the losses in the flow axial momentum close to the kerf surface and because of the radial flow caused by streamline curvature of the impinging flow in the kerf. This appears as radially expanding flow in the kerf. This is more pronounced for the large kerf wedge angle. The blockage effect of the wedge angle is responsible for the radial expansion of the flow in the kerf. As the flow exits from the kerf bottom surface, it expands in both axial and radial directions. This situation is particularly observed for the large kerf wedge angle; i.e., kerf wedge acts as a throttling passage for the flow causing the flow expansion on set of leaving the kerf wedge.

Figures 5.4 and 5.5 show normalized temperature contours (T/T_j, T_j is the jet temperature at the nozzle exit) in the symmetry plane for two different jet averaged velocities and two kerf wedge angles. Temperature contours follow almost the velocity contours provided that the flow mixing upon the jet expansion modifies temperature contours. It should be noted that the kerf wall temperature is kept at 1500 K while jet temperature is at 300 K.

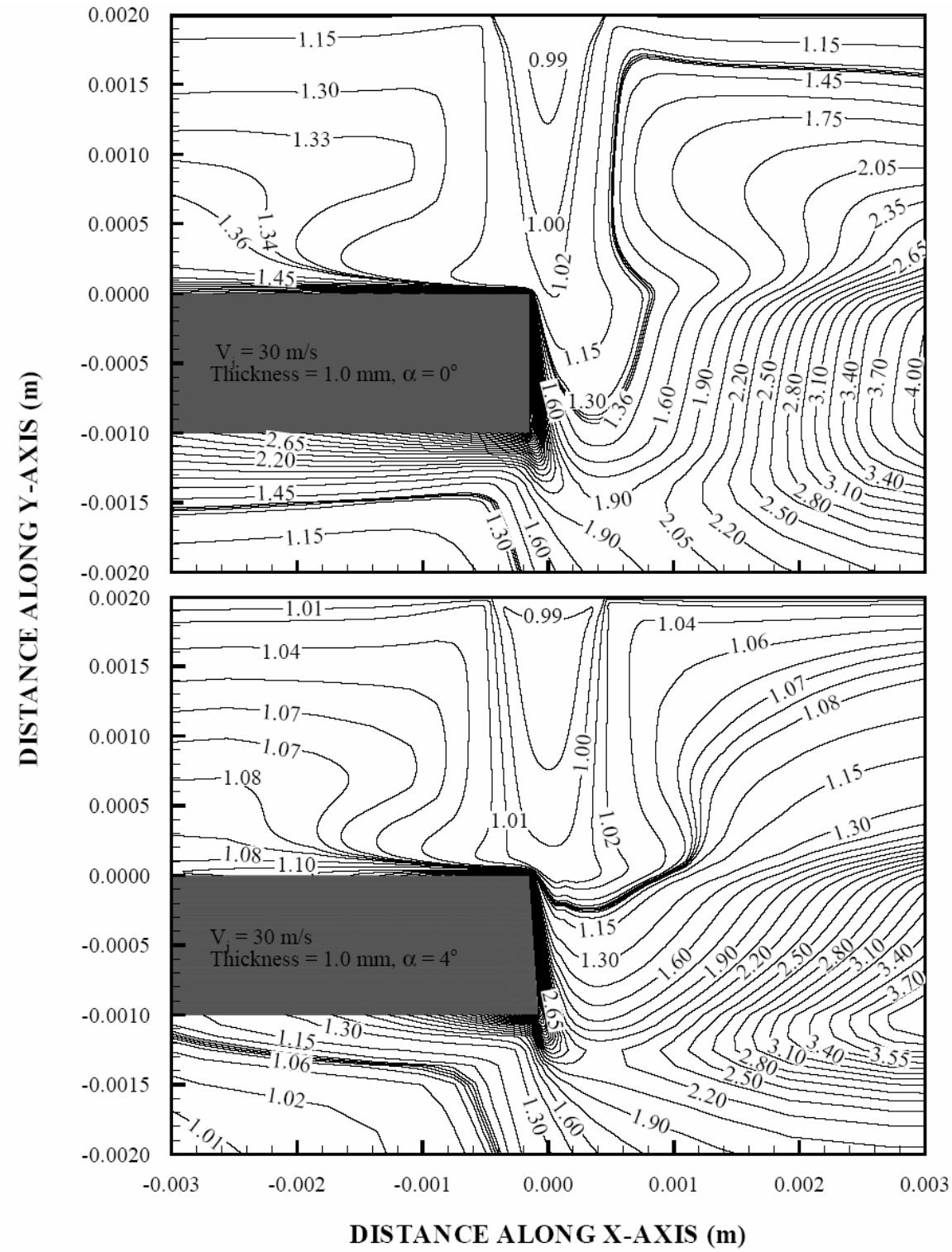

Figure 5.4 Normalized temperature for one averaged jet velocity (30 m/s) and two kerf wedge angles (0° and 4°)

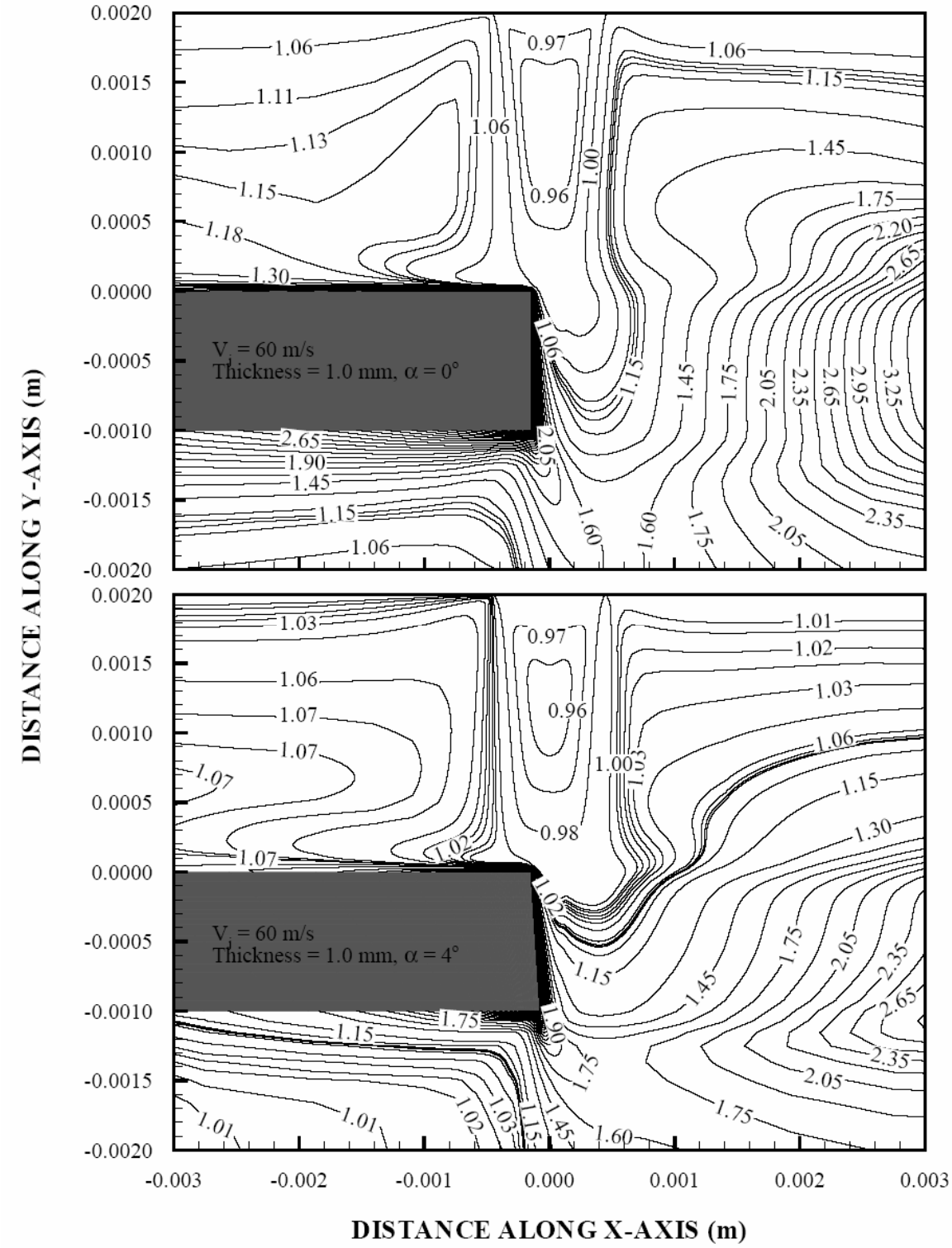

Figure 5.5 Normalized temperature for one averaged jet velocity (60 m/s) and two kerf wedge angles (0° and 4°)

This arrangement is because of resembling the actual cutting situation; in which case, the kerf wall temperature remains at melting temperature of the substrate material (steel). The jet exiting the nozzle is at low temperature and because of the stagnation flow and the high kerf wall temperature, the fluid temperature increases in the kerf. This is particularly true in the region close to kerf wall. Temperature of the fluid also increases in the jet at x-axis locations away from the jet axis. This is because of the flow deceleration along the x-axis in the kerf. The loss of momentum due to flow deceleration in this region enhances the heat transfer from the hot kerf wall to the fluid. Consequently, the fluid temperature increases. Once the flow leaves the kerf at the kerf exit, it mixes with its low temperature surrounding ambient. As a consequence, fluid temperature decreases. Increasing the averaged jet velocity at the nozzle exit lowers the fluid temperature rise in the kerf due to the flow acceleration in this region. The influence of the wedge angle on temperature field is not significant in the region away from the kerf wall. However, in the vicinity of the kerf wall, the fluid temperature remains high and thermal boundary layer thickness increases. This is more pronounced in the region close to the kerf bottom edges.

Figures 5.6 and 5.7 shows the pressure coefficient in the symmetry plane for two jet averaged velocities and two kerf wedge angles. The presence of negative pressure coefficient indicates the reverse flow and the possible formation of the circulation cell. The circulation cell formed next to the jet outer boundaries undergoes a clockwise circulation which is due to the radial expansion of the impinging jet and the shear flow developed in the vicinity of jet outer boundary. However, the flow expansion along the x-axis in the kerf results in negative value of pressure coefficient. Moreover, close to the

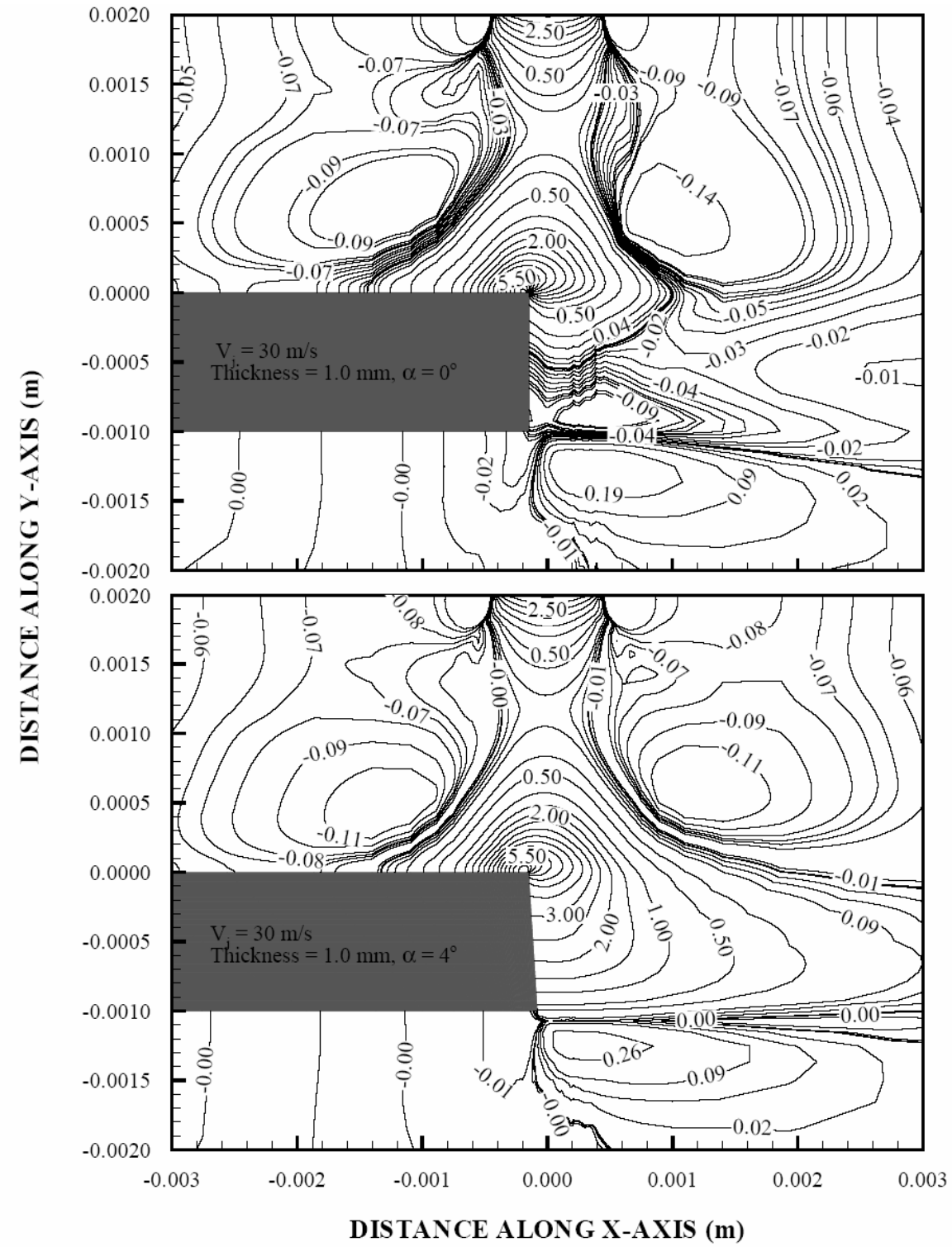

Figure 5.6 Pressure Coefficient for one averaged jet velocity (30 m/s) and two kerf wedge angles (0° and 4°)

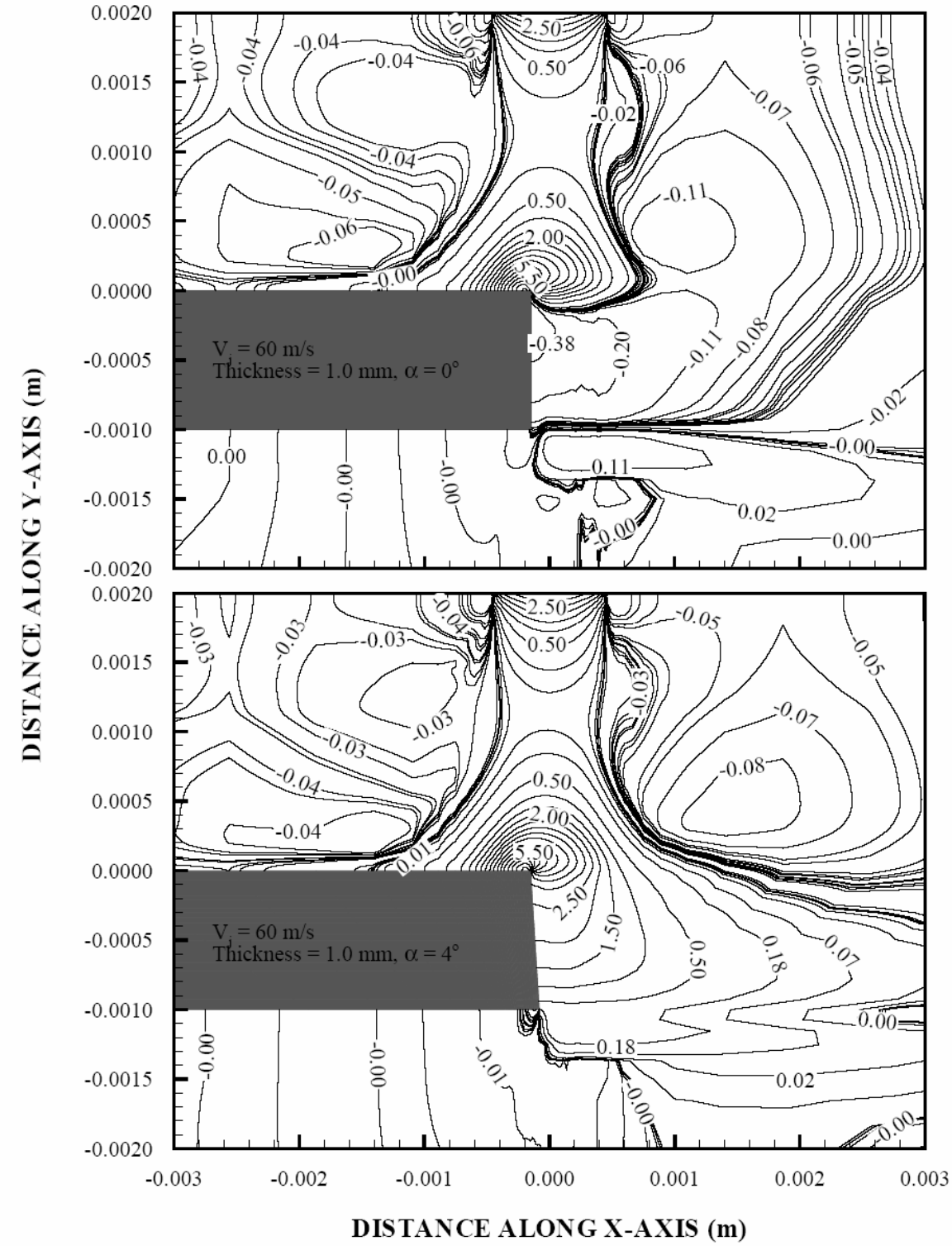

Figure 5.7 Pressure Coefficient for one averaged jet velocity (60 m/s) and two kerf wedge angles (0° and 4°)

kerf wall, temperature increase results in the increased thermodynamic pressure in this region. This, in turn, increases the pressure coefficient in the vicinity of the kerf wall. Increasing the averaged jet velocity at the nozzle exit modifies the flow field and changes the location of the circulation cells in the solution domain. In this case, circulation becomes smaller in size in the region next to the jet outer boundary. Pressure increase becomes significantly high at the tip of the kerf edge due to the jet impingement and formation of the stagnation point in this region. The influence of wedge angle on the pressure coefficient is not significant, provided that it increases slightly the values of the pressure coefficient in the kerf.

Figure 5.8 shows velocity magnitude distribution along the laser beam axis for different jet velocities and two kerf wedge angles. It should be noted that the locations $y = 0$ represents the workpiece surface, $y = 0.002$ m corresponds to the nozzle exit and $0 \geq y \geq -0.001$ m is the workpiece thickness (kerf depth), and $y < -0.001$ m corresponds to distance below the workpiece bottom surface (Figure 5.8). The jet velocity increases immediately after leaving the nozzle exit, which is due to the expansion of the jet. However, it reduces towards the kerf surface due to blockage effect of the kerf. In addition, the jet expansion in the kerf takes place towards the exit of the kerf. This is more pronounced for high jet average velocity at the nozzle exit. In this case, the axial momentum remains high in the jet core, along the laser beam axis within the kerf. Moreover, upon expansion of the jet in all directions at the kerf exit, axial momentum reduces while reducing the velocity magnitude in this region. However, the effect of kerf wedge angle on the velocity magnitude is considerable. In this case, at larger kerf wedge

angle (α = 4°), jet expansion is suppressed towards the wedge surface due to the increased blockage effect of the wedge. Jet behavior in the kerf is influenced by the kerf wedge angle. The blockage effect lowers the increase of the jet expansion in the entry region of the kerf, and the pressure builds up in the kerf. Moreover, the jet acceleration towards the kerf exit results in increased velocity magnitude towards the kerf exit. This behavior is observed for all averaged jet velocities at the nozzle exit. However, jet acceleration is higher at the kerf inlet and decays gradually towards the kerf exit for kerf wedge angle of 0°. Consequently, the blockage effect of the kerf wedge angle on the jet expansion becomes less significant for the kerf wedge angle of 0°.

Figure 5.9 shows pressure distribution along the laser beam axis for different averaged jet velocities at nozzle exit and two different kerf wedge angles. Static pressure reduces as jet expands towards the kerf top surface. Pressure then increases towards the kerf because of stagnation formation and because of the blockage effect of the kerf. However, sudden drop in static pressure is observed close to the kerf surface. This pressure drop continues within the kerf. This is because of the jet expansion in this region. This is more pronounced for high averaged jet velocity at the nozzle exit. The influence of the kerf wedge angle on pressure distribution is significant; in which case, pressure rise towards the kerf becomes considerably high because of the enhanced blockage effect of the kerf wedge. Moreover, pressure drop is sharp for the kerf wedge angle = 0° in the neighborhood of the kerf inlet while it is gradual for the kerf wedge angle = 4°. The attainment of negative pressure in the kerf for the kerf wedge angle = 0° indicates the overexpansion of the jet in this region. It should be noted that the gradual drop in

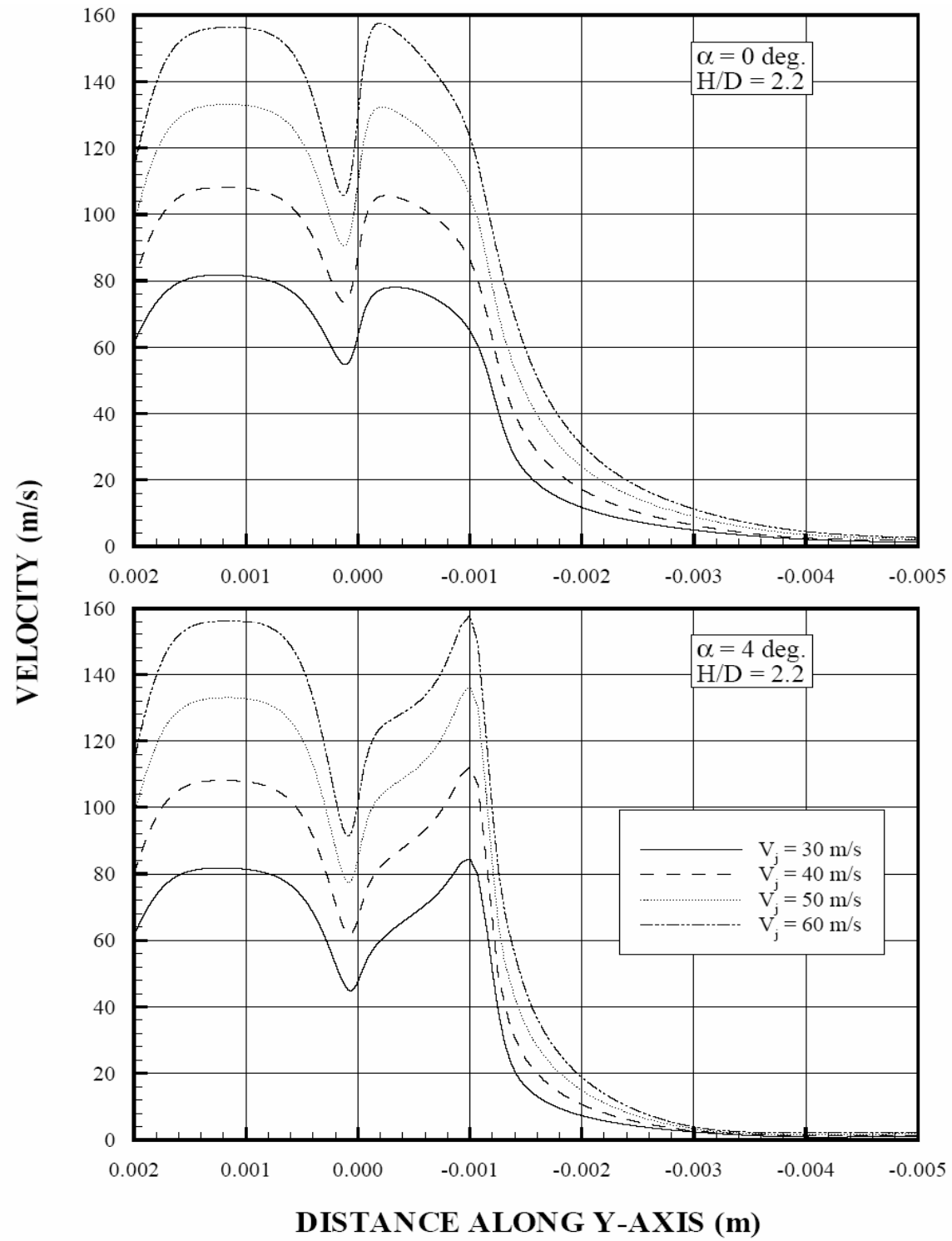

Figure 5.8 Velocity magnitude along laser beam axis for different averaged jet velocities kerf wedge angles of 0° and 4°

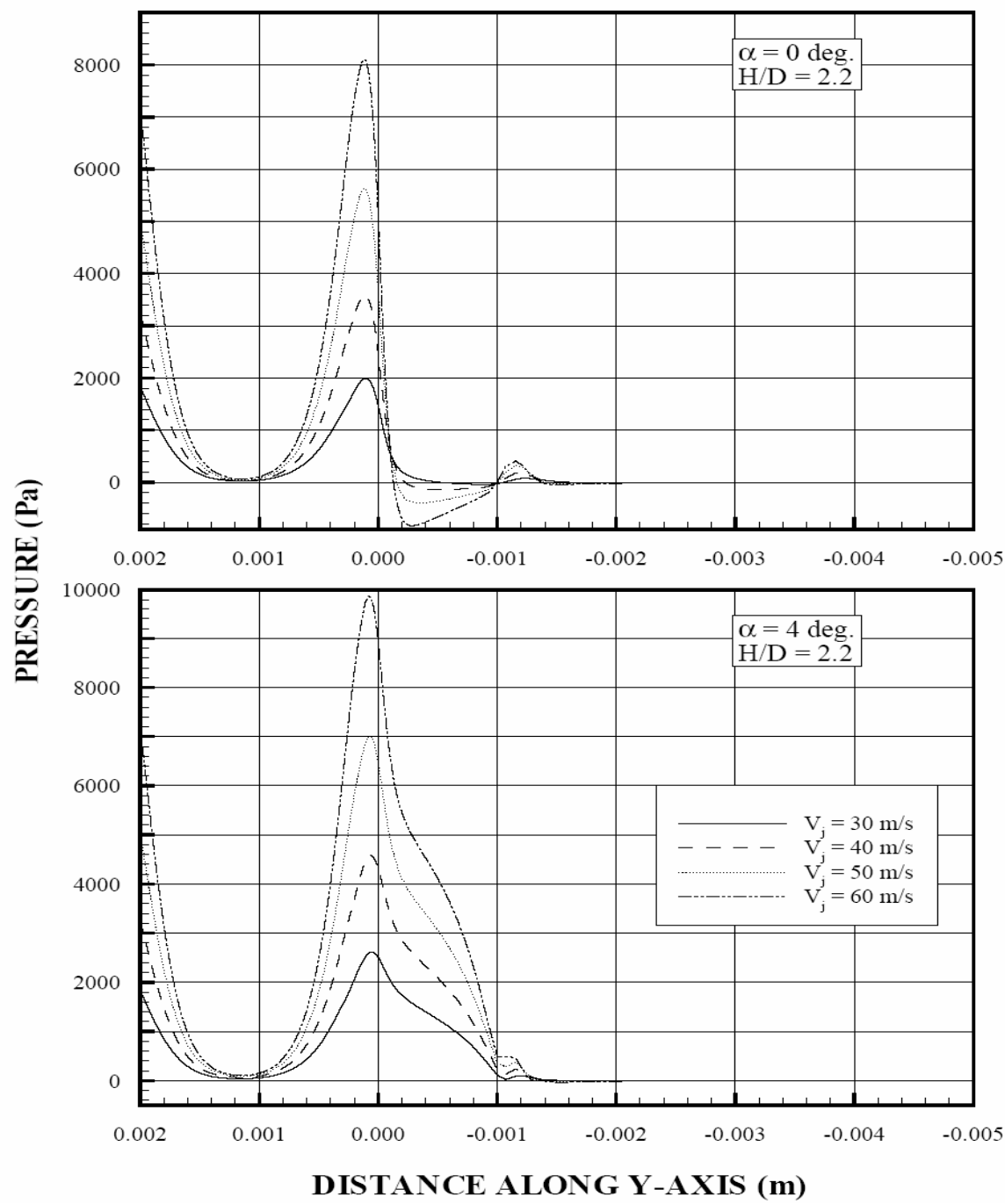

Figure 5.9 Pressure variation along laser beam axis for different averaged jet velocities kerf wedge angles of 0° and 4°

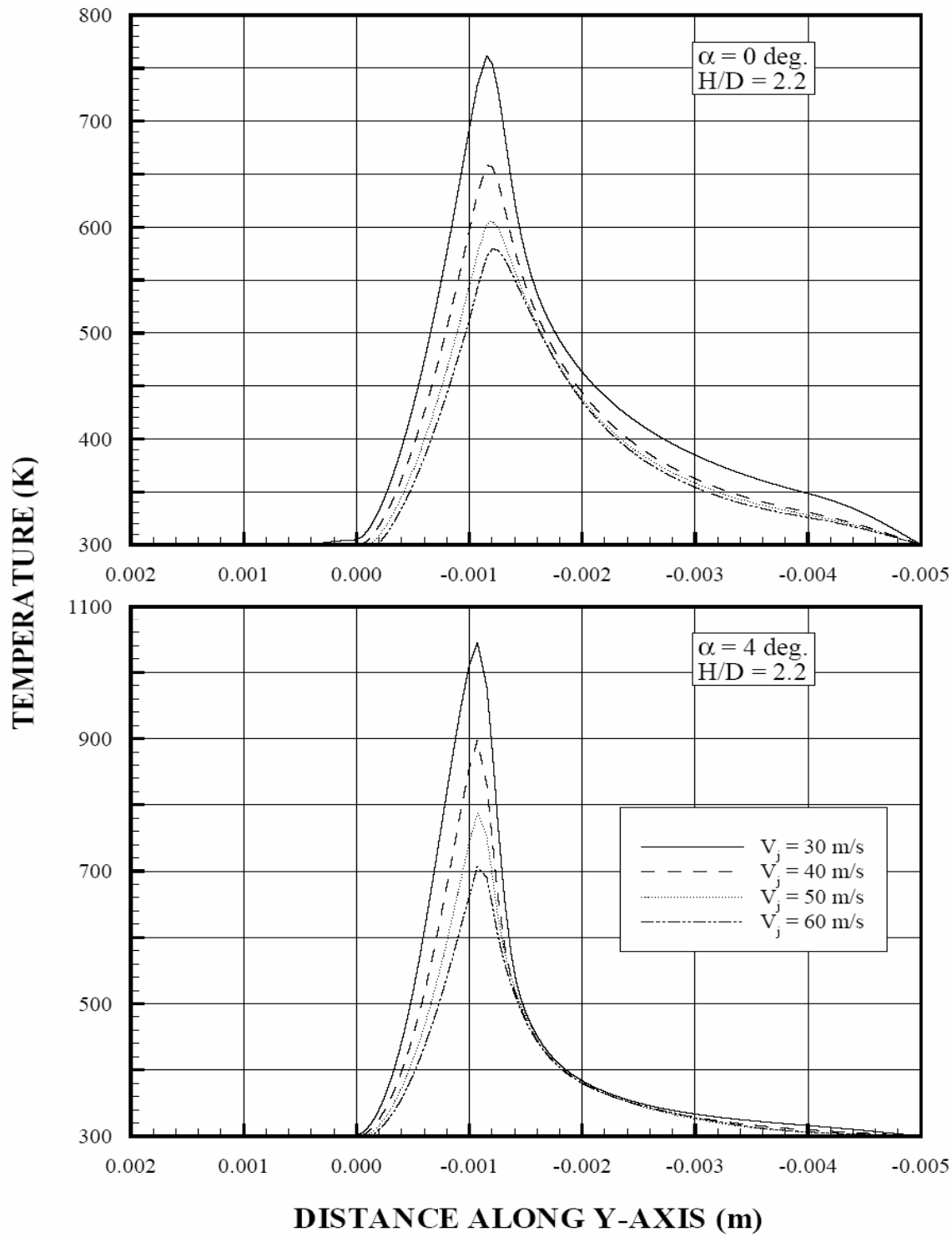

Figure 5.10 Temperature variation along laser beam axis for different averaged jet velocities kerf wedge angles of 0° and 4°

pressure for the higher kerf wedge angle can be associated with the temperature rise in the kerf due to heat transfer from the kerf wall to the jet. This can be seen from Figure 5.10 in which temperature distribution along the laser beam axis is shown. Although increasing fluid temperature contributes to pressure rise in the kerf, jet expansion towards the kerf exit lowers the pressure in this region despite the fact that the fluid temperature continuously increases towards the kerf exit.

Figure 5.11 shows the Nusselt number distribution along the normalized kerf wall thickness for different averaged jet velocities at nozzle exit and two kerf wedge angles. The kerf wall thickness is normalized with the maximum thickness; i.e., normalized kerf wall thickness = 0 represents the kerf inlet and normalized kerf wall thickness = -1 is the kerf exit. The curves are plotted at a location (x = -0.000075 m; z = 0.000129 m) where the Nusselt number attained the highest value. The Nusselt number increases sharply from the kerf edge due to convective cooling of the jet in the kerf. It should be noted that the kerf wall temperature was kept at 1500 K to resemble the laser cutting process. The Nusselt number decreases gradually in the kerf, and then reduces sharply towards the kerf exit. The radial acceleration of the flow in the kerf influences the Nusselt number; in which case, the Nusselt number increases with increasing jet velocity. However, this increase is not significant in the regions close to the kerf inlet and kerf exit. As the kerf wedge angle increases ($\alpha = 4°$), the Nusselt number increases gradually towards the kerf exit. The gradual increase is associated with the blockage effect of the kerf. In this case, pressure buildup increases the density of the fluid in the kerf while enhancing the amount of heat transfer in the kerf. Moreover, the Nusselt number reduces sharply towards the

exit of the kerf similar to the case for which the kerf wedge angle = 0°. The influence of averaged jet velocity at the nozzle exit on the Nusselt number is more pronounced for the kerf wedge angle = 4°.

Figure 5.12 shows the skin friction distribution along the normalized kerf thickness for different averaged jet velocities at the nozzle exit and two kerf wedge angles. The location (x = -0.000075 m; z = 0.000129 m) correspond to the location of the maximum Nusselt number. The skin friction increases sharply at the inlet of the kerf due to the flow acceleration within the kerf. As the kerf depth increases, the skin friction reduces. This is attributed to the shear layer developed within the vicinity of the kerf wall, which is influenced by high wall temperature because of the formation of high thermodynamic pressure in this region. The influence of the mean jet velocity at the nozzle exit is notable in such a way that increasing mean jet velocity reduces the skin friction. This is because of the thermal boundary layer formed in the vicinity of the kerf wall; that is, reducing the mean jet velocity enhances the thermal boundary layer thickness because of the low axial momentum of the flow in the surface region. Consequently, thickening of the thermal boundary layer increases the shear stress at the wall. In addition, reducing the averaged jet velocity reduces the velocity head ($1/2\ \rho V_j^2$) while increasing the skin friction. The influence of kerf wedge angle on the skin friction is considerable; in which case, skin friction first drops, and later increases with increasing depth along the kerf wall. The increase in the skin friction towards the kerf exit is because of the blockage effect of the wedge angle. Therefore, pressure buildup towards the kerf exit modifies the boundary layer thickness and the rate of fluid strain in this

region. Consequently, the skin friction increases. This is more pronounced for the low averaged jet velocity (V_j = 30 m/s).

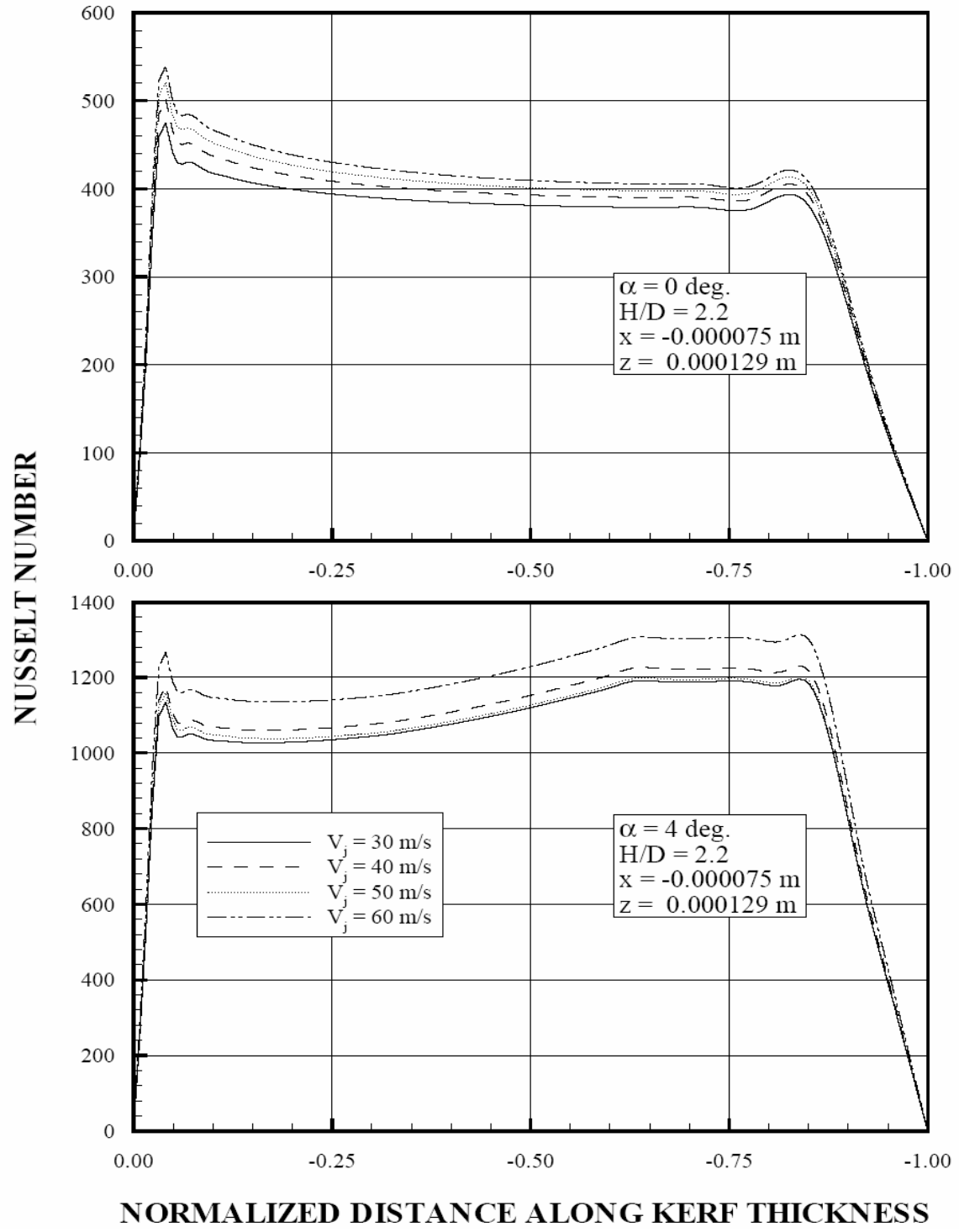

Figure 5.11 Nusselt number distribution along the normalized kerf wall thickness for different averaged jet velocities at nozzle exit and kerf wedge angles of 0° and 4°

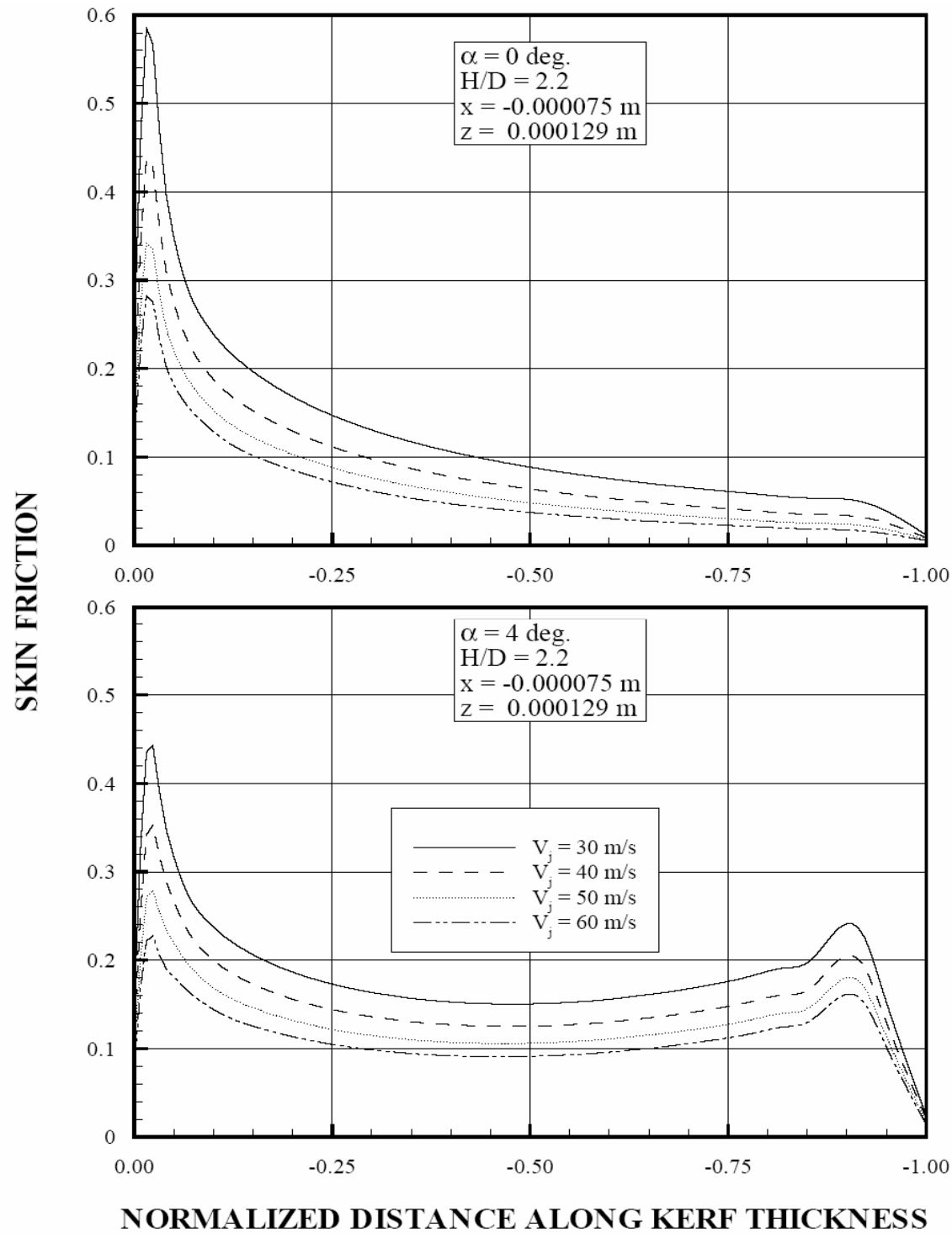

Figure 5.12 Skin friction distribution along the normalized kerf wall thickness for different averaged jet velocities at nozzle exit and kerf wedge angles of 0° and 4°

5.2 Effect of the Kerf Wedge Angle on Heat Transfer Rates and Skin Friction

The effect of the kerf wedge angle on heat transfer rates and skin friction is further investigated in this section by considering two kerf depths (thicknesses) and four corresponding wedge angles: $\alpha = 0°$, 2°, 4°, and 6°. The kerf thicknesses accommodated in this investigation are 0.5 mm and 1.0 mm. Results will be shown for two averaged jet velocities at nozzle exit: 30 m/s and 60 m/s.

Figures 5.13 and 5.14 show normalized velocity contours in the symmetry plane for kerf thickness = 0.5 mm and averaged jet velocity = 30 m/s and four kerf wedge angles. The jet exits the nozzle and exchanges momentum with the ambient forming a free boundary or a shear layer as it approaches the kerf top surface. No significant effect of the kerf wedge angle on the width of the free boundary or on the rate of decrease of the jet velocity as it approaches the kerf surface is observed. After impingement onto the kerf occurs, the flow undergoes radial acceleration in the region close to the kerf side wall. Consequently, radial expansion of the flow is observed in the kerf. Radial expansion gets more pronounced as the kerf wedge angle increases from 0° to 6°. This is caused by the blockage effect of the kerf which increases with the wedge angle. The radial acceleration does not continue indefinitely and the accelerating flow is transformed to a decelerating flow towards the kerf outlet in the positive x-axis direction. Higher velocity magnitudes are observed in the kerf for larger kerf wedge angles. Moreover, the circulation cell developed in the outer region of the impinging jet above the kerf top surface shifts away

from the kerf surface region as the kerf wedge angle increases. No significant effect on this circulation cell is observed as the kerf wedge angle changes from 4° to 6°.

Figures 5.15 and 5.16 show normalized velocity contours for kerf thickness = 0.5 mm, averaged velocity at nozzle exit = 60 m/s, and four kerf wedge angles. The effect of kerf wedge angle on velocity magnitudes attained in the kerf is less pronounced than the case for which averaged jet velocity = 30 m/s. This may be due to the higher axial momentum associated with the jet in this case. Figures 5.17 and 5.18 show normalized velocity contours for kerf thickness = 1.0 mm, averaged jet velocity = 30 m/s, and four kerf wedge angles. The effect of the kerf wedge angle on radial expansion of the flow in the kerf region is more pronounced than the previous case for which kerf thickness = 0.5 mm. This effect is clearly observed as the kerf wedge angle increases from 4° to 6°. In addition, a significant increase in the velocity magnitude of the flow is observed as the flow moves towards the kerf exit in the negative y-axis direction. The flow then exits the kerf and exchanges momentum with the quiescent ambient. Figures 5.19 and 5.20 show normalized velocity magnitude contours for the same geometric parameters as the previous case and averaged jet velocity at nozzle exit = 60 m/s. Same phenomena as the in the previous case are observed.

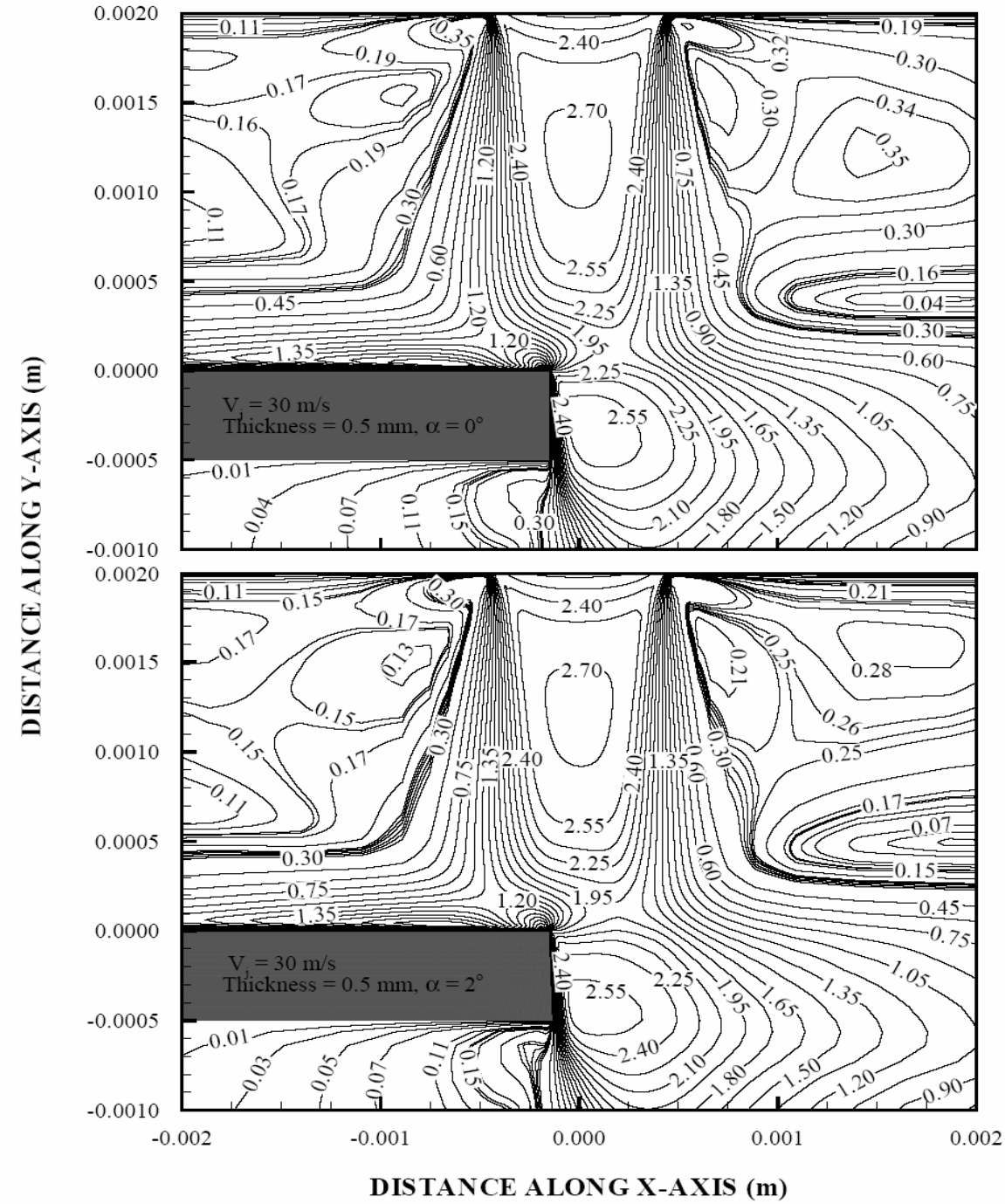

Figure 5.13 Normalized velocity magnitude (V/V_j) for jet averaged velocity of 30 m/s, kerf thickness of 0.5 mm, and kerf wedge angles of 0° and 2°

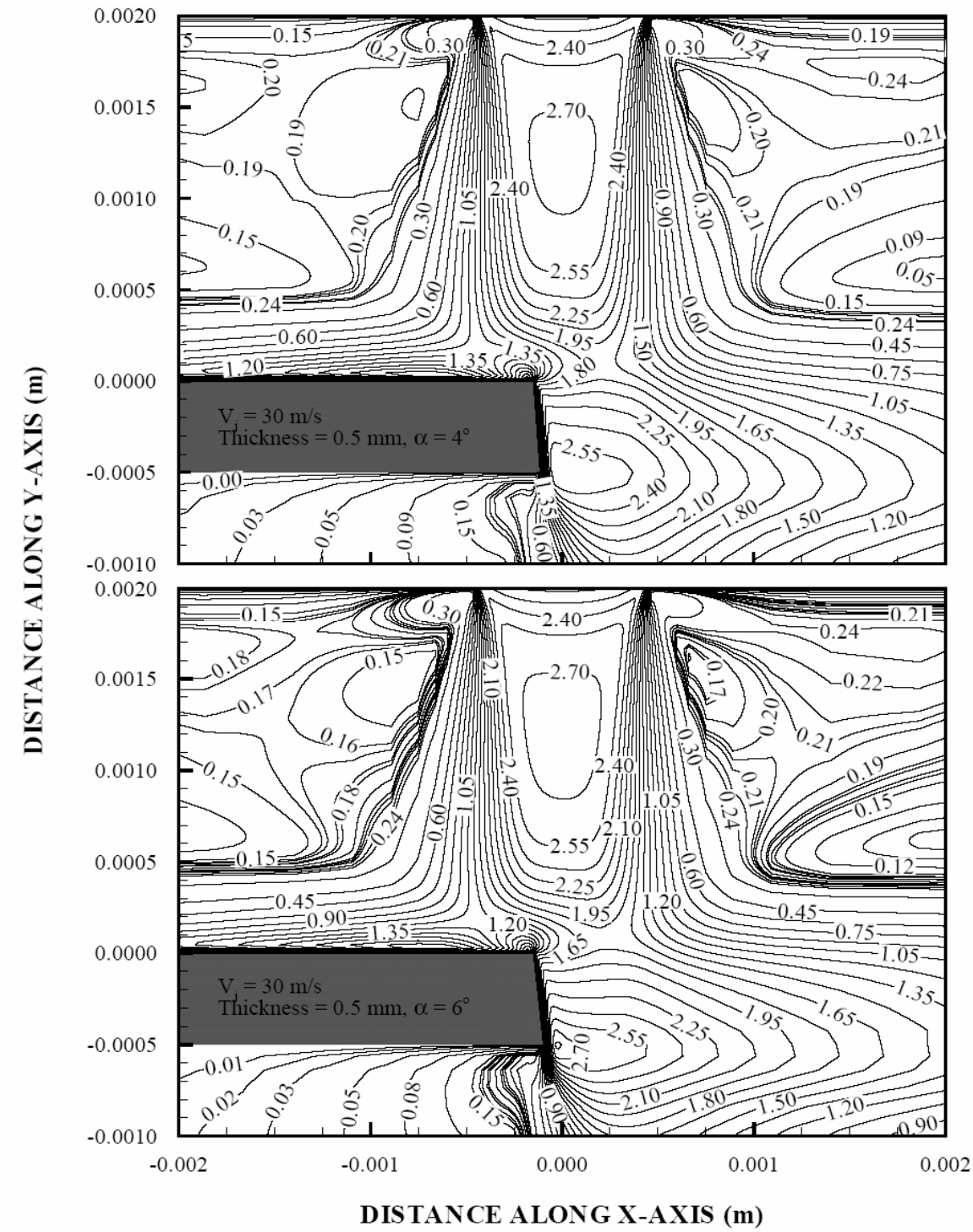

Figure 5.14 Normalized velocity magnitude (V/V_j) for jet averaged velocity of 30 m/s, kerf thickness of 0.5 mm, and kerf wedge angles of 4° and 6°

Figures 5.21 and 5.22 show the pressure coefficient in the symmetry plane for kerf thickness = 0.5 mm, averaged jet velocity at nozzle exit = 30 m/s, and four kerf wedge angles. Figures 5.23 and 5.24 show the pressure coefficient for the same geometric parameters and averaged jet velocity = 60 m/s. The negative pressure coefficient observed in the jet outer boundaries preceding impingement indicates the reverse flow and the possible formation of circulation cell in this region. This is observed for all kerf wedge angles with a slight change in pressure coefficient values obtained in each case. The decrease in the flow velocity as the flow approaches the kerf is associated with pressure increase in this region.

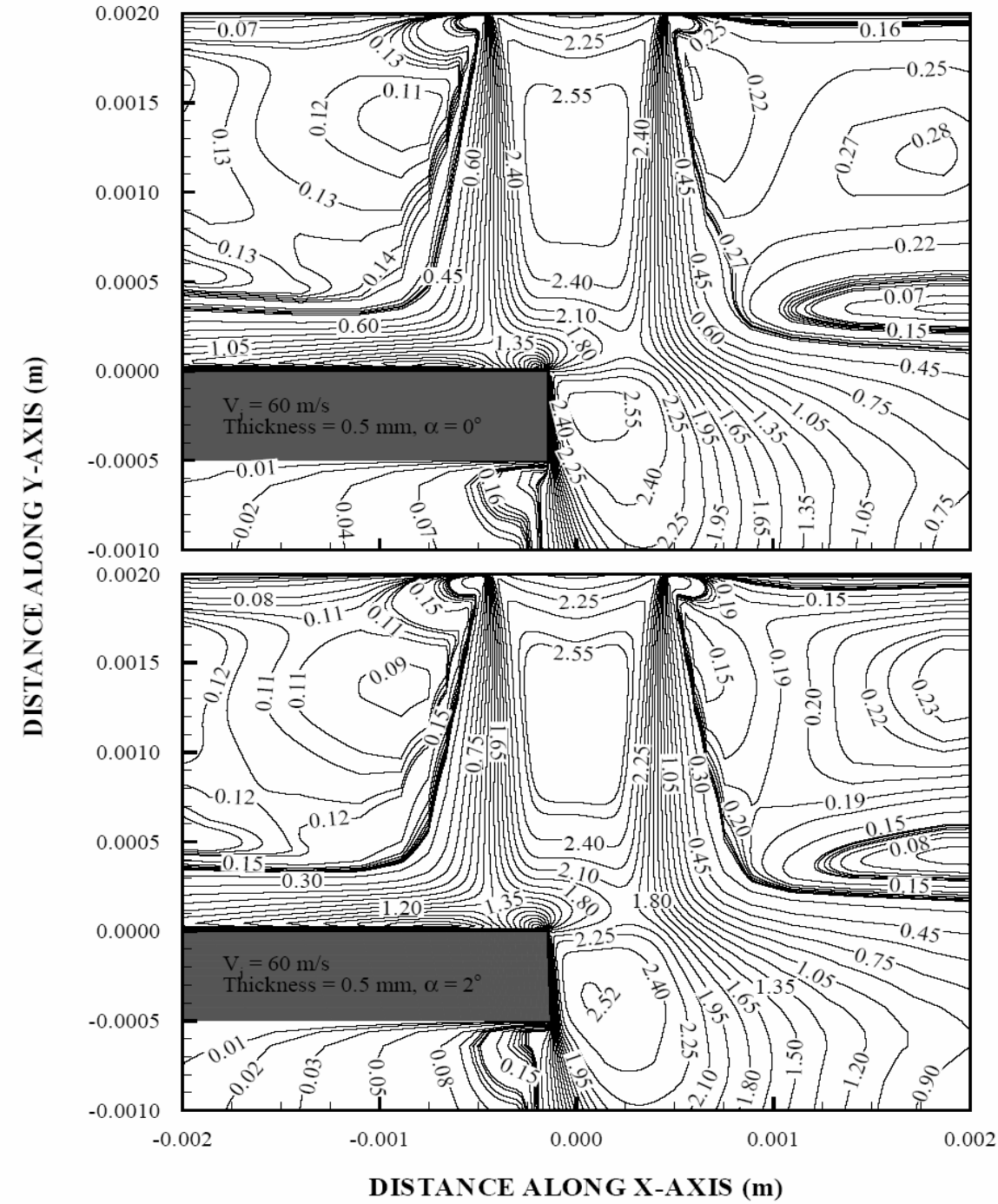

Figure 5.15 Normalized velocity magnitude (V/V_j) for jet averaged velocity of 60 m/s, kerf thickness of 0.5 mm, and kerf wedge angles of 0° and 2°

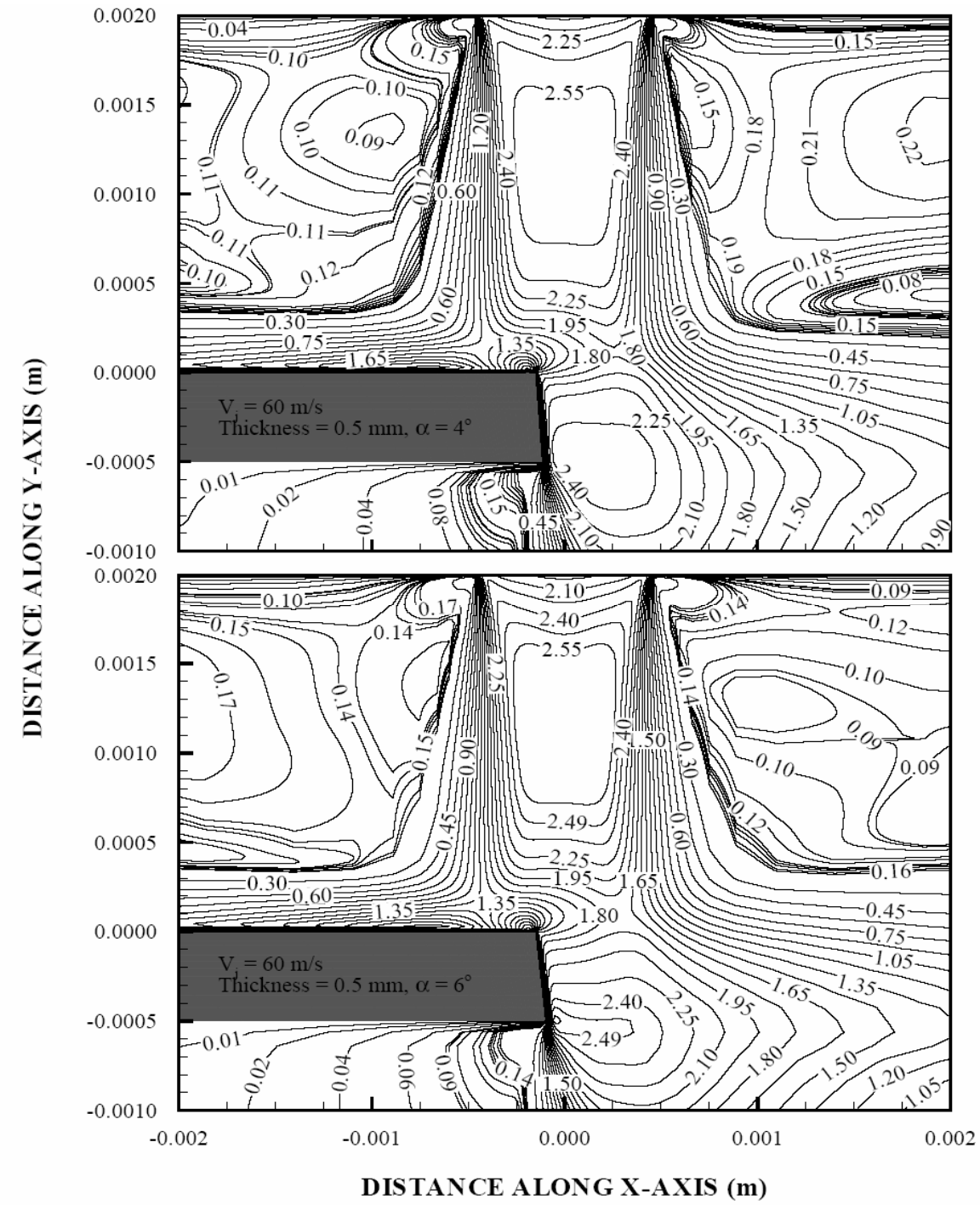

Figure 5.16 Normalized velocity magnitude (V/V_j) for jet averaged velocity of 60 m/s, kerf thickness of 0.5 mm, and kerf wedge angles of 4° and 6°

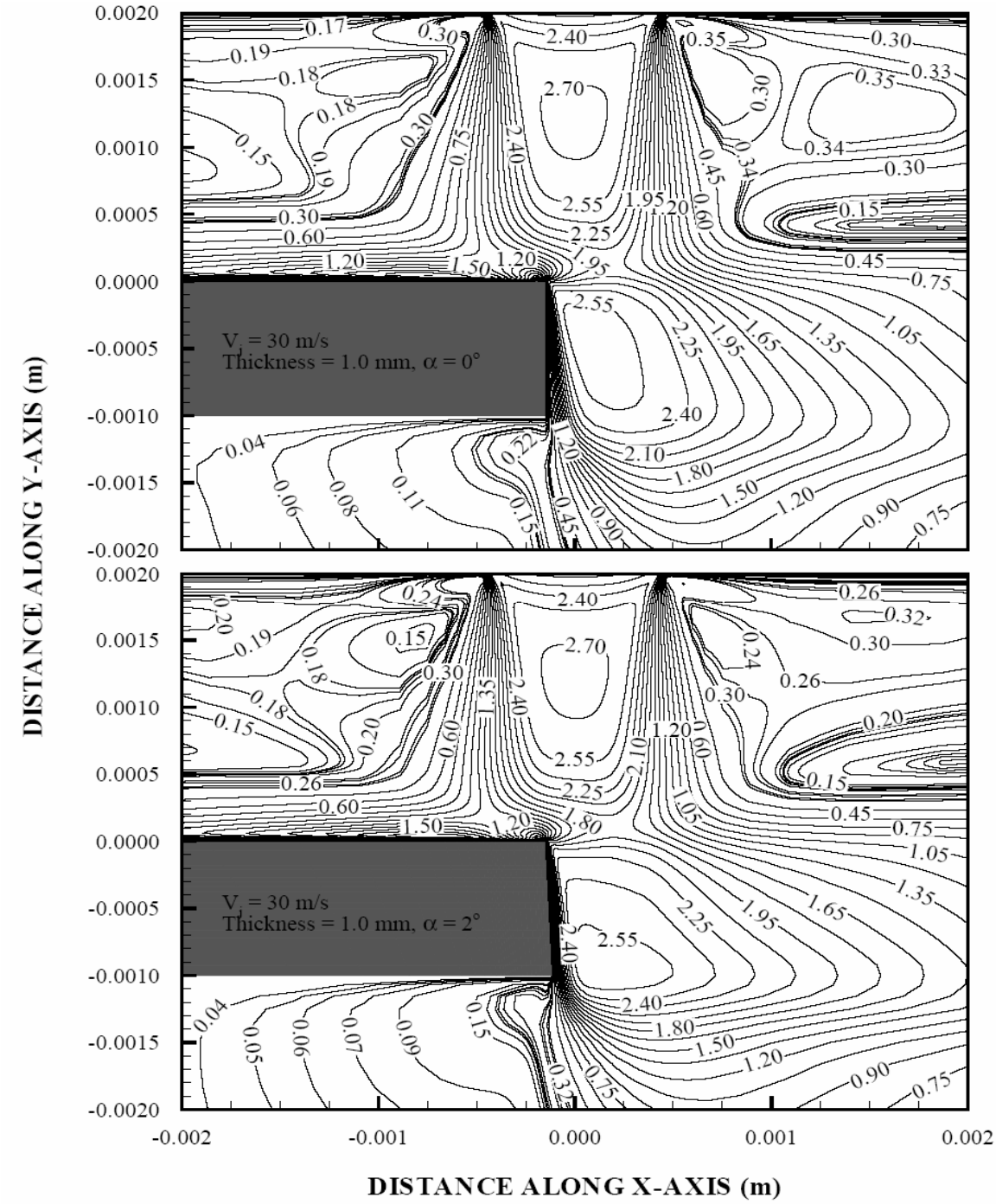

Figure 5.17 Normalized velocity magnitude (V/V_j) for jet averaged velocity of 30 m/s, kerf thickness of 1.0 mm, and kerf wedge angles of 0° and 2°

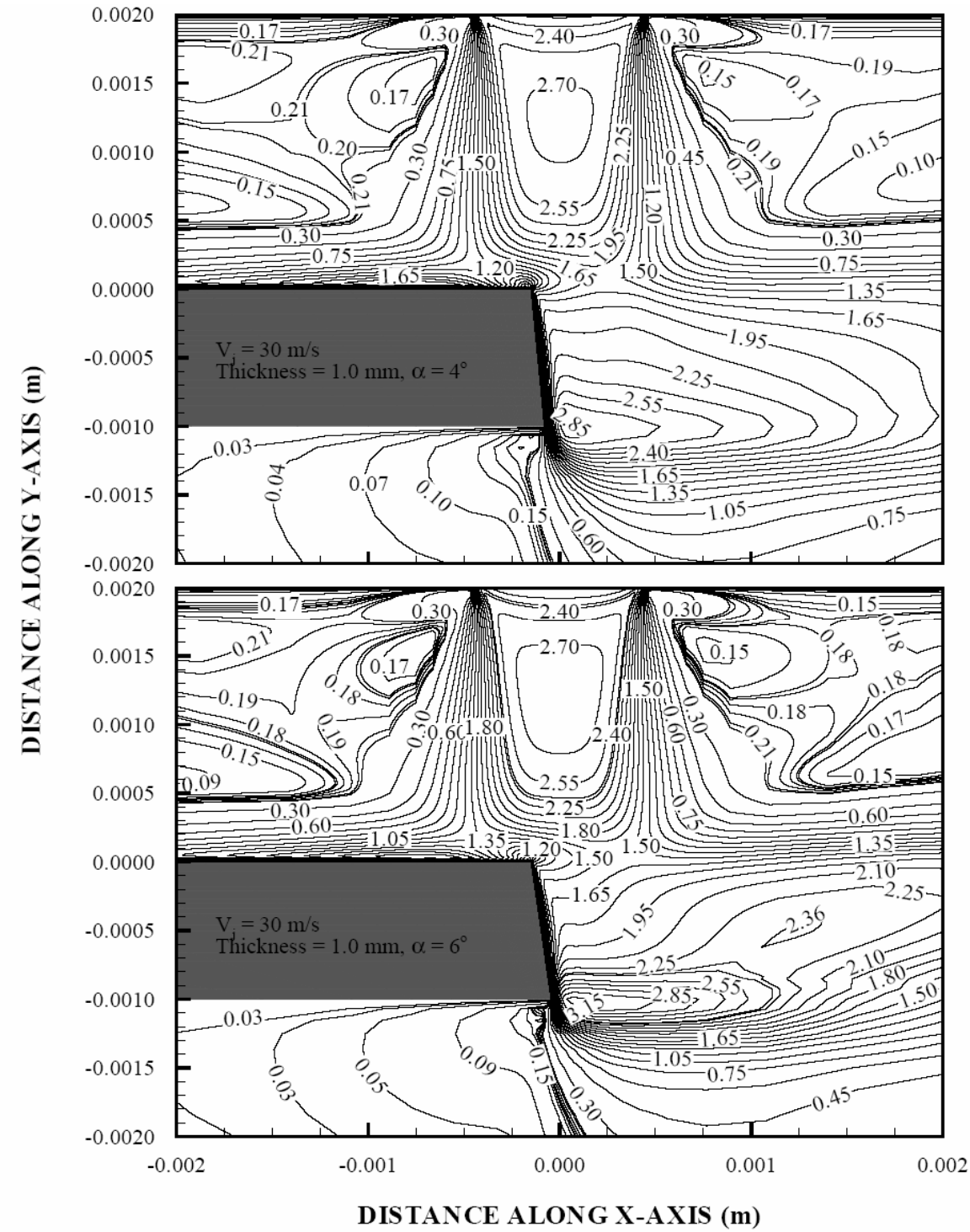

Figure 5.18 Normalized velocity magnitude (V/V_j) for jet averaged velocity of 30 m/s, kerf thickness of 1.0 mm, and kerf wedge angles of 4° and 6°

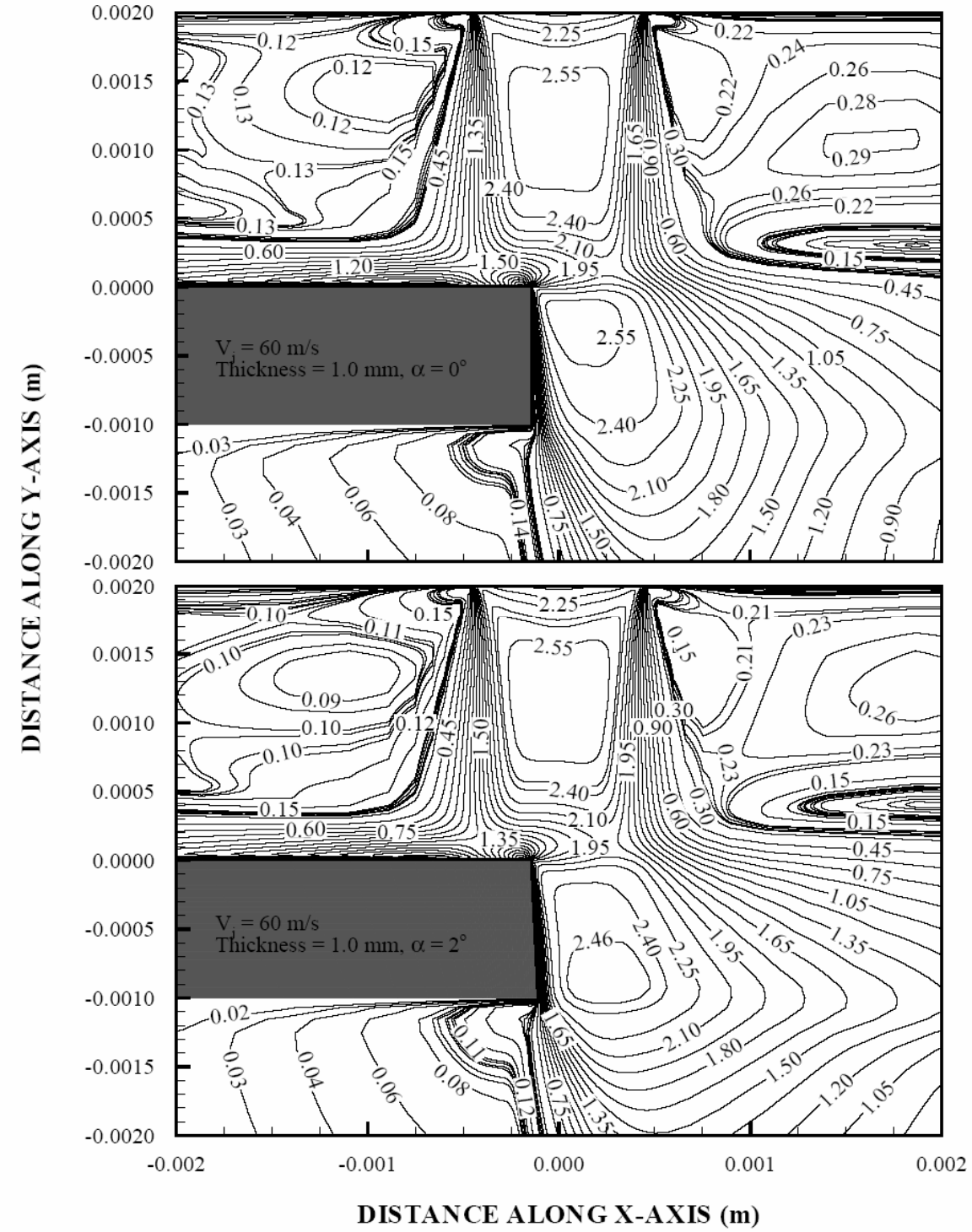

Figure 5.19 Normalized velocity magnitude (V/V_j) for jet averaged velocity of 60 m/s, kerf thickness of 1.0 mm, and kerf wedge angles of 0° and 2°

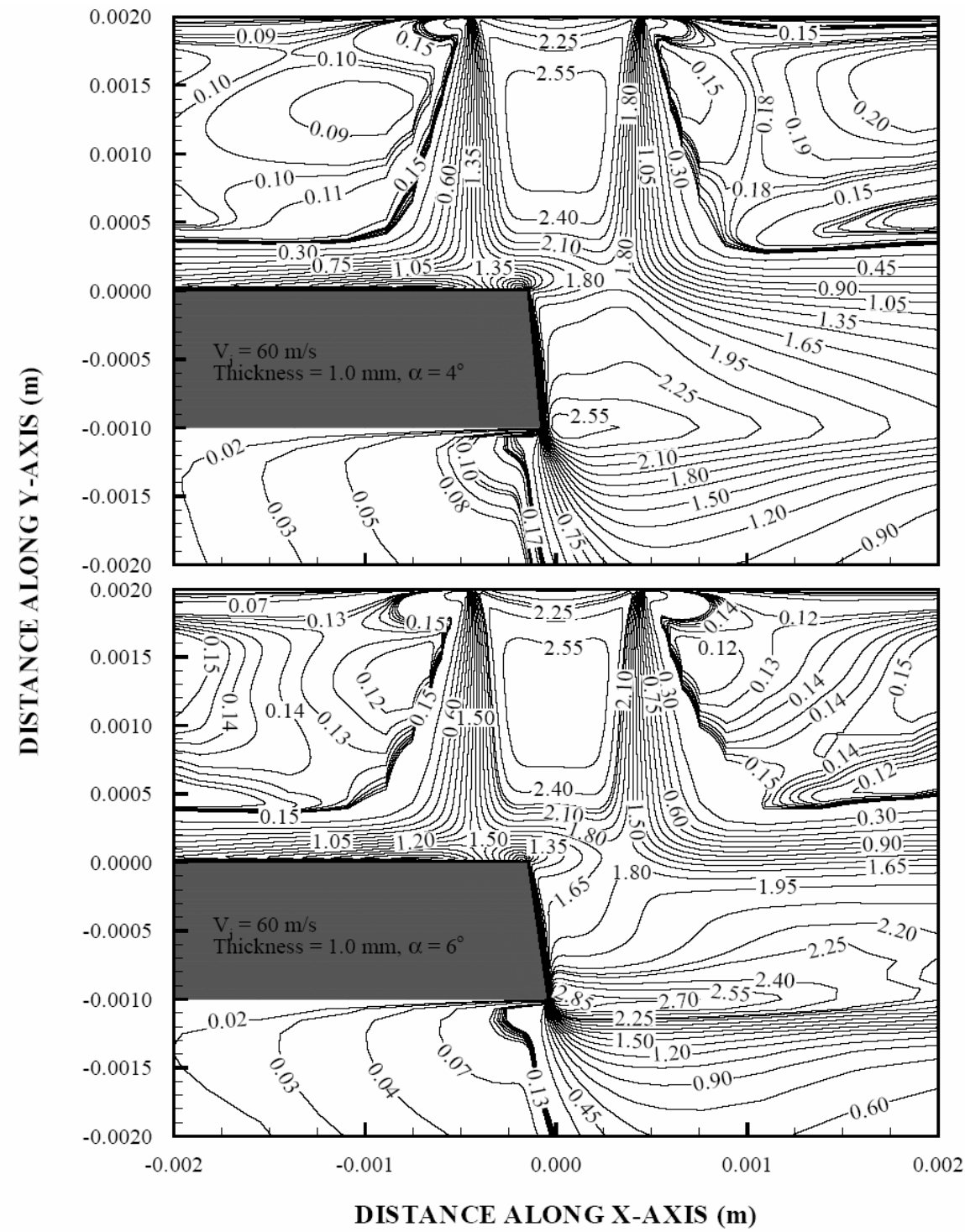

Figure 5.20 Normalized velocity magnitude (V/V_j) for jet averaged velocity of 60 m/s, kerf thickness of 1.0 mm, and kerf wedge angles of 4° and 6°

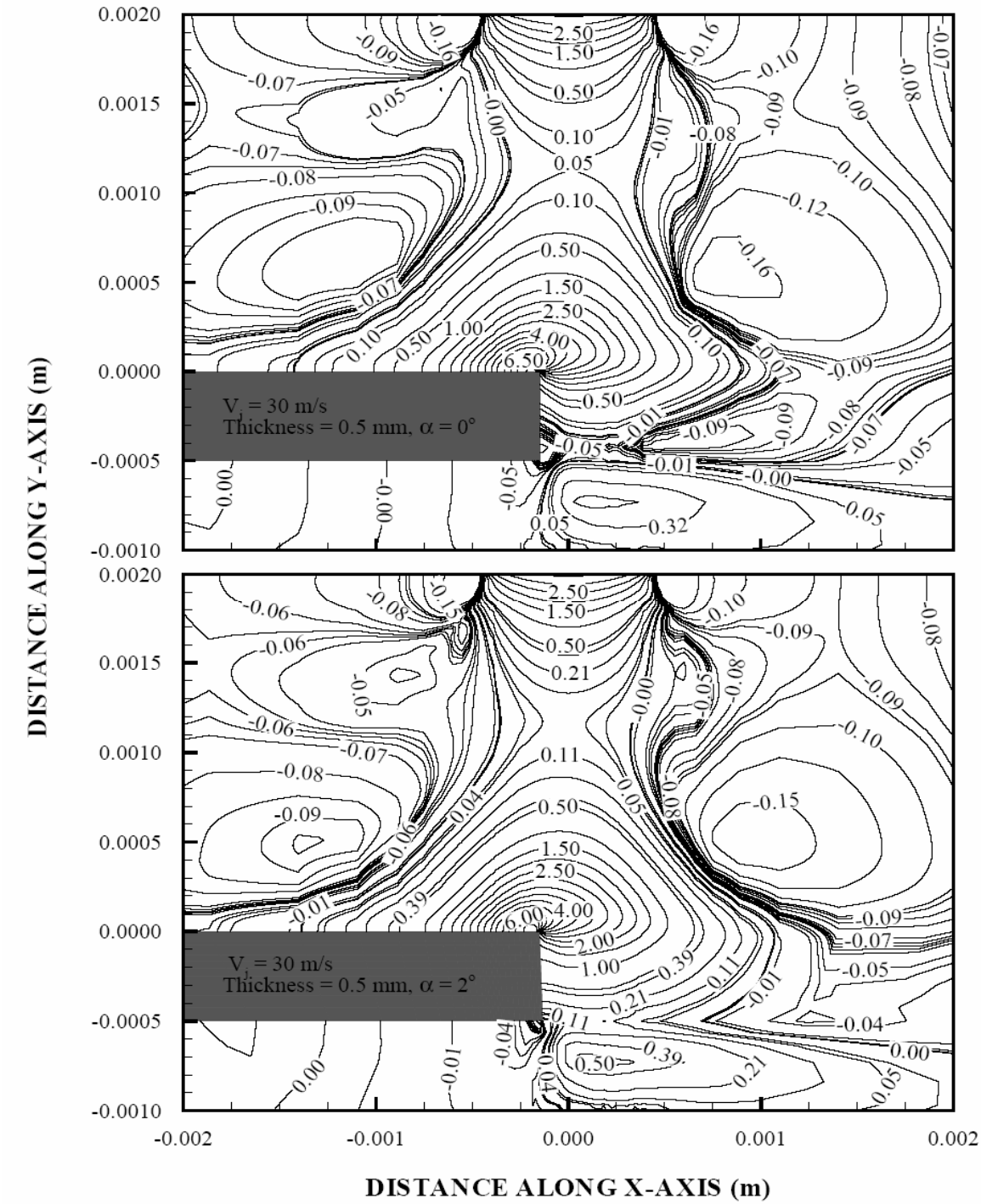

Figure 5.21 Pressure coefficient in the symmetry plane for jet averaged velocity of 30 m/s, kerf thickness of 0.5 mm, and kerf wedge angles of 0° and 2°

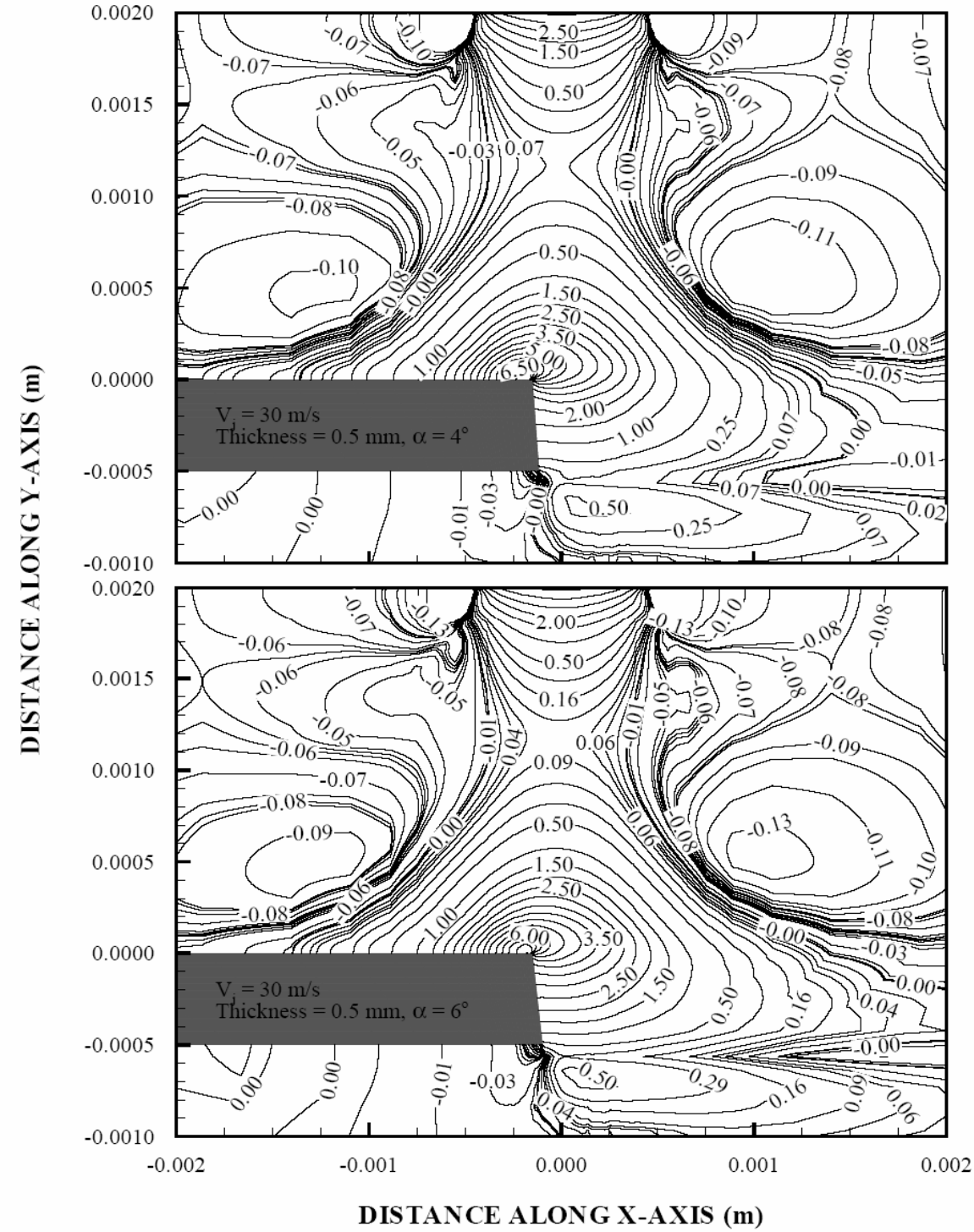

Figure 5.22 Pressure coefficient in the symmetry plane for jet averaged velocity of 30 m/s, kerf thickness of 0.5 mm, and kerf wedge angles of 4° and 6°

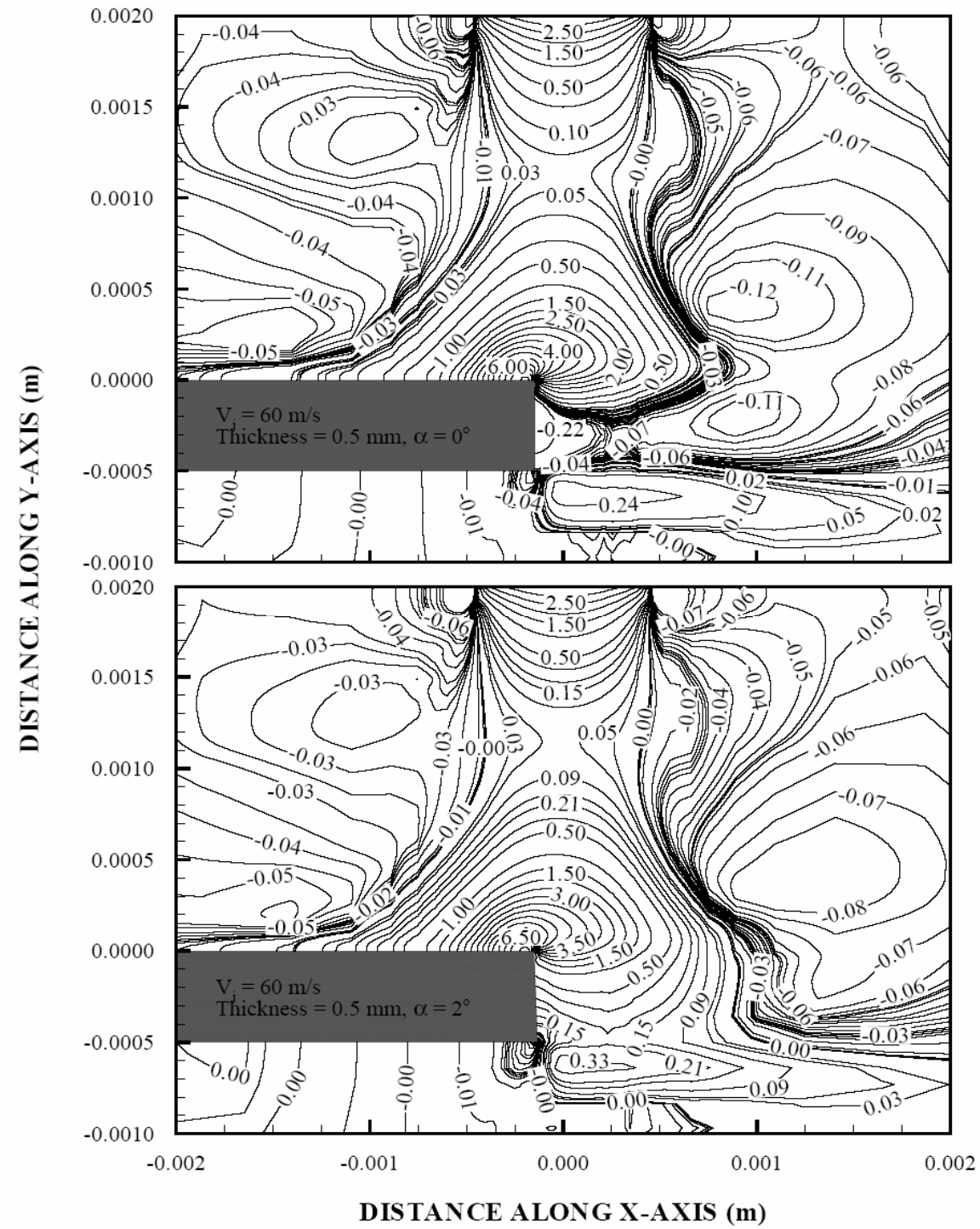

Figure 5.23 Pressure coefficient in the symmetry plane for jet averaged velocity of 60 m/s, kerf thickness of 0.5 mm, and kerf wedge angles of 0° and 2°.

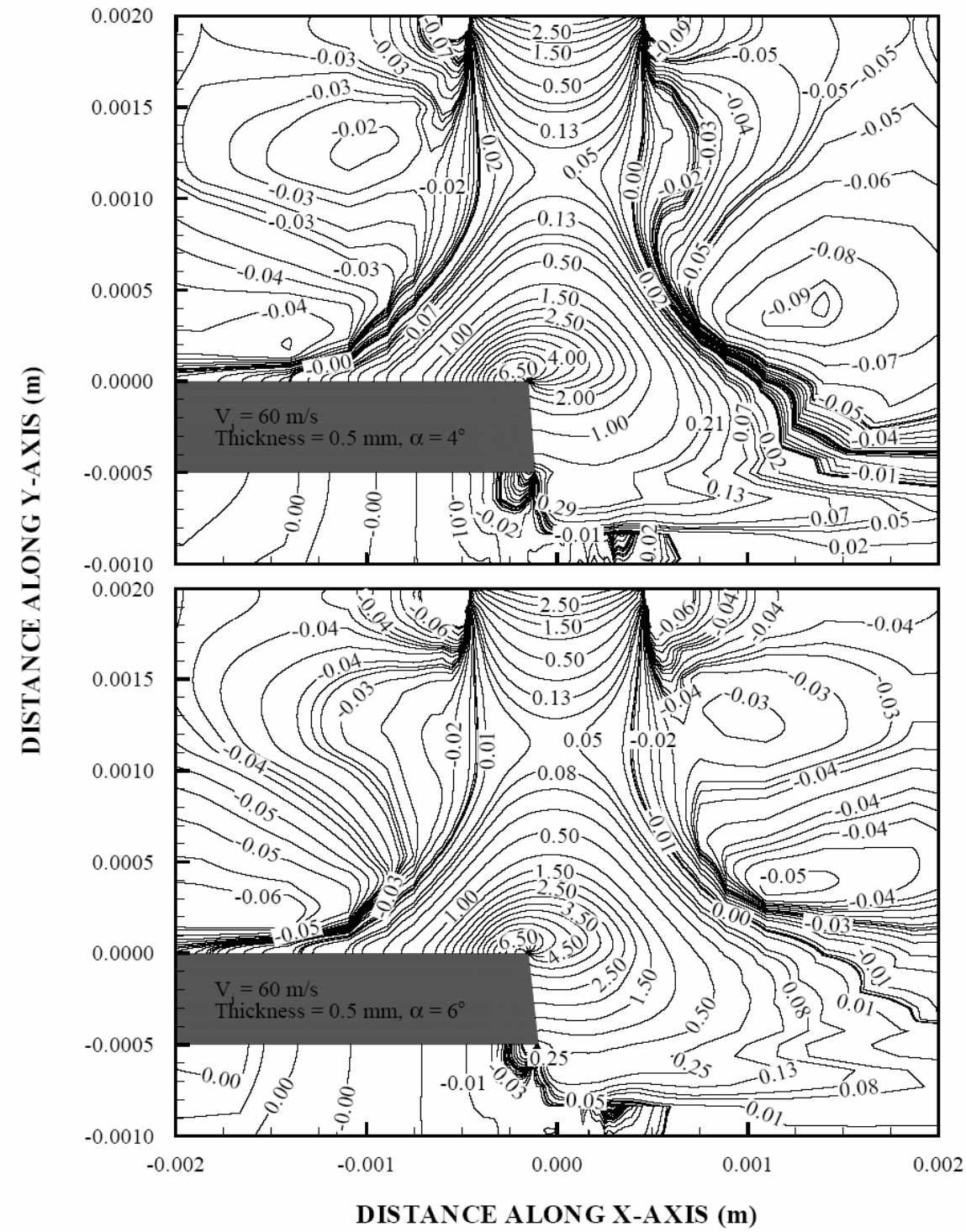

Figure 5.24 Pressure coefficient in the symmetry plane for jet averaged velocity of 60 m/s, kerf thickness of 0.5 mm, and kerf wedge angles of 4° and 6°.

The increase in pressure as the flow approaches the kerf becomes significant at the tip of the kerf edge due to jet impingement and the formation of stagnation point in this region. The influence of the wedge angle on this effect is not significant. As the kerf wedge angle increases, the pressure coefficient in the region close to the kerf wall increases. This is partially due to the increase in thermodynamic pressure as effect of the increase in temperature as is shown later in the temperature contours. The blockage effect of the kerf wedge also contributes to this increase in pressure. Negative pressure coefficients observed in the kerf region for small kerf wedge angles almost do not exist for larger angles. This is especially true for wedge angle = 6°. This can also be associated with the pressure increase in the kerf region due to the increased blockage effect resulting from larger wedge angles. Figures 5.25, 5.26, 5.27, and 5.28 show pressure coefficient contours for kerf thickness = 1.0 mm, two averaged jet velocities, and four kerf wedge angles. The effect of increasing the kerf wedge angle on increasing the pressure coefficient close to the kerf side wall and in the kerf region is more pronounced than in the previous consideration for which kerf thickness = 0.5 mm. This is observed as the kerf wedge angle increases from 0° to 6° in steps of 2°.

Figures 5.29, 5.30, 5.31, and 5.32 show normalized temperature contours in the symmetry plane for kerf thickness = 0.5 mm, two different averaged jet velocities at nozzle exit, and four kerf wedge angles. It should be reemphasized that the kerf wall temperature is maintained at 1500 K while jet temperature is at 300 K. This simulates the actual laser cutting situation. The free jet temperature is almost equal to the jet temperature at nozzle exit. Fluid temperature increases in the kerf, with remarkable

increase close to the kerf wall. Temperature first decreases and later increases in the fluid at positive x-axis locations away from the jet axis. The decrease in temperature is due to the radial expansion, while the increase in temperature is due to the flow deceleration in this region, which enhances heat transfer from the kerf wall to the fluid.

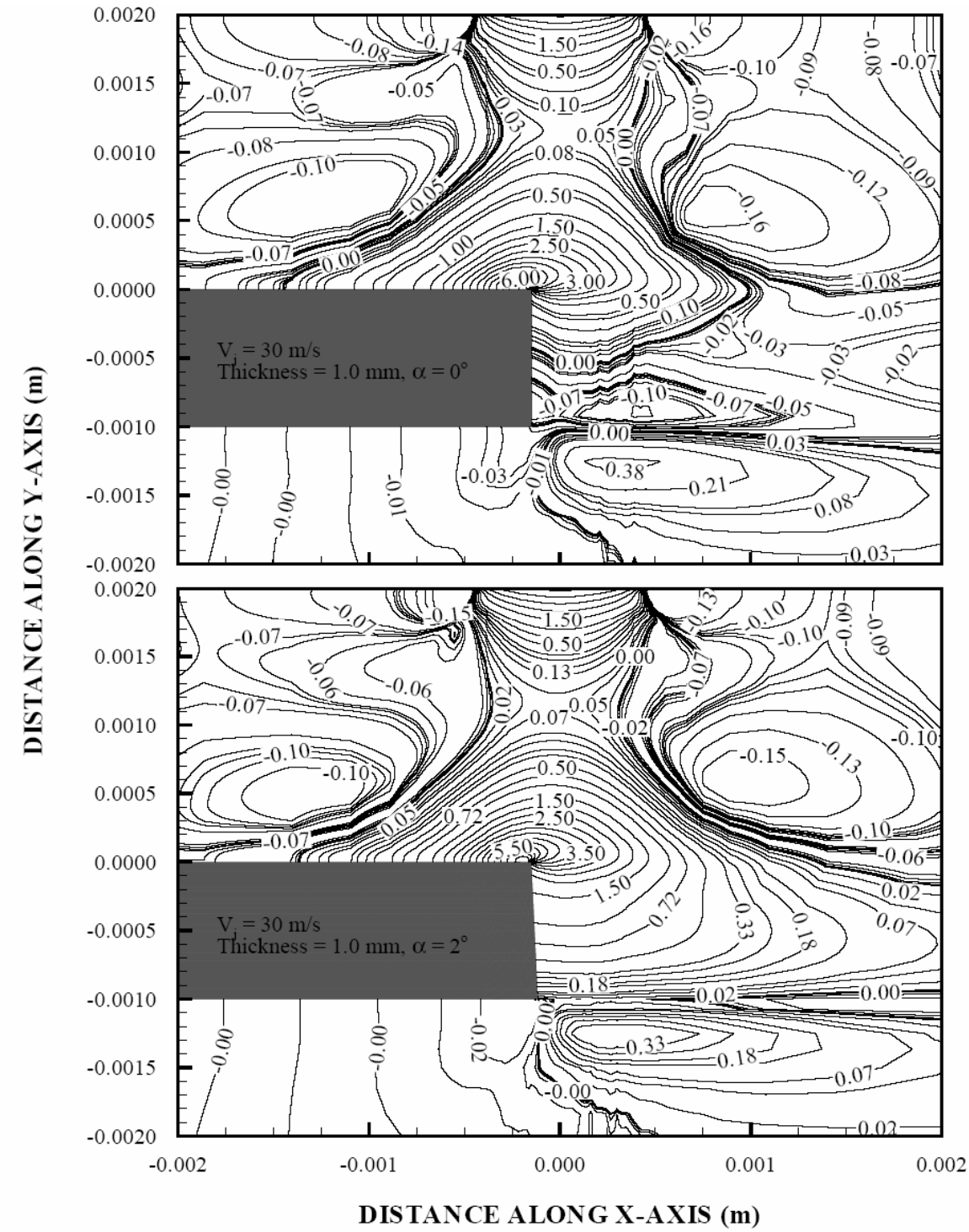

Figure 5.25 Pressure coefficient in the symmetry plane for jet averaged velocity of 30 m/s, kerf thickness of 1.0 mm, and kerf wedge angles of 0° and 2°

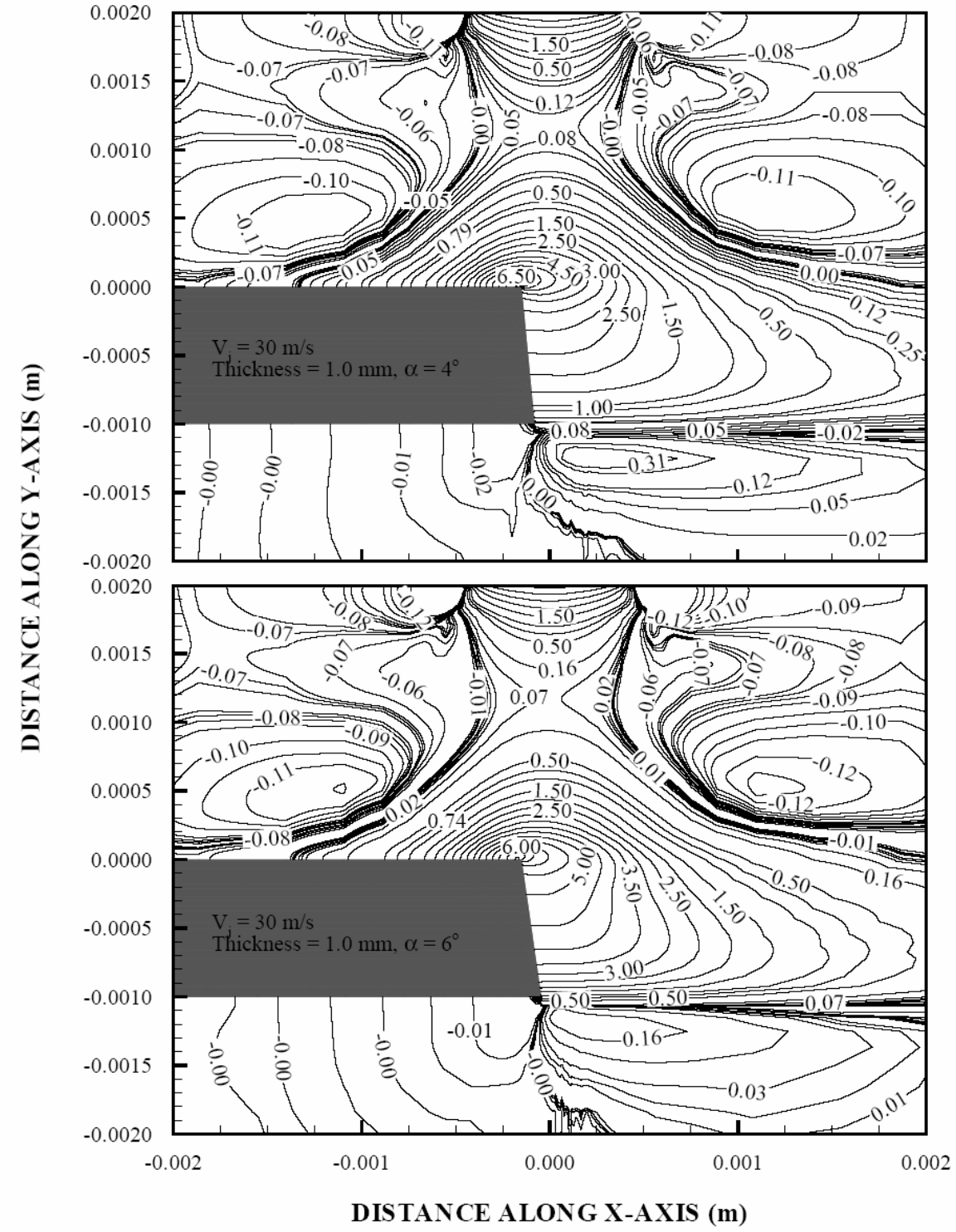

Figure 5.26 Pressure coefficient in the symmetry plane for jet averaged velocity of 30 m/s, kerf thickness of 1.0 mm, and kerf wedge angles of 4° and 6°

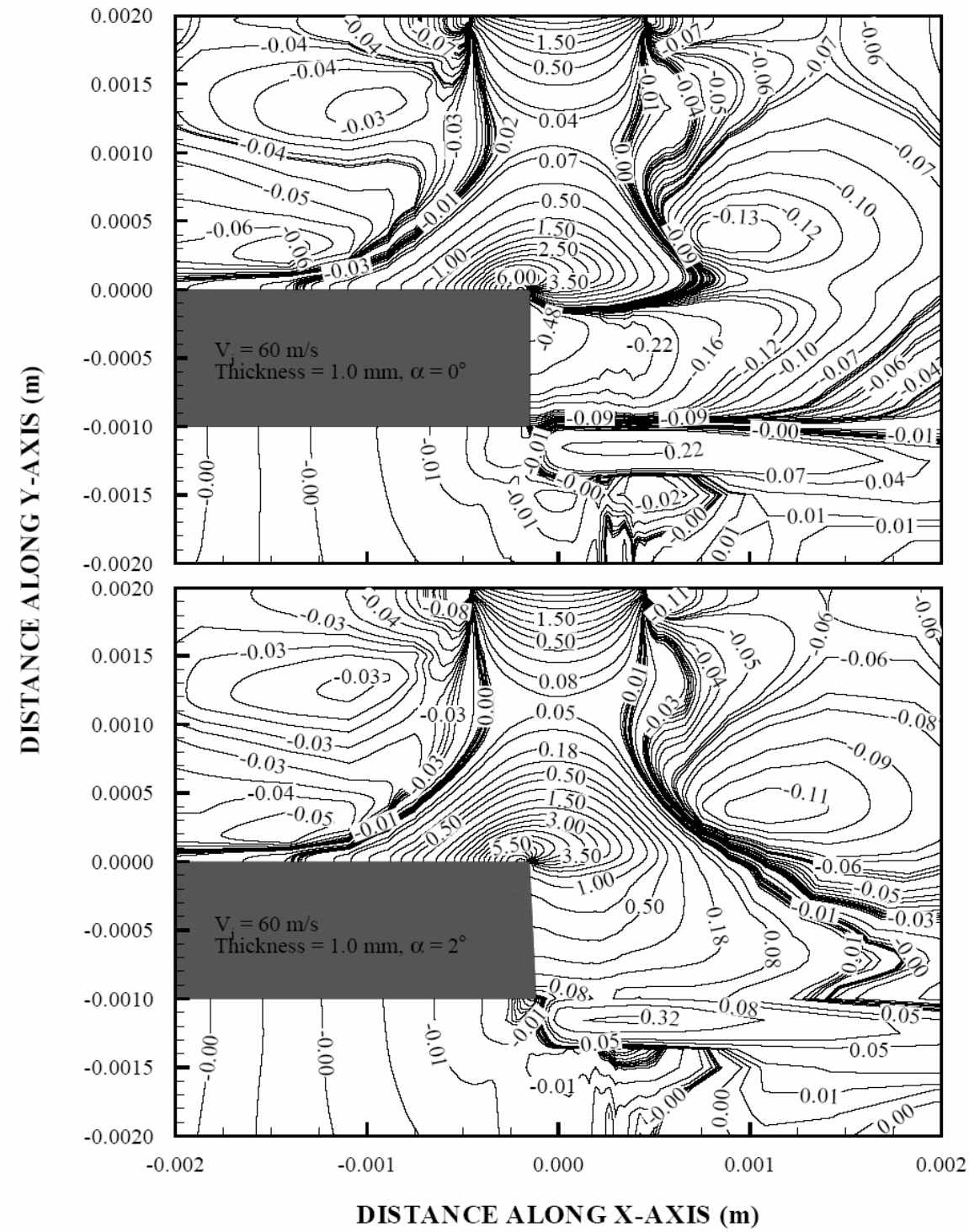

Figure 5.27 Pressure coefficient in the symmetry plane for jet averaged velocity of 60 m/s, kerf thickness of 1.0 mm, and kerf wedge angles of 0° and 2°

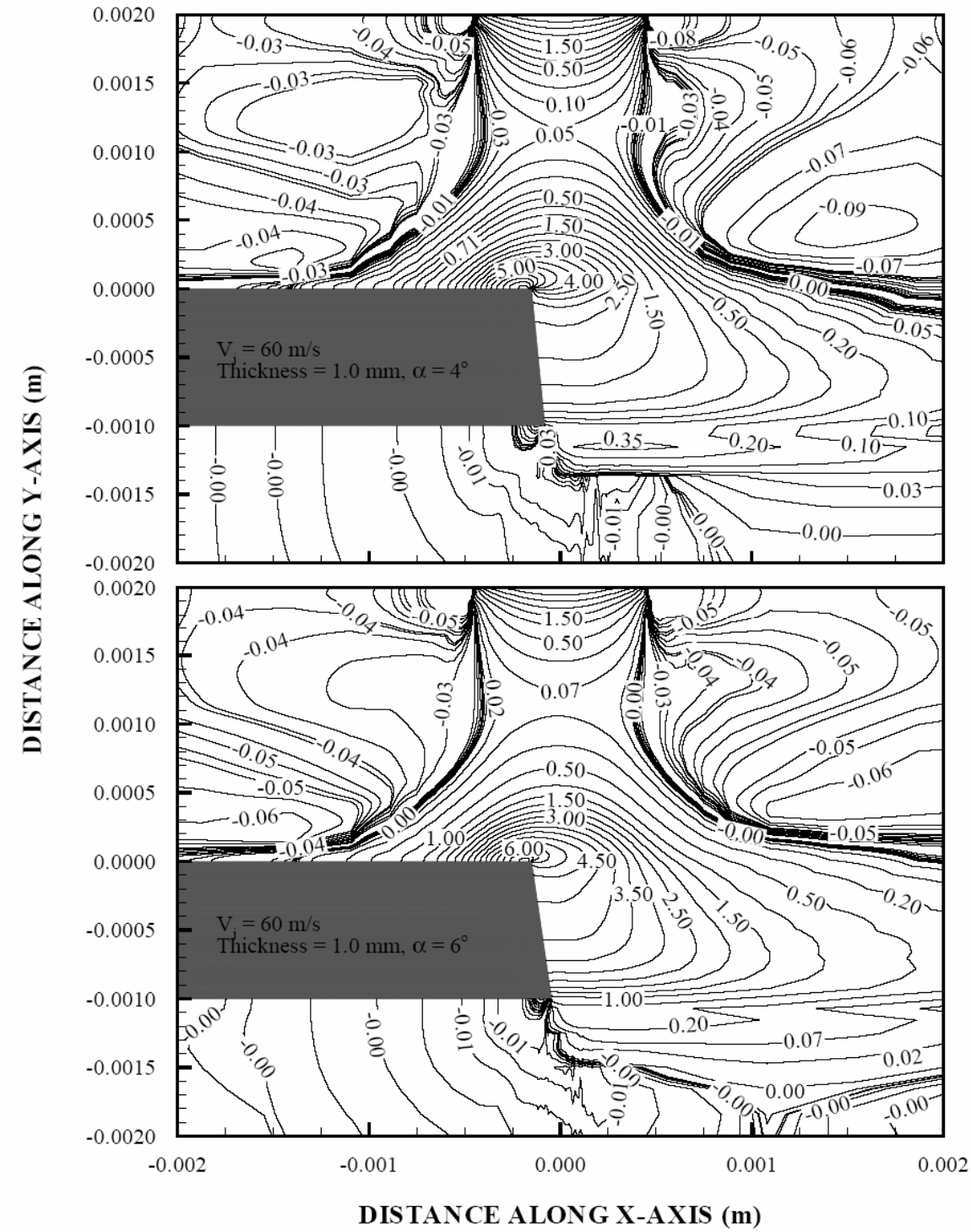

Figure 5.28 Pressure coefficient in the symmetry plane for jet averaged velocity of 60 m/s, kerf thickness of 1.0 mm, and kerf wedge angles of 4° and 6°

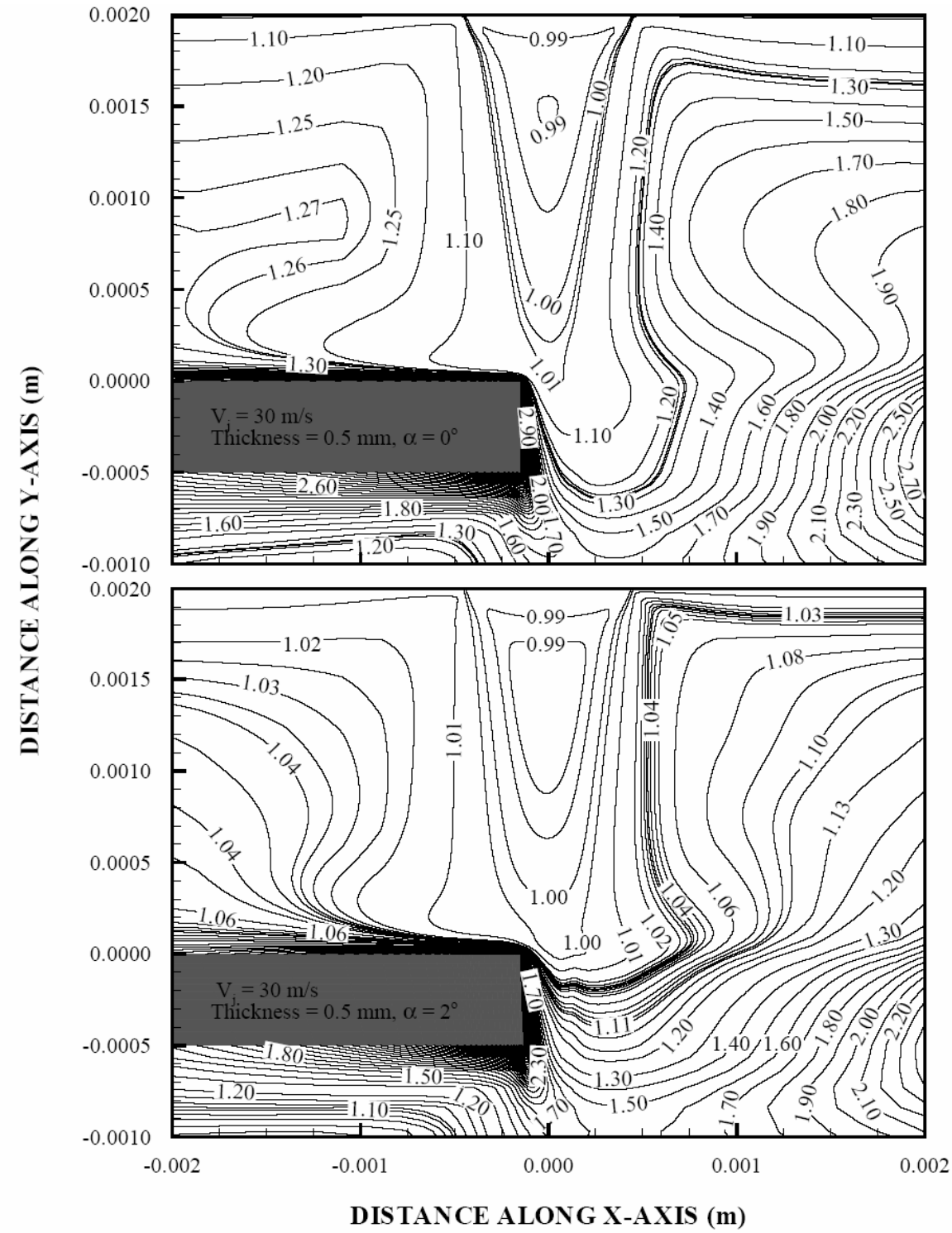

Figure 5.29 Normalized temperature (T/T_j) in the symmetry plane for jet averaged velocity of 30 m/s, kerf thickness of 0.5 mm, and kerf wedge angles of 0° and 2°

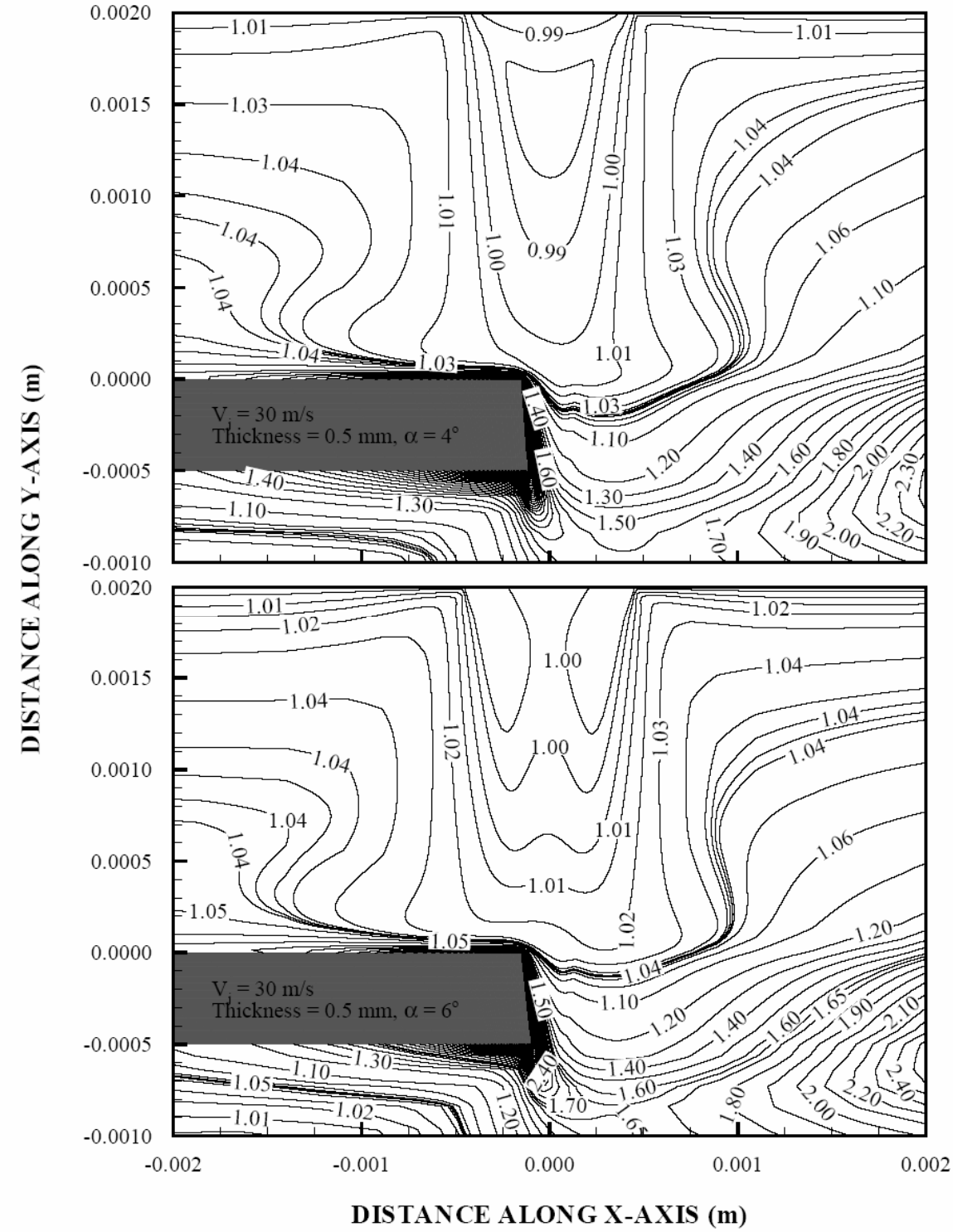

Figure 5.30 Normalized temperature (T/T_j) in the symmetry plane for jet averaged velocity of 30 m/s, kerf thickness of 0.5 mm, and kerf wedge angles of 4° and 6°

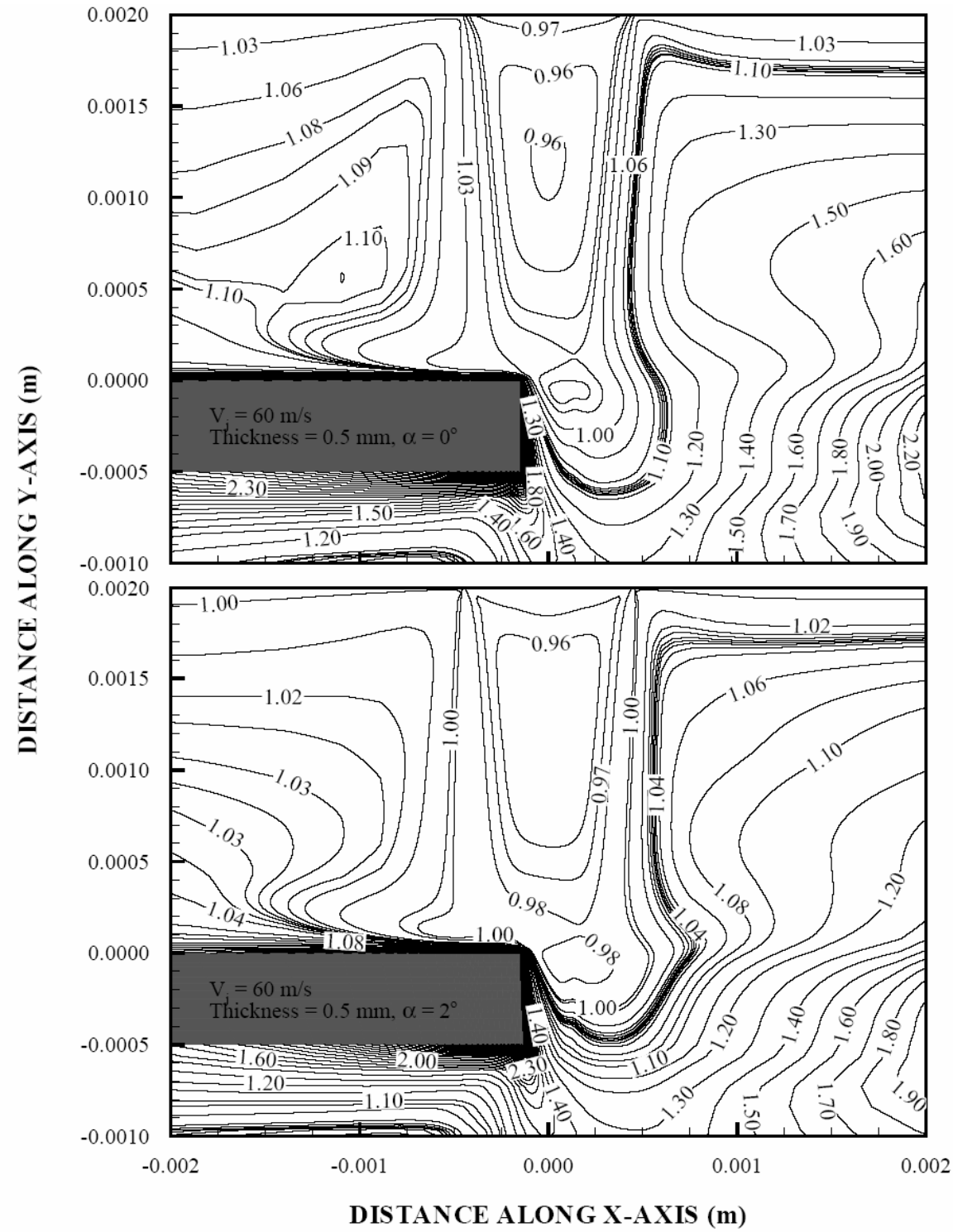

Figure 5.31 Normalized temperature (T/T_j) in the symmetry plane for jet averaged velocity of 60 m/s, kerf thickness of 0.5 mm, and kerf wedge angles of 0° and 2°

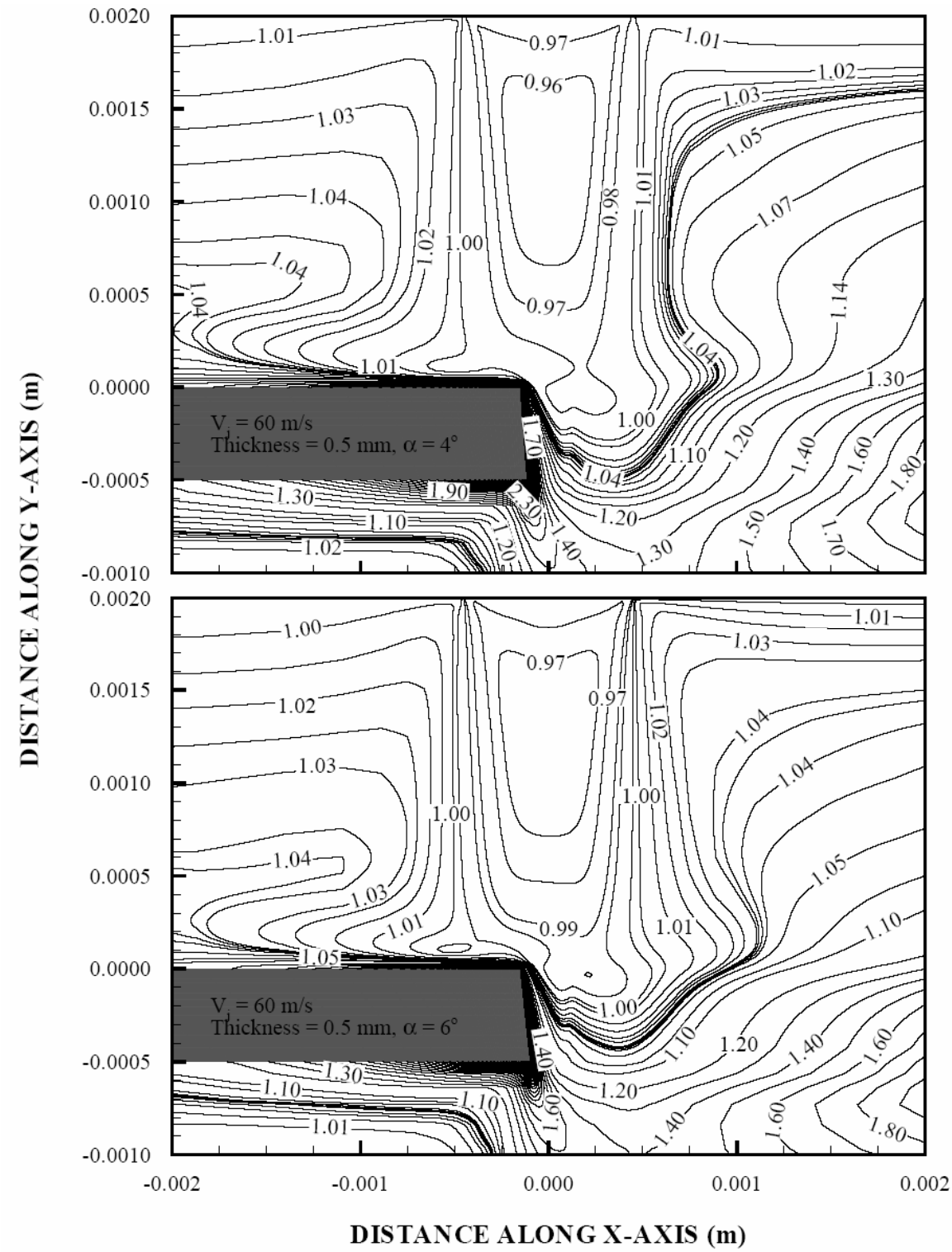

Figure 5.32 temperature (T/T_j) in the symmetry plane for jet averaged velocity of 60 m/s, kerf thickness of 0.5 mm, and kerf wedge angles of 4° and 6°

As the kerf wedge angle increases, the increase in temperature at locations away from the jet axis is less remarkable. This can be associated with the relative acceleration of the flow associated with increasing the kerf wedge angle (Figures 5.13, 5.14, 5.15, and 5.16). That is, the relatively higher velocities at locations away from the jet axis lead to the lower temperatures attained in that region. Figures 5.33, 5.34, 5.35, and 5.36 show normalized temperature contours in the symmetry plane for kerf thickness = 1.0 m, two averaged jet velocities at nozzle exit, and four kerf wedge angles. A remarkable increase in the thermal boundary layer thickness is observed towards the kerf bottom as kerf wedge angle increases from 4° to 6°. Associated with this are higher fluid temperatures attained in the bottom region of the kerf, especially at locations away from the jet axis. This effect is more pronounced for the lower averaged jet velocity (V_j = 30 m/s).

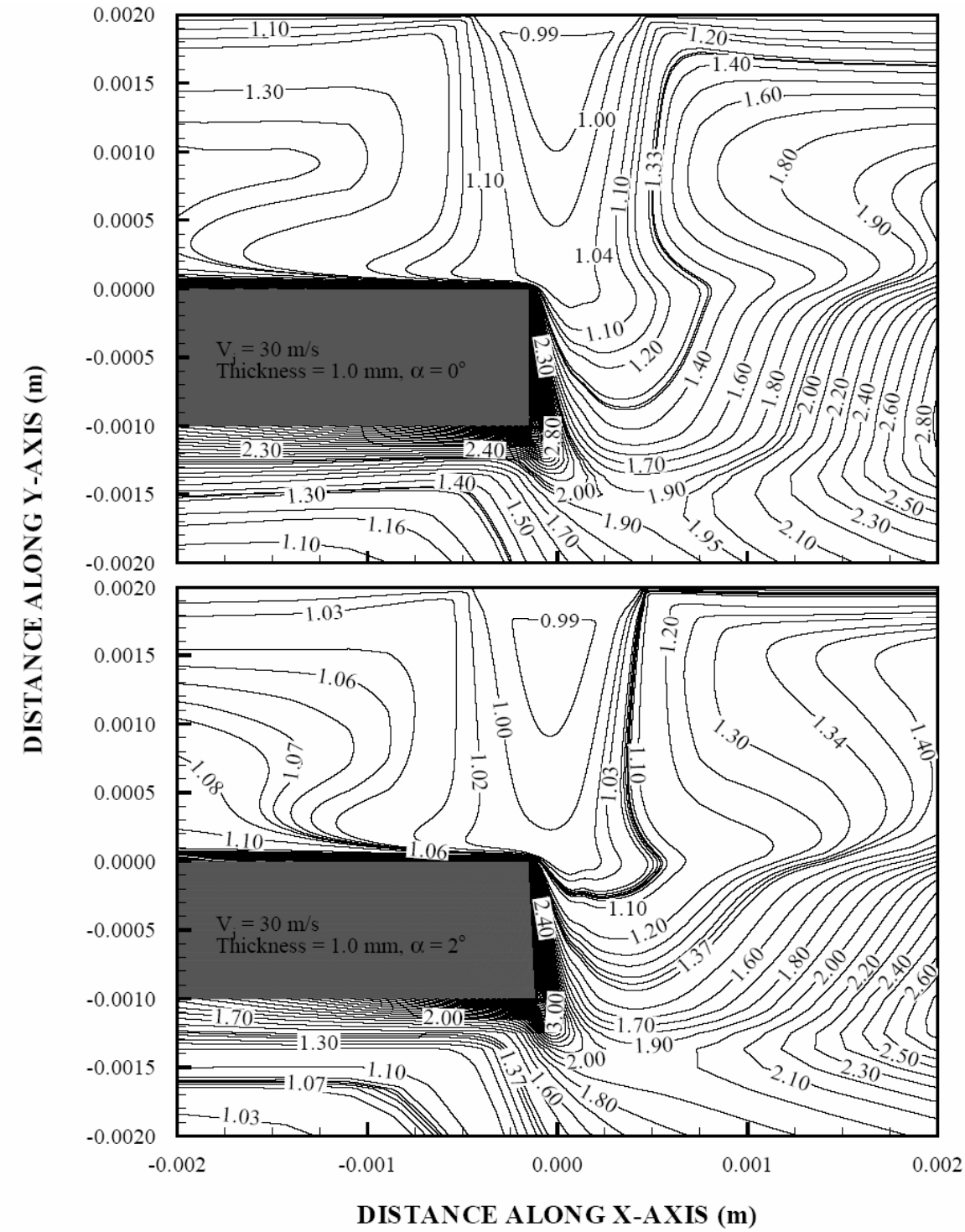

Figure 5.33 Normalized temperature (T/T_j) in the symmetry plane for jet averaged velocity of 30 m/s, kerf thickness of 1.0 mm, and kerf wedge angles of 0° and 2°

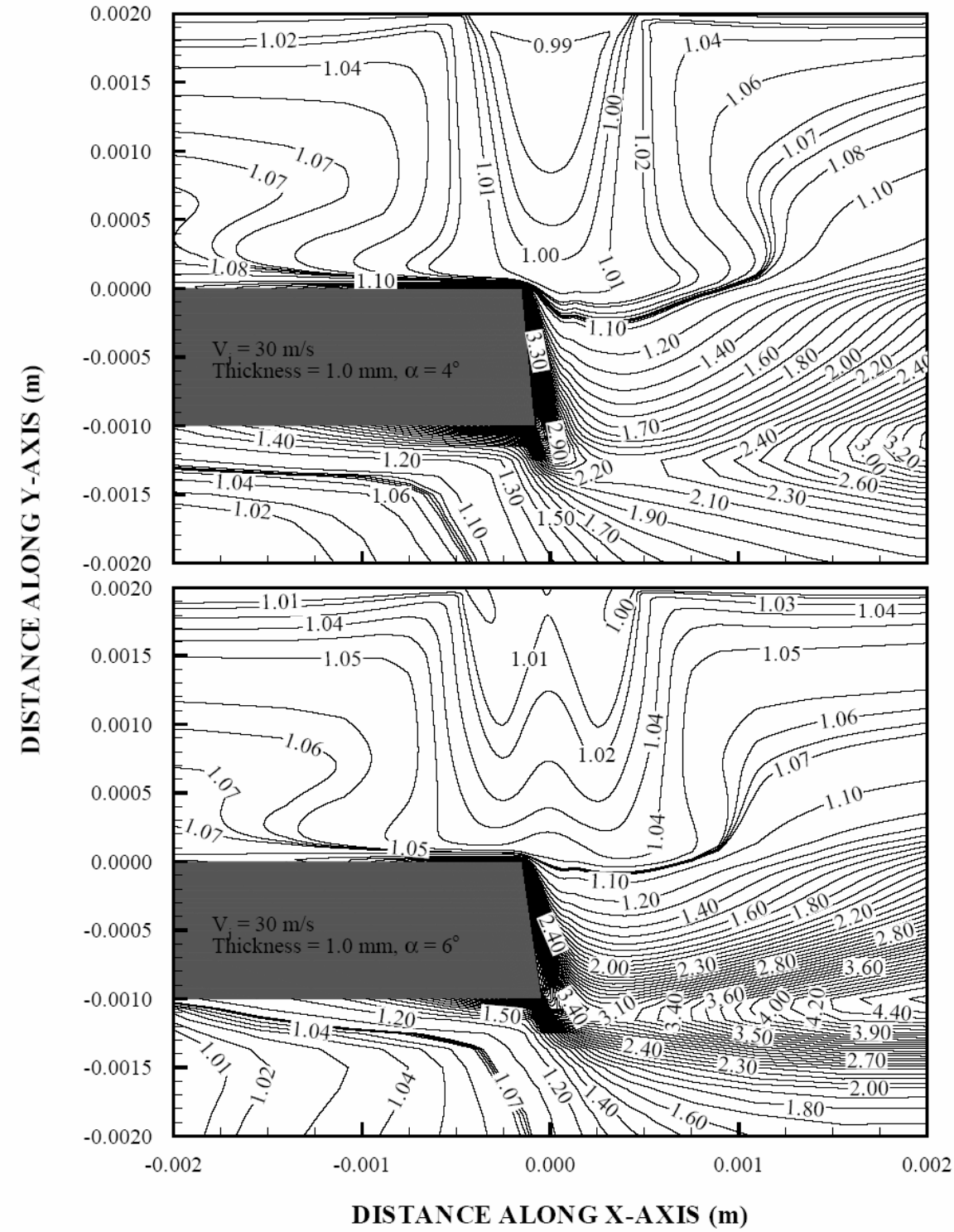

Figure 5.34 Normalized temperature (T/T_j) in the symmetry plane for jet averaged velocity of 30 m/s, kerf thickness of 1.0 mm, and kerf wedge angles of 4° and 6°

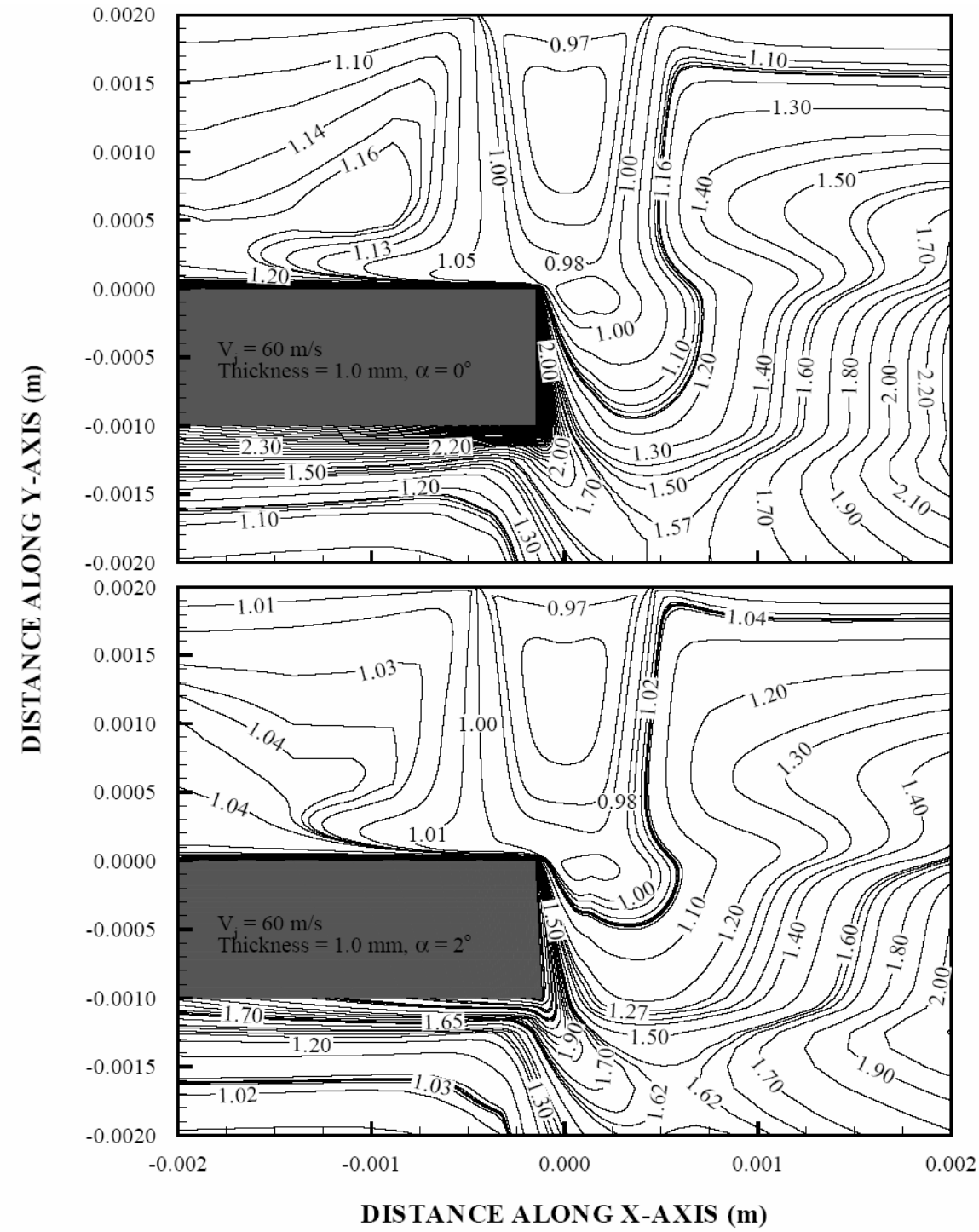

Figure 5.35 Normalized temperature (T/T_j) in the symmetry plane for jet averaged velocity of 60 m/s, kerf thickness of 1.0 mm, and kerf wedge angles of 0° and 2°

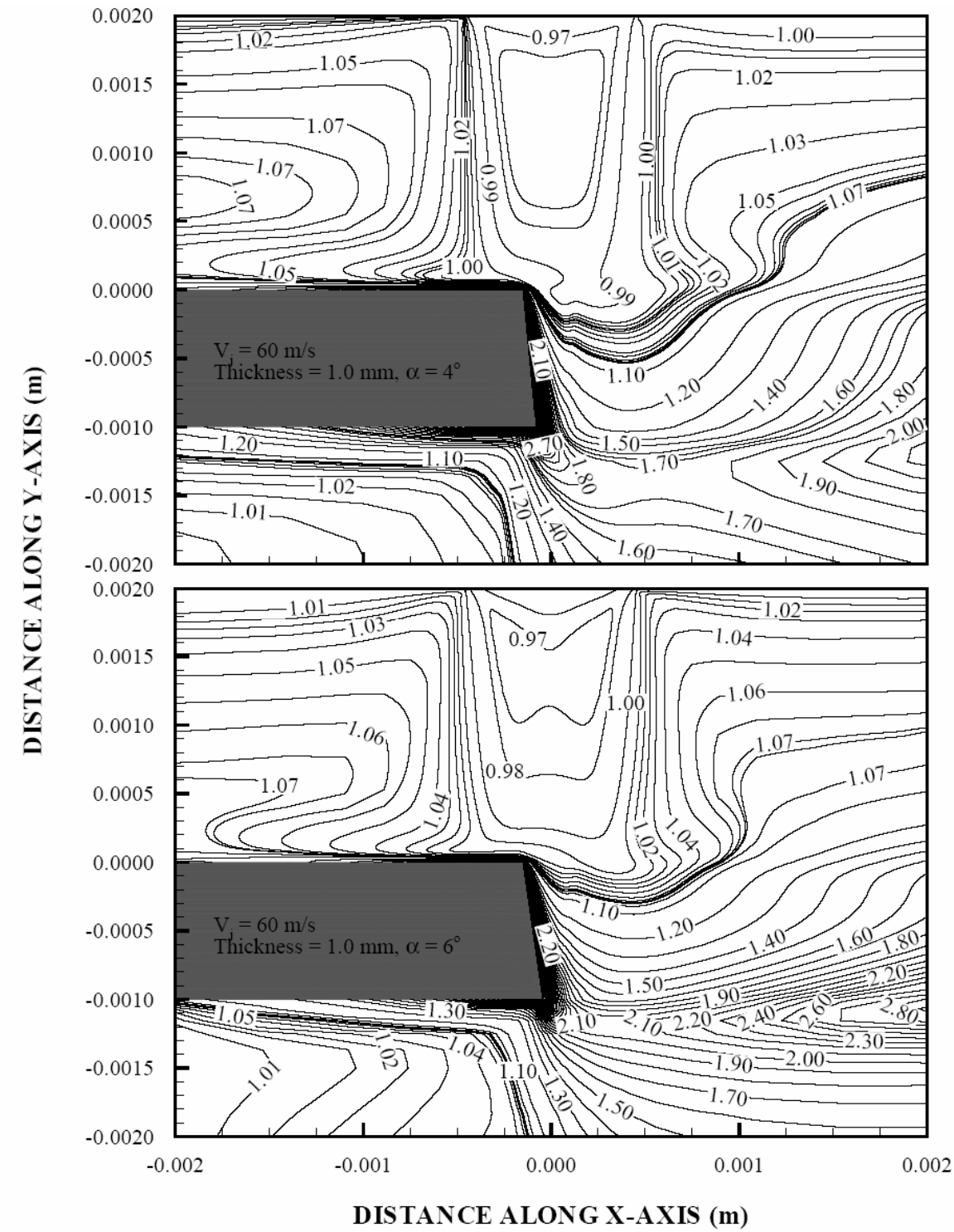

Figure 5.36 Normalized temperature (T/T_j) in the symmetry plane for jet averaged velocity of 60 m/s, kerf thickness of 1.0 mm, and kerf wedge angles of 4° and 6°

Figure 5.37 shows velocity magnitude distribution along the laser beam axis for kerf thickness = 0.5 mm, two averaged jet velocities, and four kerf wedge angles. It should be noted that the locations y = 0, y = 0.002, and y = -0.0005 represent the workpiece surface, nozzle exit, and kerf depth (workpiece or kerf thickness) respectively. The jet velocity increases after exiting from the nozzle reaching the first maximum velocity after a distance of about one nozzle diameter, after which it reduces to a minimum just before impingement onto the kerf surface. The value of the minimum velocity reached is lower for the larger kerf wedge angle. This is due to the more pronounced blockage effect of the kerf. The velocity then increases as flow approaches kerf bottom exit until it reaches second maximum velocity. The magnitude and location of this second maximum velocity are slightly affected by the kerf wedge angle. The second maximum velocity location is shifted towards the kerf exit (negative direction of the x-axis) as the kerf wedge angle increases. This is true for both averaged jet velocities. The increase in magnitude of second maximum velocity as kerf wedge angle increases is not remarkable for the case for which averaged jet velocity is higher. This can be due to the higher axial momentum already associated with the higher velocity jet. Figure 5.38 shows the velocity magnitude distribution along the laser beam axis for kerf thickness = 1.0 mm, two averaged jet velocities, and four kerf wedge angles. It should be noted that the location y = -0.001 corresponds to the kerf depth. In addition to observations noted for the previous case, an inflection point is observed as the velocity magnitude increases in the kerf before reaching second maximum velocity magnitude. This is true for the case for which kerf wedge angle = 6° and averaged jet velocity at nozzle exit = 30 m/s. It is also true for the

cases for which kerf wedge angle = 4° and 6° and averaged jet velocity = 60 m/s. A significant increase in the magnitude of the second maximum velocity is observed for the case for which averaged jet velocity at nozzle exit = 60 m/s and wedge angle = 6°. This value is also significantly higher than the value of first maximum velocity attained before impingement. Its location almost coincides with the kerf exit at the maximum kerf depth.

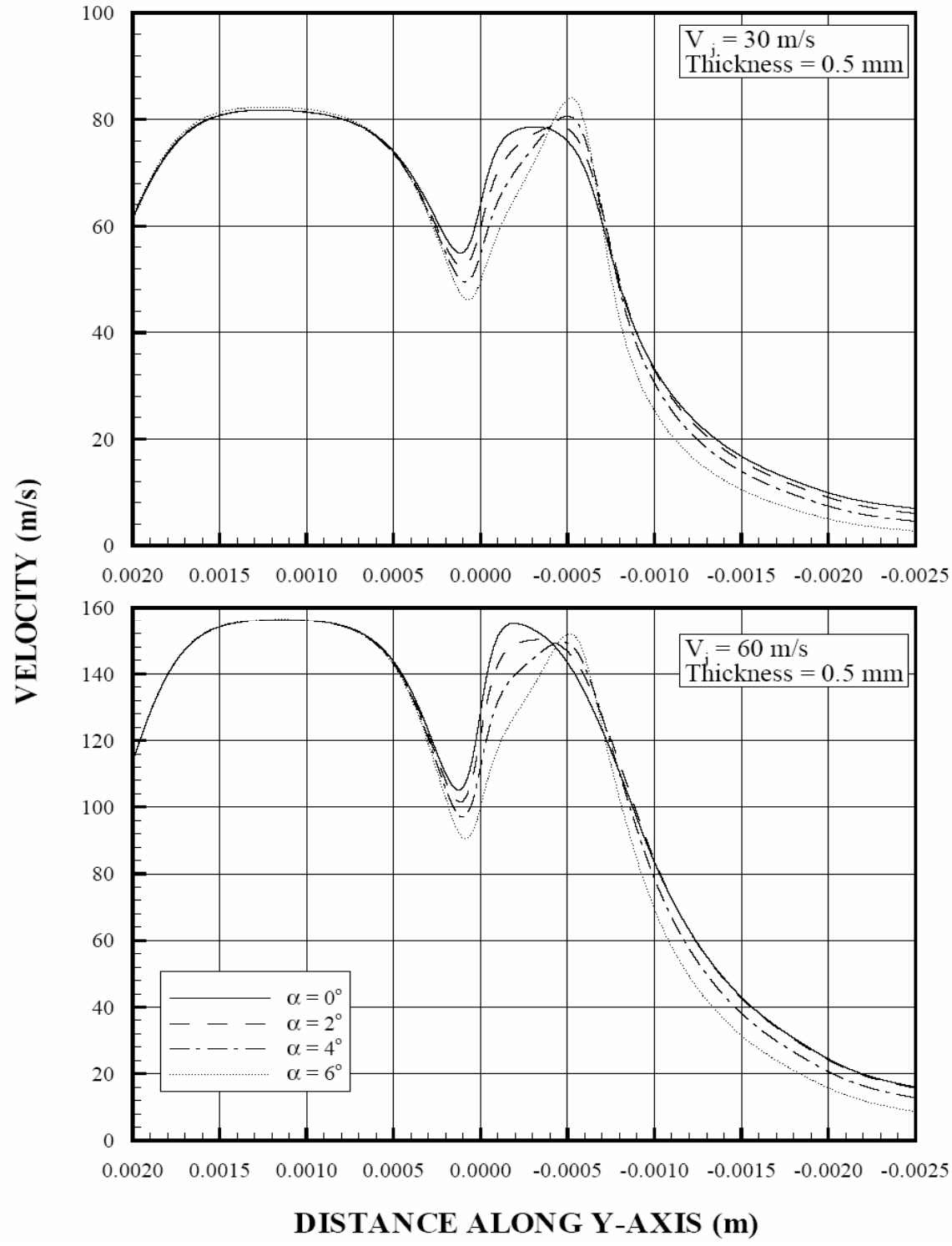

Figure 5.37 Velocity magnitude along laser beam axis for two different averaged jet velocities, kerf thickness of 0.5 mm, and four kerf wedge angles

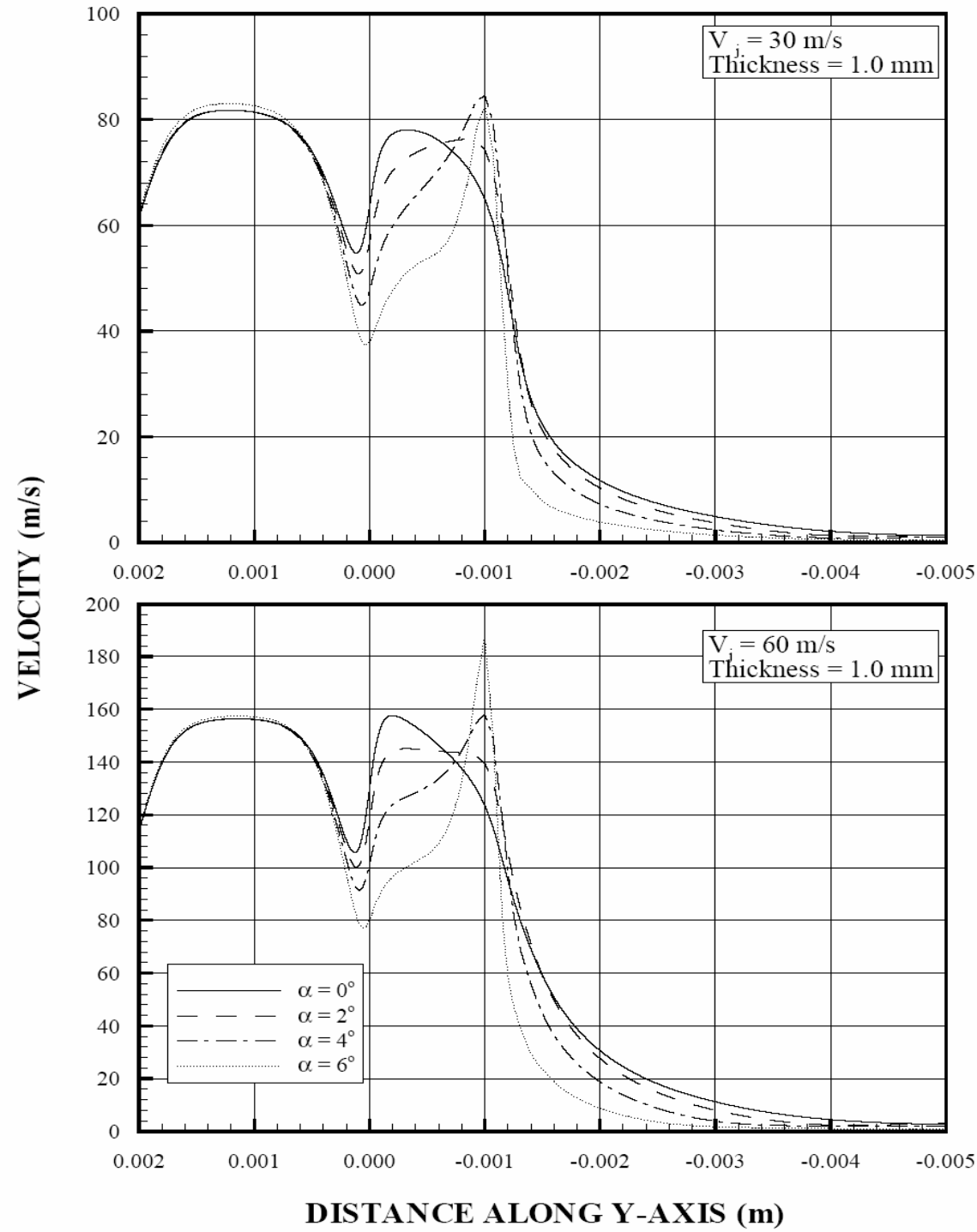

Figure 5.38 Velocity magnitude along laser beam axis for two different averaged jet velocities, kerf thickness of 1.0 mm, and four kerf wedge angles

Figures 5.39 and 5.40 show pressure distribution in the fluid along the laser beam axis for kerf thickness = 0.5 and 1.0 mm, two averaged jet velocities at nozzle exit, and four kerf wedge angles. Static pressure reduces after exiting the nozzle because of jet expansion and then increases to a maximum at a location close to the kerf top surface because of stagnation formation and blockage effect of the kerf. Pressure drop continues in the kerf because of the jet radial expansion in this region. Pressure drop is sharp in the case for which kerf wedge angle = 0° and becomes more gradual as kerf wedge angle increases to 6° in steps of 2°. This increase in pressure can be associated with the increase in thermodynamic pressure resulting from the increased heat transfer to the fluid as the kerf wedge angle increases. The static pressure reaches another minimum in the kerf whose value decreases as kerf wedge angle decreases. The location corresponding to this minimum moves closer to the kerf exit as the kerf wedge angle increases. A negative pressure is observed for all cases for which kerf wedge angle = 0°. This was emphasized when pressure contours in the symmetry plane were discussed and associated with the kerf blockage effect. A slight increase in pressure is observed upon exiting the kerf. The pressure then reduces to atmospheric pressure (gage pressure = 0 pascal).

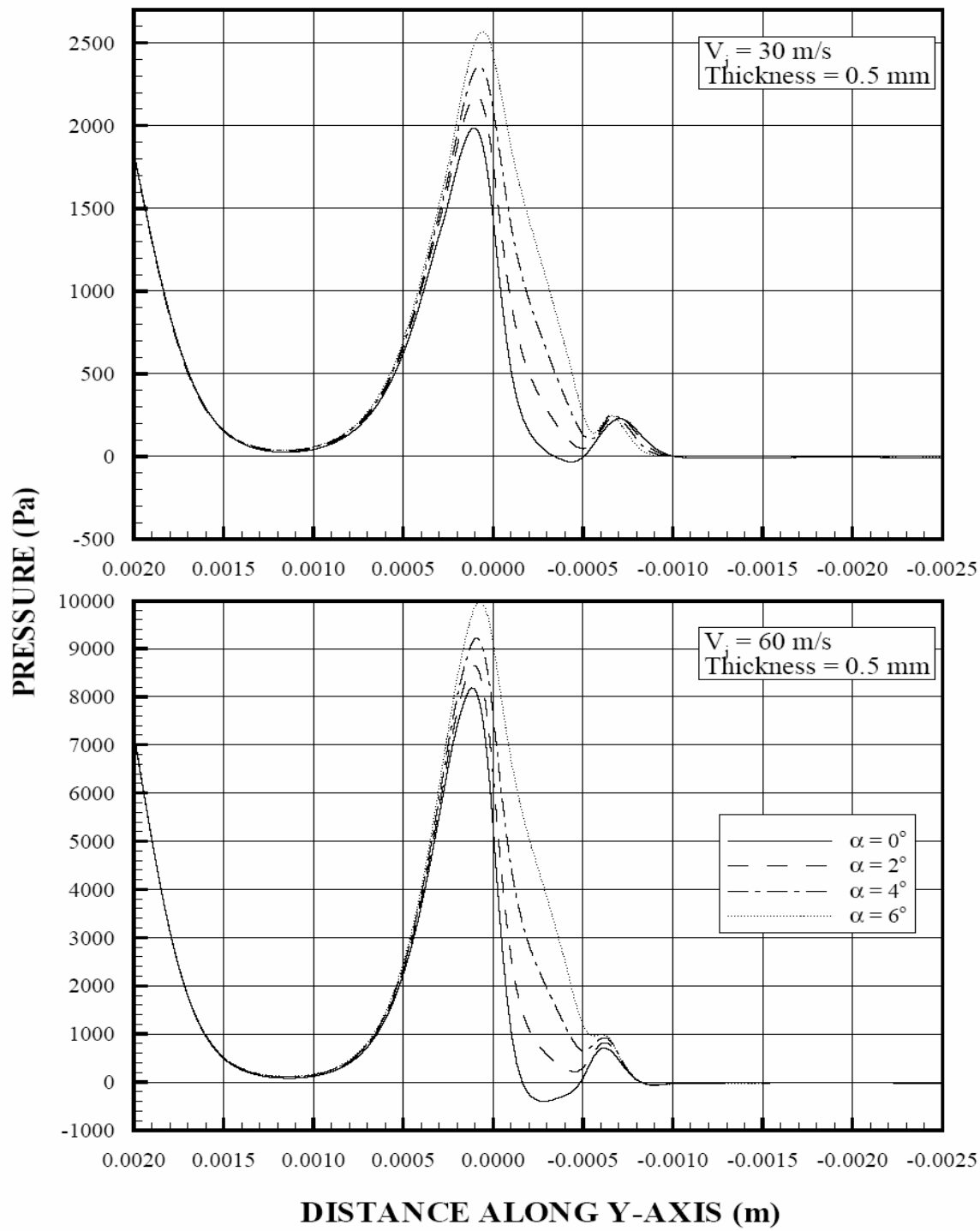

Figure 5.39 Pressure distribution along laser beam axis for two different averaged jet velocities, kerf thickness of 0.5 mm, and four kerf wedge angles

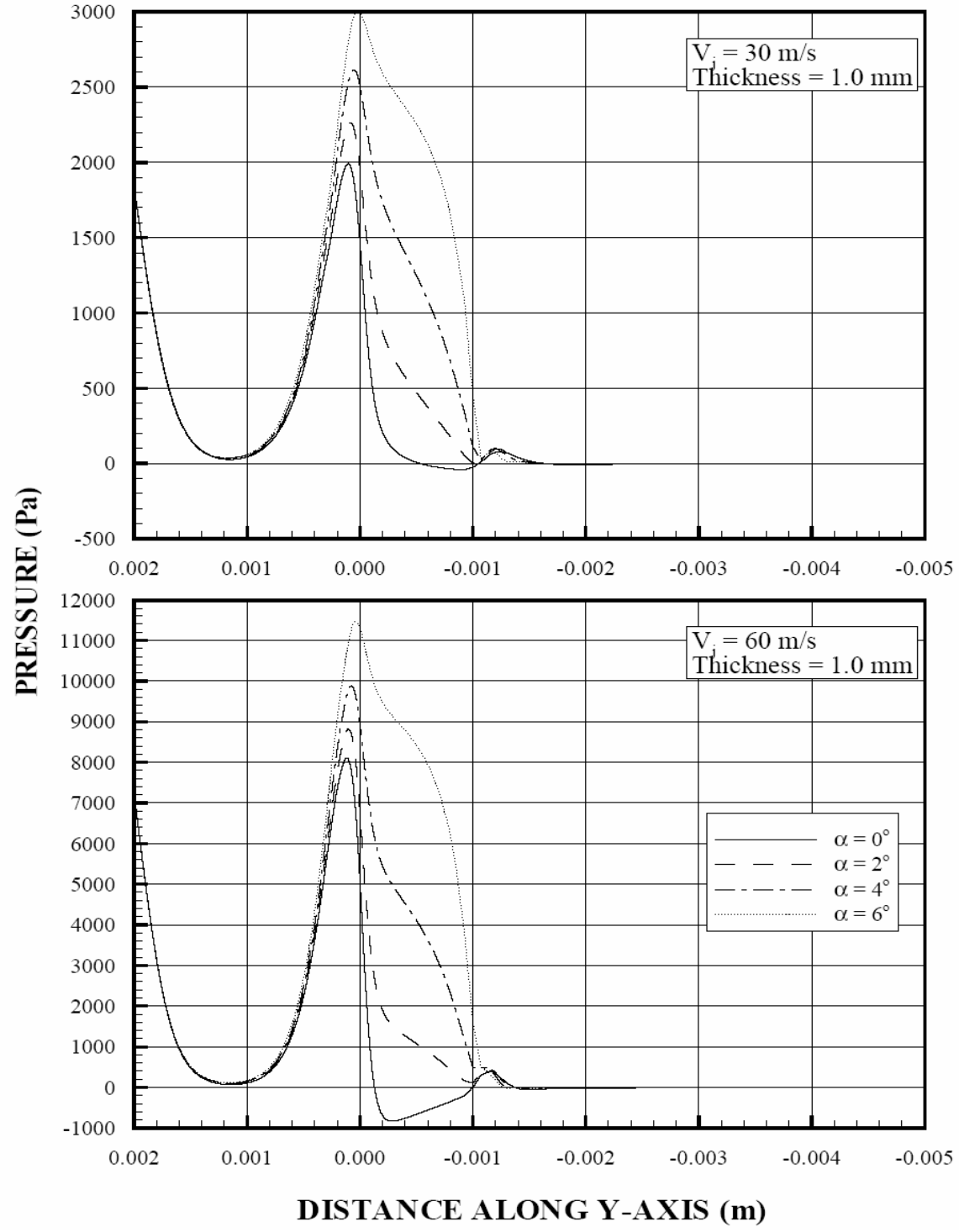

Figure 5.40 Pressure distribution along laser beam axis for two different averaged jet velocities, kerf thickness of 1.0 mm, and four kerf wedge angles

Figures 5.41 and 5.42 show fluid temperature distribution along the laser beam axis for kerf thickness = 0.5 and 1.0 mm, two averaged jet velocities, and four kerf wedge angles. Temperature increases onset fluid enters the kerf region. In this region, fluid temperature increases as kerf wedge angle increases. Fluid temperature reaches a maximum value whose value and location depends on kerf wedge angle. Increasing the wedge angle from 0° to 2° has negligible effect on the maximum temperature attained. However, increasing the wedge angle from 2° to 6° in steps of 2° increases the maximum temperature attained and moves its location closer to the kerf region. Increasing the kerf wedge angle in the case for which kerf thickness = 1.0 mm has more noticeable effect on the maximum temperature attained. Fluid temperature then reduces such that temperature decreases as wedge angle increases.

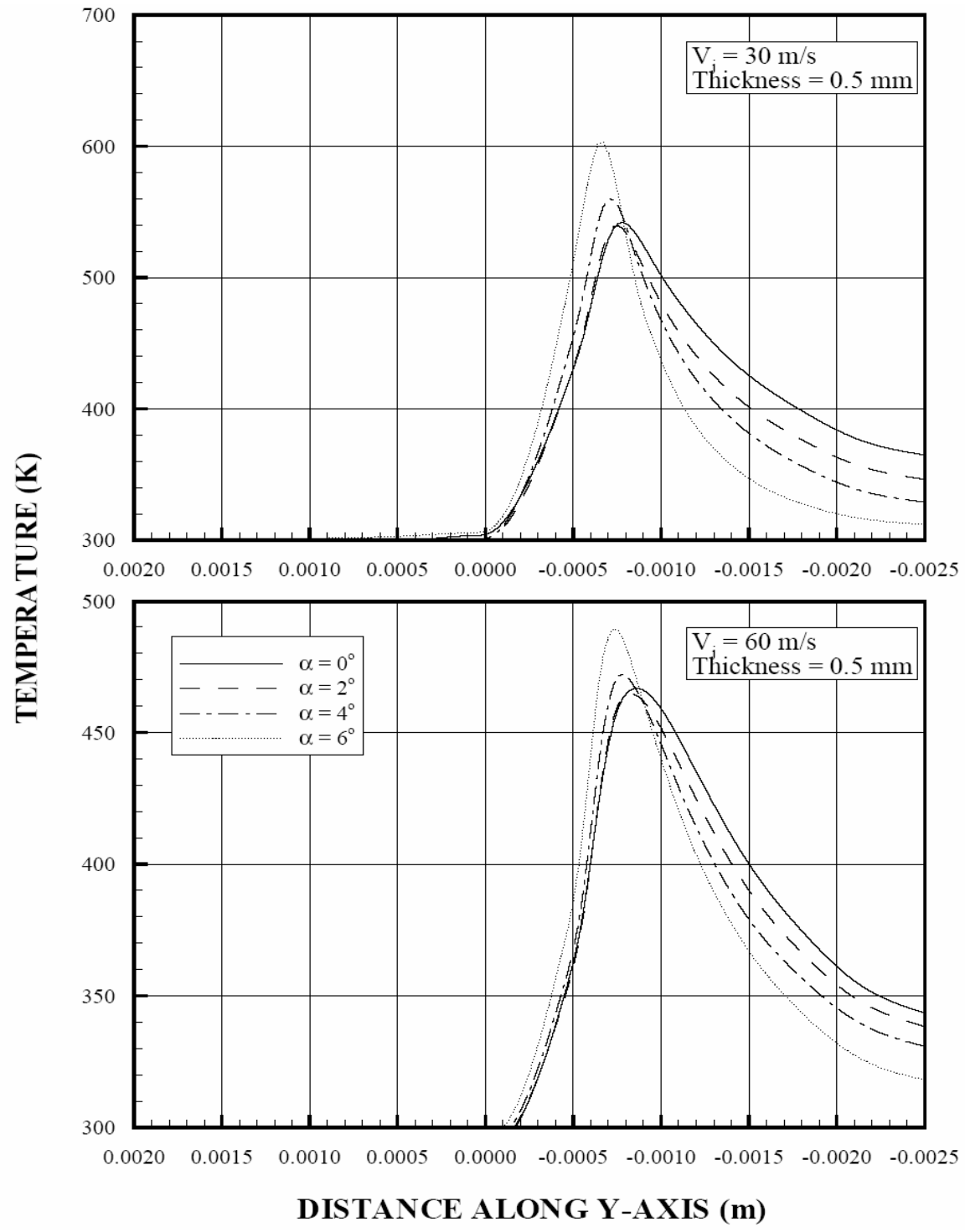

Figure 5.41 Temperature distribution along laser beam axis for two different averaged jet velocities, kerf thickness of 0.5 mm, and four kerf wedge angles

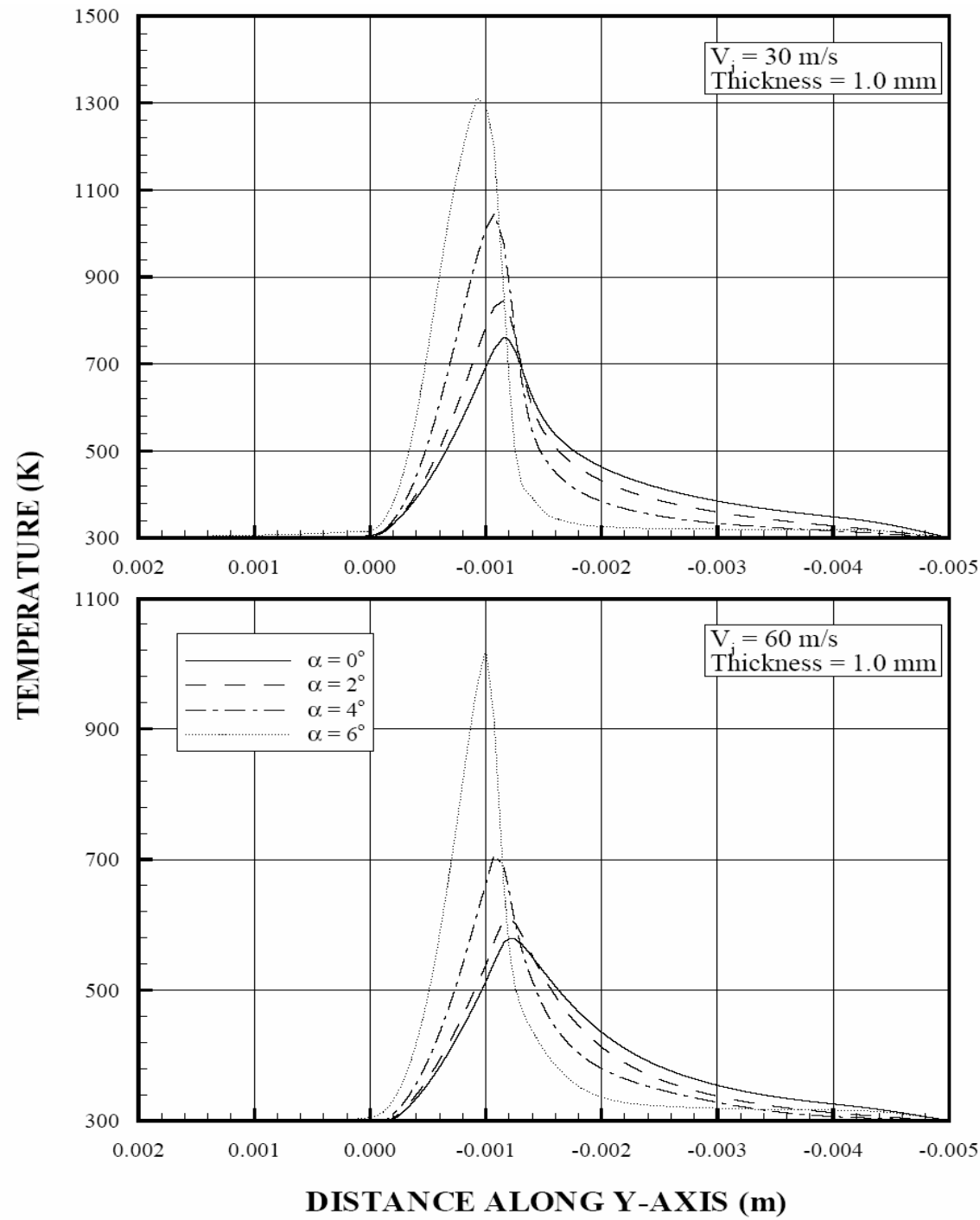

Figure 5.42 Temperature distribution along laser beam axis for two different averaged jet velocities, kerf thickness of 1.0 mm, and four kerf wedge angles

Figure 5.43 shows the Nusselt number distribution along the normalized kerf thickness for four different kerf wedge angles. The kerf thickness = 0.5 mm and the averaged jet velocity = 30 m/s. The kerf thickness = 0.5 mm and the averaged jet velocity = 30 m/s. The kerf thickness is normalized with the maximum thickness; that is, normalized kerf thickness = 0 corresponds to the kerf inlet, and normalized kerf thickness = -1 corresponds to the kerf exit. The Nusselt number distribution is shown at 5 locations along the kerf wall. Location A (x = -0.00015, z = 0.0000094 m) is almost the kerf edge (where the kerf wall intersects the symmetry plane). The other 4 locations (B, C, D, and E) are distributed along the kerf wall (see figure). Similar trends of variation among the various locations are observed for the different kerf wedge angles. Location B (x = -0.000125, z = 0.000075 m) corresponds to the location where Nusselt number attains the highest values.

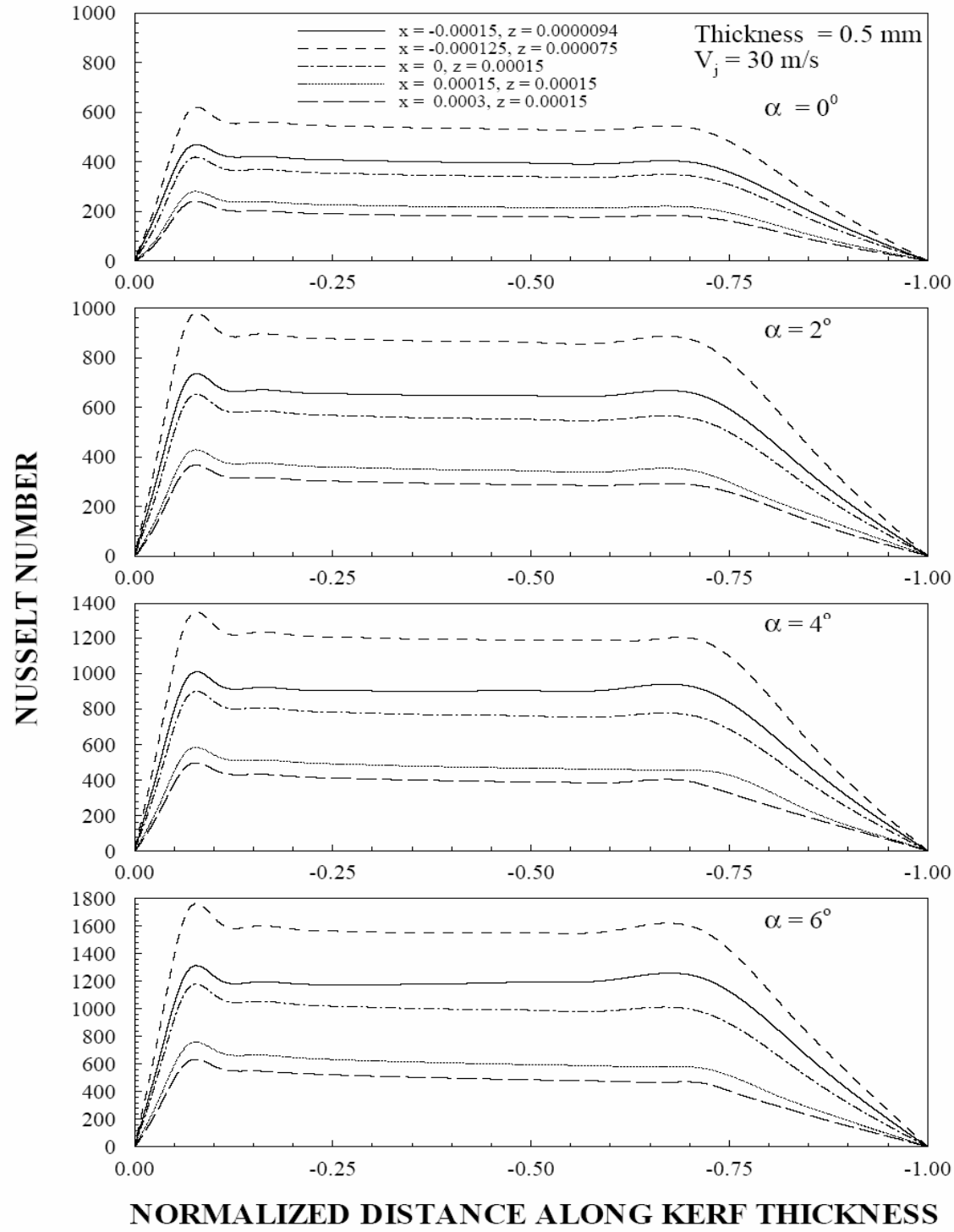

Figure 5.43 Nusselt number distribution at five locations along the kerf wall for kerf thickness = 0.5 mm, averaged jet velocity = 30 m/s, and four kerf wedge angles

The trends obtained show that Nusselt number show that Nusselt number increases as one moves along the kerf wall from location A (x = -0.00015, z = 0.000094) in the direction of the positive x-axis to attain maximum values at a certain location which can be approximated by location B (x = -0.000125, z = 0.000075 m). The Nusselt number then decreases as one moves from location B in the direction of positive x-axis (see Figure 5.1). The trends show that Nusselt number increases sharply from the kerf top edge due to convective cooling of the jet in the kerf. The Nusselt number attains a maximum value and then decreases gradually. Constant Nusselt number or even a gradual increase in Nusselt number values along the kerf thickness is observed for some locations. A second maximum Nusselt number can also be attained. Nusselt number then decays along the wall towards the kerf exit. The decay in Nusselt number gets sharper as the kerf wedge angle increases. Figure 5.44 shows the Nusselt number distribution along the normalized kerf thickness for same geometric parameters as the previous case and averaged jet velocity = 60 m/s. Trends observed are the same as the previous case. Figures 5.45 and 5.46 show the Nusselt number distribution along the normalized kerf thickness for kerf thickness = 1.0 mm, two averaged jet velocities, and four kerf wedge angles. The second maximum in Nusselt number values attained is observed for several locations. The Nusselt number distribution for the case for which kerf wedge angle = 6° is clearly characterized by secondary maximum at locations A, B, and C (see Figure 5.1). These maxima even exceed the first maxima attained at the corresponding locations.

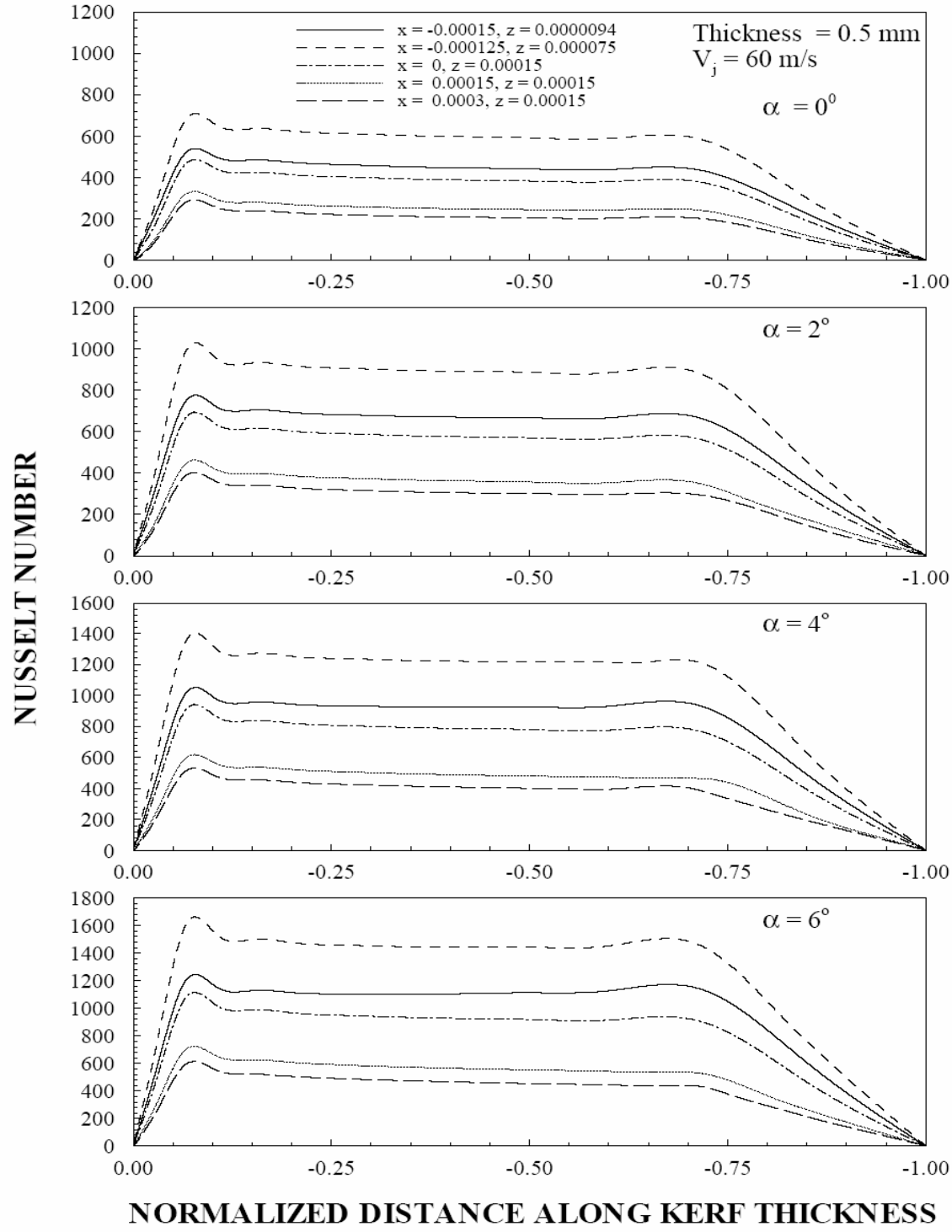

Figure 5.44 Nusselt number distribution at five locations along the kerf wall for kerf thickness = 0.5 mm, averaged jet velocity = 60 m/s, and four kerf wedge angles

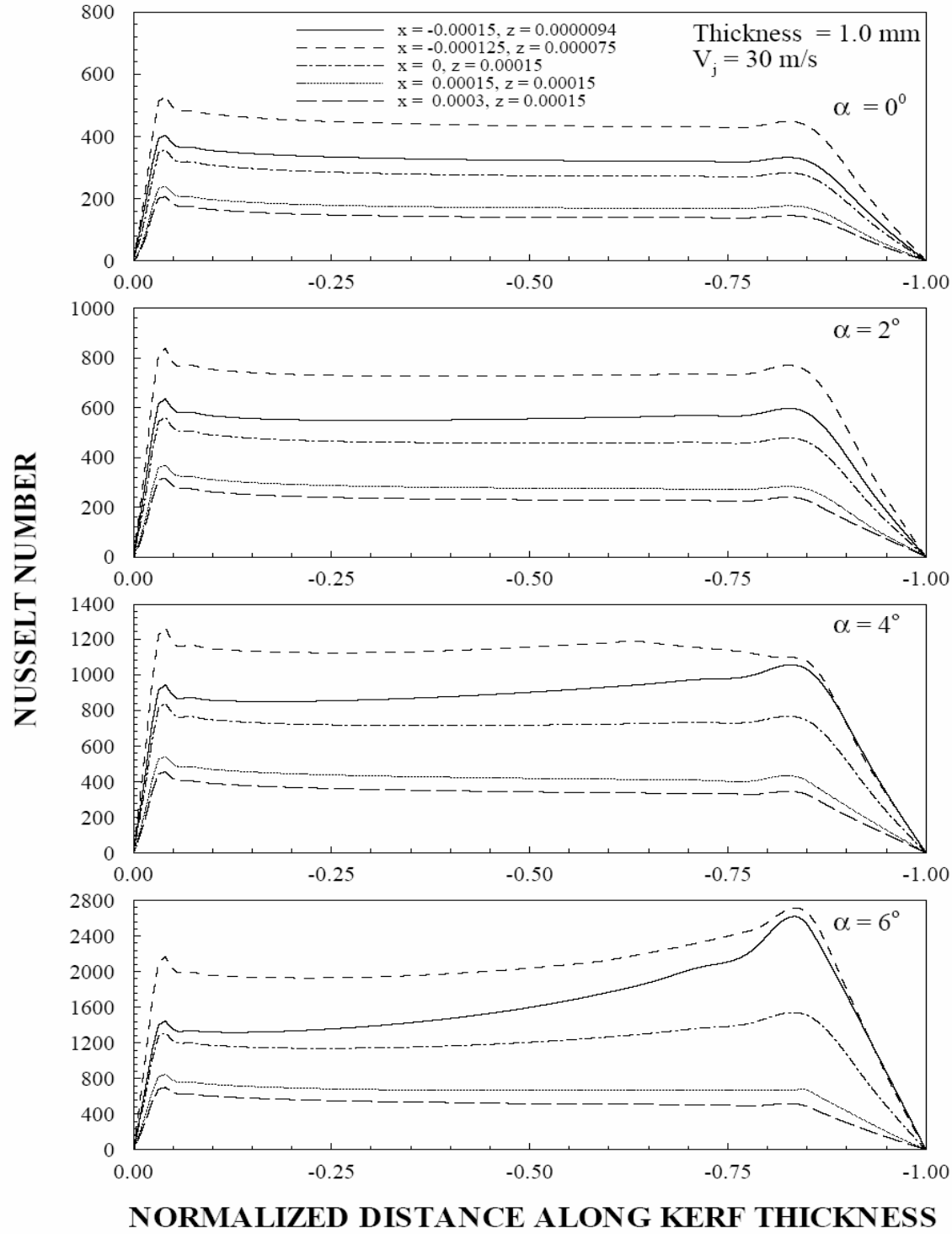

Figure 5.45 Nusselt number distribution at five locations along the kerf wall for kerf thickness = 1.0 mm, averaged jet velocity = 30 m/s, and four kerf wedge angles

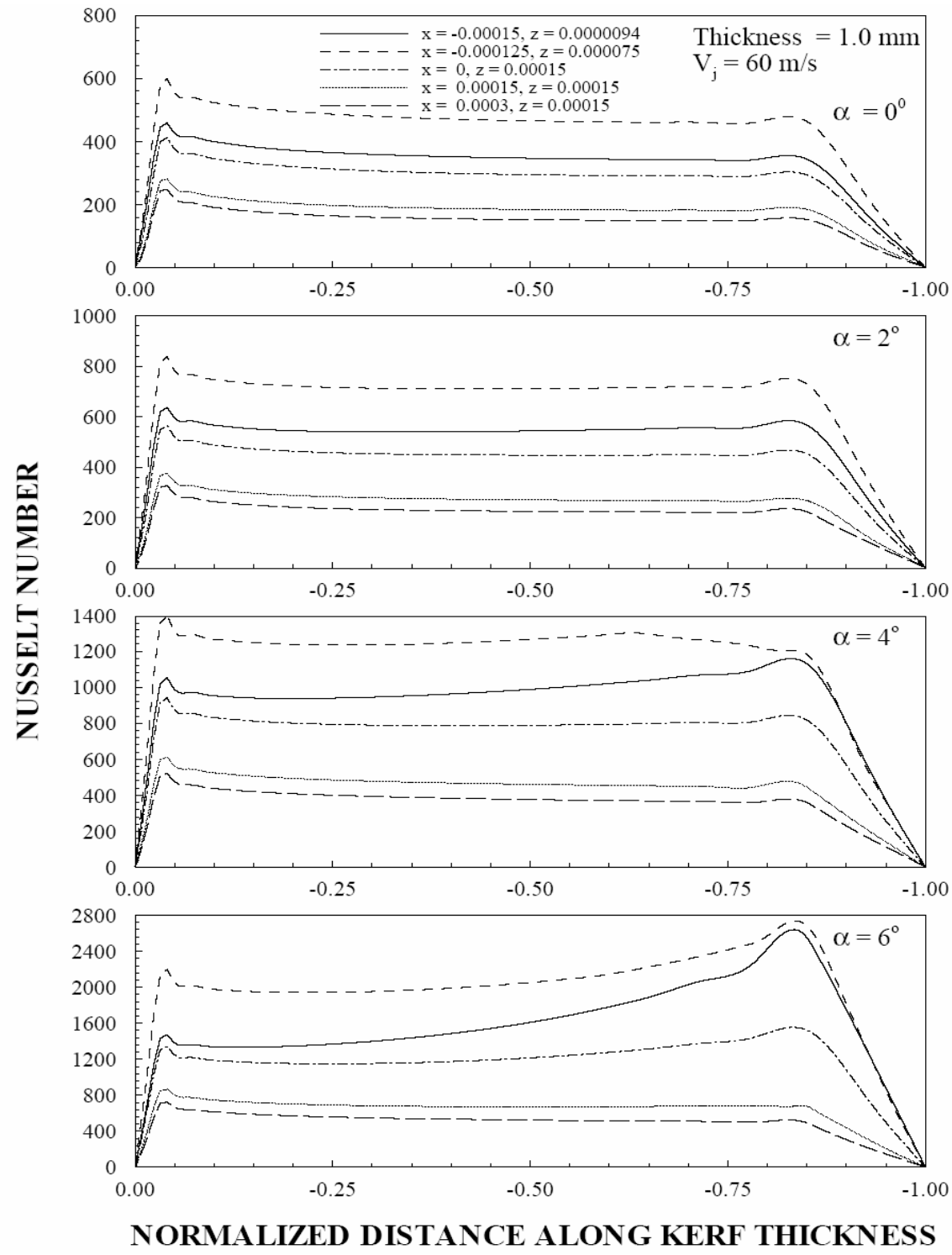

Figure 5.46 Nusselt number distribution at five locations along the kerf wall for kerf thickness = 1.0 mm, averaged jet velocity = 60 m/s, and four kerf wedge angles

Appearance of the secondary maximum in Nusselt number distribution is attributed to a sharp rise in the turbulence level which accompanies transition from an accelerating stagnation region flow to a decelerating wall jet [93]. The formation of the secondary maximum can also be attributed to the increased transport resulting from the transition from a laminar to a turbulent boundary layer.

Figures 5.47 and 5.48 compare the Nusselt number distribution at location B, where the Nusselt number attains highest values, for kerf thickness = 0.5 and 1.0 mm, two averaged jet velocities, and four kerf wedge angles. As the wedge angle increases, Nusselt number increases. The blockage effect of the kerf leads to pressure buildup that increases the density of the fluid in the kerf while enhancing the amount of heat transfer in the kerf.

Figure 5.49 shows the skin friction distribution along the normalized kerf thickness for four different kerf wedge angles. The kerf thickness = 0.5 mm and the averaged jet velocity = 30 m/s. The kerf thickness = 0.5 mm and the averaged jet velocity = 30 m/s. Location A (x = -0.00015, z = 0.0000094 m) is almost the kerf edge (where the kerf wall intersects the symmetry plane). The other 4 locations (B, C, D, and E) are distributed along the kerf wall and are the same locations for which the Nusselt number distribution is shown above (see Figure 5.1). The skin friction increases at the inlet of the kerf due to flow acceleration in this region. At locations A, B, and C, the skin friction reduces as the kerf depth increases. This is attributed to the shear layer developed within the vicinity of the kerf wall, which is influenced by high wall temperature leading to high thermodynamic pressure in this region. At locations D and E the skin friction gradually

increases as kerf depth increases until a second maximum skin friction is attained. The skin friction then decreases towards the kerf exit. This effect is more pronounced for the cases for which wedge angle = 4° and 6°, in which the second maximum attained is higher than the first maximum.

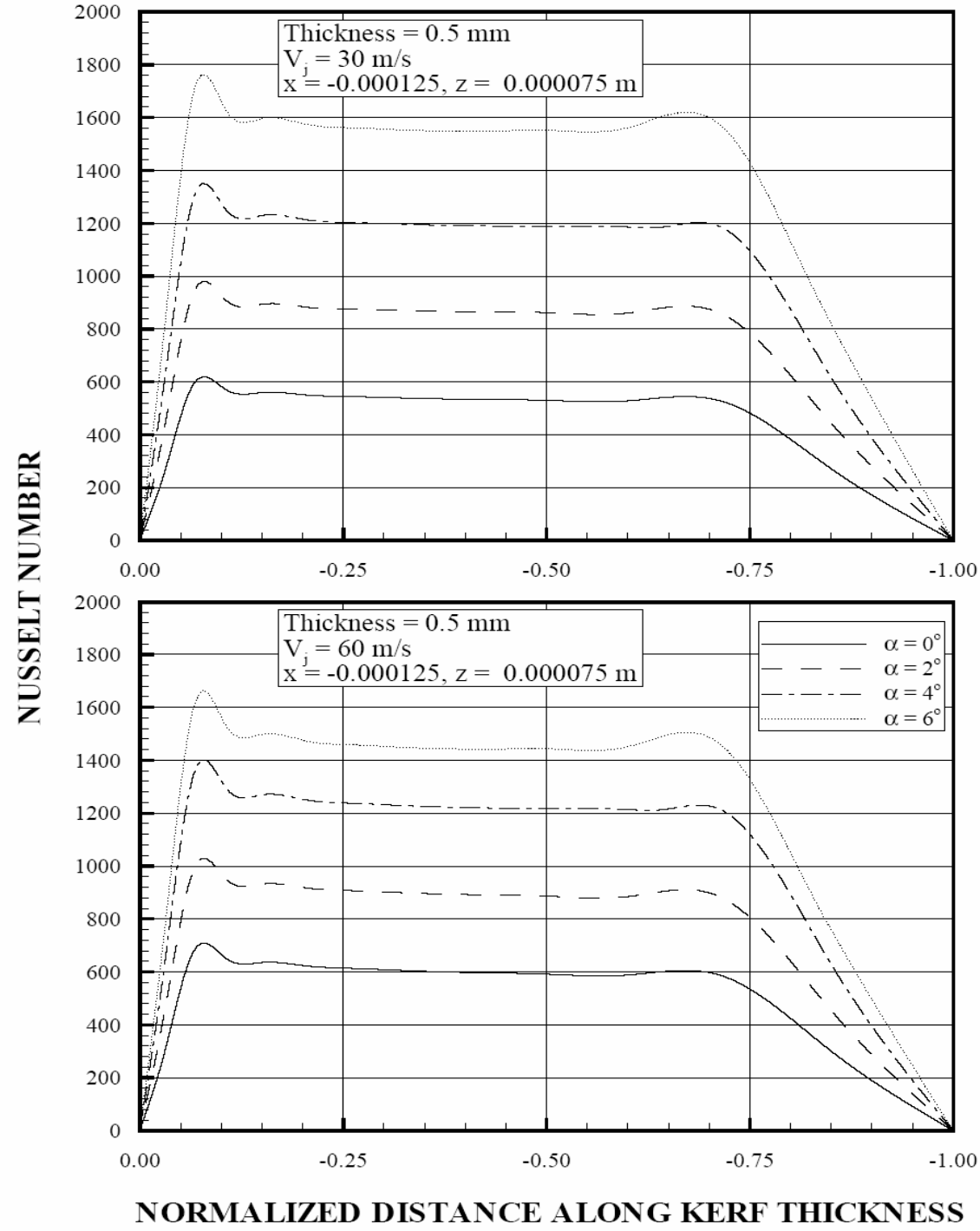

Figure 5.47 Nusselt number distribution at location B (x = -0.000125, z = 0.000075 m) along kerf wall for kerf thickness = 0.5 mm, two averaged jet velocities, and four kerf wedge angles

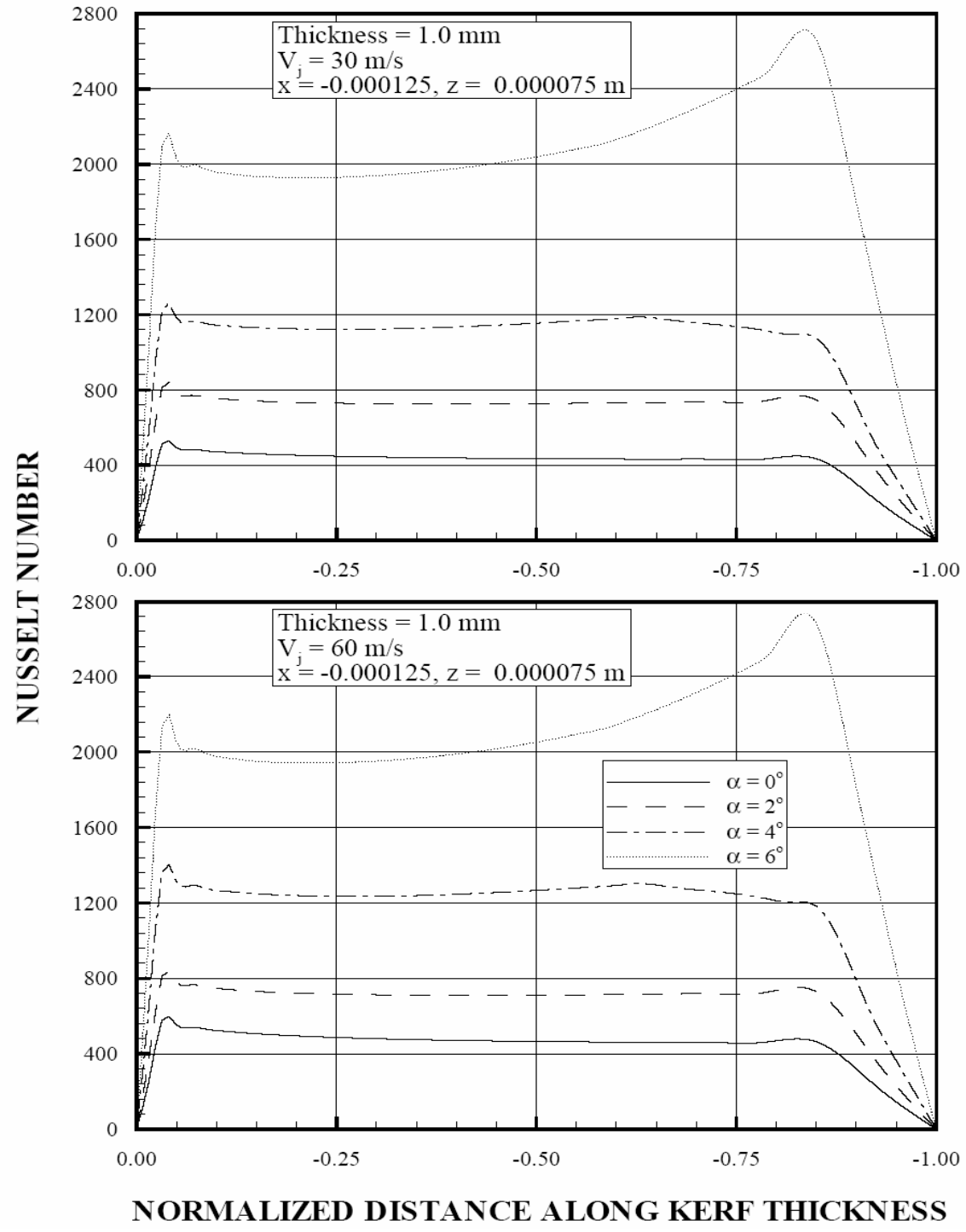

Figure 5.48 Nusselt number distribution at location B (x = -0.000125, z = 0.000075 m) along kerf wall for kerf thickness = 1.0 mm, two averaged jet velocities, and four kerf wedge angles

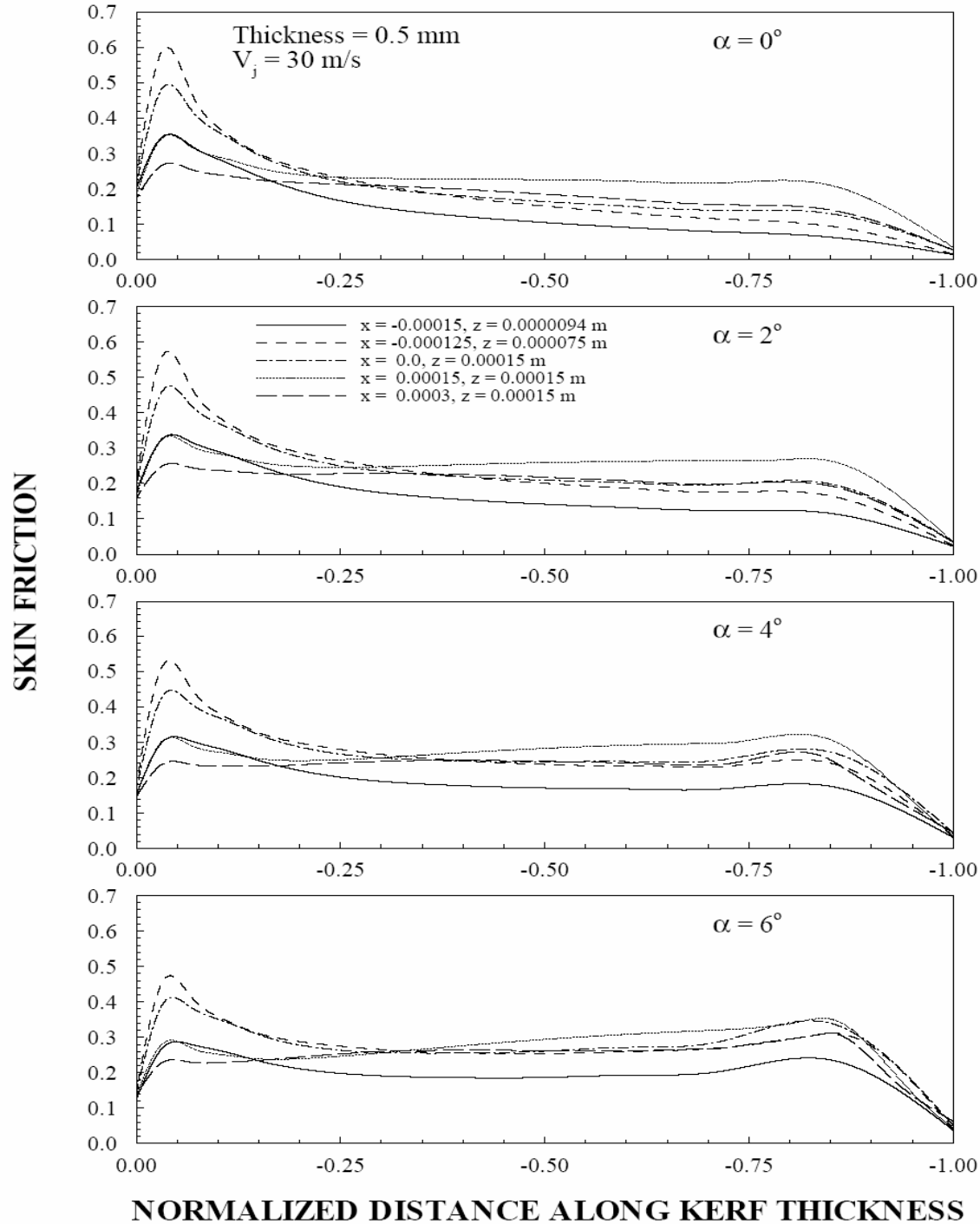

Figure 5.49 Skin Friction distribution at five locations along the kerf wall for kerf thickness = 0.5 mm, averaged jet velocity = 30 m/s, and four kerf wedge angles

Figure 5.50 shows the skin friction distribution along the normalized kerf thickness for the same geometric parameters as the previous case and averaged jet velocity = 60 m/s. The effect of increasing kerf wedge angle on skin friction distribution at locations D and E and on the second maximum skin friction attained is more pronounced than the previous case. Figure 5.51 shows skin friction distribution for kerf thickness = 1.0 mm, averaged jet velocity = 30 m/s, and four kerf wedge angles. Trends obtained are similar to previous cases except for configurations for which wedge angle = 4° and 6°. The skin friction increases sharply at the inlet of the kerf until it reaches a maximum. A decrease in skin friction is then observed after which skin friction increases gradually as the kerf depth increases until a second maximum is attained. The value of the second maximum is greater than the first maximum for locations D and E for the case for which kerf wedge angle = 4°. The value of the second maximum is greater than the first maximum for the five locations at which skin friction distribution is shown for the case for which kerf wedge angle = 6°. Figure 5.52 shows skin friction distribution along the normalized kerf thickness for kerf thickness = 1.0 mm, averaged jet velocity = 60 m/s, and four kerf wedge angles. Trends obtained are similar to the previous case for which averaged jet velocity = 30 m/s.

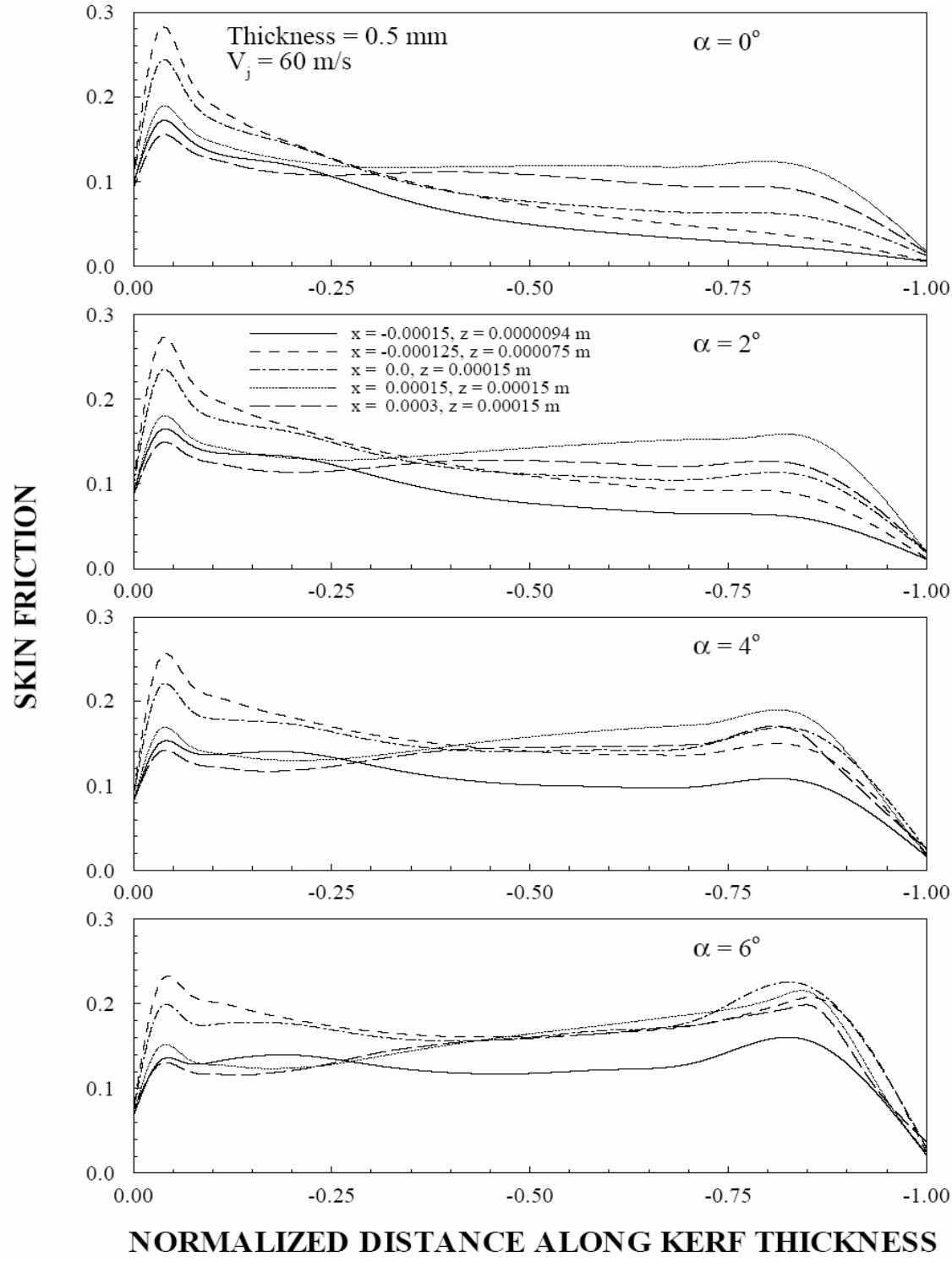

Figure 5.50 Skin Friction distribution at five locations along the kerf wall for kerf thickness = 0.5 mm, averaged jet velocity = 60 m/s, and four kerf wedge angles

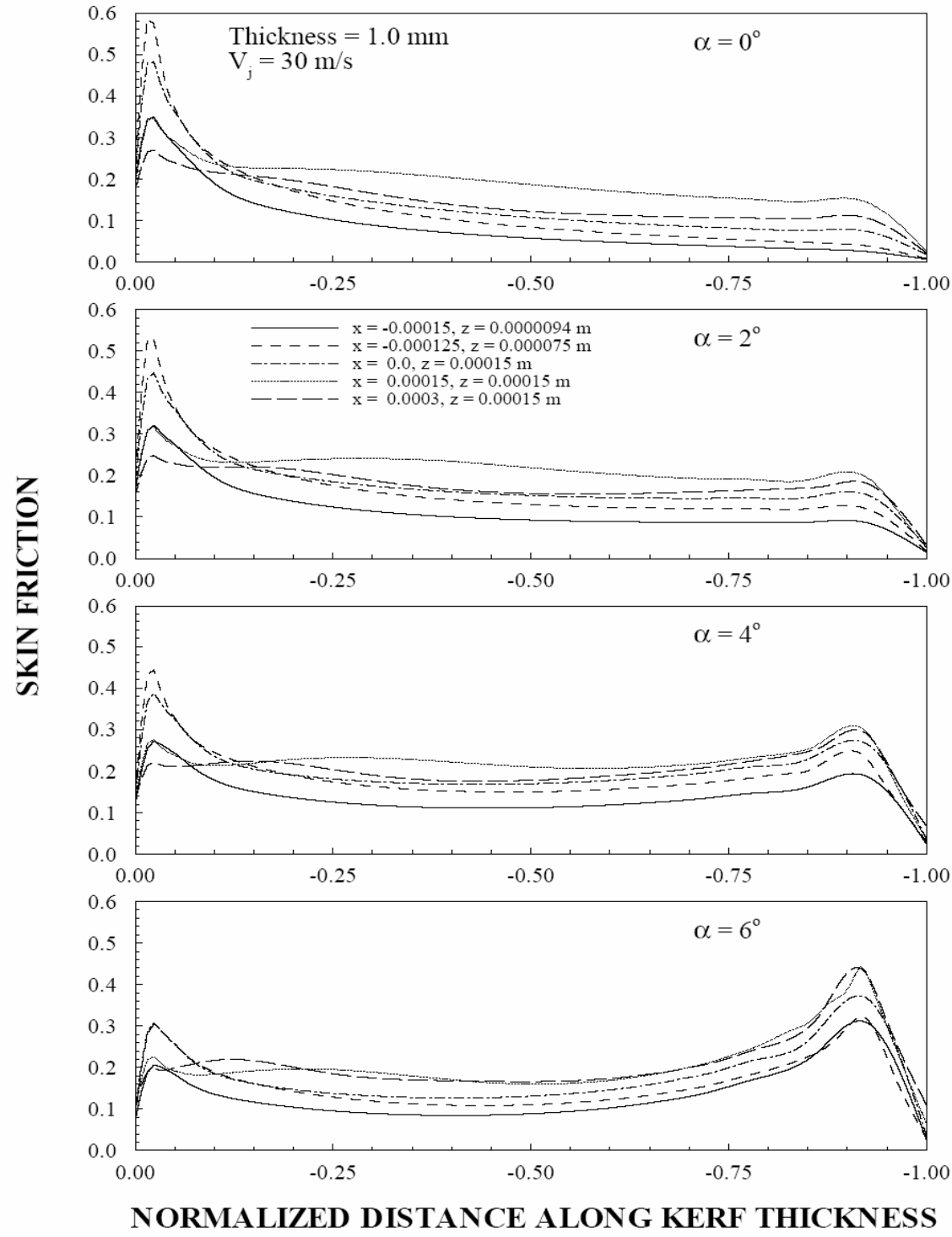

Figure 5.51 Skin Friction distribution at five locations along the kerf wall for kerf thickness = 1.0 mm, averaged jet velocity = 30 m/s, and four kerf wedge angles

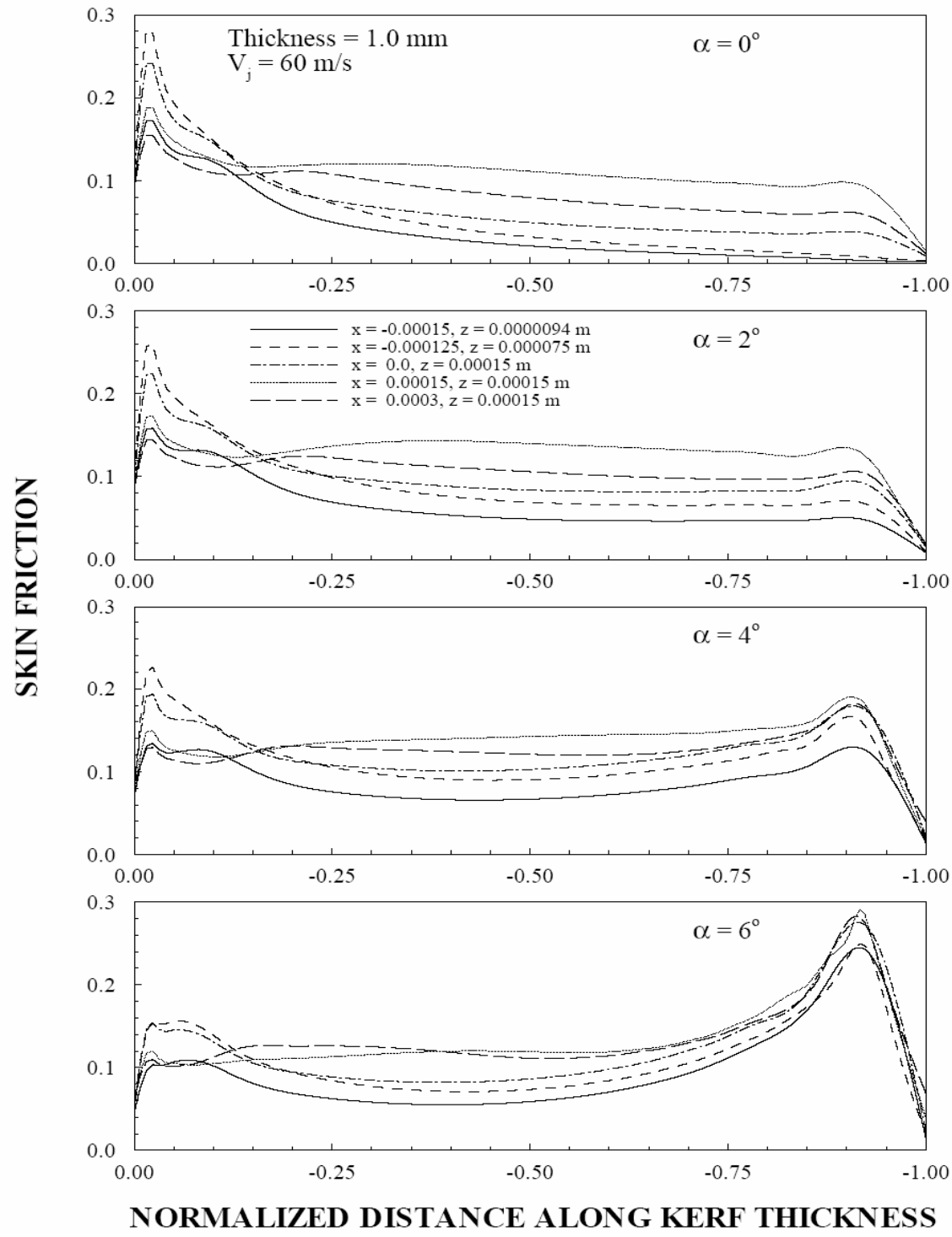

Figure 5.52 Skin Friction distribution at five locations along the kerf wall for kerf thickness = 1.0 mm, averaged jet velocity = 60 m/s, and four kerf wedge angles

Figures 5.53 and 5.54 show the skin friction distribution along the normalized kerf thickness for kerf thickness = 0.5 and 1.0 mm, two averaged jet velocities, and four kerf wedge angles. The location (x = -0.000125, z = 0.000075 m) corresponds to location of maximum Nusselt number (Figures 5.43, 5.44, 5.45, and 5.46). Skin friction increases sharply at the inlet of the kerf. In this region, skin friction decreases with increasing kerf wedge angle. A maximum skin friction is attained. Then, a sharp decrease is observed. Then, skin friction decreases monotonically as the kerf depth increases for the case for which wedge angle = 0°. This is true for both thicknesses and both averaged jet velocities. A gradual increase in skin friction is then observed in the cases for which thickness = 0.5 mm and kerf wedge angle = 4° and 6° until a second maximum skin friction is attained. Then, skin friction decreases towards the kerf exit. In this region, skin friction decreases as wedge angle decreases in the case for which kerf thickness = 0.5 mm. Additional observations can be made from the case for which kerf thickness = 1.0 mm and wedge angle = 6°. After attaining the first maximum, the skin friction decreases to attain a minimum skin friction. In this region, the skin friction is less than skin friction attained in kerfs with different wedge angles in the cases for which averaged jet velocity = 30 m/s. However, it is larger than skin friction attained in the kerf whose wedge angle = 0° and less than skin friction attained in the kerfs whose wedge angles = 2° and 4° in the cases for which averaged jet velocity = 60 m/s. After attaining the minimum skin friction, an increase is observed until a second maximum skin friction is attained. The second maximum is larger than the first maximum skin friction. Skin friction then decreases towards the kerf exit. In this region, skin friction decreases as kerf wedge angle increases.

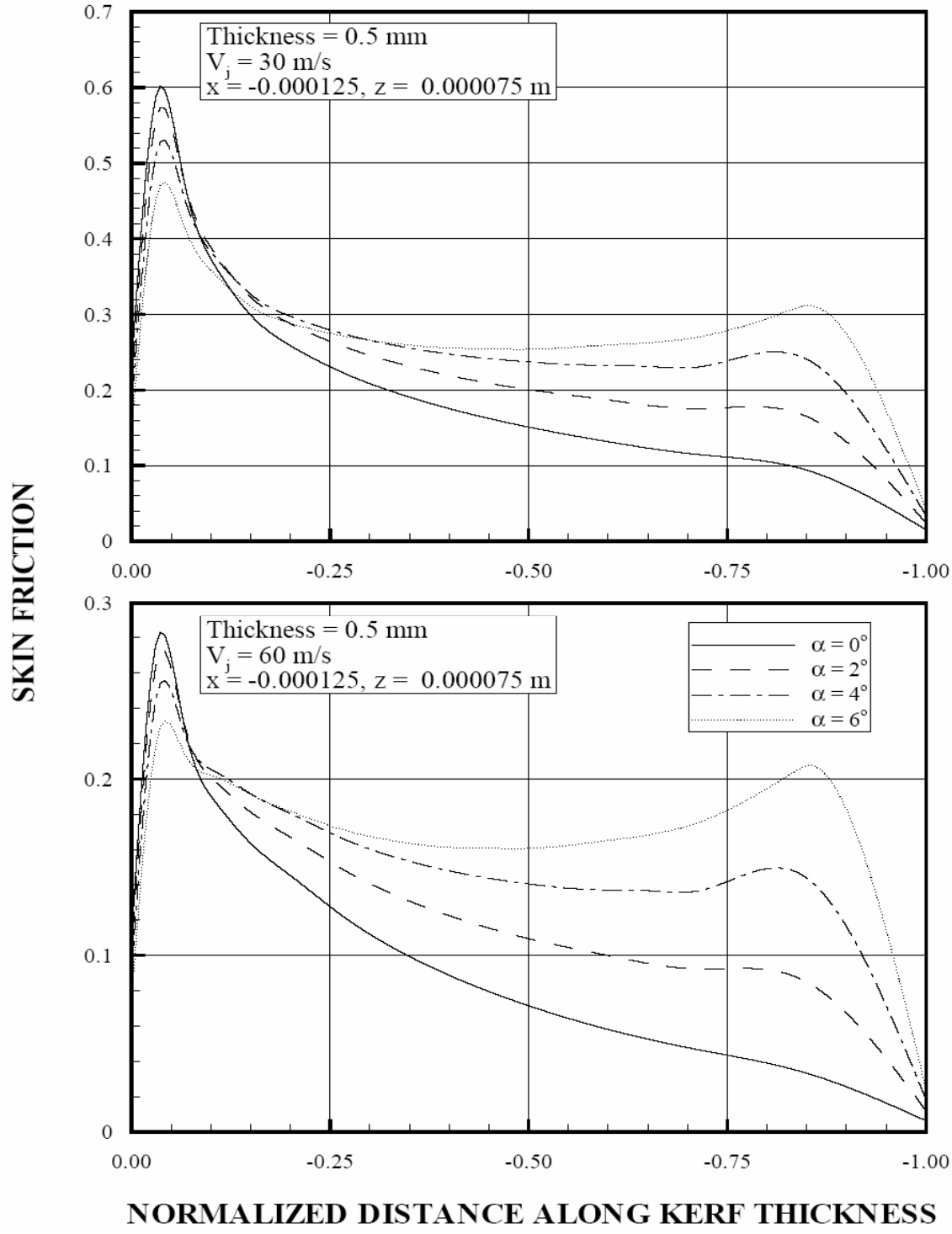

Figure 5.53 Skin friction distribution at location B (x = -0.000125, z = 0.000075 m) along kerf wall for kerf thickness = 0.5 mm, two averaged jet velocities, and four kerf wedge angles

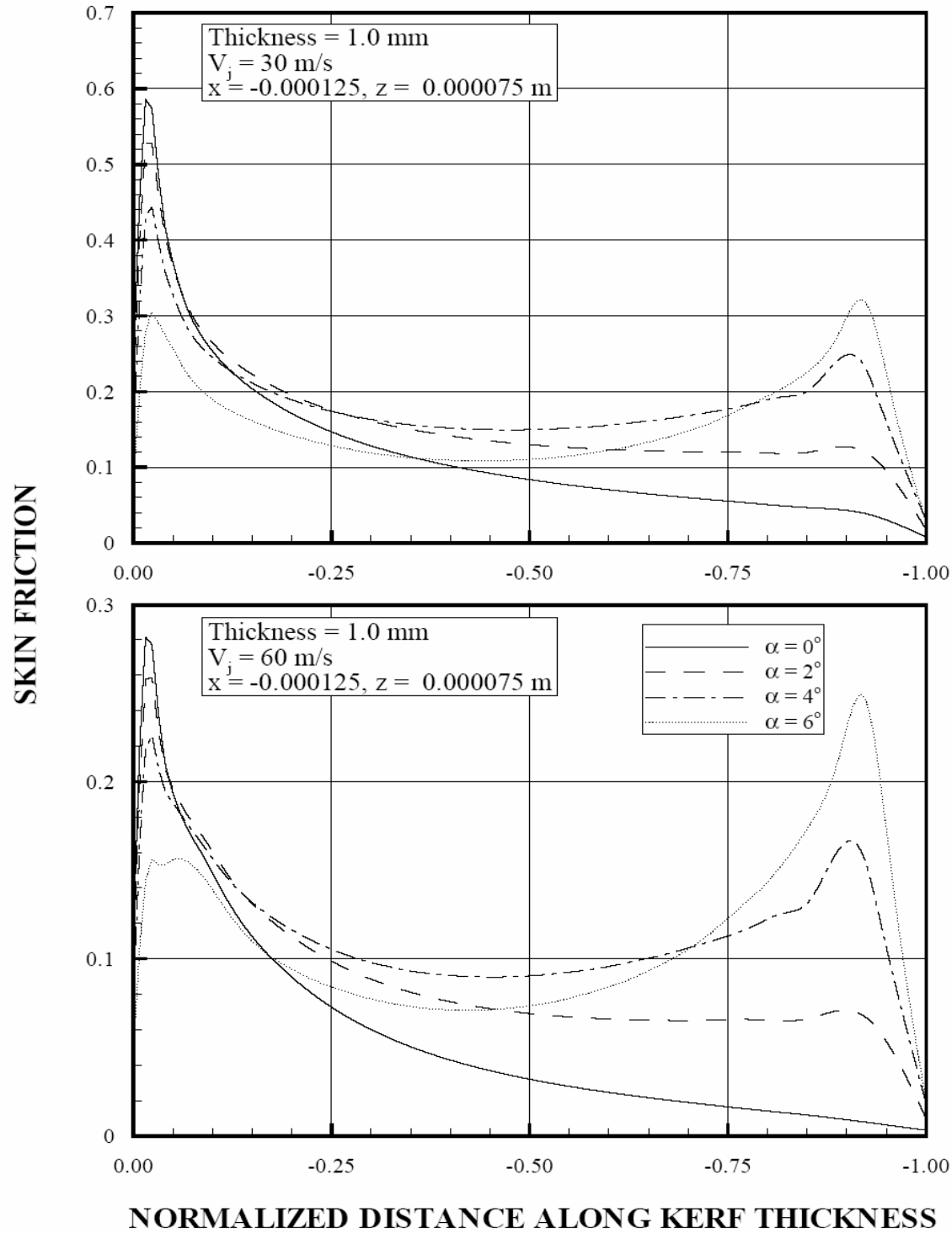

Figure 5.54 Skin friction distribution at location B (x = -0.000125, z = 0.000075 m) along kerf wall for kerf thickness = 1.0 mm, two averaged jet velocities, and four kerf wedge angles

5.3 Effect of Kerf Thickness on Heat Transfer Rates and Skin Friction

In this section, the kerf thickness is varied and the corresponding effect on heat transfer rates and skin friction is investigated. Four kerf depths (0.5, 1.0, 1.5, and 2.0 mm) and two kerf wedge angles (0° and 4°) are considered. Because of geometric constraints the maximum wedge angle that can be modeled in the case for which kerf thickness = 2.0 mm is 2°. This is the reason why results pertaining to thickness = 2.0 mm can not be shown in some of the figures that will follow. Results will be shown for two averaged jet velocities at nozzle exit: 30 m/s and 60 m/s.

Figures 5.55 and 5.56 show normalized velocity contours in the symmetry plane for kerf thickness = 0.5, 1.0, 1.5, and 2.0 mm, averaged jet velocity = 30 m/s, and kerf wedge angle = 0°. The jet exits the nozzle and exchanges momentum with the ambient forming a free boundary or a shear layer as it approaches the kerf top surface. No significant effect of the kerf thickness on the flow field preceding impingement is observed. After impingement onto the kerf occurs, the flow undergoes radial acceleration in the region close to the kerf side wall. Consequently, radial expansion of the flow is observed in the kerf. A slight modification of the flow field in the kerf is observed as the kerf depth increases. Deceleration along the y-axis gets more pronounced as the kerf thickness increases, such that higher velocities at the kerf exit are associated with kerfs of smaller thickness.

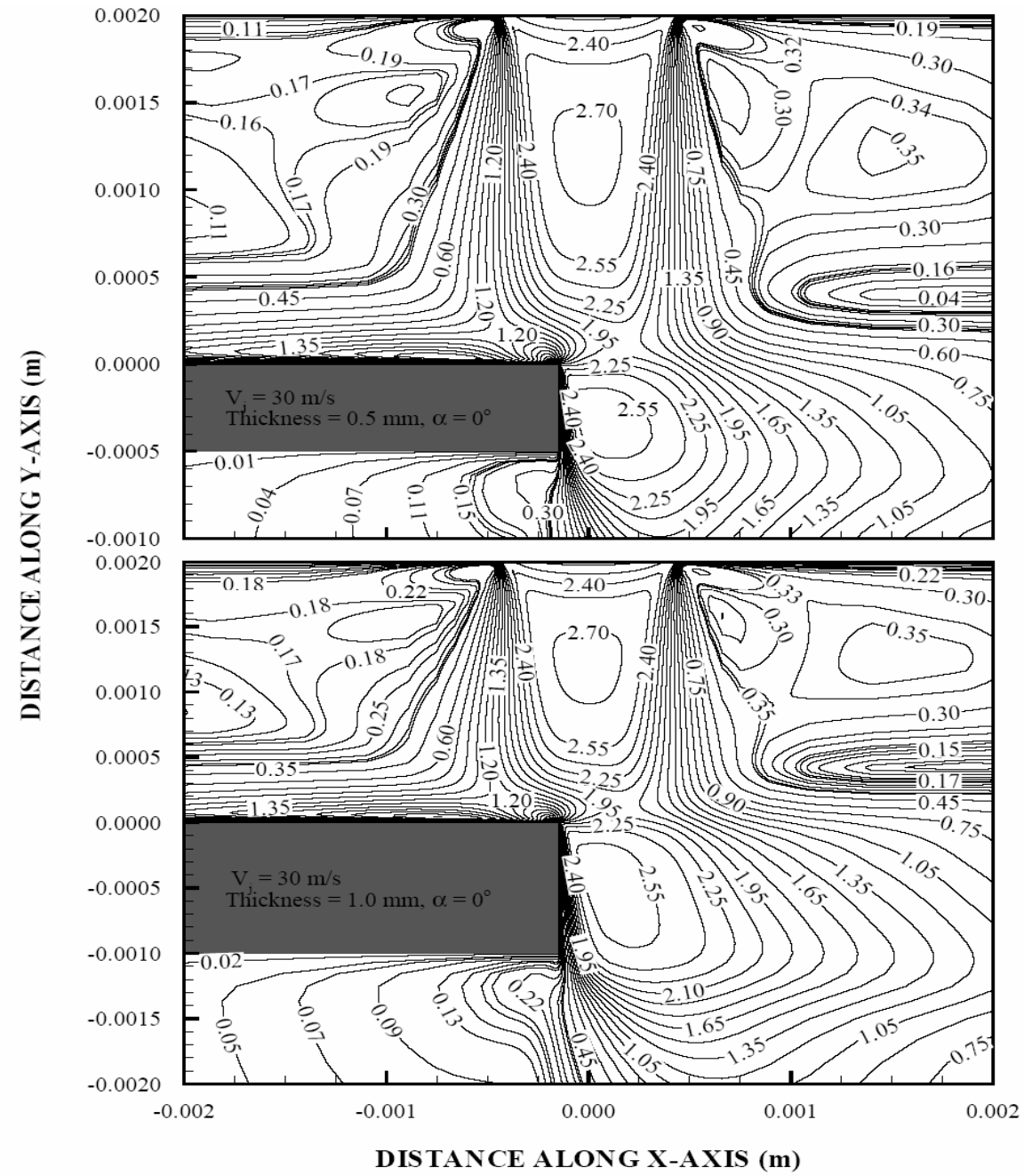

Figure 5.55 Normalized velocity magnitude (V/V_j) for jet averaged velocity of 30 m/s, kerf thickness of 0.5 and 1.0 mm, and kerf wedge angle of 0°

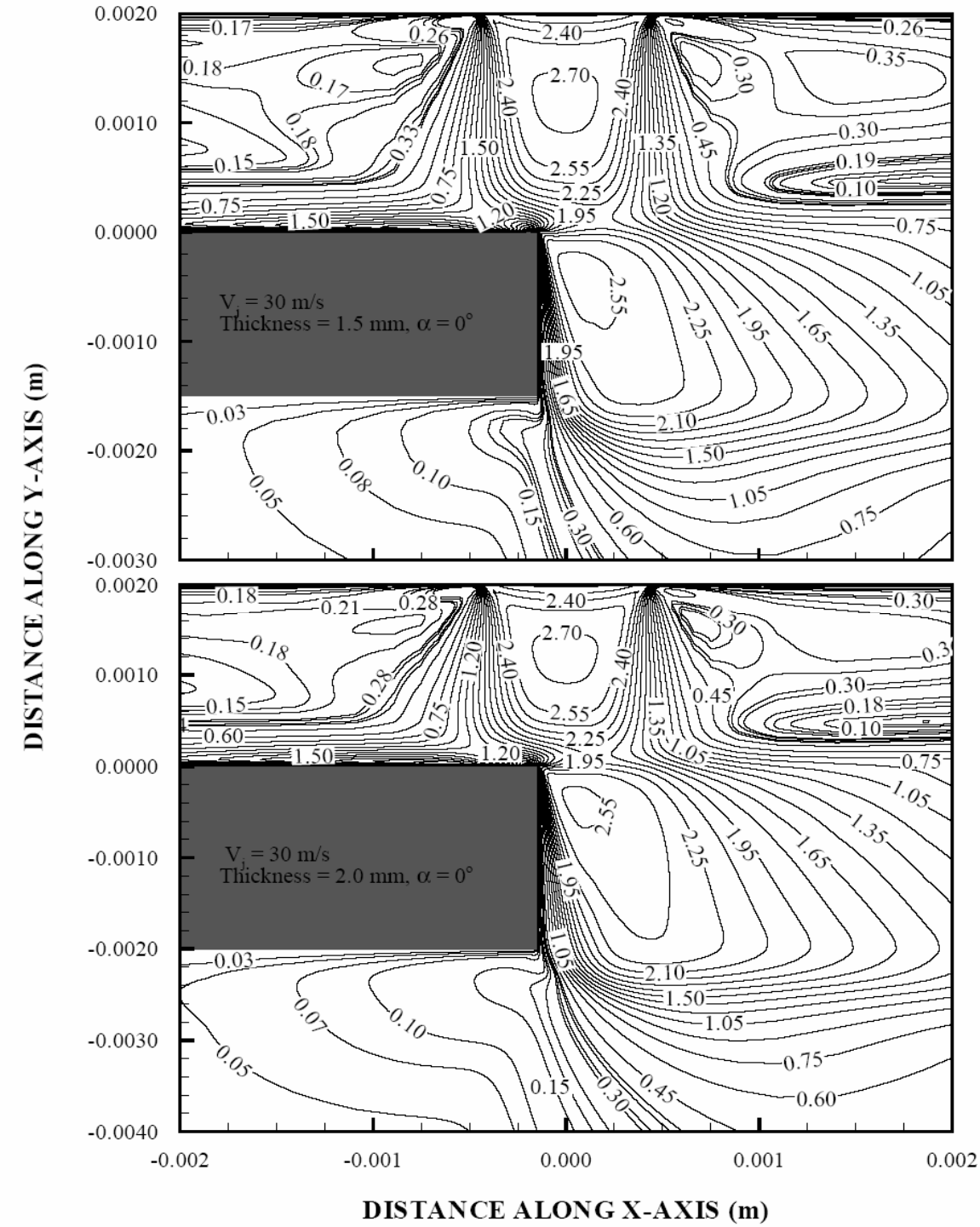

Figure 5.56 Normalized velocity magnitude (V/V_j) for jet averaged velocity of 30 m/s, kerf thickness of 1.5 and 2.0 mm, and kerf wedge angle of 0°

Figures 5.57 and 5.58 show normalized velocity contours in the symmetry plane for kerf thickness = 0.5, 1.0, 1.5, and 2.0 mm, averaged jet velocity = 60 m/s, and kerf wedge angle = 0°. Same observations as the previous case can be made. Figures 5.59 and 5.60 show normalized velocity contours in the symmetry plane for kerf thickness = 0.5, 1.0, and 1.5 mm, averaged jet velocity at nozzle exit = 30 m/s, and kerf wedge angle = 4°. In this case the effect of the kerf thickness is more pronounced. The impinging jet expands radially in the region close to the surface of the kerf. The radial expansion of the impinging jet in this region becomes more pronounced as the kerf thickness increases. Moreover, the flow field within the kerf is significantly altered as the kerf thickness increases compared to the case for which wedge angle = 0°. The radial expansion in the kerf region gets more pronounced and higher velocities are attained as the kerf wedge angle increases. Moreover, higher velocities are attained towards the kerf exit as the kerf thickness increases. Figures 5.61 and 5.62 show normalized velocity contours in the symmetry plane for same geometric parameters as the previous case and averaged jet velocity at nozzle exit = 60 m/s. Same effect of the kerf thickness on the flow filed can be noted as in the previous case for which averaged jet velocity = 30 m/s.

Figures 5.63 and 5.64 show the pressure coefficient in the symmetry plane for kerf thickness = 0.5, 1.0, 1.5, and 2.0 mm, averaged jet velocity at nozzle exit = 30 m/s, and kerf wedge angle = 0°. Figures 5.65 and 5.66 show the pressure coefficient for the same geometric parameters and averaged jet velocity = 60 m/s. The negative pressure coefficient observed in the jet outer boundaries preceding impingement indicates the reverse flow and the possible formation of circulation cell in this region. This is observed

for all kerf thicknesses with negligible effect of kerf thickness on pressure field obtained. The decrease in the flow velocity as the flow approaches the kerf is associated with pressure increase in this region. Also, the kerf thickness has negligible effect on the pressure field in this region. As the kerf thickness increases from 1.0 to 1.5 mm and then to 2.0 mm, a slight rise in pressure coefficient in the kerf is observed. This can be associated with radial expansion this region which decreases lowers the pressure. This pressure rise was noticed in the case for which averaged jet velocity = 30 m/s and not in the case for which averaged jet velocity = 60 m/s. This hints that the slight pressure rise in the kerf region is due to the increase in thermodynamic pressure associated with temperature rise. Temperature rise in the kerf region was less pronounced for higher averaged jet velocity (Section 5.1).

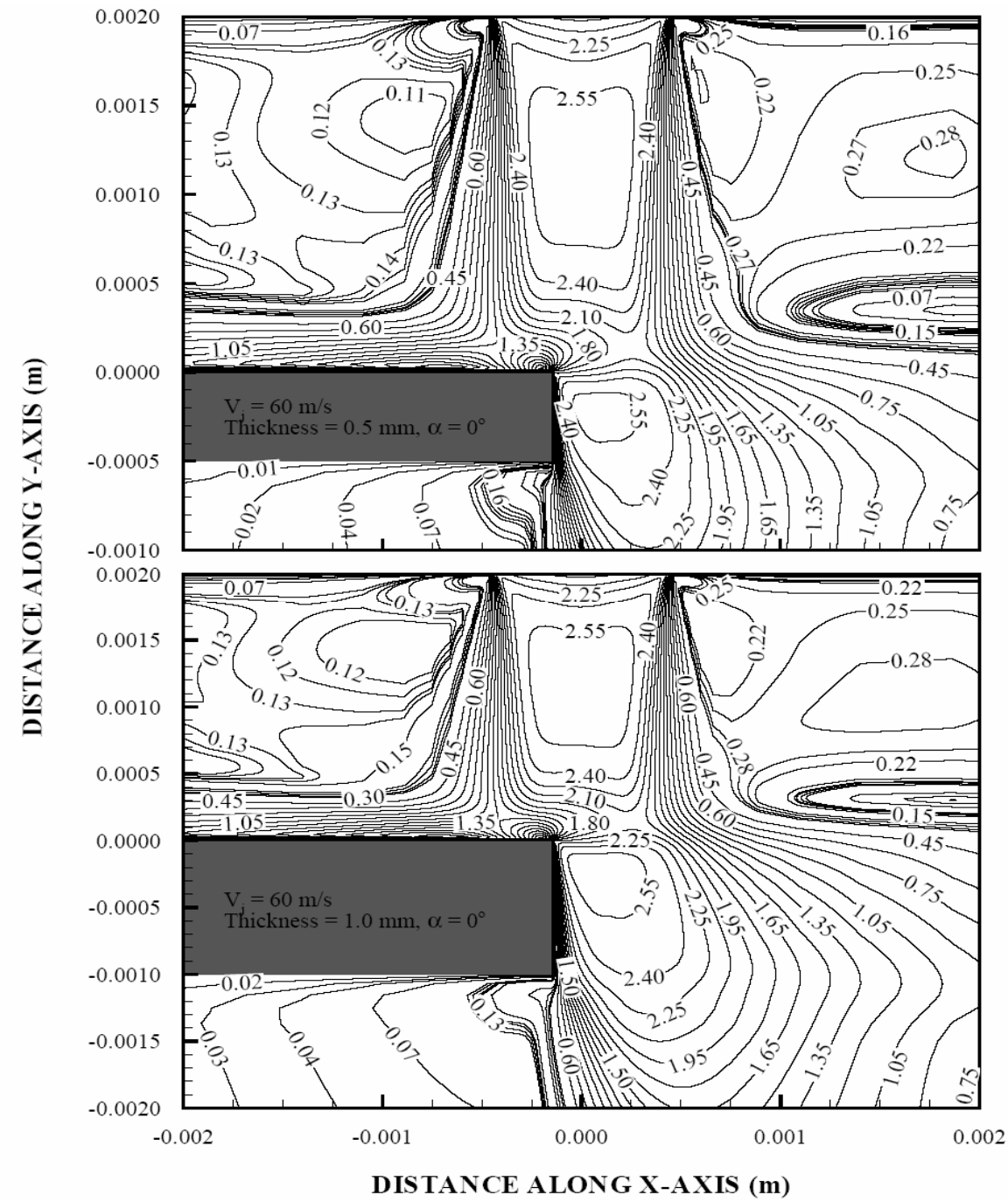

Figure 5.57 Normalized velocity magnitude (V/V_j) for jet averaged velocity of 60 m/s, kerf thickness of 0.5 and 1.0 mm, and kerf wedge angle of 0°

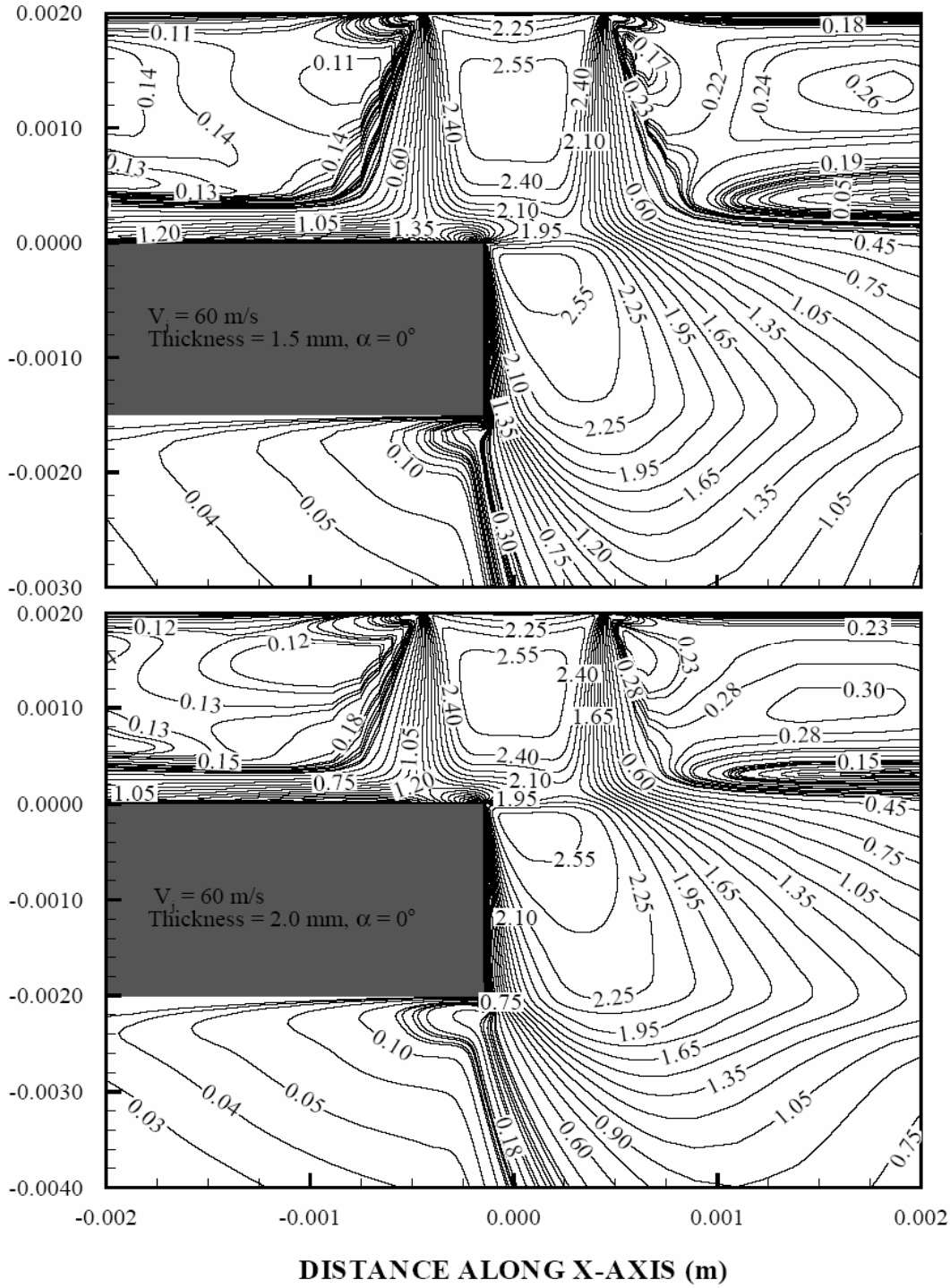

Figure 5.58 Normalized velocity magnitude (V/V_j) for jet averaged velocity of 60 m/s, kerf thickness of 1.5 and 2.0 mm, and kerf wedge angle of 0°

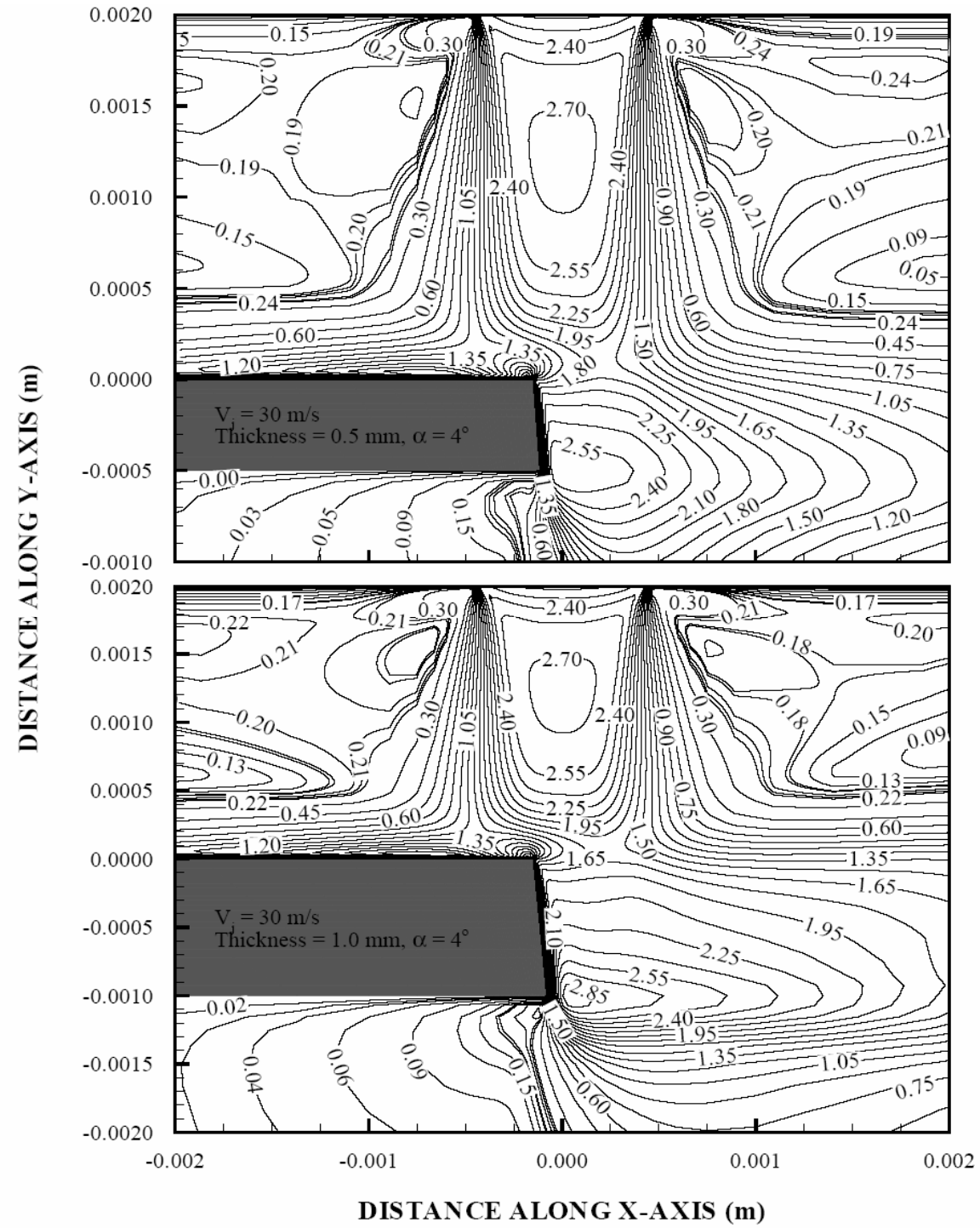

Figure 5.59 Normalized velocity magnitude (V/V_j) for jet averaged velocity of 30 m/s, kerf thickness of 0.5 and 1.0 mm, and kerf wedge angle of 4°

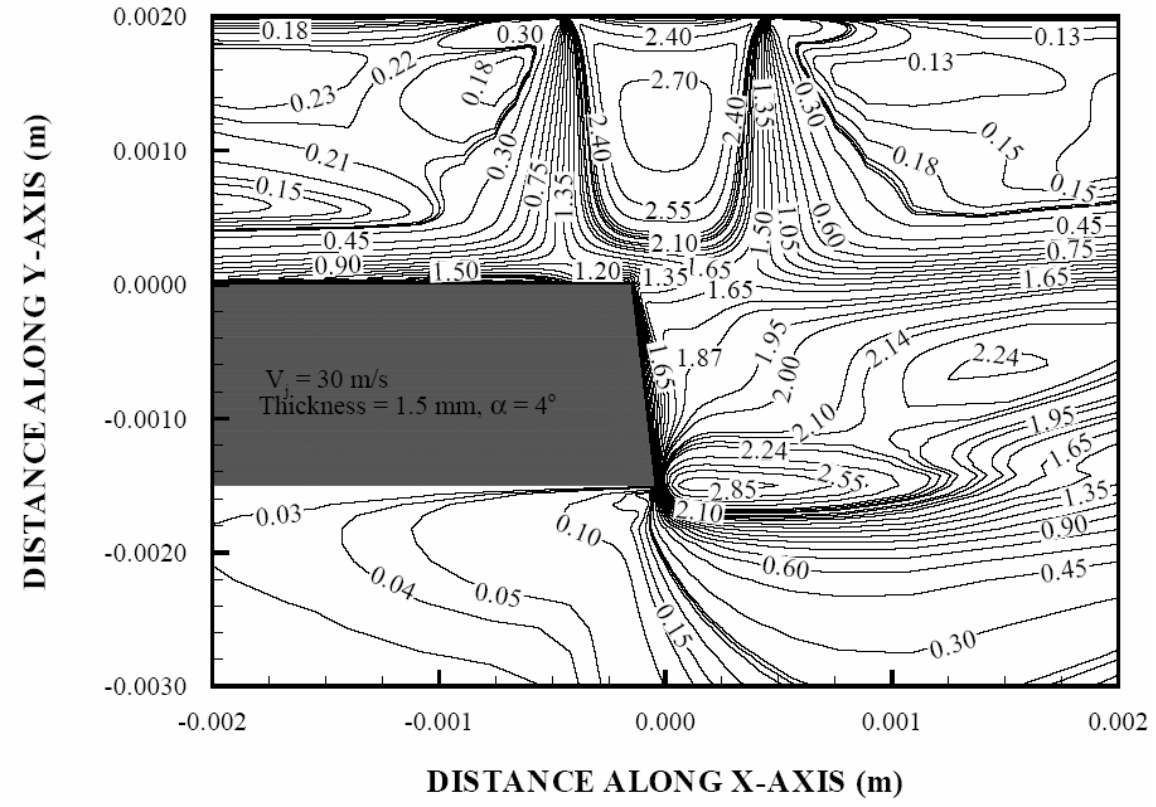

Figure 5.60 Normalized velocity magnitude (V/V_j) for jet averaged velocity of 30 m/s, kerf thickness of 1.5 mm, and kerf wedge angle of 4°

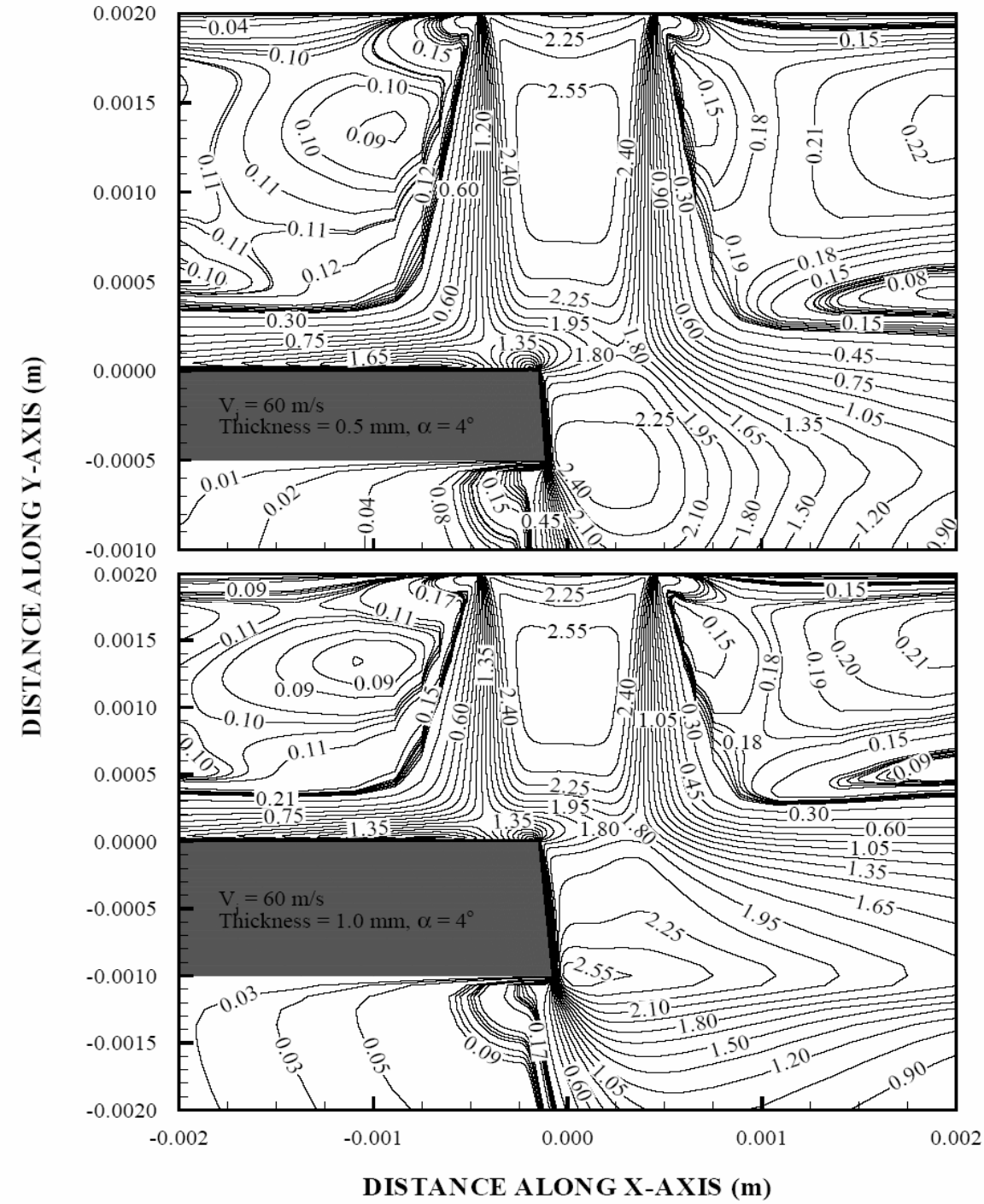

Figure 5.61 Normalized velocity magnitude (V/V_j) for jet averaged velocity of 60 m/s, kerf thickness of 0.5 and 1.0 mm, and kerf wedge angle of 4°

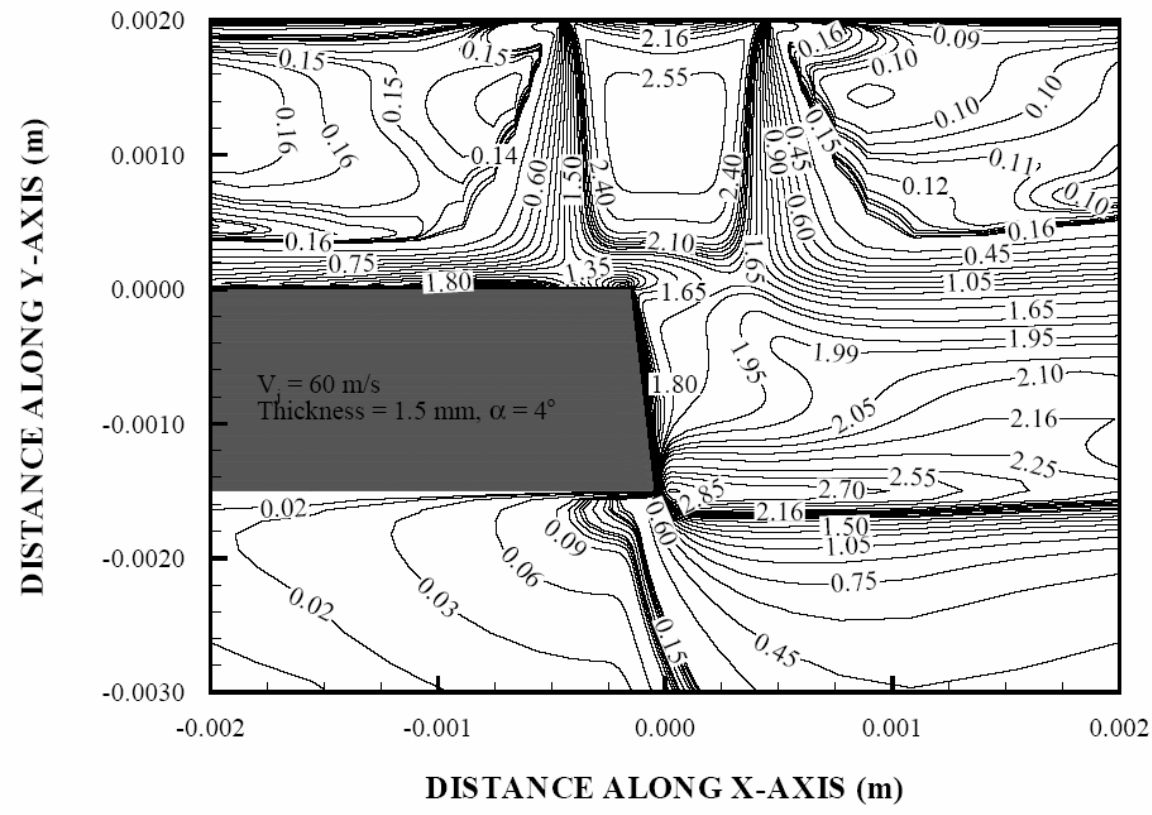

Figure 5.62 Normalized velocity magnitude (V/V_j) for jet averaged velocity of 60 m/s, kerf thickness of 1.5 mm, and kerf wedge angles of 4°

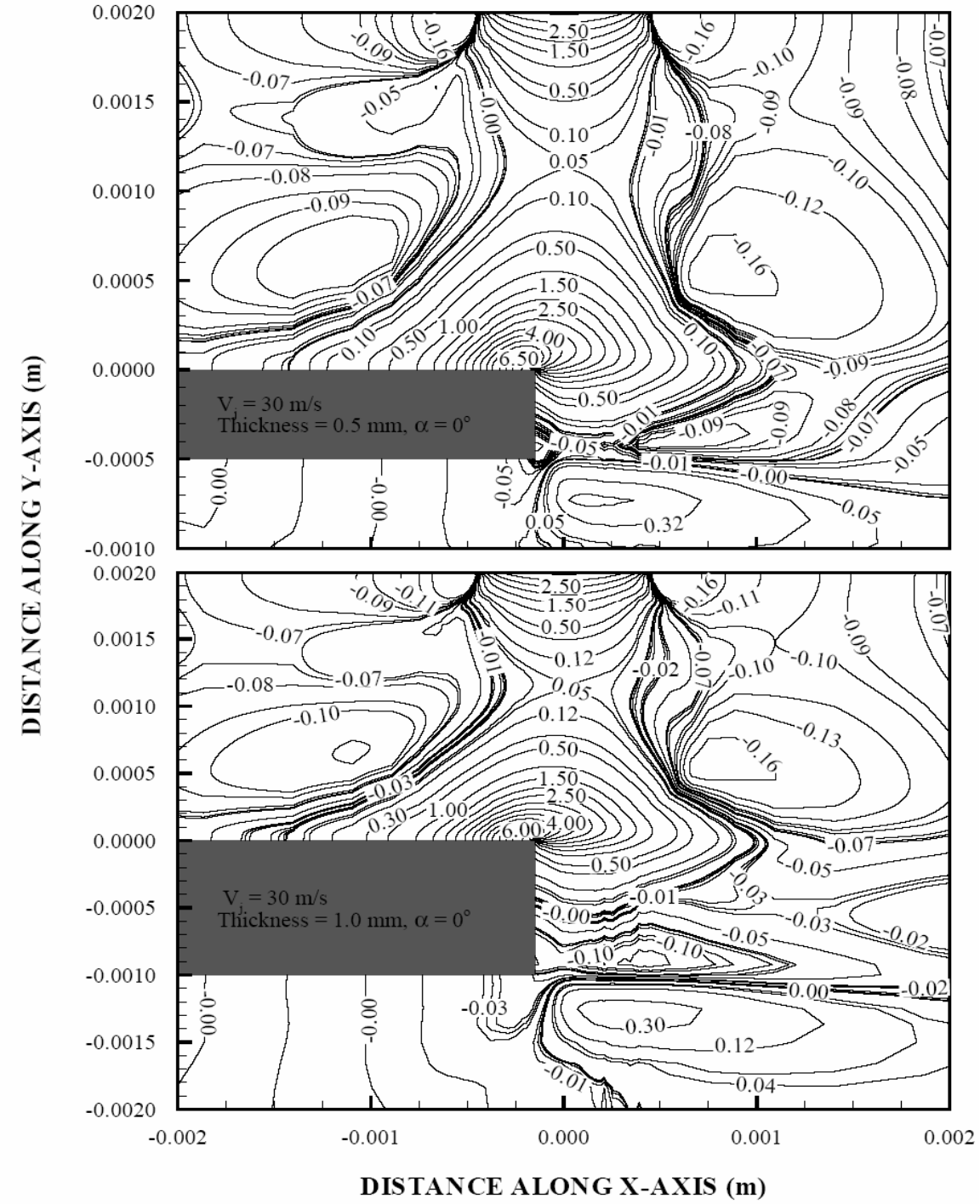

Figure 5.63 Pressure coefficient in the symmetry plane for jet averaged velocity of 30 m/s, kerf thickness of 0.5 and 1.0 mm, and kerf wedge angle of 0°

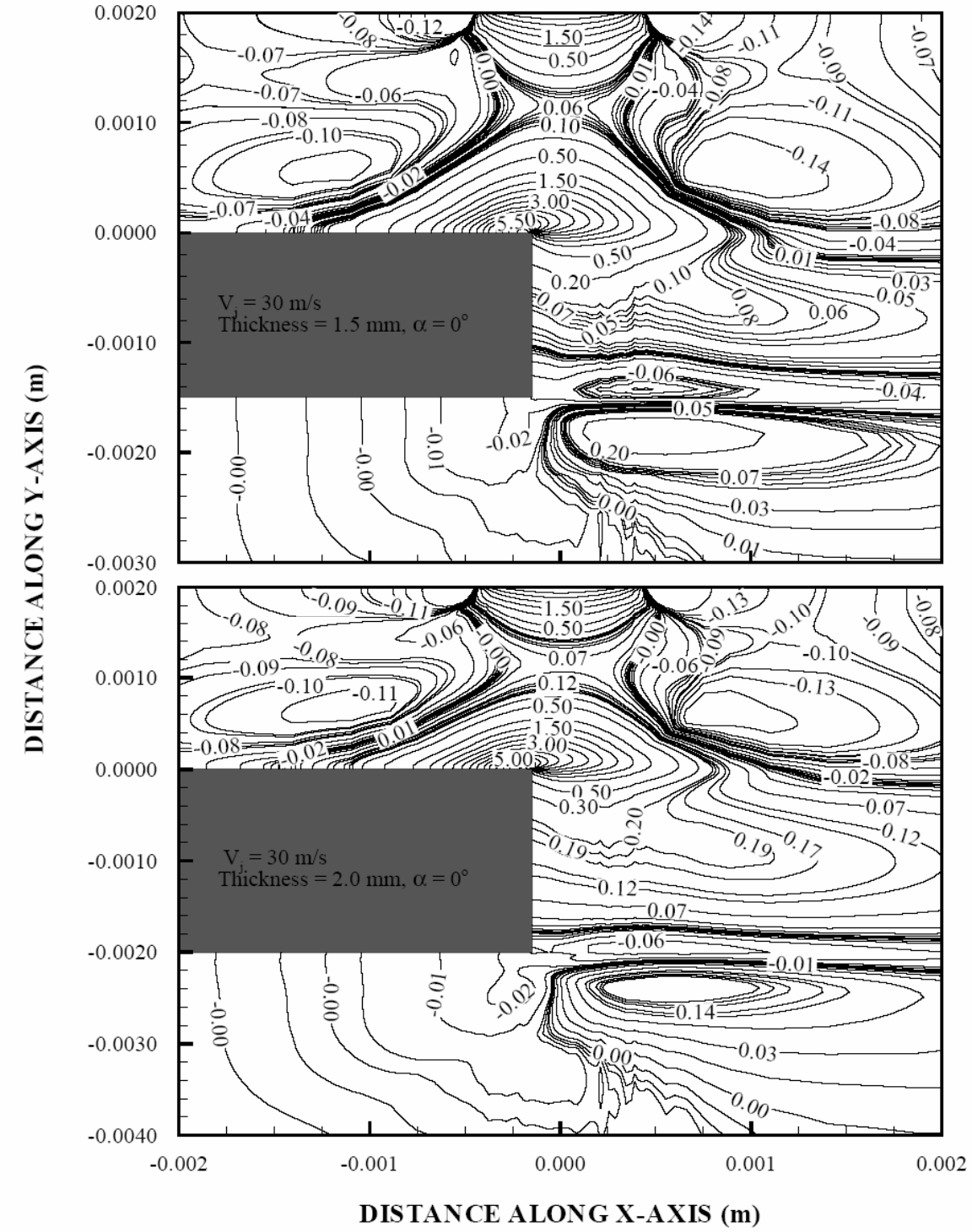

Figure 5.64 Pressure coefficient in the symmetry plane for jet averaged velocity of 30 m/s, kerf thickness of 1.5 and 2.0 mm, and kerf wedge angle of 0°

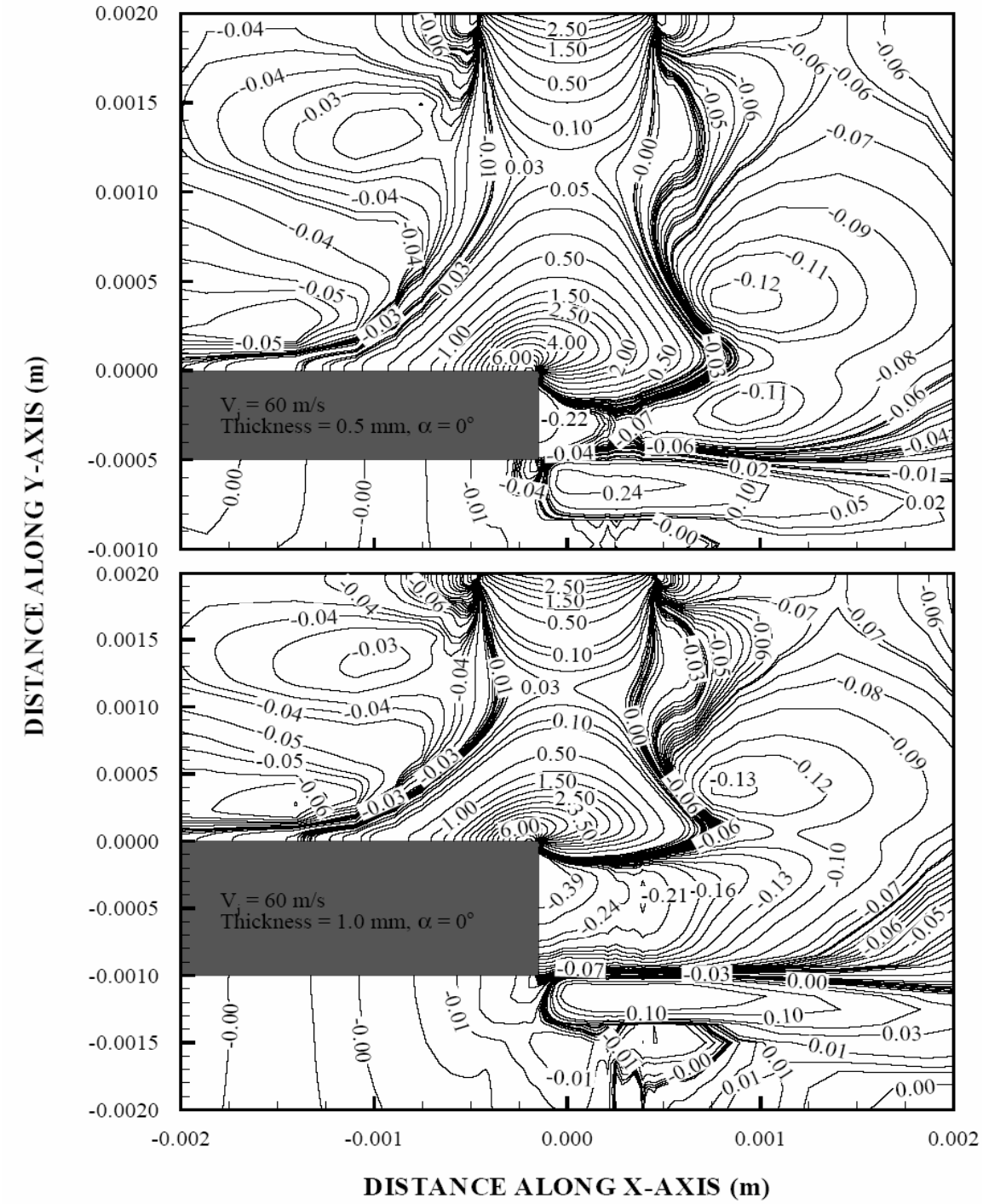

Figure 5.65 Pressure coefficient in the symmetry plane for jet averaged velocity of 60 m/s, kerf thickness of 0.5 and 1.0 mm, and kerf wedge angle of 0°

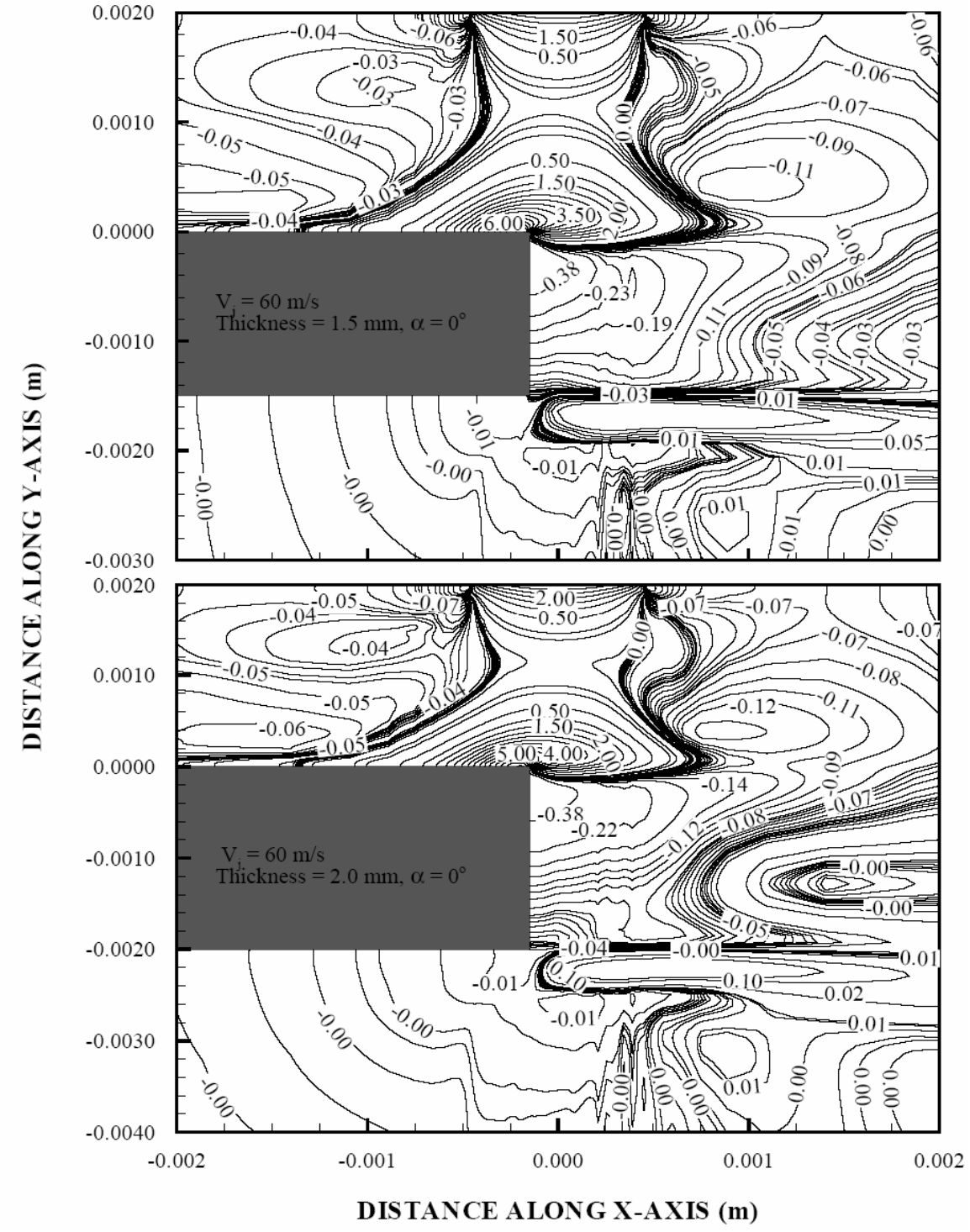

Figure 5.66 Pressure coefficient in the symmetry plane for jet averaged velocity of 60 m/s, kerf thickness of 1.5 and 2.0 mm, and kerf wedge angle of 0°

Figures 5.67 and 5.68 show the pressure coefficient in the symmetry plane for kerf thickness = 0.5, 1.0, and 1.5 mm, averaged jet velocity at nozzle exit = 30 m/s, and kerf wedge angle = 4°. Figures 5.69 and 5.70 show the pressure coefficient in the symmetry plane for kerf thickness = 0.5, 1.0, and 1.5 mm, averaged jet velocity at nozzle exit = 60 m/s, and kerf wedge angle = 4°. The effect of kerf thickness on pressure field in the kerf is more significant in this case than the case for which kerf wedge angle = 4°. As thickness increases, pressure coefficient in the kerf attains higher values. This pressure rise can be associated with increase in thermodynamic pressure resulting from higher temperatures attained as thickness increases. This can also be attributed to the pressure increase in the kerf region due to the increased blockage effect resulting from larger depth at larger wedge angle.

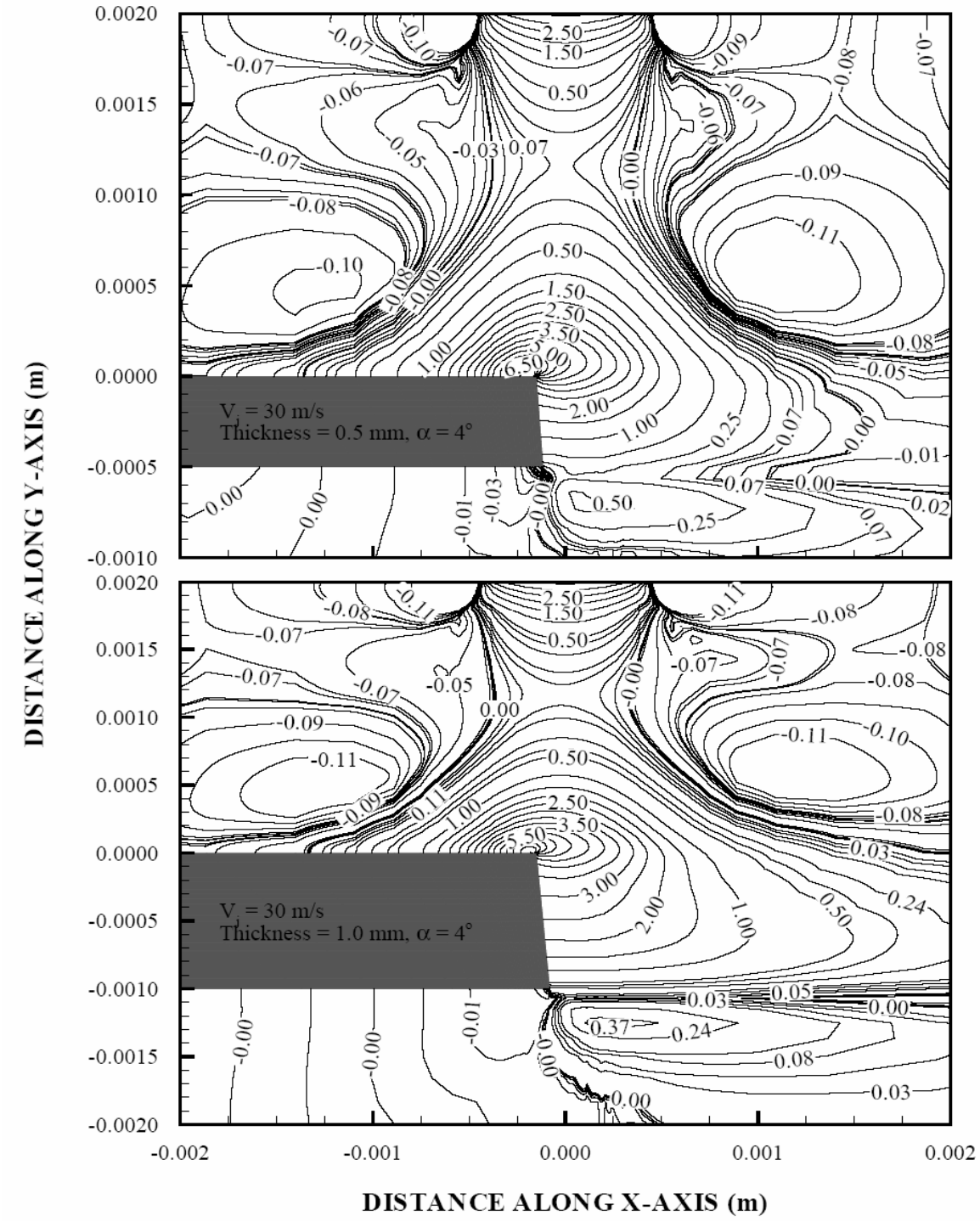

Figure 5.67 Pressure coefficient in the symmetry plane for jet averaged velocity of 30 m/s, kerf thickness of 0.5 and 1.0 mm, and kerf wedge angle of 4°

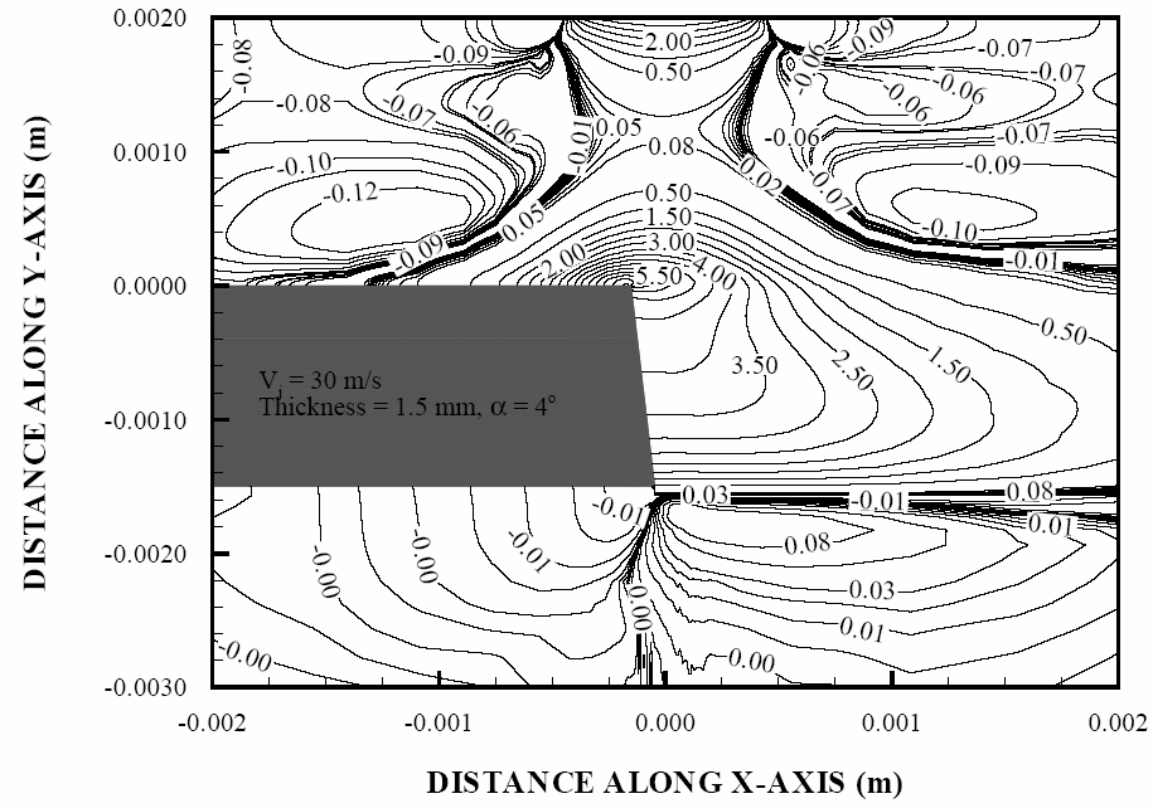

Figure 5.68 Pressure coefficient in the symmetry plane for jet averaged velocity of 30 m/s, kerf thickness of 1.5 mm, and kerf wedge angle of 4°

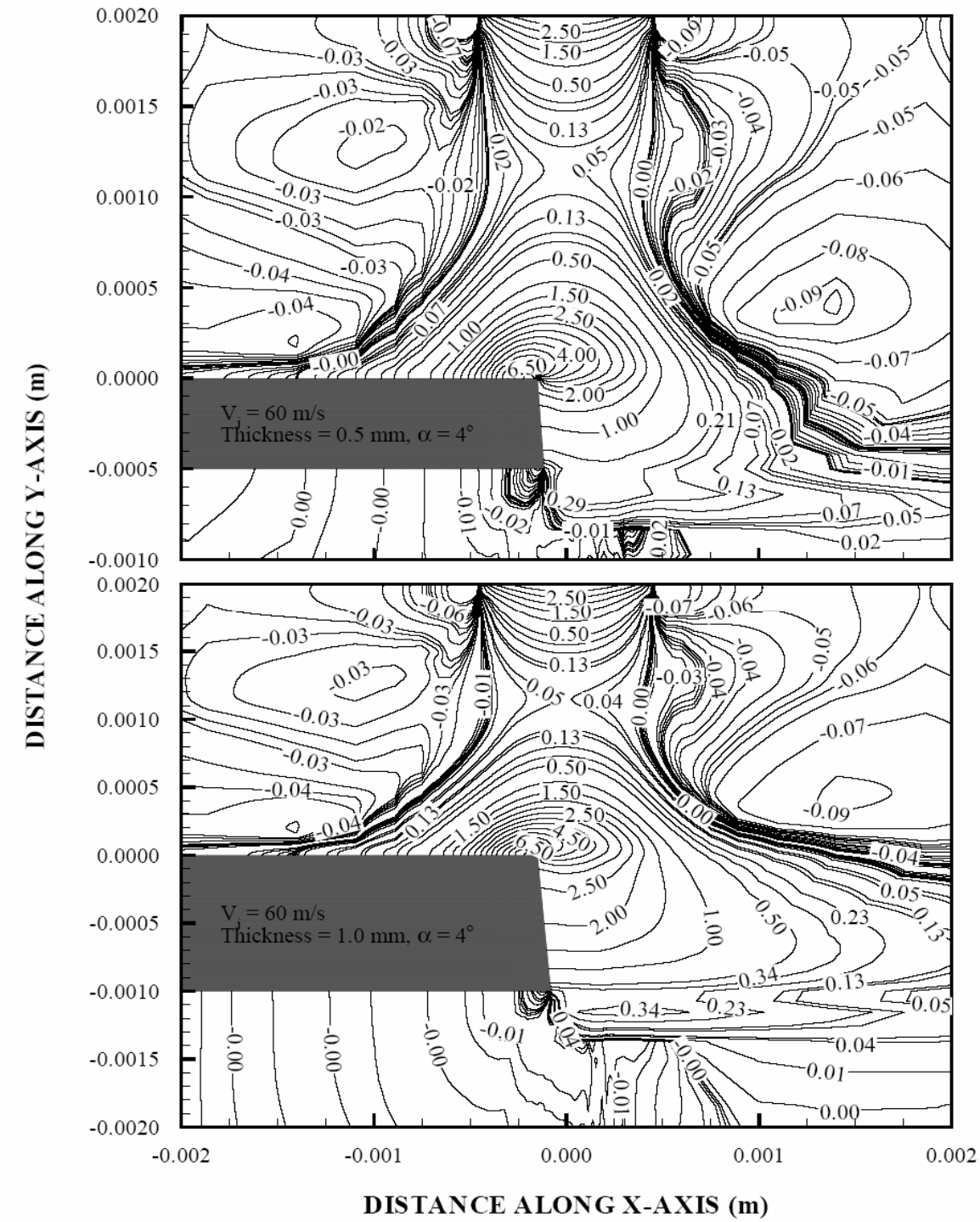

Figure 5.69 Pressure coefficient in the symmetry plane for jet averaged velocity of 60 m/s, kerf thickness of 0.5 and 1.0 mm, and kerf wedge angle of 4°

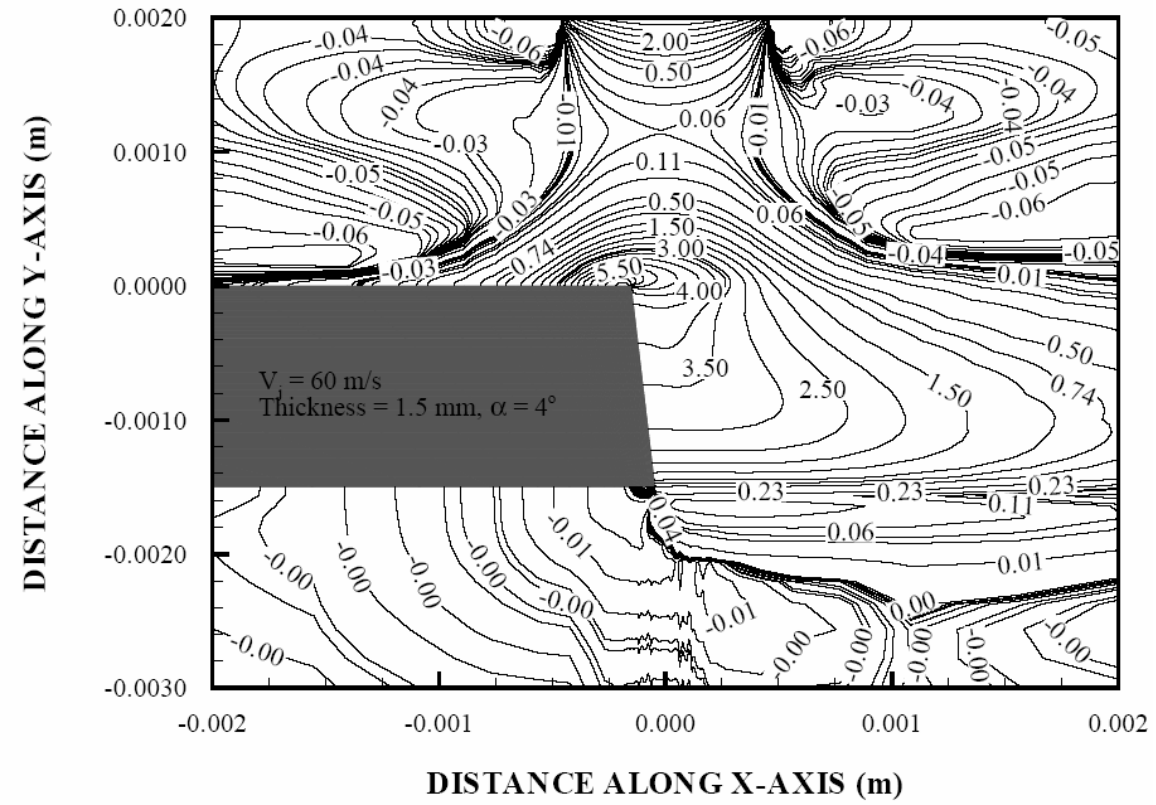

Figure 5.70 Pressure coefficient in the symmetry plane for jet averaged velocity of 60 m/s, kerf thickness of 1.5 mm, and kerf wedge angle of 4°

Figures 5.71 and 5.72 show normalized temperature contours in the symmetry plane for kerf thickness = 0.5, 1.0, 1.5, and 2.0 mm, averaged jet velocities at nozzle exit = 30 m/s, and kerf wedge angle = 0°. Figures 5.73 and 5.74 show normalized temperature contours in the symmetry plane for kerf thickness = 0.5, 1.0, 1.5, and 2.0 mm, averaged jet velocities at nozzle exit = 60 m/s, and kerf wedge angle = 0°.It should be reemphasized that the kerf wall temperature is maintained at 1500 K while jet temperature is at 300 K. This simulates the actual laser cutting situation. The free jet temperature is almost equal to the jet temperature at nozzle exit. Fluid temperature increases in the kerf, with remarkable increase close to the kerf wall. Temperature first decreases and later increases in the fluid at positive x-axis locations away from the jet axis. The decrease in temperature is due to the radial expansion, while the increase in temperature is due to the flow deceleration in this region, which enhances heat transfer from the kerf wall to the fluid. The temperature increase in the fluid at positive x-axis locations away from the jet axis is slightly more significant for kerfs with larger thickness. This was observed in the case for which averaged jet velocity = 30 m/s and not in the case for which averaged jet velocity = 60 m/s. Figures 5.75 and 5.76 show normalized temperature contours in the symmetry plane for kerf thickness = 0.5, 1.0, and 1.5 mm, averaged jet velocities at nozzle exit = 30 m/s, and kerf wedge angle = 4°. Figures 5.77 and 5.78 show normalized temperature contours in the symmetry plane for kerf thickness = 0.5, 1.0, and 1.5 mm, averaged jet velocities at nozzle exit = 60 m/s, and kerf wedge angle = 4°. As the kerf thickness increases, the increase in temperature at locations away from the jet axis is more remarkable. This is especially true as the kerf thickness is increased from 1.0 to 1.5

mm in the case for which averaged jet = 30 m/s. Moreover, the jet temperature is significantly higher in the bottom region of the kerf in the case for which thickness = 1.5 mm and averaged jet velocity = 30 m/s. A relatively less increase in the temperature field is observed as kerf thickness changes in the case for which averaged jet velocity = 60 m/s.

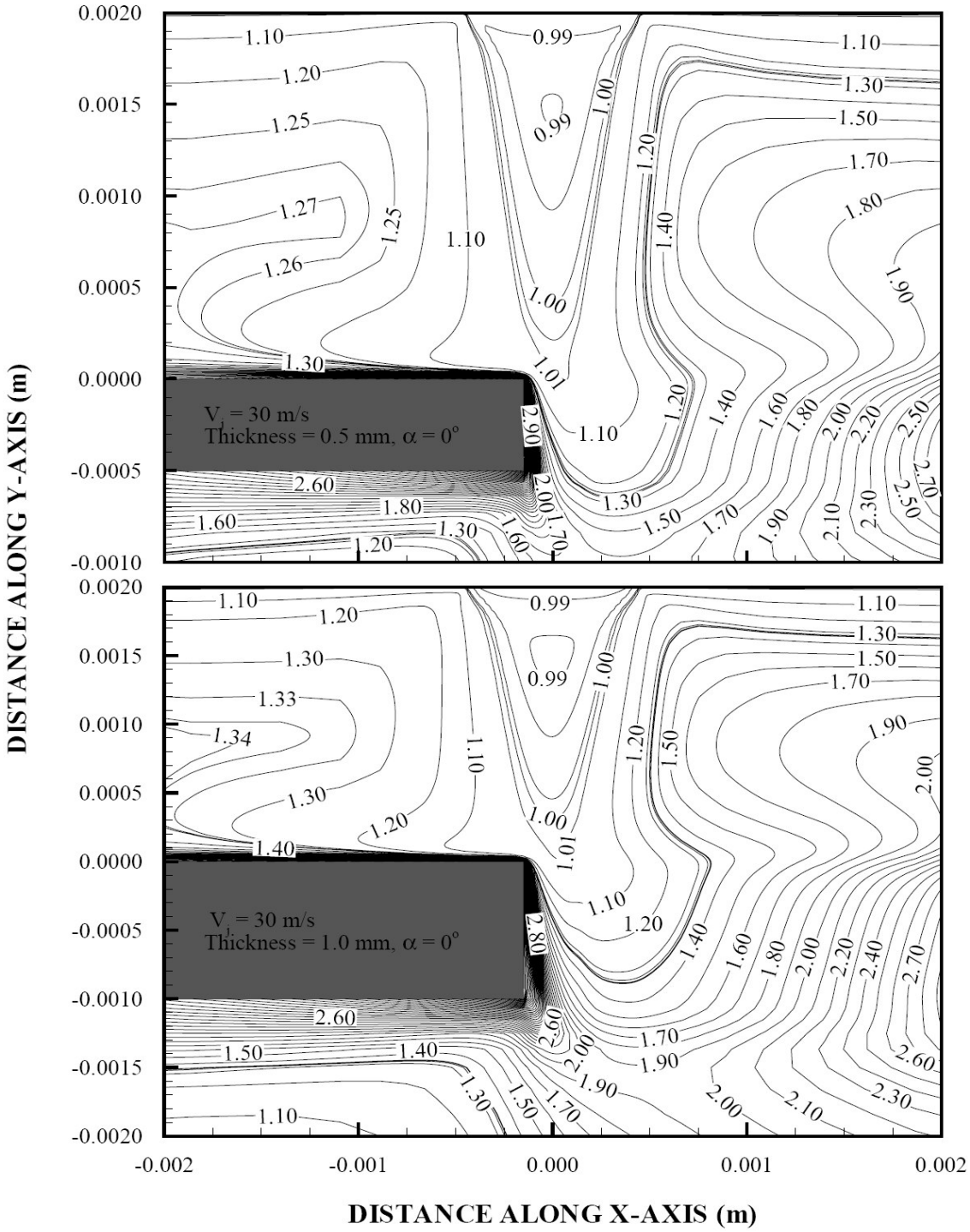

Figure 5.71 Normalized temperature (T/T_j) in the symmetry plane for jet averaged velocity of 30 m/s, kerf thickness of 0.5 and 1.0 mm, and kerf wedge angle of 0°

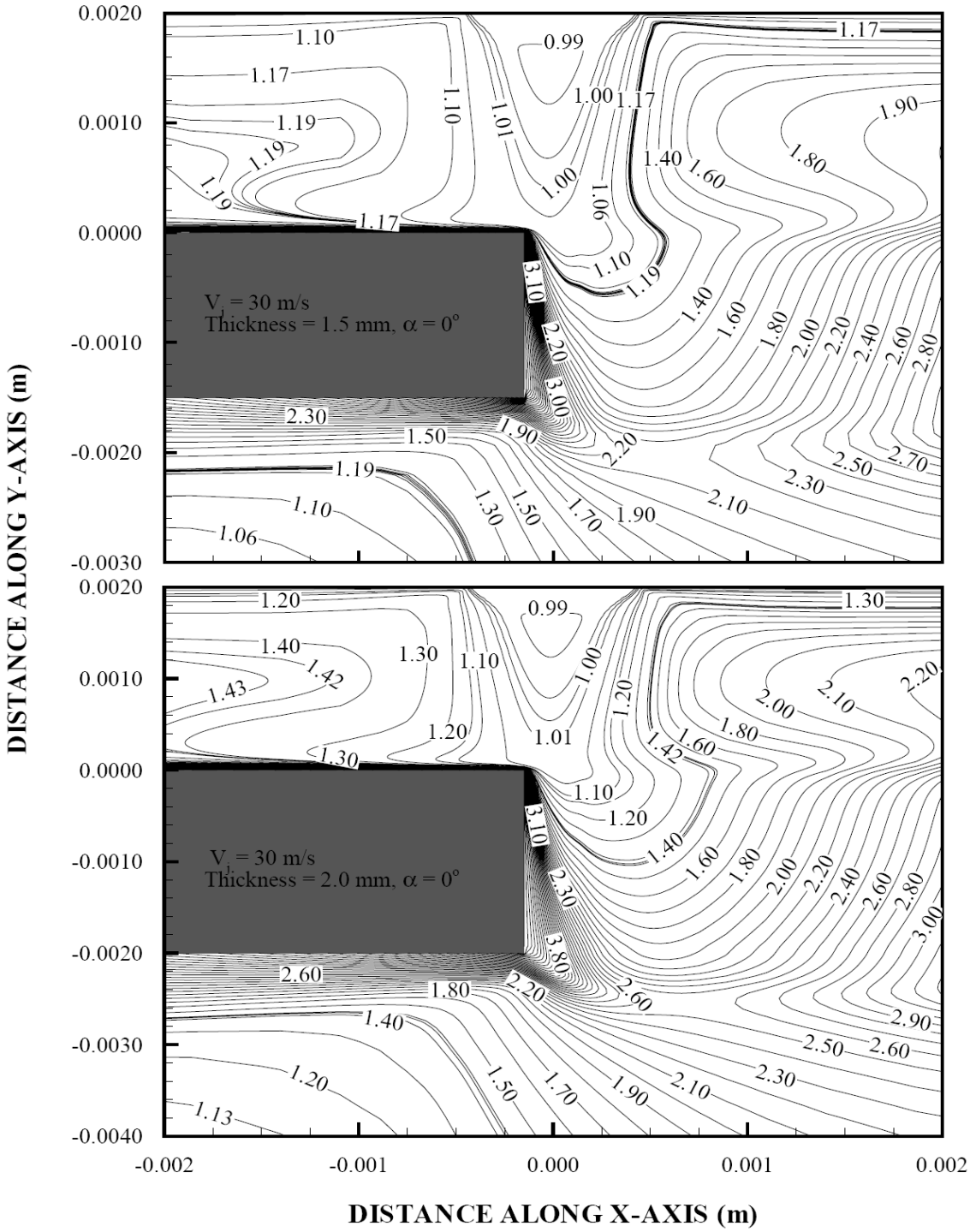

Figure 5.72 Normalized temperature (T/T_j) in the symmetry plane for jet averaged velocity of 30 m/s, kerf thickness of 1.5 and 2.0 mm, and kerf wedge angle of 0°

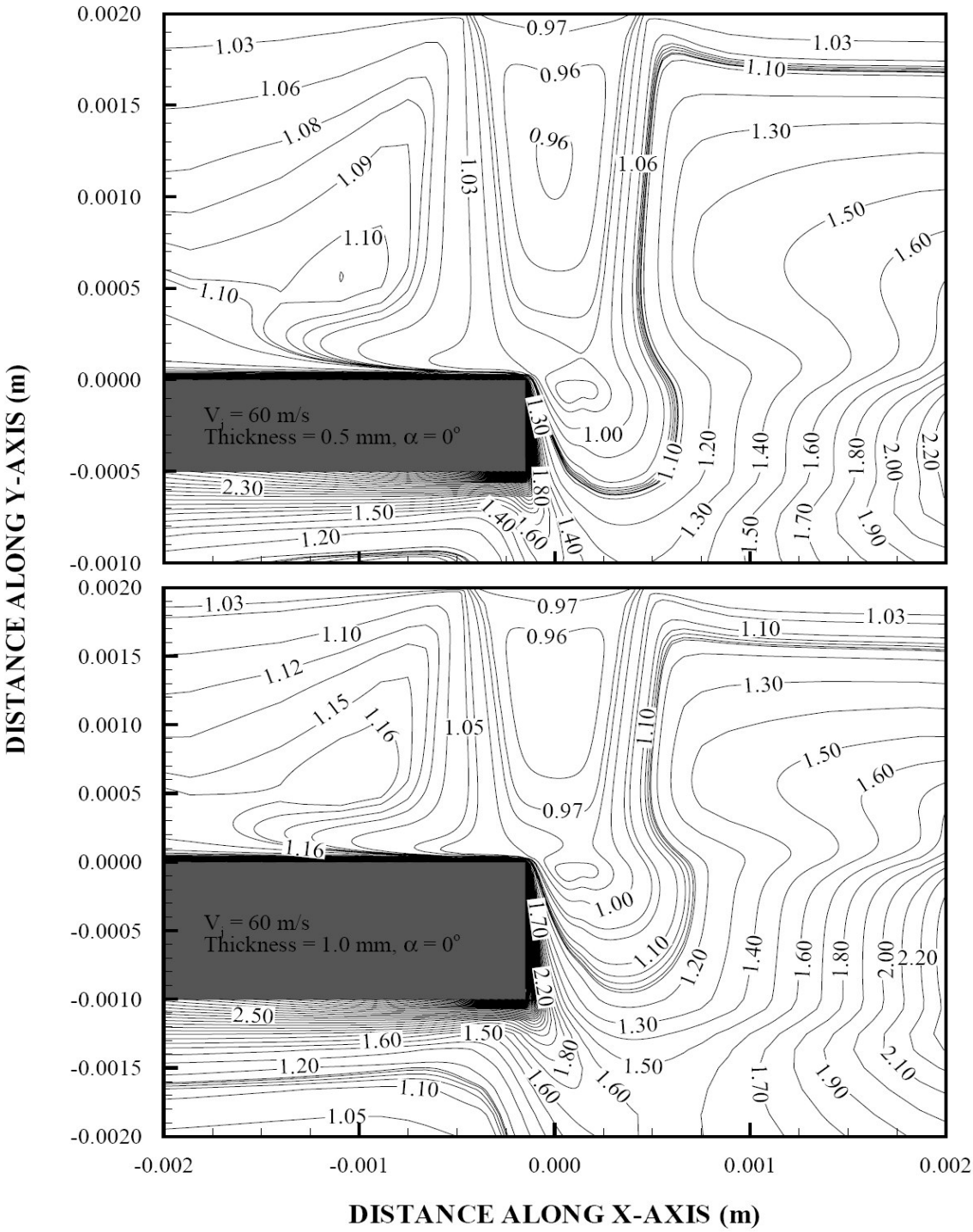

Figure 5.73 Normalized temperature (T/T_j) in the symmetry plane for jet averaged velocity of 60 m/s, kerf thickness of 0.5 and 1.0 mm, and kerf wedge angles of 0°

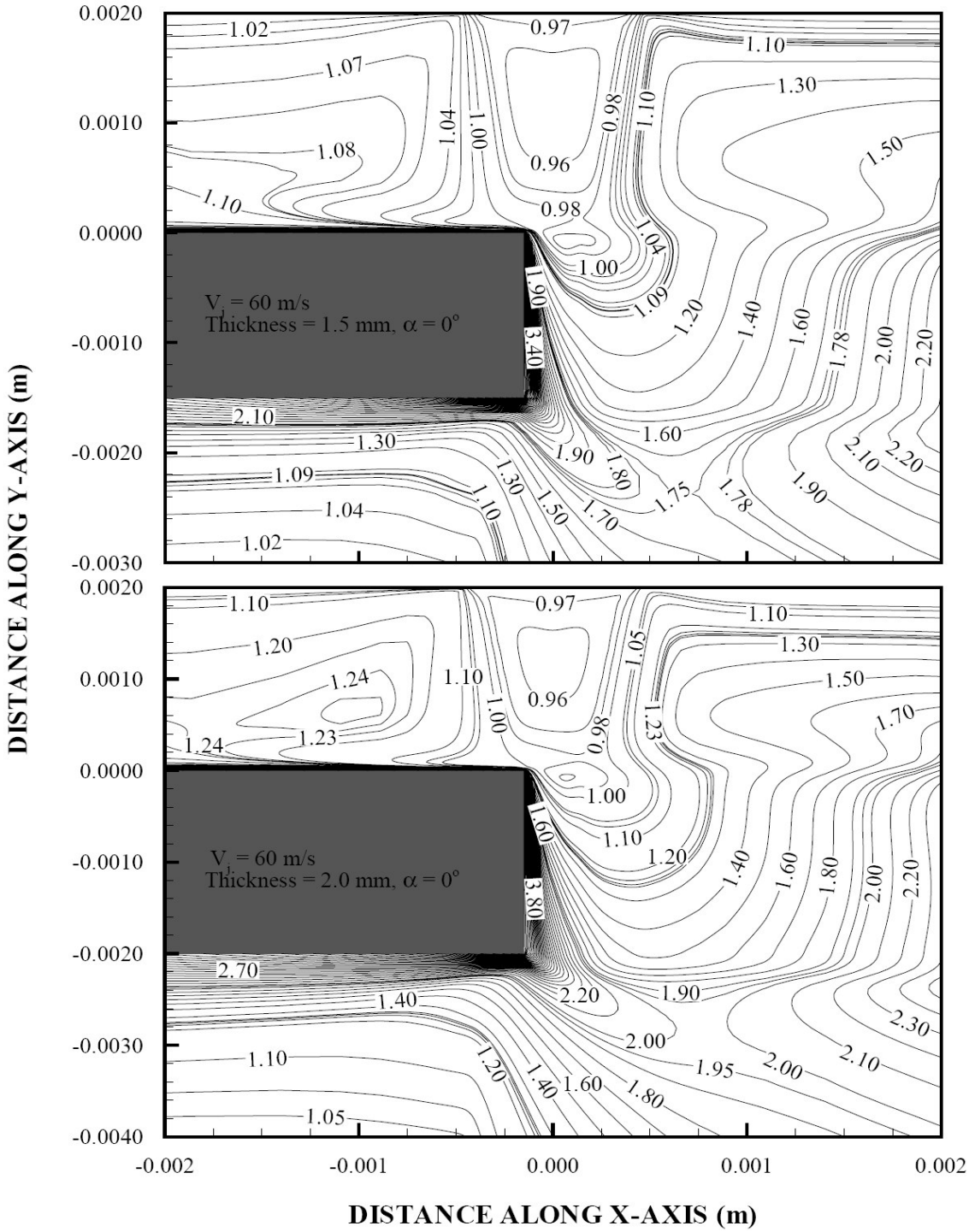

Figure 5.74 Normalized temperature (T/T_j) in the symmetry plane for jet averaged velocity of 60 m/s, kerf thickness of 1.5 and 2.0 mm, and kerf wedge angle of 0°

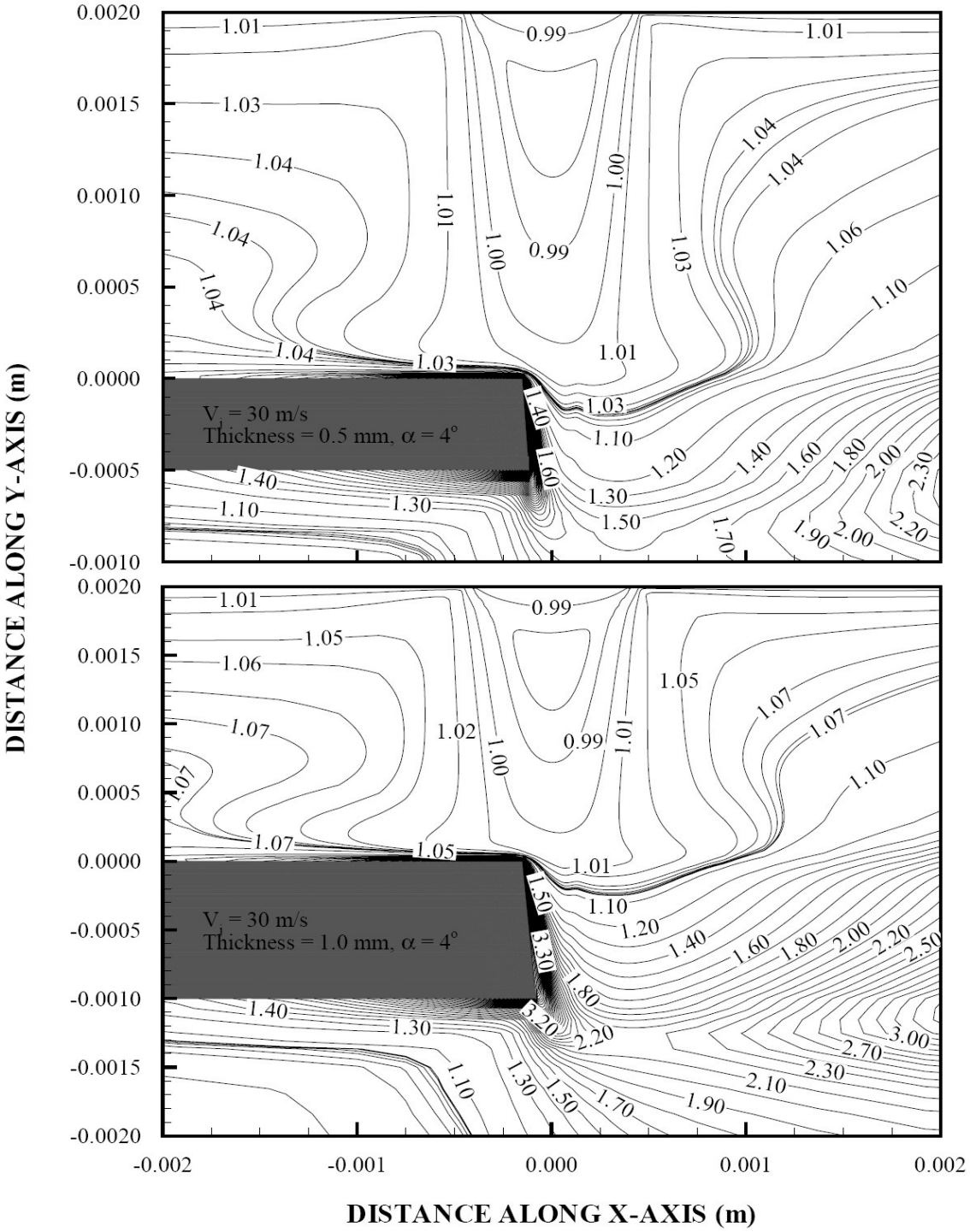

Figure 5.75 Normalized temperature (T/T_j) in the symmetry plane for jet averaged velocity of 30 m/s, kerf thickness of 0.5 and 1.0 mm, and kerf wedge angle of 4°

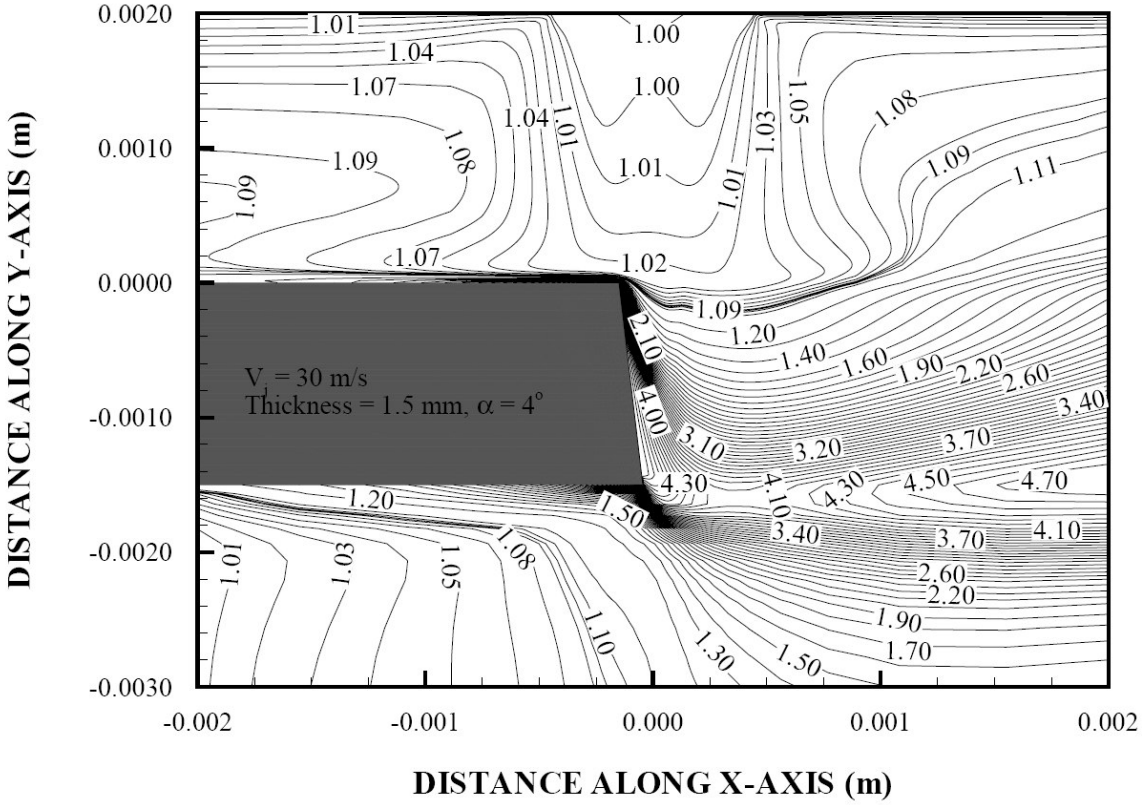

Figure 5.76 Normalized temperature (T/T_j) in the symmetry plane for jet averaged velocity of 30 m/s, kerf thickness of 1.5 mm, and kerf wedge angle of 4°

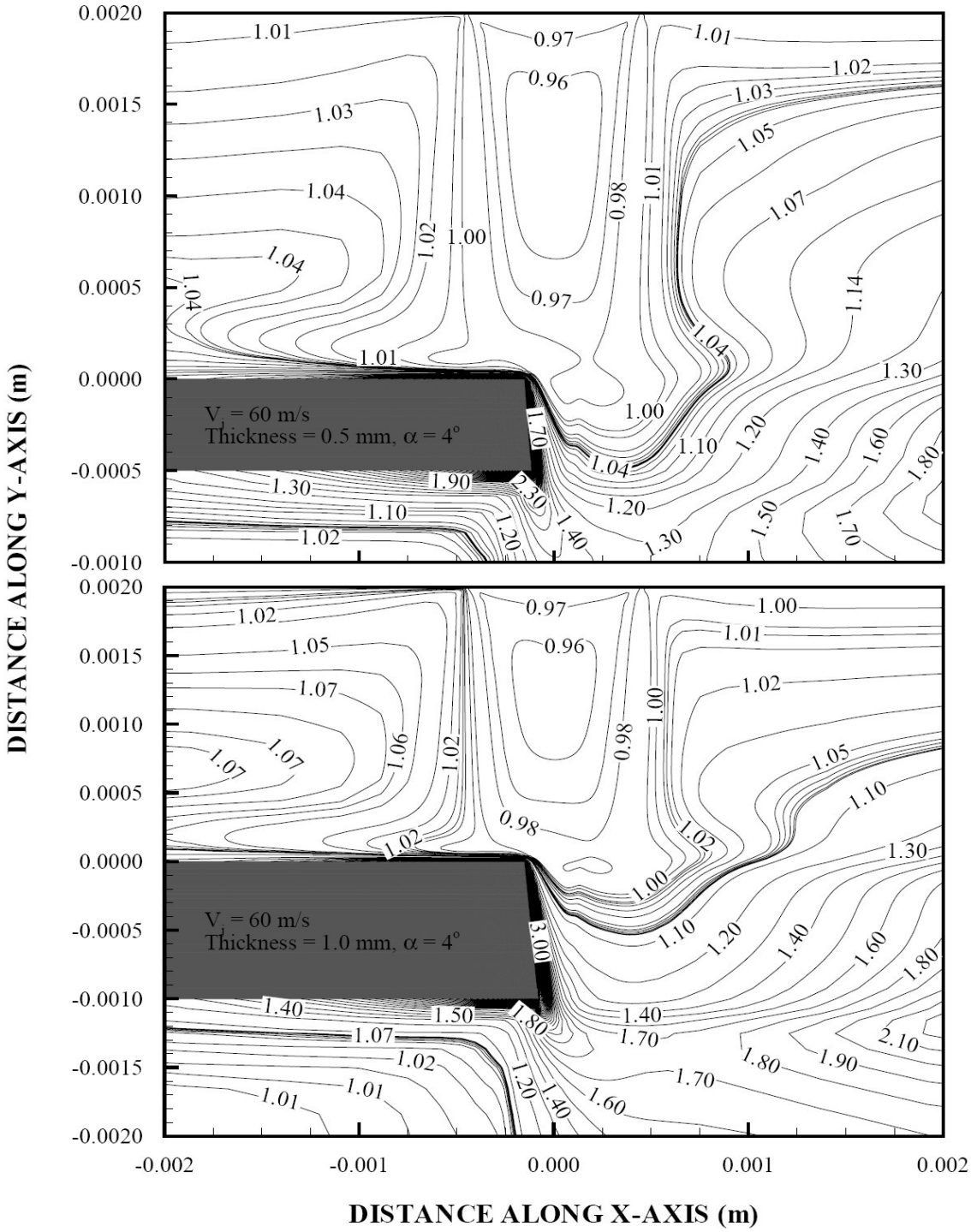

Figure 5.77 Normalized temperature (T/T_j) in the symmetry plane for jet averaged velocity of 60 m/s, kerf thickness of 0.5 and 1.0 mm, and kerf wedge angles of 4°

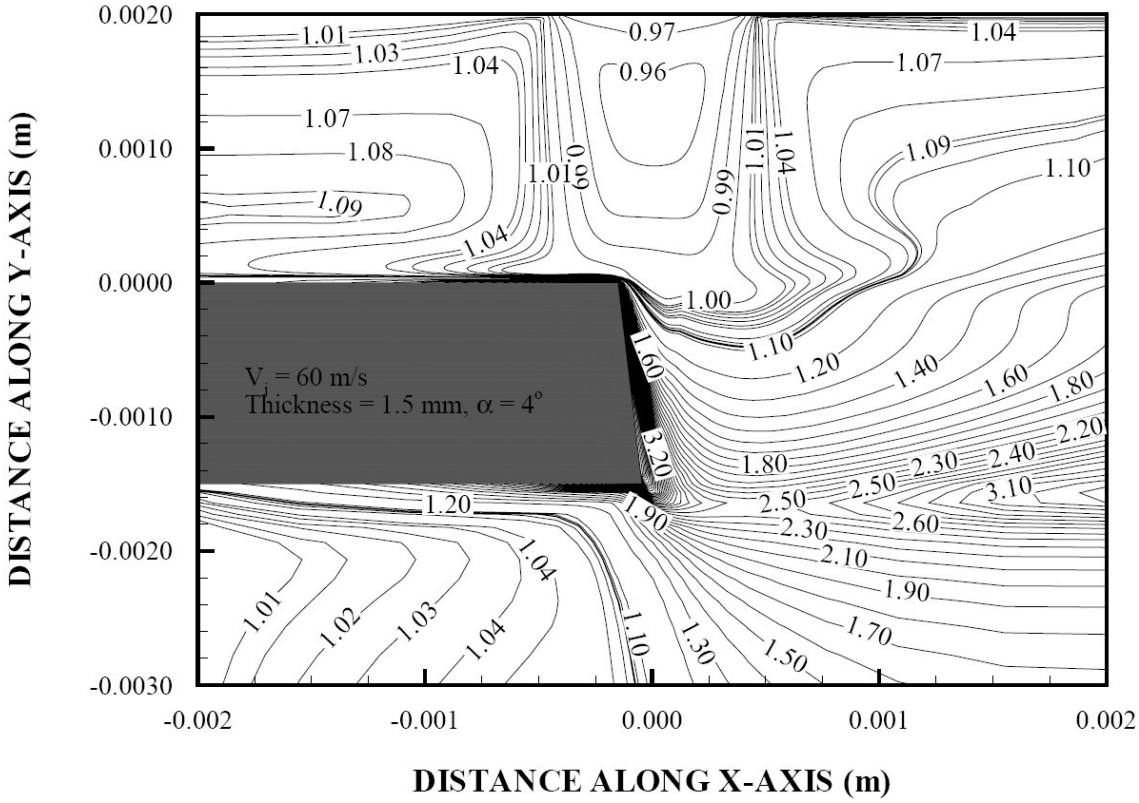

Figure 5.78 Normalized temperature (T/T_j) in the symmetry plane for jet averaged velocity of 60 m/s, kerf thickness of 1.5 mm, and kerf wedge angles of 4°

Figure 5.79 shows velocity magnitude distribution along the laser beam axis for kerf thickness = 0.5, 1.0, 1.5, and 2.0 mm, two averaged jet velocities, and kerf wedge angle = 0°. It should be noted that the locations y = 0 and y = 0.002 represent the workpiece surface and nozzle exit respectively. The locations y = -0.0005, y = -0.0010, y = -0.0015, and y = -0.0020 represent kerf thicknesses. The jet velocity increases after exiting from the nozzle reaching the first maximum velocity after a distance of about one nozzle diameter, after which it reduces to a minimum just before impingement onto the kerf surface. The kerf thickness does not affect the velocity distribution in this region. The velocity then increases until it reaches second maximum velocity. The magnitude and location of this second maximum velocity are almost not altered as the kerf thickness increases. In other words, the location of second maximum gets relatively farther from kerf bottom exit as kerf thickness increases. This is true for both averaged jet velocities. Velocity then decreases towards the kerf exit. The rate of decrease of velocity after attaining the second maximum is remarkably less in the case for which kerf thickness = 2.0 mm than other cases. After exiting the kerf, a sharp decrease in velocity is observed in the case for which thickness = 2.0 mm. Figure 5.80 shows velocity magnitude distribution along the laser beam axis for kerf thickness = 0.5, 1.0, and 1.5 mm, two averaged jet velocities, and kerf wedge angle = 4°. The magnitude of the minimum velocity attained just before kerf surface decreases with increasing thickness. An inflection point is observed in the velocity distribution as the velocity magnitude increases in the kerf in the case for which kerf thickness = 1.0 mm. A second maximum velocity followed by a decrease in velocity magnitude to a minimum is observed in the

velocity distribution in the kerf in the case for which kerf thickness = 1.5 mm. A maximum velocity is attained at a location which almost coincides with the kerf exit for all kerf thicknesses. This is true for both jet velocities at nozzle exit. The value of this maximum is higher than the first maximum velocity attained before impingement in the case for which thickness = 1.0 mm and averaged jet velocity = 30 m/s. The value of this maximum is also higher than the first maximum velocity attained before impingement in the cases for which thickness = 1.0 and 1.5 mm and averaged jet velocity = 60 m/s. Velocity then decreases after exiting from the kerf region.

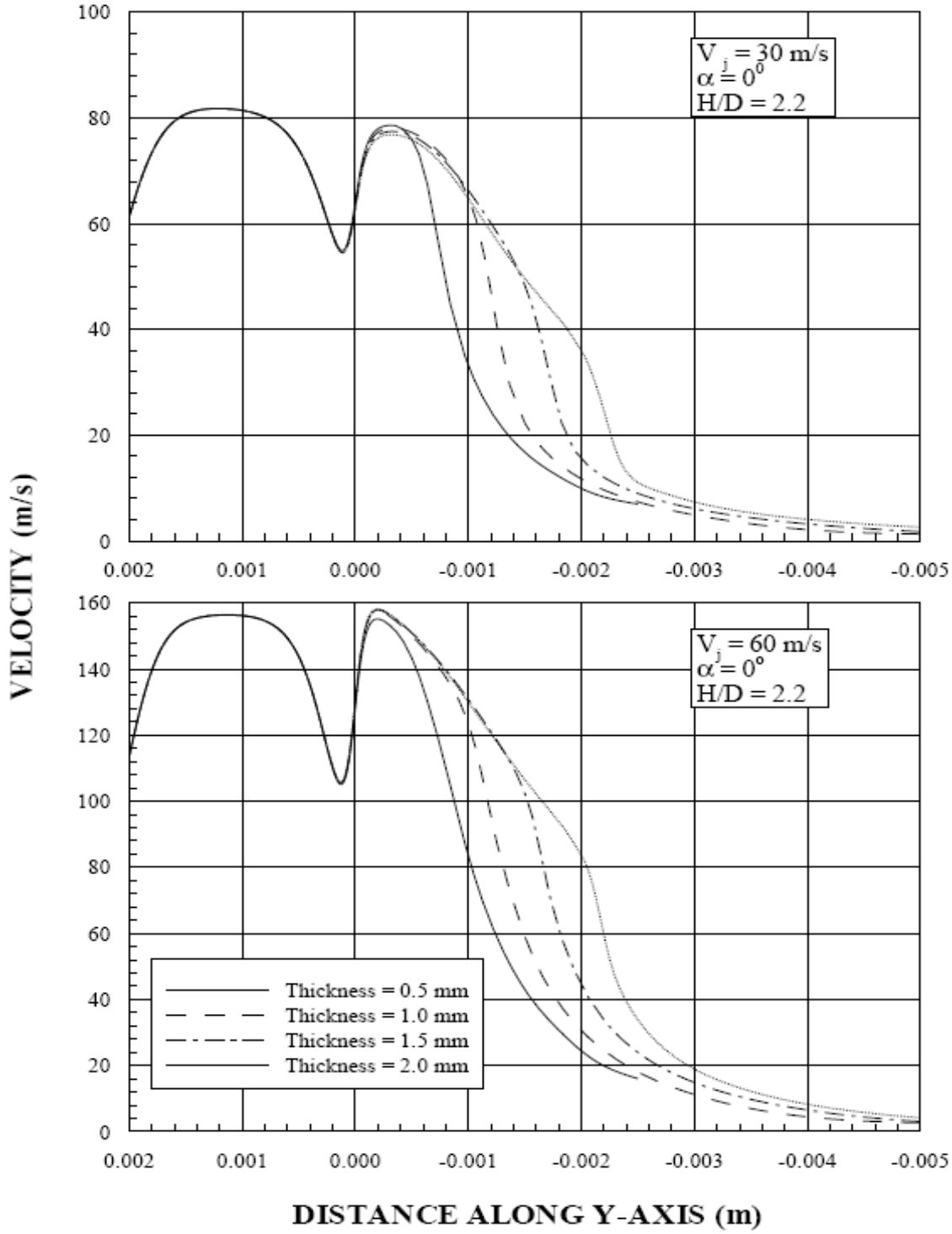

Figure 5.79 Velocity magnitude along laser beam axis for two different averaged jet velocities, kerf thickness of 0.5, 1.0, 1.5, and 2.0 mm, and kerf wedge angle = 0°

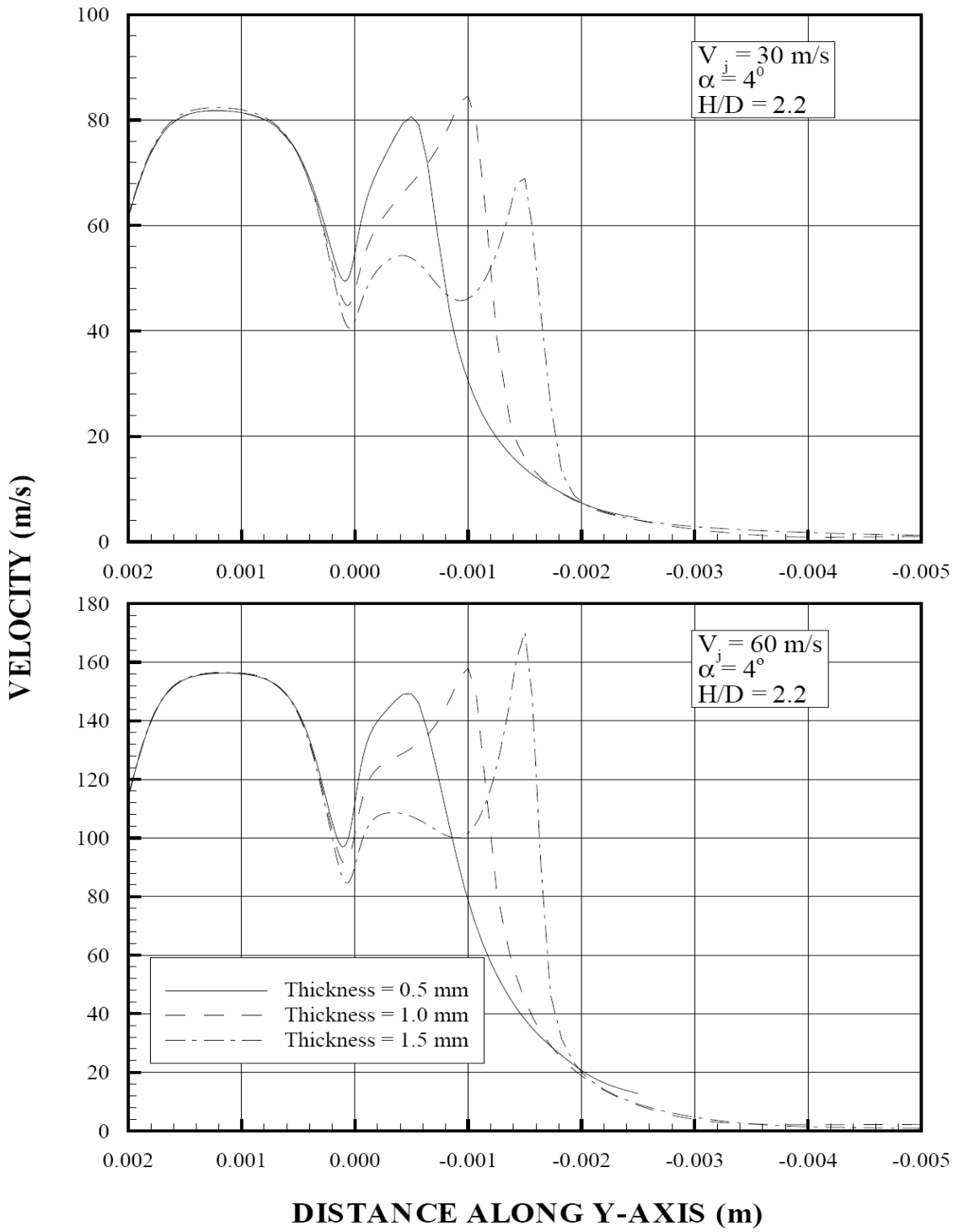

Figure 5.80 Velocity magnitude along laser beam axis for two different averaged jet velocities, kerf thickness of 0.5, 1.0, and 1.5 mm, and kerf wedge angle = 4°

Figures 5.81 show pressure distribution in the fluid along the laser beam axis for kerf thickness = 0.5, 1.0, 1.5, and 2.0 mm, two averaged jet velocities at nozzle exit, and kerf wedge angle = 0°. Static pressure reduces after exiting the nozzle because of jet expansion and then increases to a maximum at a location close to the kerf top surface because of stagnation formation and blockage effect of the kerf. Kerf thickness has no effect on pressure distribution in this region. A sharp pressure drop is observed in the entry region of the kerf for all thicknesses. The sharp pressure drop is followed by a gradual drop towards the kerf exit in the case for which kerf thickness = 2.0 mm and averaged jet velocity = 30 m/s. A minimum negative pressure coefficient is attained in all other cases. The location of this minimum is close to the kerf bottom exit in all cases for which averaged jet velocity = 30 m/s. The location of the minimum pressure is in the entry region of the kerf and is unaffected by the kerf thickness in all cases for which averaged jet velocity = 60 m/s. Pressure then slightly increases onset exiting the kerf and then it decreases to atmospheric pressure. Figures 5.82 show pressure distribution in the fluid along the laser beam axis for kerf thickness = 0.5, 1.0, and 1.5 mm, two averaged jet velocities at nozzle exit, and kerf wedge angle = 4°. Static pressure reduces after exiting the nozzle because of jet expansion and then increases to a maximum at a location close to the kerf top surface because of stagnation formation and blockage effect of the kerf. The value of maximum pressure attained in this region increases as kerf thickness increases. Pressure drops in the kerf region until a minimum pressure is attained at the kerf exit. Although pressure in the kerf is higher for kerfs with larger thickness, the

minimum pressure attained at the exit decreases as kerf thickness increases. This is true for all thicknesses and both averaged jet velocities.

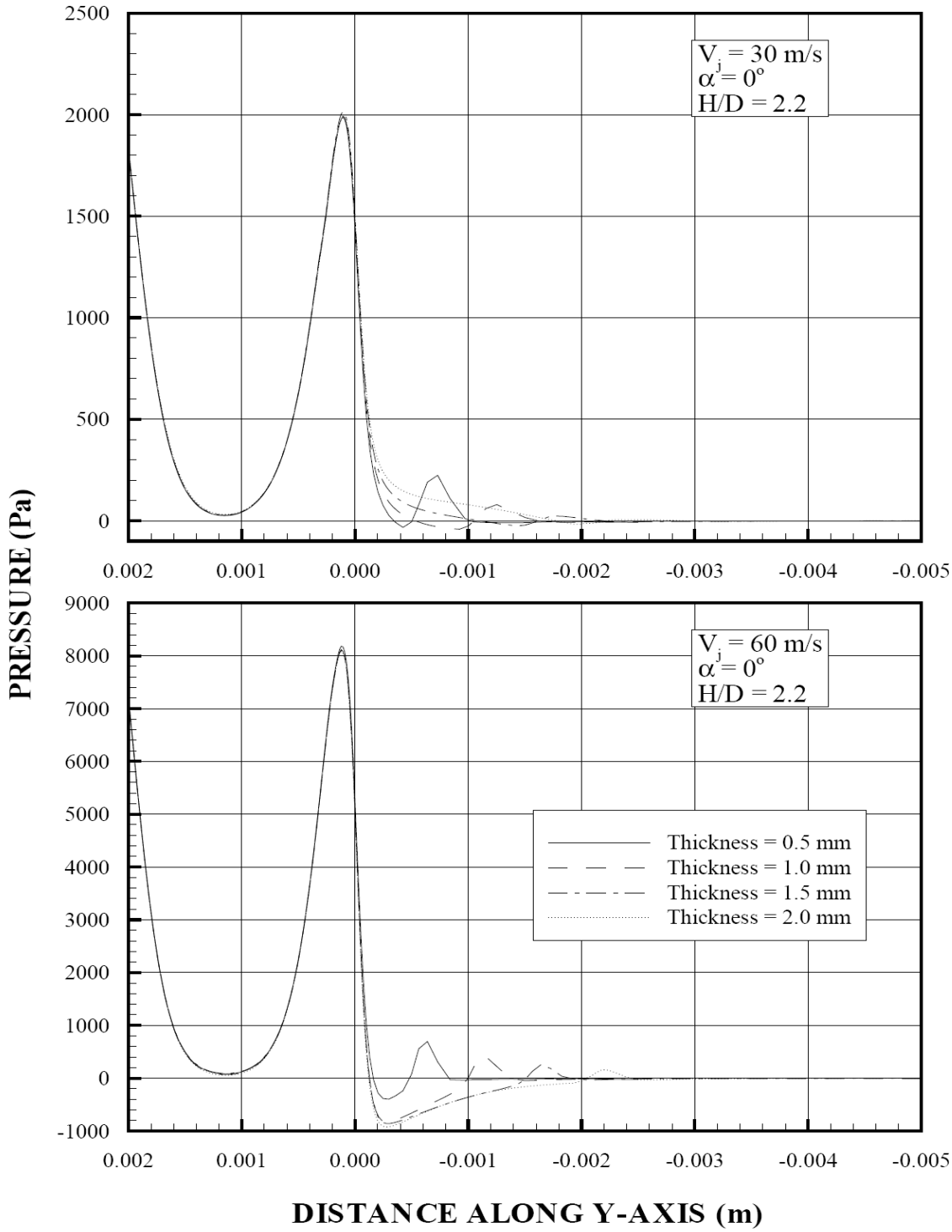

Figure 5.81 Pressure distribution along laser beam axis for two different averaged jet velocities, kerf thickness of 0.5, 1.0, 1.5, and 2.0 mm, and kerf wedge angle = 0°

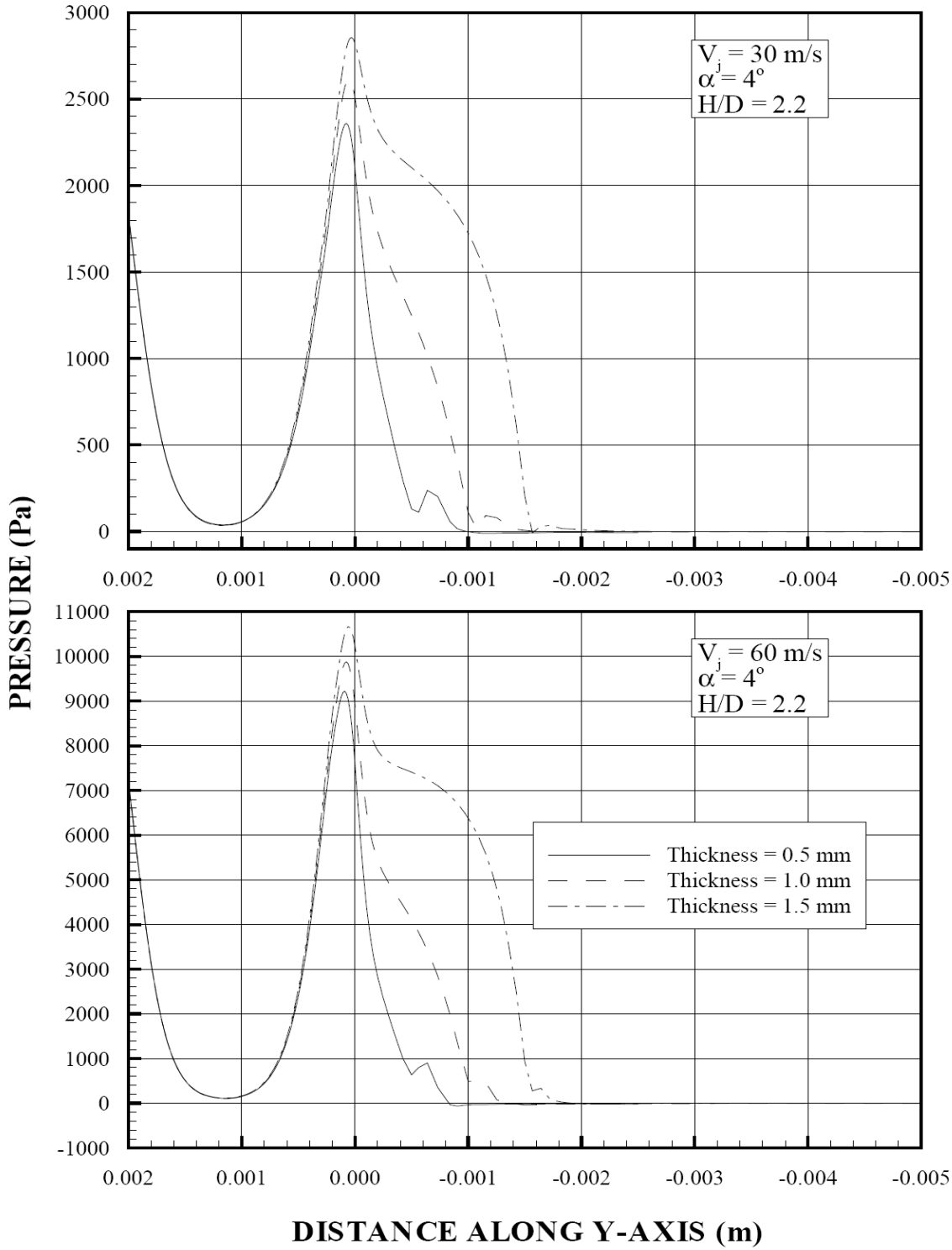

Figure 5.82 Pressure distribution along laser beam axis for two different averaged jet velocities, kerf thickness of 0.5, 1.0, and 1.5 mm, and kerf wedge angle = 4°

Figures 5.83 show temperature distribution in the fluid along the laser beam axis for kerf thickness = 0.5, 1.0, 1.5, and 2.0 mm, two averaged jet velocities at nozzle exit, and kerf wedge angle = 0°. Figures 5.84 show temperature distribution in the fluid along the laser beam axis for kerf thickness = 0.5, 1.0, and 1.5 mm, two averaged jet velocities at nozzle exit, and kerf wedge angle = 4°. Temperature increases onset fluid enters the kerf region. Fluid temperature reaches a maximum value at a certain location after exiting the kerf. A significant increase in the maximum temperature attained is observed as the kerf thickness increases. This can be attributed to the higher heat transfer associated with the increasing the extent of the domain with high temperature that fluid particles are exposed to. Fluid temperature then reduces. In this region, temperature increases as kerf thickness increases. This is true for both averaged jet velocities and both wedge angles.

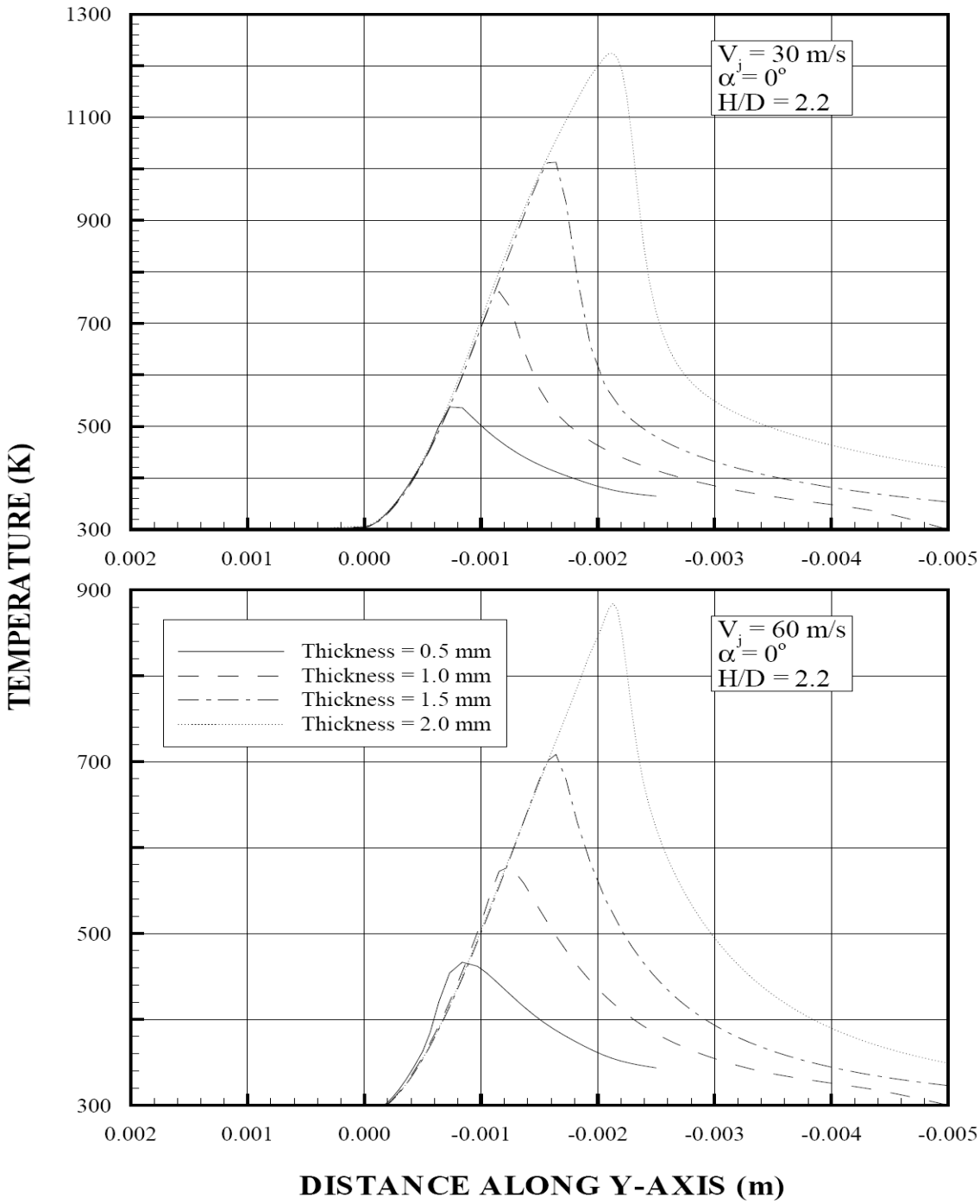

Figure 5.83 Temperature distribution along laser beam axis for two different averaged jet velocities, kerf thickness of 0.5, 1.0, 1.5, and 2.0 mm, and kerf wedge angle = 0°

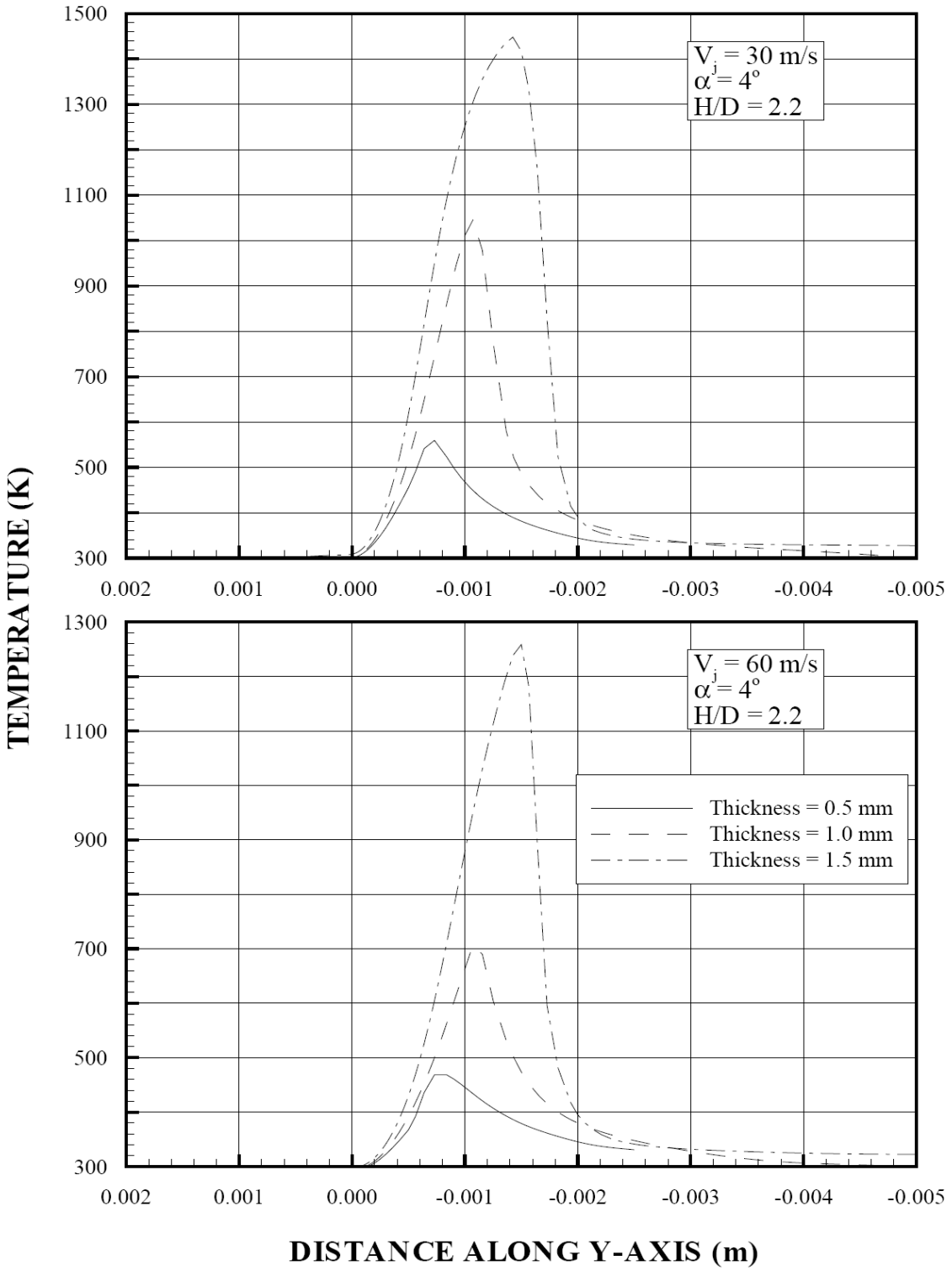

Figure 5.84 Temperature distribution along laser beam axis for two different averaged jet velocities, kerf thickness of 0.5, 1.0, and 1.5 mm, and kerf wedge angle = 4°

Figure 5.85 shows the Nusselt number distribution along the normalized kerf thickness for four different kerf thicknesses. The kerf wedge angle = 0° and the averaged jet velocity = 30 m/s. The kerf thickness is normalized with the maximum thickness; that is, normalized kerf thickness = 0 corresponds to the kerf inlet, and normalized kerf thickness = -1 corresponds to the kerf exit. The Nusselt number distribution is shown at 5 locations along the kerf wall. Location A (x = -0.00015, z = 0.0000094 m) is almost the kerf edge (where the kerf wall intersects the symmetry plane). The other 4 locations (B, C, D, and E) are distributed along the kerf wall (see Figure 5.1). Similar trends of variation among the various locations are observed for the different kerf wedge angles. Location B (x = -0.000125, z = 0.000075 m) corresponds to the location where Nusselt number attains the highest values. The trends obtained show that Nusselt number show that Nusselt number increases as one moves along the kerf wall from location A (x = -0.00015, z = 0.000094) in the direction of the positive x-axis to attain maximum values at a certain location which can be approximated by location B (x = -0.000125, z = 0.000075 m). The Nusselt number then decreases as one moves from location B in the direction of positive x-axis (see Figure 5.1). The trends show that Nusselt number increases sharply from the kerf top edge due to convective cooling of the jet in the kerf. The Nusselt number attains a maximum value and then decreases gradually. A second maximum Nusselt number can also be attained at some locations. Nusselt number then decays along the wall towards the kerf exit. Figure 5.86 shows the Nusselt number distribution along the normalized kerf thickness for same geometric parameters as the previous case and averaged jet velocity = 60 m/s. Trends observed are the same as the previous case. Figures 5.87 and 5.88 show

the Nusselt number distribution along the normalized kerf thickness for kerf thickness = 0.5, 1.0, and 1.5 mm, two averaged jet velocities, and kerf wedge angle = 4°. The Nusselt number distribution at location A in case for which kerf thickness = 1.0 mm, and at locations A and B in the case for which kerf thickness = 1.5 mm clearly shows a second attained maximum Nusselt number whose value exceeds the first attained maximum. Appearance of the secondary maximum in Nusselt number distribution is attributed to a sharp rise in the turbulence level which accompanies transition from an accelerating region flow to a decelerating jet [93].

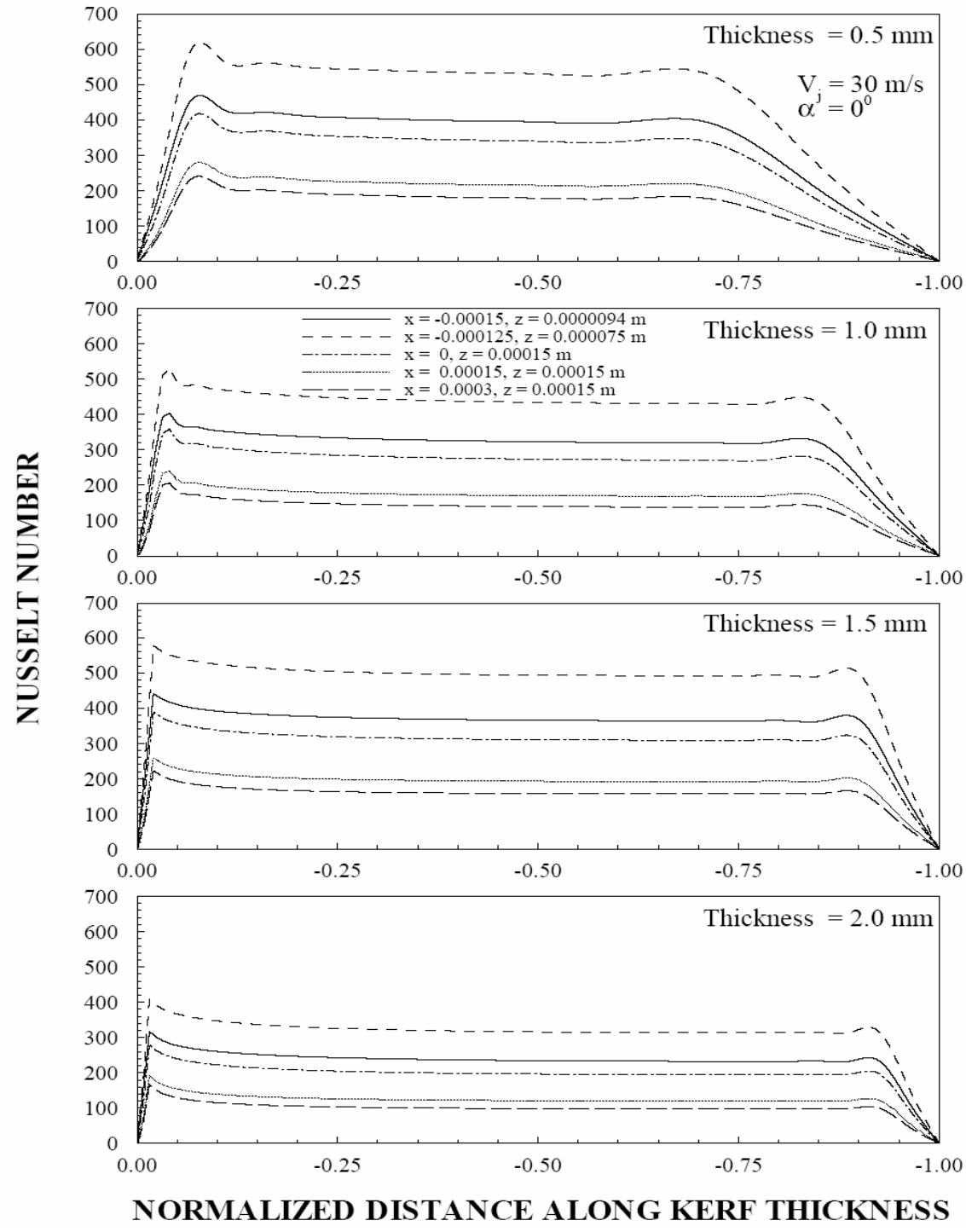

Figure 5.85 Nusselt number distribution at five locations along the kerf wall for kerf thickness = 0.5, 1.0, 1.5, and 2.0 mm, averaged jet velocity = 30 m/s, and kerf wedge angle = 0°

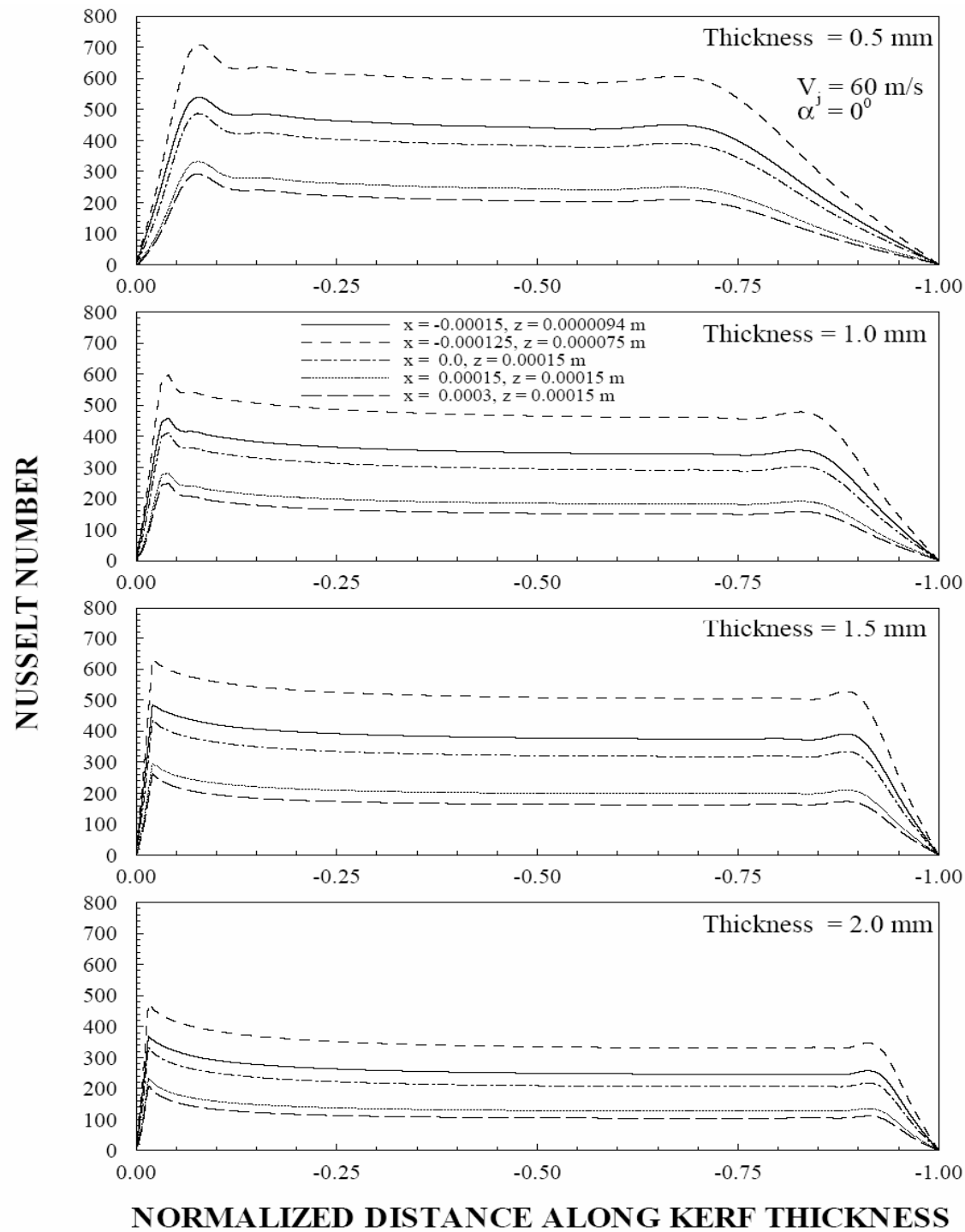

Figure 5.86 Nusselt number distribution at five locations along the kerf wall for kerf thickness = 0.5, 1.0, 1.5, and 2.0 mm, averaged jet velocity = 60 m/s, and kerf wedge angle = 0°

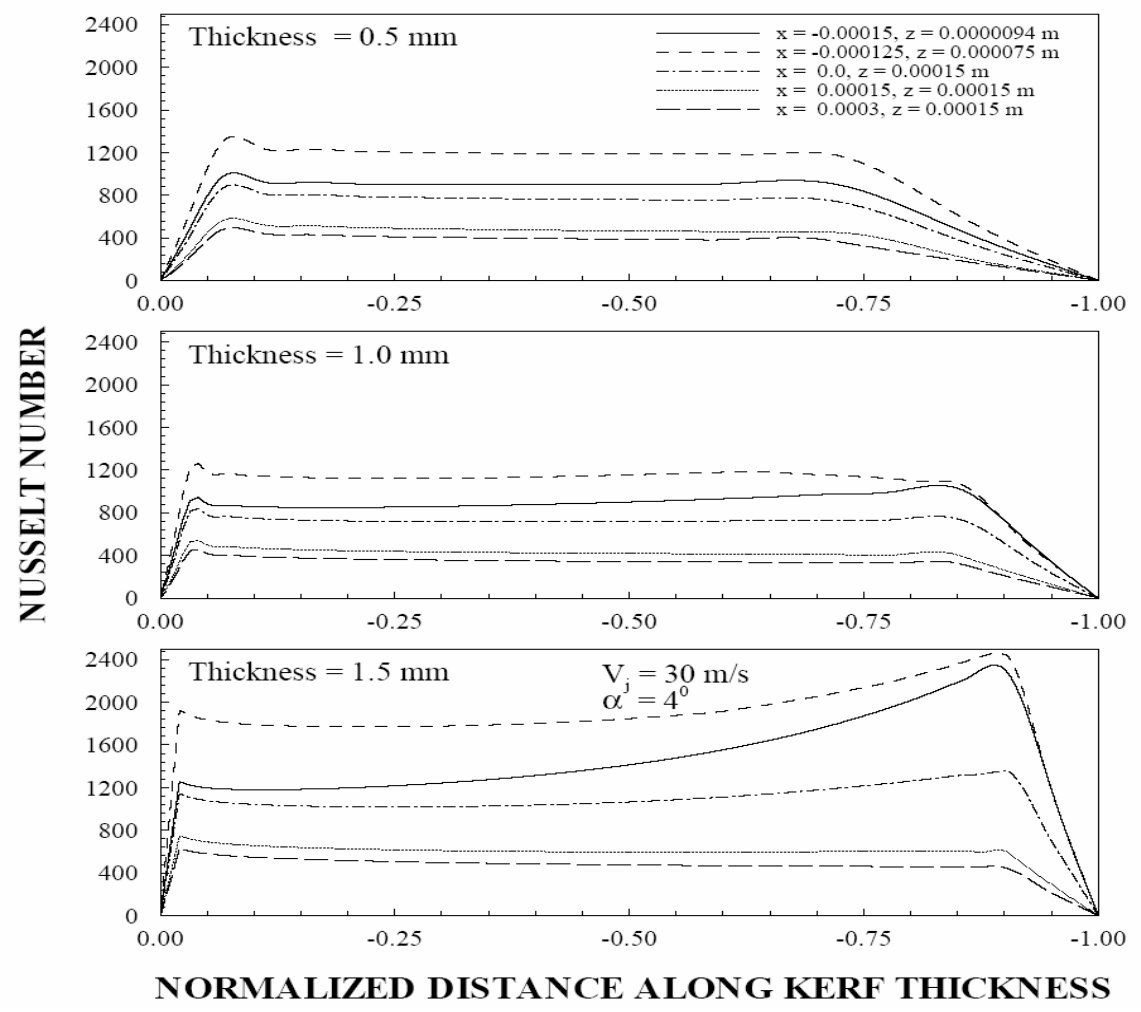

Figure 5.87 Nusselt number distribution at five locations along the kerf wall for kerf thickness = 0.5, 1.0, and 1.5 mm, averaged jet velocity = 30 m/s, and kerf wedge angle = 4°

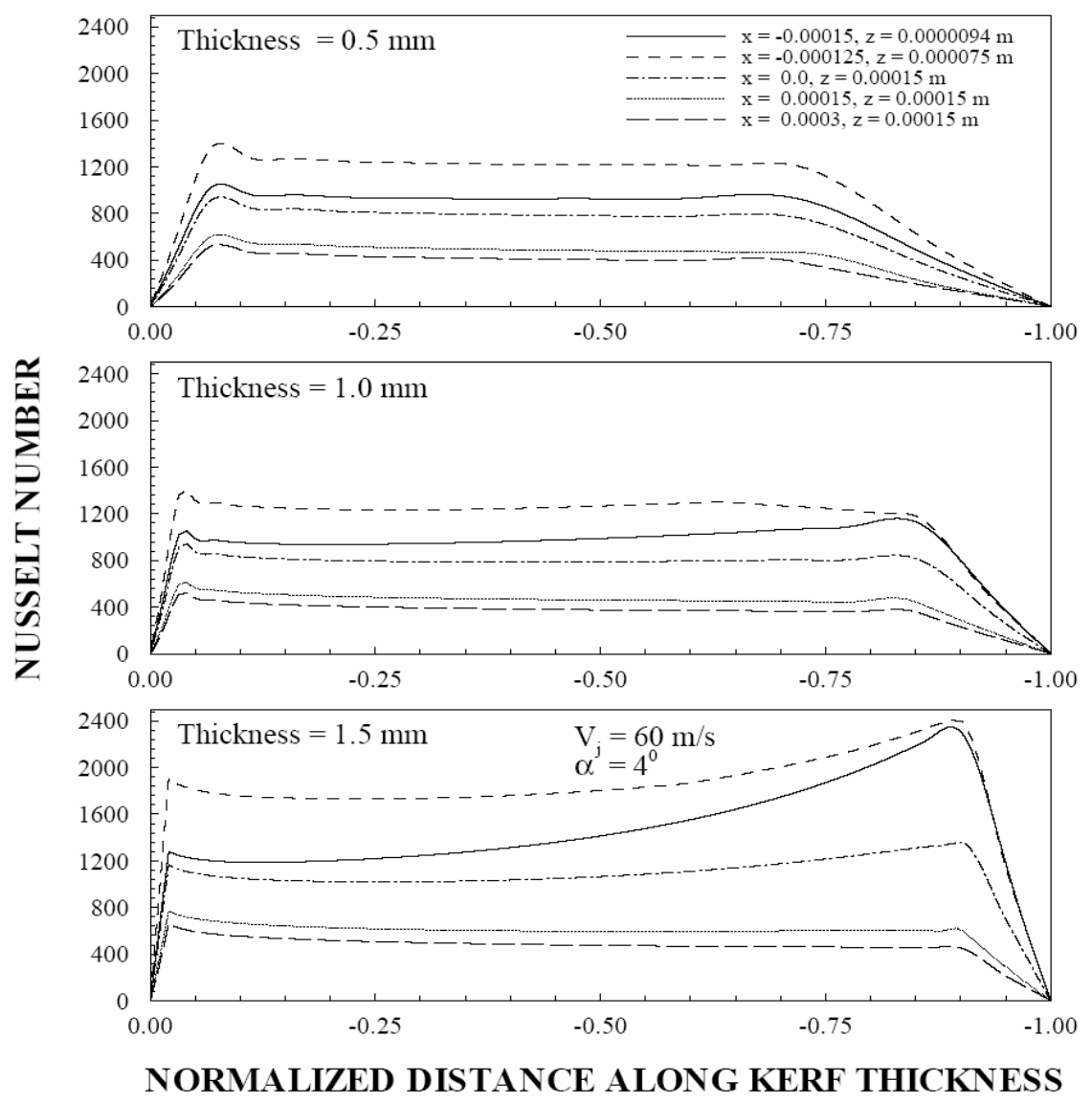

Figure 5.88 Nusselt number distribution at five locations along the kerf wall for kerf thickness = 0.5, 1.0, and 1.5 mm, averaged jet velocity = 60 m/s, and kerf wedge angle = 4°

Figures 5.89 compares the Nusselt number distribution at location B, where the Nusselt number attains highest values, for kerf thickness = 0.5, 1.0, 1.5, and 2.0 mm, two averaged jet velocities, and kerf wedge angle = 0°. The kerf thickness is normalized with the maximum thickness; that is, normalized kerf thickness = 0 corresponds to the kerf inlet, and normalized kerf thickness = -1 corresponds to the kerf exit of the kerf whose thickness = 2.0 mm. Normalized kerf thickness = -0.25 corresponds to the kerf exit of the kerf whose thickness = 0.5 mm; normalized kerf thickness = -0.5 corresponds to the kerf exit of the kerf whose thickness = 1.0 mm; and normalized kerf thickness = -0.75 corresponds to the kerf exit of the kerf whose thickness = 1.5 mm. Nusselt number attained highest values at location B in the kerf whose thickness = 0.5 mm. Nusselt number values attained at location B in the kerf whose thickness = 1.5 mm are higher than those attained in the kerf with thickness = 1.0 mm which are higher than those attained in the kerf whose thickness = 2.0 mm. Figures 5.90 compares the Nusselt number distribution at location B, where the Nusselt number attains highest values, for kerf thickness = 0.5, 1.0, and 1.5 mm, two averaged jet velocities, and kerf wedge angle = 4°. The kerf thickness is normalized with the maximum thickness; that is, normalized kerf thickness = 0 corresponds to the kerf inlet, and normalized kerf thickness = -1 corresponds to the kerf exit of the kerf whose thickness = 1.5 mm. Normalized kerf thickness = -0.33 corresponds to the kerf exit of the kerf whose thickness = 0.5 mm; and normalized kerf thickness = -0.67 corresponds to the kerf exit of the kerf whose thickness = 1.0 mm. Nusselt number attained highest values at location B in the kerf whose thickness = 1.5 mm. This is true for both jet velocities. Nusselt number values attained at

location B in the kerf whose thickness = 0.5 mm are higher than those attained in the kerf with thickness = 1.0 mm in the case for which averaged jet velocity = 30 m/s. They are almost the same in the case for which averaged jet velocity = 60 m/s.

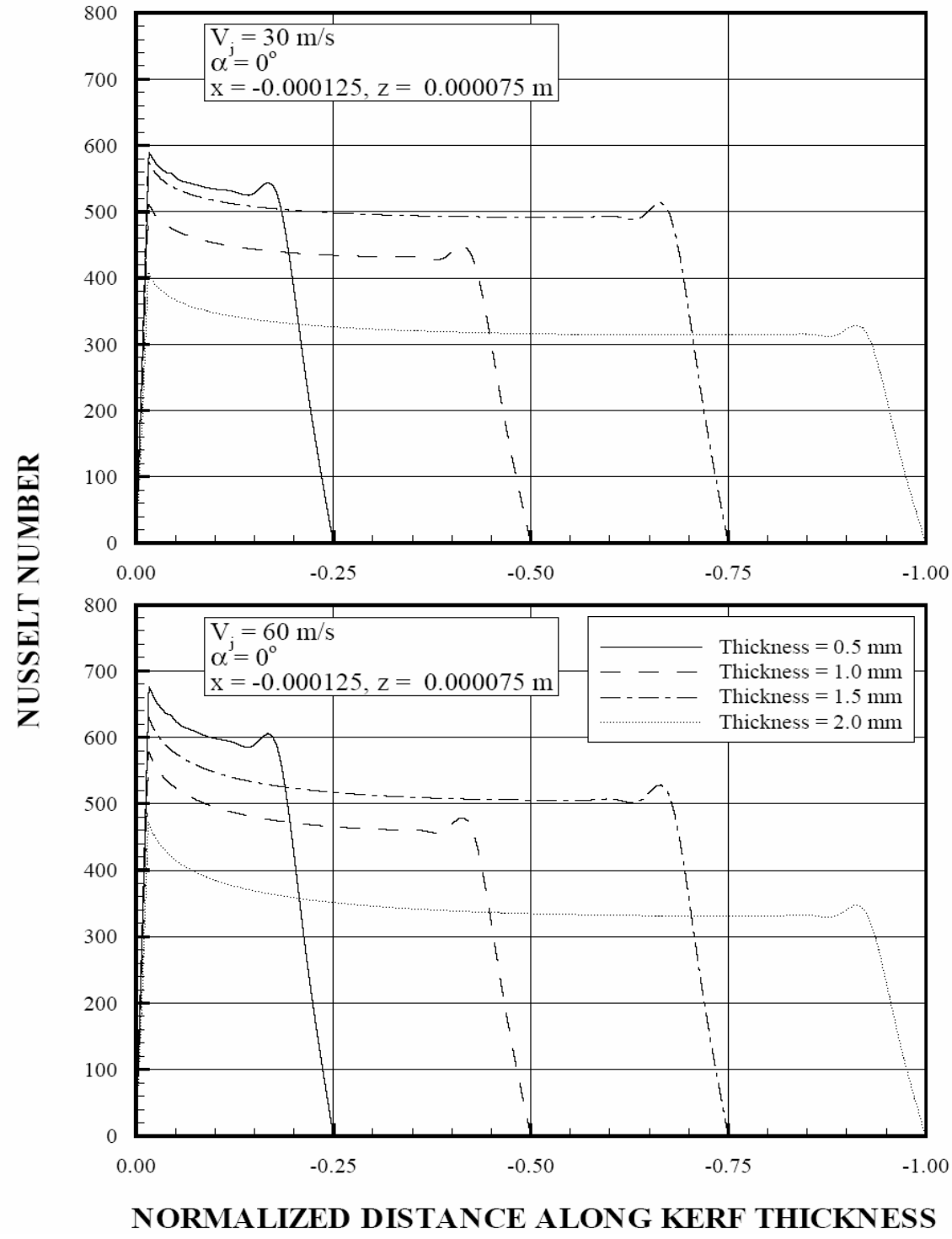

Figure 5. 89 Nusselt number distribution at location B (x = -0.000125, z = 0.000075 m) along kerf wall for kerf thickness = 0.5, 1.0, 1.5, and 2.0 mm, two averaged jet velocities, and kerf wedge angle = 0°

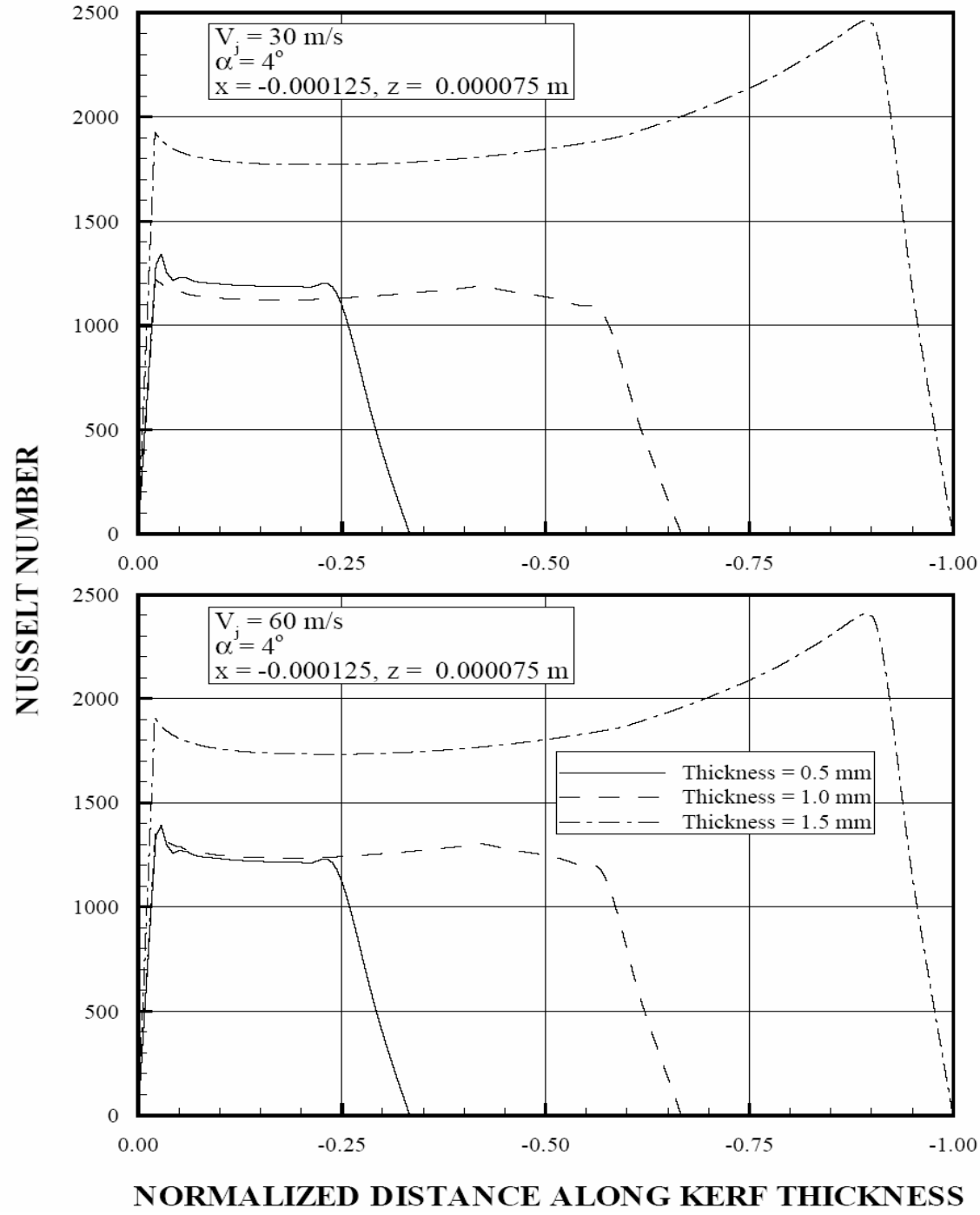

Figure 5.90 Nusselt number distribution at location B (x = -0.000125, z = 0.000075 m) along kerf wall for kerf thickness = 0.5, 1.0, and 1.5 mm, two averaged jet velocities, and kerf wedge angles = 4°

Figure 5.91 shows the skin friction distribution along the normalized kerf thickness for four different kerf thicknesses. The kerf wedge angle = 0° and the averaged jet velocity = 30 m/s. The kerf thickness is normalized with the maximum thickness; that is, normalized kerf thickness = 0 corresponds to the kerf inlet, and normalized kerf thickness = -1 corresponds to the kerf exit. The skin friction distribution is shown at 5 locations along the kerf wall. Location A (x = -0.00015, z = 0.0000094 m) is almost the kerf edge (where the kerf wall intersects the symmetry plane). The other 4 locations (B, C, D, and E) are distributed along the kerf wall and are the same locations for which the Nusselt number distribution is shown above (see Figure 5.1). Similar trends of variation among the various locations are observed for the different kerf wedge angles. The skin friction increases at the inlet of the kerf due to flow acceleration in this region. The skin friction then reduces as the kerf depth increases. This is attributed to the shear layer developed within the vicinity of the kerf wall, which is influenced by high wall temperature leading to high thermodynamic pressure in this region. A slight increase over a short distance is then observed. A second maximum skin friction is attained at some locations. The skin friction then decreases towards the kerf exit. Figure 5.92 shows the skin friction distribution along the normalized kerf thickness for the same geometric parameters as the previous case and averaged jet velocity = 60 m/s. Figure 5.93 shows the skin friction distribution along the normalized kerf thickness for four different kerf thicknesses. The kerf wedge angle = 4° and the averaged jet velocity = 30 m/s. The skin friction increases sharply at the inlet of the kerf until it reaches a maximum. A decrease in skin friction is then observed. Skin friction then increases gradually until a second

maximum skin friction exceeding the first maximum is attained at location D in the case for which thickness = 0.5 mm, locations D and E in the case for which thickness = 1.0 mm, and locations A, D, and E in the case for which thickness = 1.5 mm. Figure 5.94 shows the skin friction distribution along the normalized kerf thickness for the same geometric parameters as the previous case and averaged jet velocity = 60 m/s. Trends obtained are almost similar to the previous case. However, it should be noted that the second maxima attained at the five locations in the case for which thickness = 1.5 mm are all higher than the first maxima.

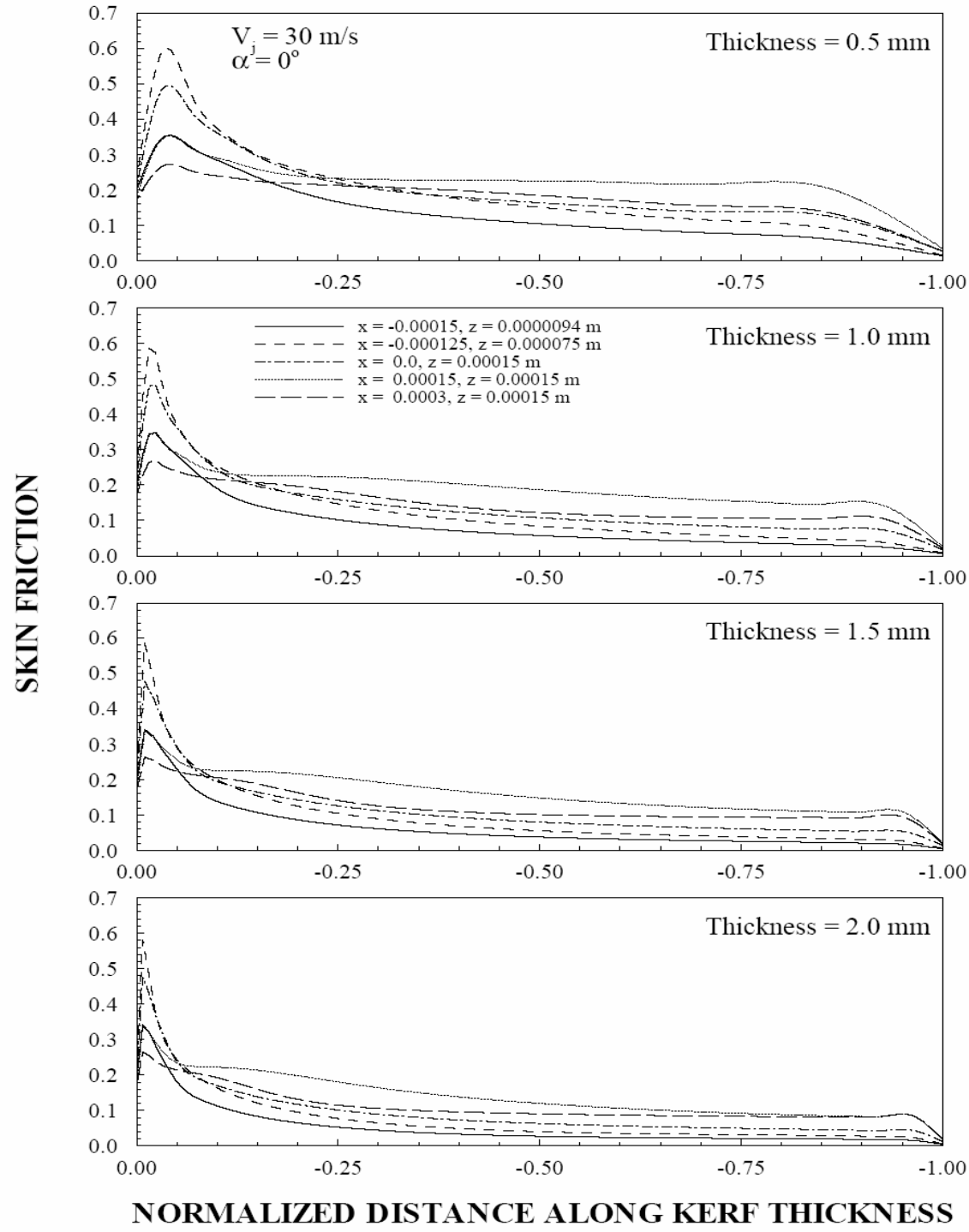

Figure 5.91 Skin friction distribution at five locations along the kerf wall for kerf thickness = 0.5, 1.0, 1.5, and 2.0 mm, averaged jet velocity = 30 m/s, and kerf wedge angle = 0°

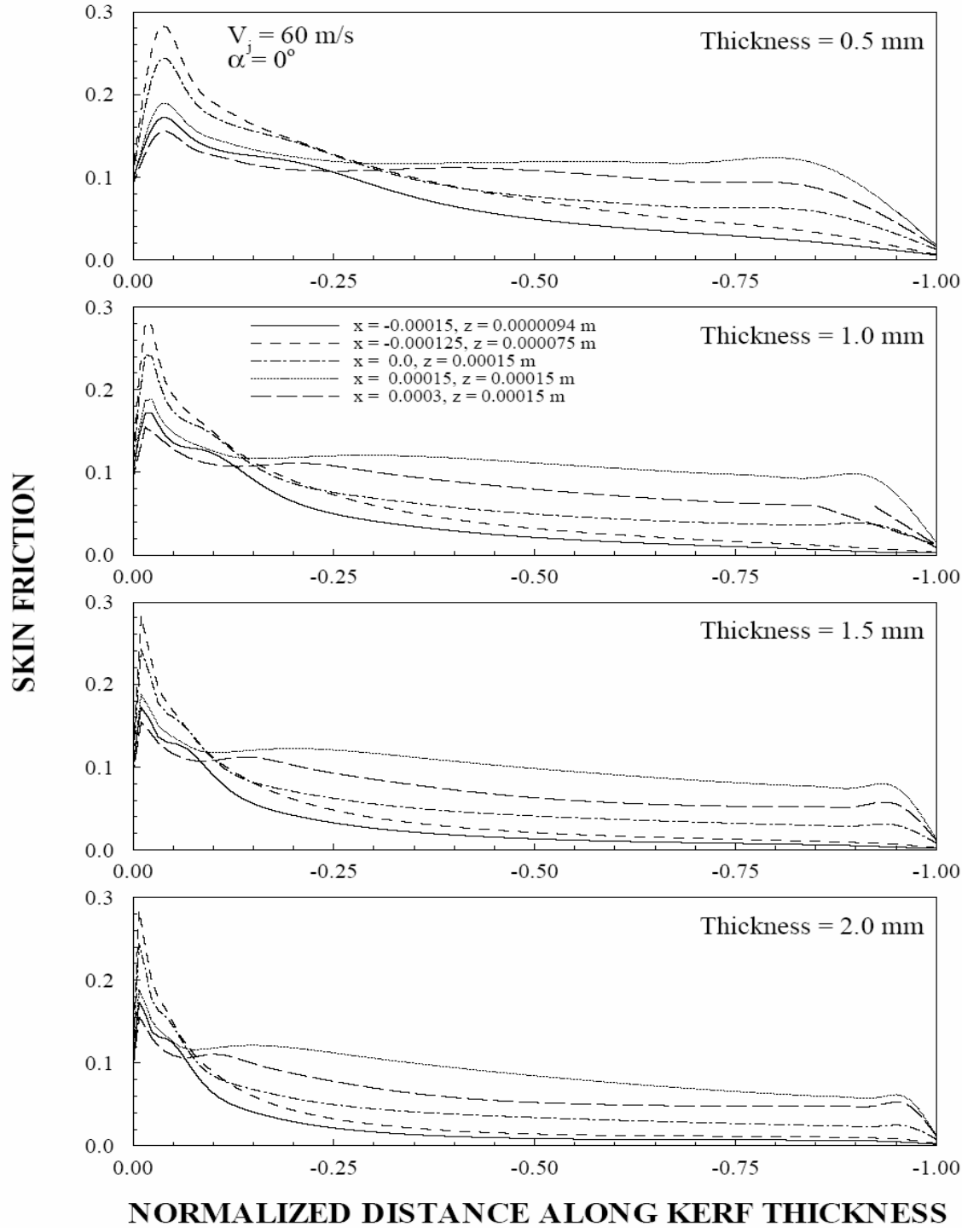

Figure 5.92 Skin friction distribution at five locations along the kerf wall for kerf thickness = 0.5, 1.0, 1.5, and 2.0 mm, averaged jet velocity = 60 m/s, and kerf wedge angle = 0°

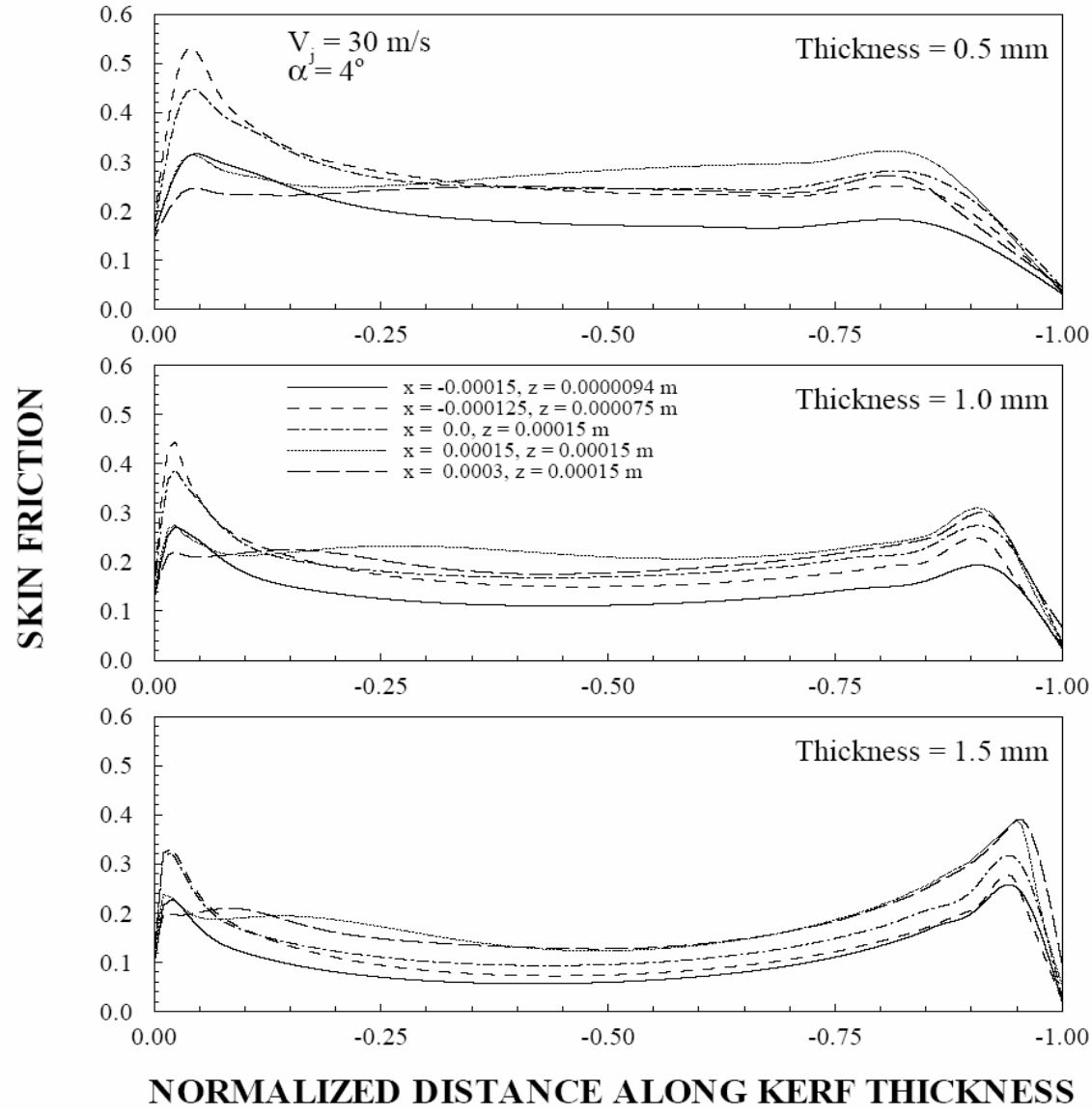

Figure 5.93 Skin friction distribution at five locations along the kerf wall for kerf thickness = 0.5, 1.0, and 1.5 mm, averaged jet velocity = 30 m/s, and kerf wedge angle = 4°

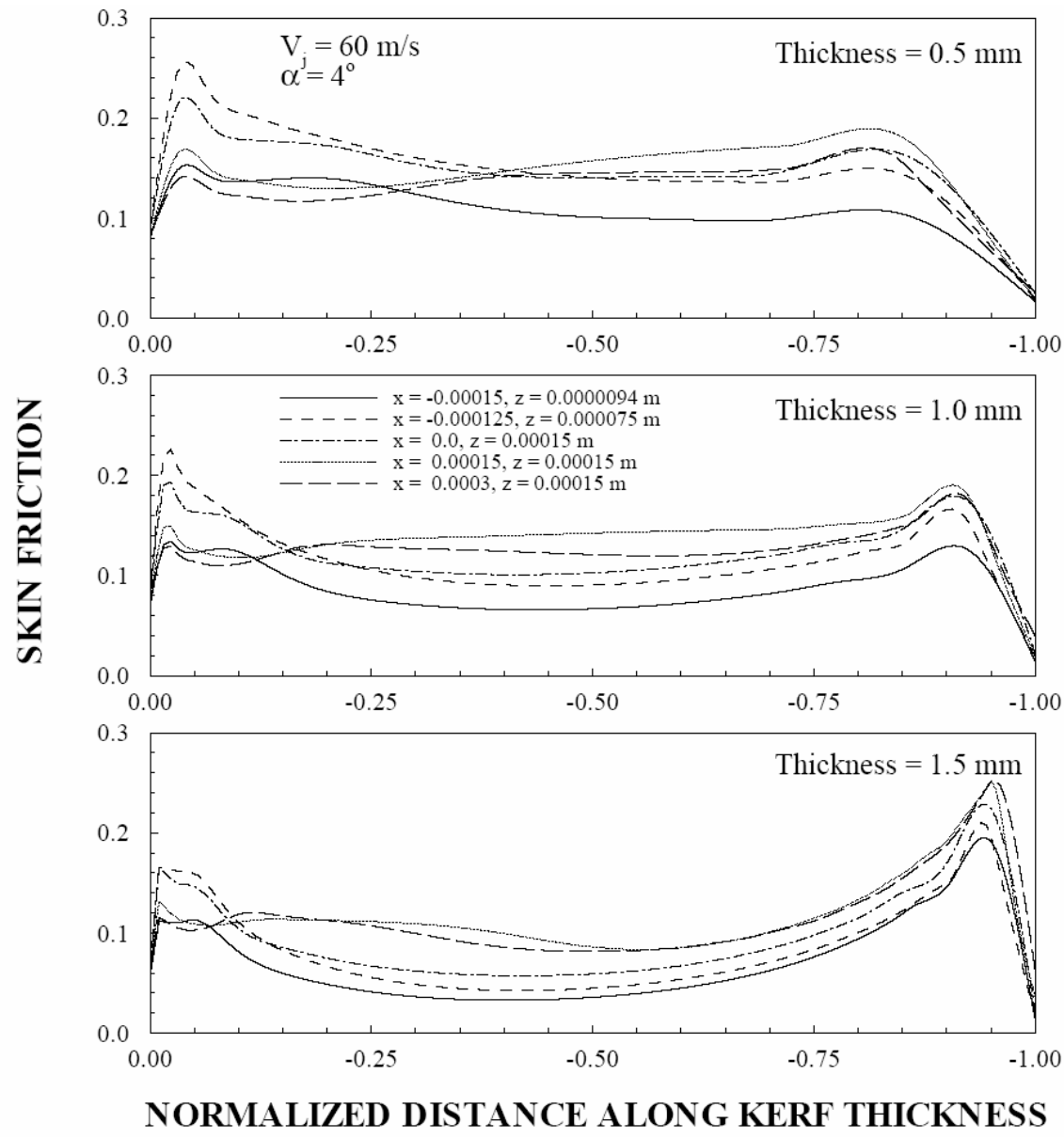

Figure 5.94 Skin friction distribution at five locations along the kerf wall for kerf thickness = 0.5, 1.0, and 1.5 mm, averaged jet velocity = 60 m/s, and kerf wedge angle = 4°

Figures 5.95 shows the skin friction distribution along the normalized kerf thickness for kerf thickness = 0.5, 1.0, 1.5, and 2.0 mm, two averaged jet velocities, and kerf wedge angle = 0°. The location (x = -0.000125, z = 0.000075 m) corresponds to location of maximum Nusselt number. Skin friction increases sharply at the inlet of the kerf. In this region the kerf thickness has no effect on skin friction distribution. A maximum skin friction is attained. Skin friction then decreases as kerf depth increases towards the kerf exit. No significant effect of kerf thickness is observed on skin friction distribution or skin friction values. Figures 5.96 shows the skin friction distribution along the normalized kerf thickness for kerf thickness = 0.5, 1.0, and 1.5 mm, two averaged jet velocities, and kerf wedge angle = 4°. Skin friction increases sharply at the inlet of the kerf until a maximum skin friction is attained. The value of this maximum skin friction decreases as kerf thickness increases. Skin friction then decreases as kerf depth increases. Skin friction then increases until a second maximum skin friction is attained close to the kerf exit in all cases. The value of the second maximum attained skin friction is higher than the first maximum in the case for which kerf thickness = 1.5 mm, and averaged jet velocity at nozzle exit = 60 m/s. Skin friction then decreases sharply towards the kerf exit.

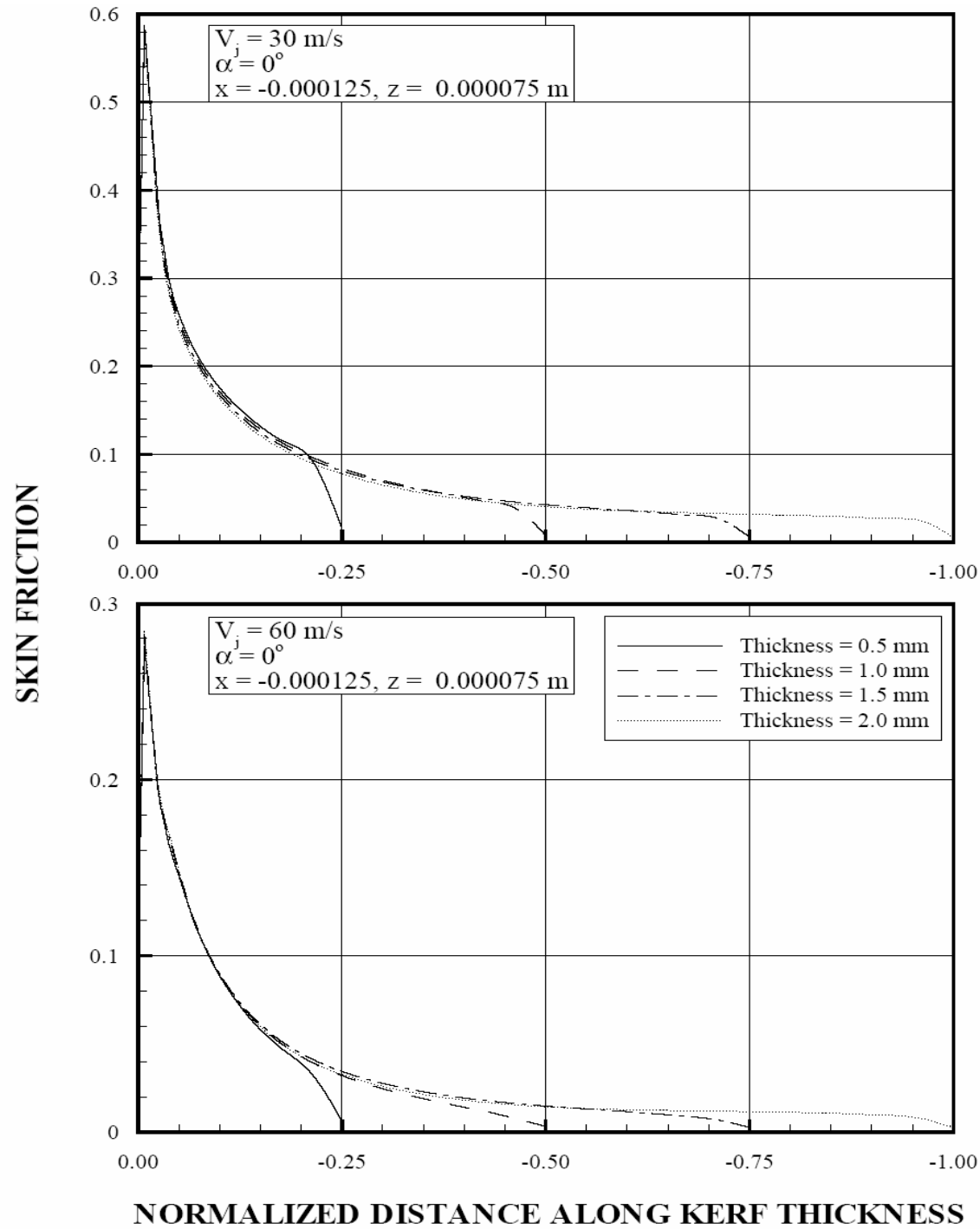

Figure 5.95 Skin friction distribution at location B (x = -0.000125, z = 0.000075 m) along kerf wall for kerf thickness = 0.5, 1.0, 1.5, and 2.0 mm, two averaged jet velocities, and kerf wedge angle = 0°

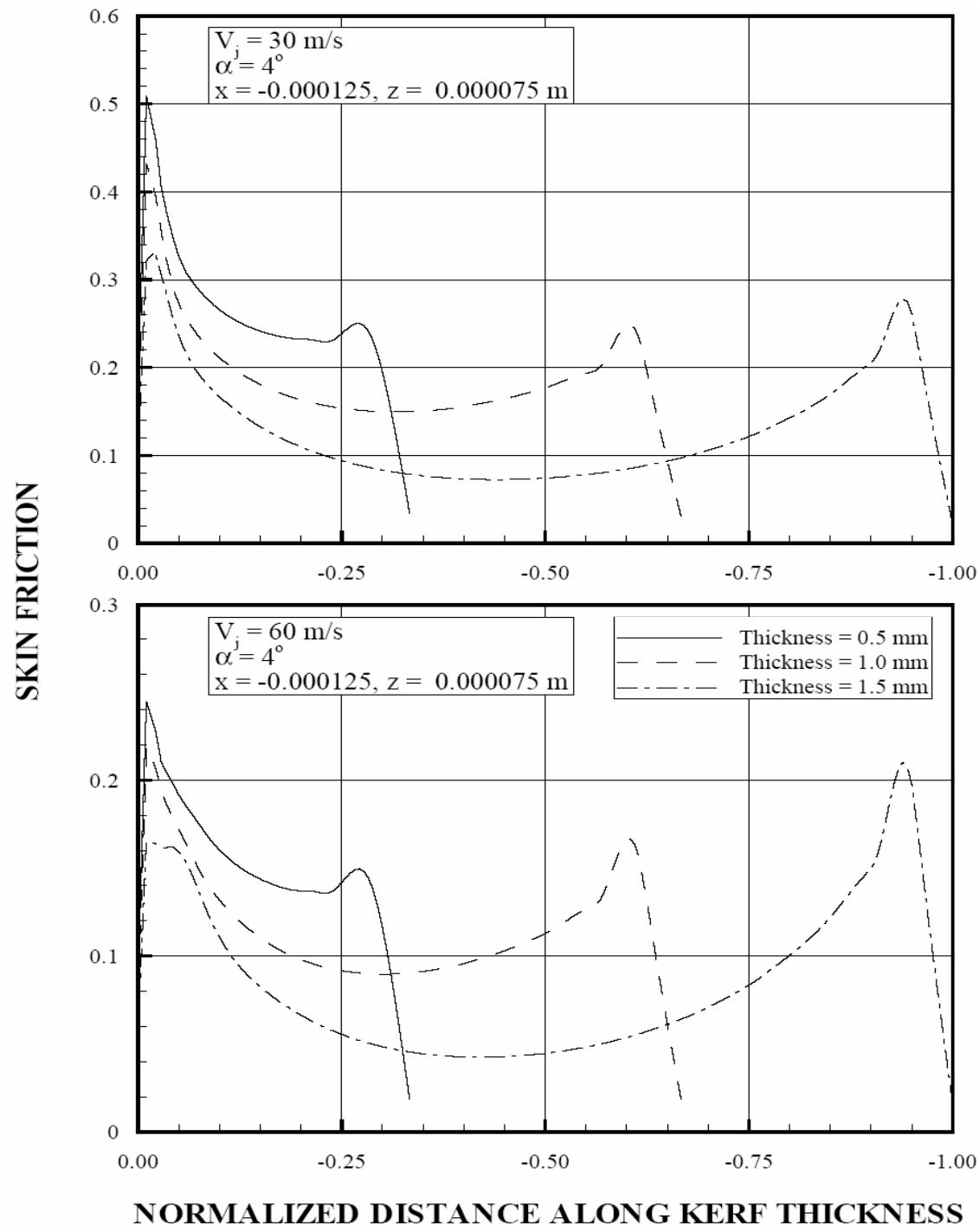

Figure 5.96 Skin friction distribution at location B (x = -0.000125, z = 0.000075 m) along kerf wall for kerf thickness = 0.5, 1.0, and 1.5 mm, two averaged jet velocities, and kerf wedge angle = 4°

5.4 Effect of the Standoff Distance on Heat Transfer Rates and Skin Friction

The effect of the standoff distance on heat transfer rates and skin friction is investigated in this section by considering a kerf of depth (thicknesses) 2 mm and kerf wedge angle, $\alpha = 0°$. The dimensionless standoff distances (H/D, D = nozzle diameter) accommodated in this investigation are 2.2 and 3.0. Results will be shown for two averaged jet velocities at nozzle exit: 30 m/s and 60 m/s.

Figures 5.97 and 5.98 show normalized velocity contours in the symmetry plane for kerf thickness = 2.0 mm, two averaged jet velocities, and two dimensionless standoff distances. The jet exits the nozzle and exchanges momentum with the ambient forming a free boundary or a shear layer as it approaches the kerf top surface. The width of the free boundary of the jet increases slightly with increasing standoff distance as the jet approaches the kerf surface. After impingement onto the kerf occurs, the flow undergoes radial acceleration in the region close to the kerf side wall. No significant effect of the standoff distance on the flow development in the kerf is observed. It should be recalled that this judgment is based on the visualization of velocity magnitude contours in symmetry plane.

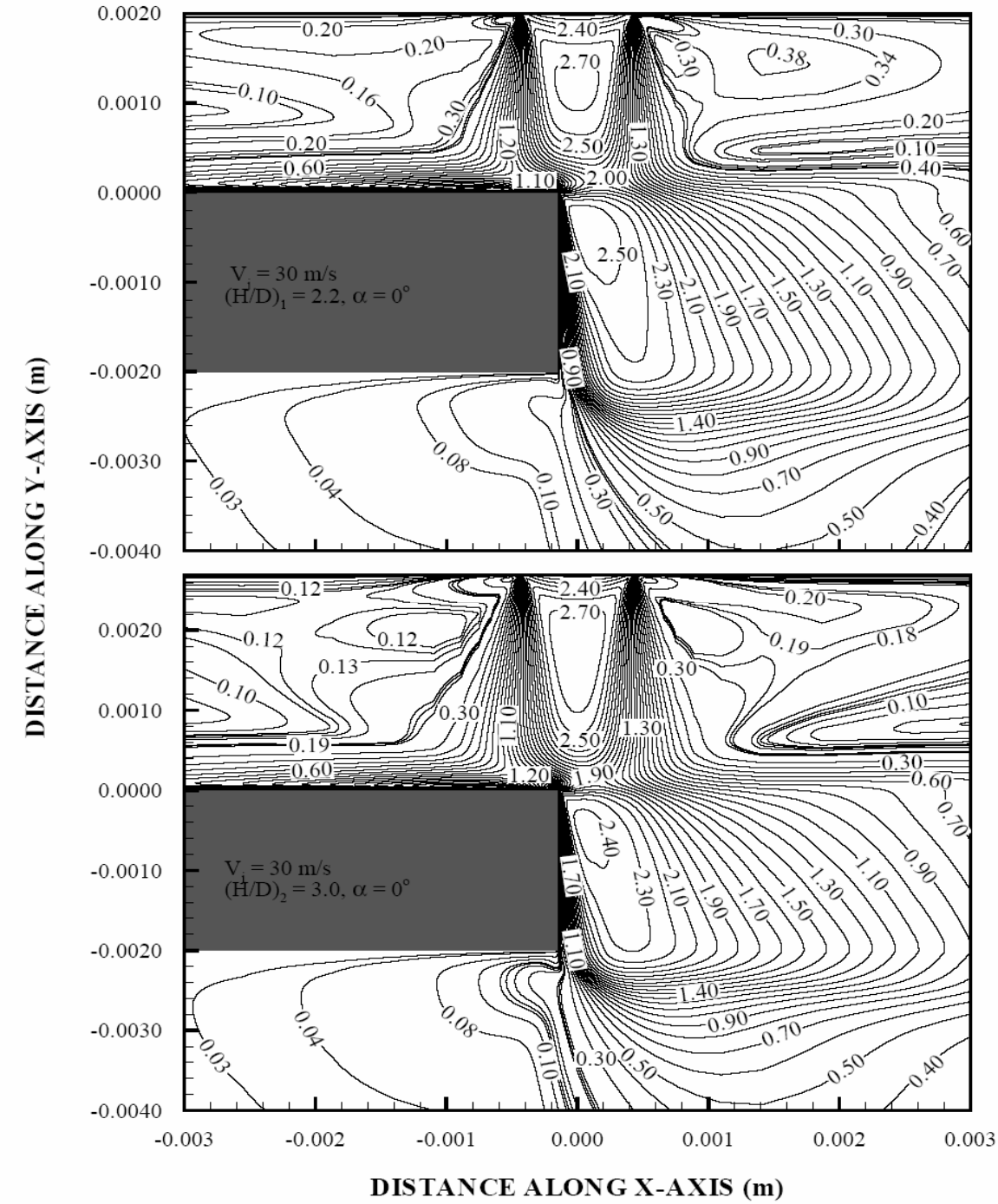

Figure 5.97 Normalized velocity magnitude (V/V_j) for jet averaged velocity of 30 m/s, kerf thickness of 2.0 mm, kerf wedge angles of 0°, and dimensionless standoff distances of 2.2 and 3.0

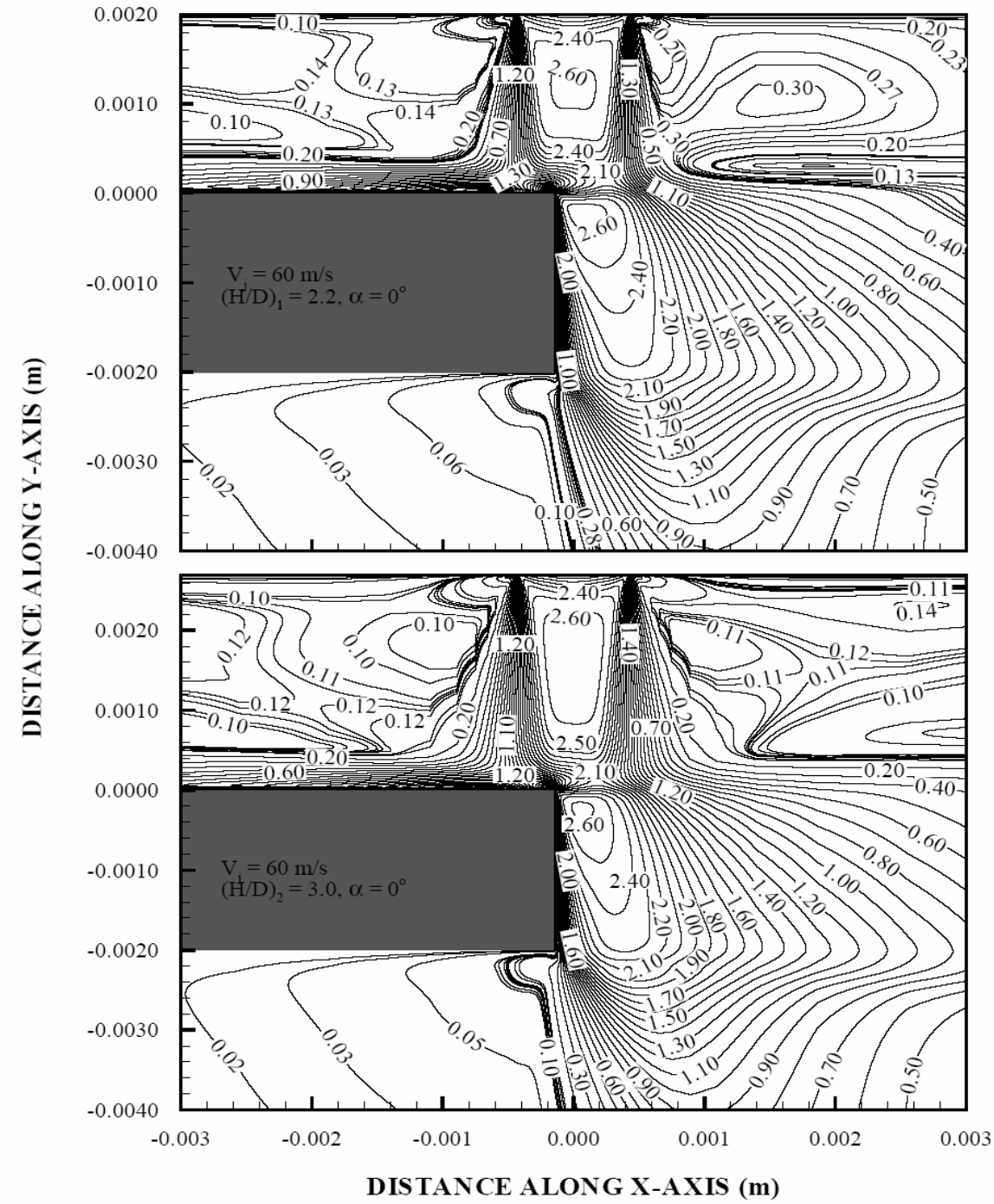

Figure 5.98 Normalized velocity magnitude (V/V_j) for jet averaged velocity of 60 m/s, kerf thickness of 2.0 mm, kerf wedge angles of 0°, and dimensionless standoff distances of 2.2 and 3.0

Figures 5.99 and 5.100 show pressure coefficient contours in the symmetry plane for kerf thickness = 2.0 mm, two averaged jet velocities, and two dimensionless standoff distances. The negative pressure coefficient observed in the jet outer boundaries preceding impingement indicates the reverse flow and the possible formation of circulation cell in this region. The decrease in the flow velocity as the flow approaches the kerf is associated with pressure increase in this region. No significant effect of standoff distance on the pressure coefficient distribution in the flow field is observed for the range of parameters considered in the present analysis.

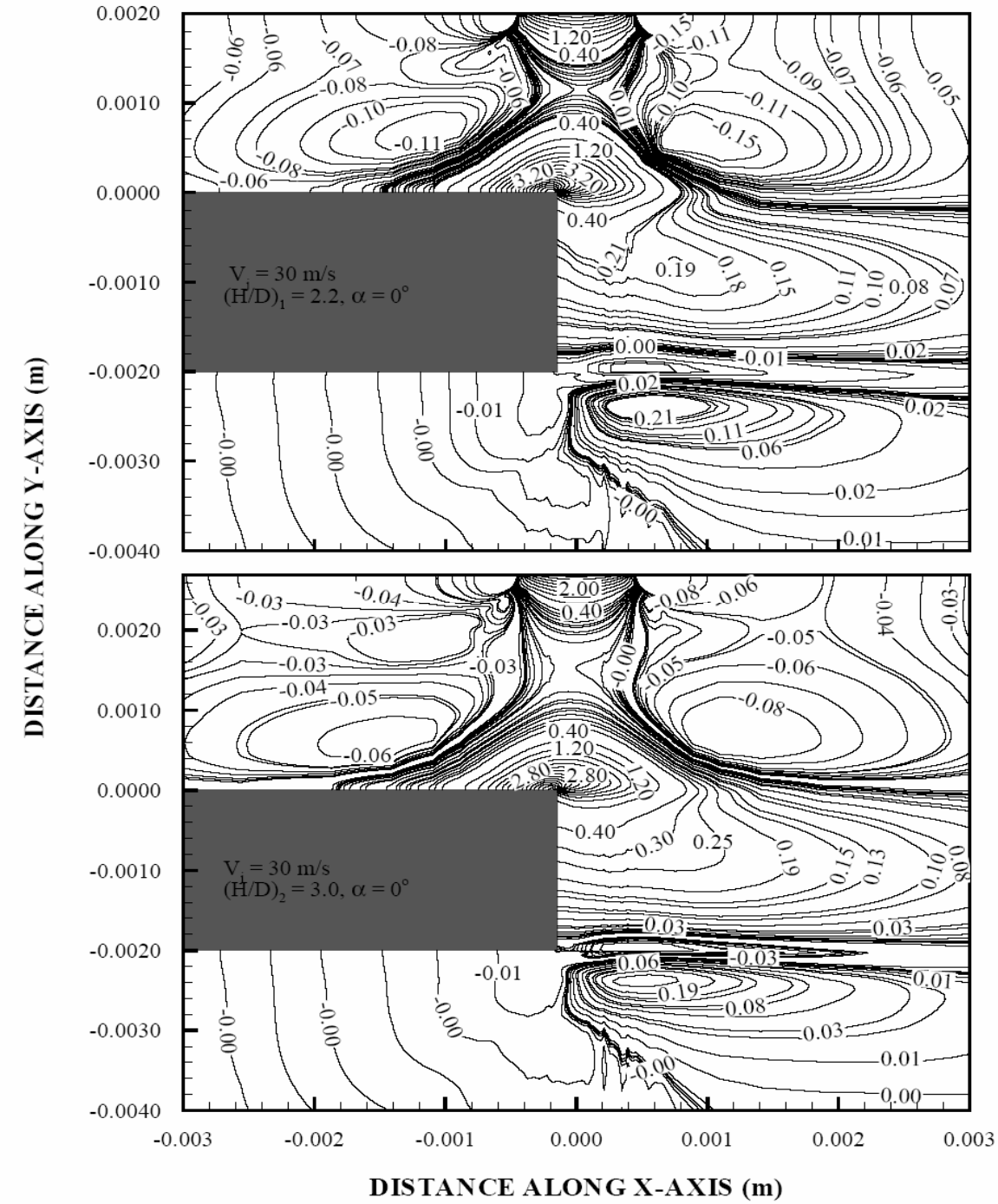

Figure 5.99 Pressure coefficient for jet averaged velocity of 30 m/s, kerf thickness of 2.0 mm, kerf wedge angles of 0°, and dimensionless standoff distances of 2.2 and 3.0

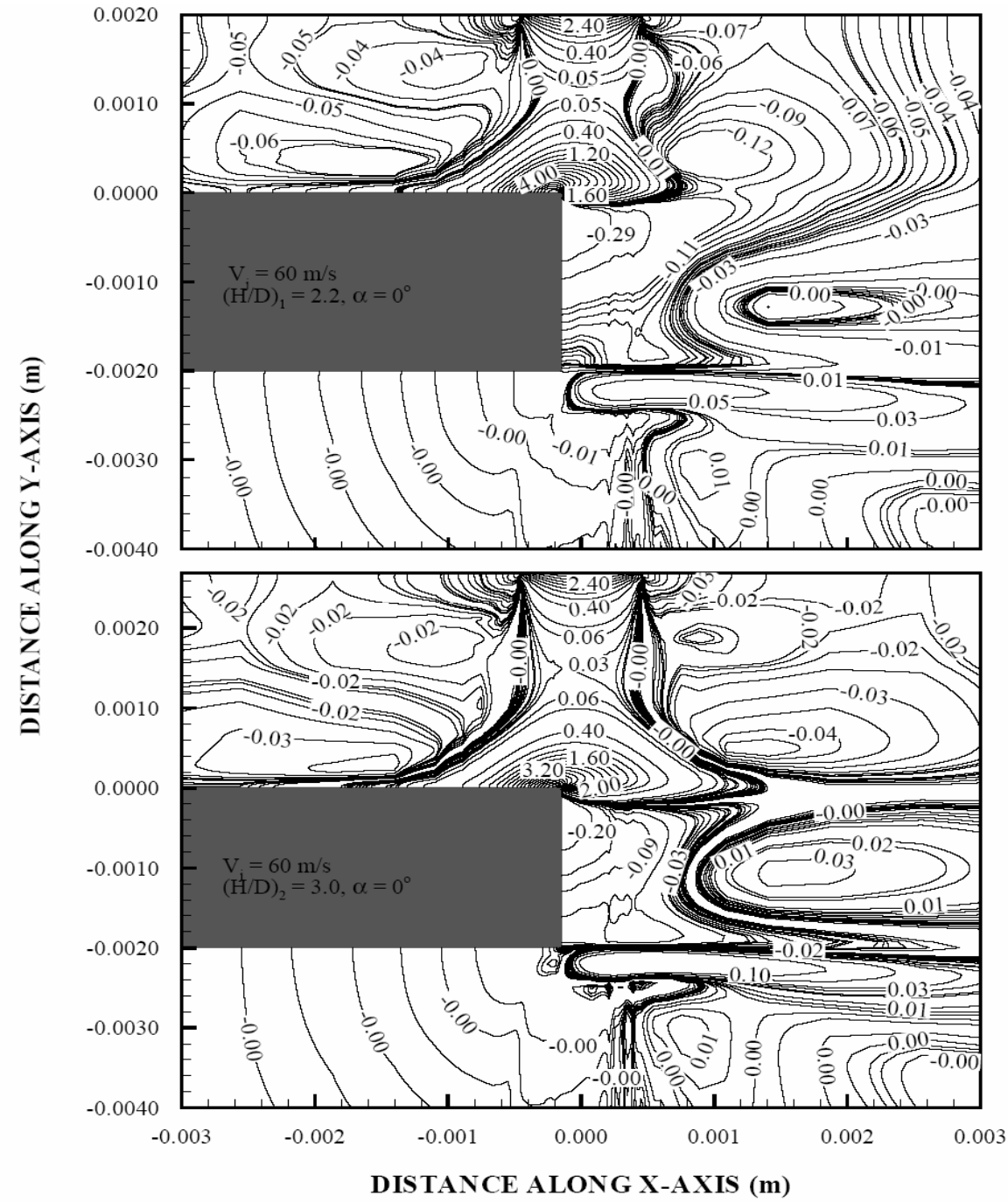

Figure 5.100 Pressure coefficient for jet averaged velocity of 60 m/s, kerf thickness of 2.0 mm, kerf wedge angles of 0°, and dimensionless standoff distances of 2.2 and 3.0

5.101 and 5.102 show dimensionless temperature contours in the symmetry plane for kerf thickness = 2.0 mm, two averaged jet velocities, and two dimensionless standoff distances. The free jet temperature is almost equal to the jet temperature at nozzle exit. Fluid temperature increases in the kerf, with remarkable increase close to the kerf wall. Temperature first decreases and later increases in the fluid at positive x-axis locations away from the jet axis. No significant effect of the standoff distance on the temperature field is observed for the range of parameters considered in this analysis.

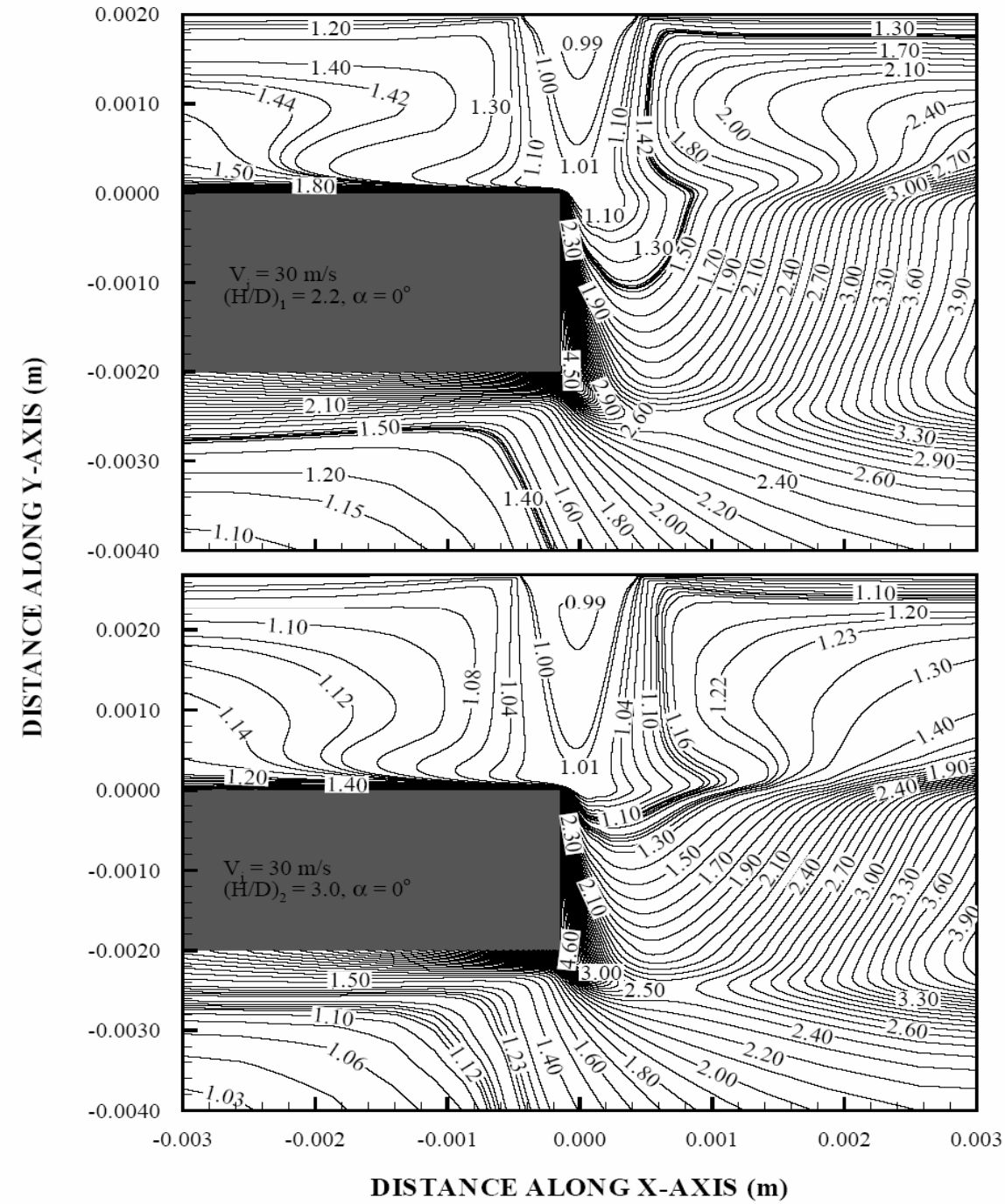

Figure 5.101 Normalized temperature (T/T_j) for jet averaged velocity of 30 m/s, kerf thickness of 2.0 mm, kerf wedge angles of 0°, and dimensionless standoff distances of 2.2 and 3.0

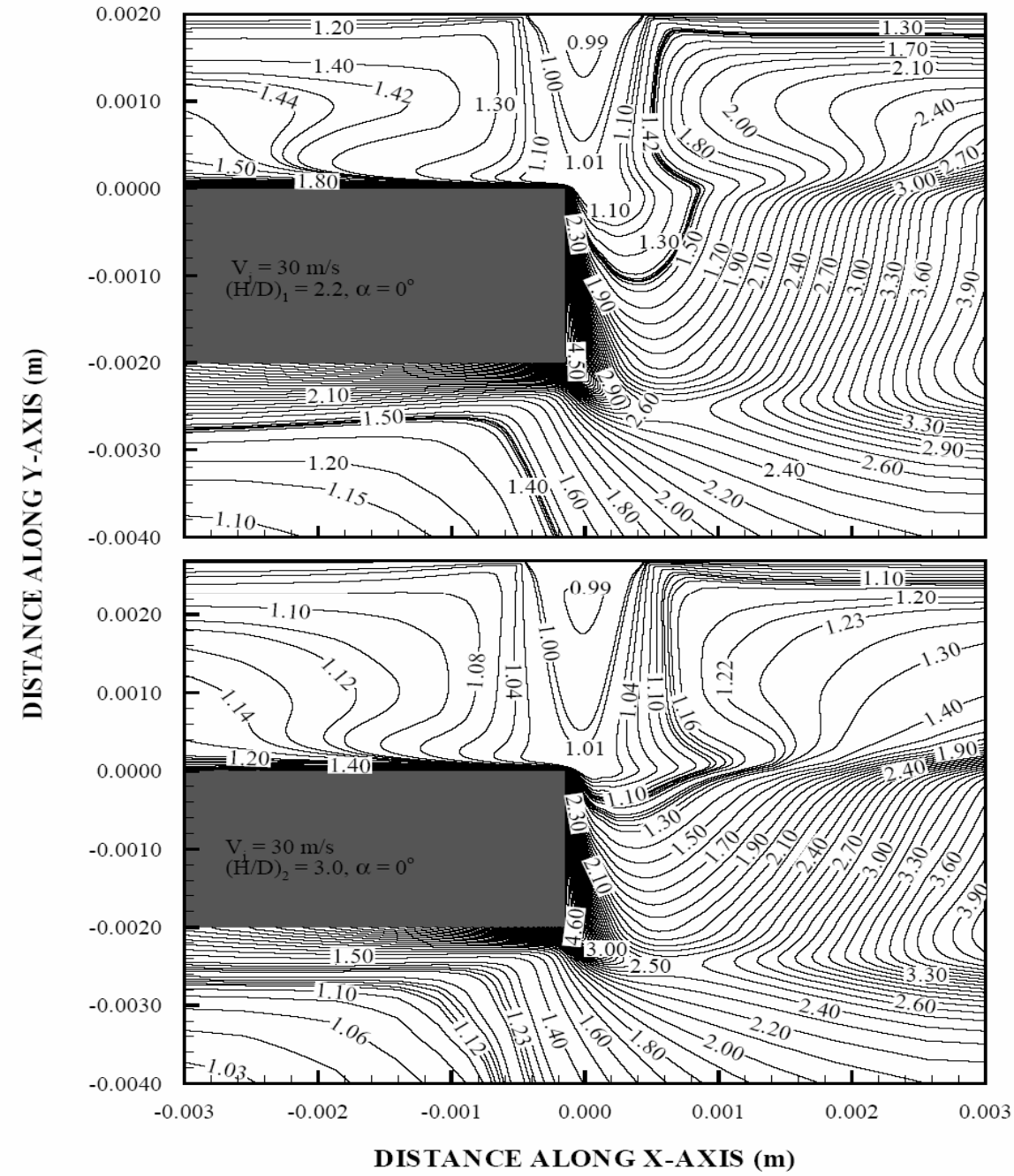

Figure 5.102 Normalized temperature (T/T_j) for jet averaged velocity of 60 m/s, kerf thickness of 2.0 mm, kerf wedge angles of 0°, and dimensionless standoff distances of 2.2 and 3.0

Figure 5.103 shows velocity magnitude distribution along the laser beam axis for kerf thickness = 2.0 mm, two averaged jet velocities, and two dimensionless standoff distances. It should be noted that the locations y = 0 and y = -0.002 represent the workpiece surface and kerf depth (workpiece or kerf thickness) respectively. The location of nozzle exit form the kerf surface varies in accordance with the dimensionless standoff distance. The jet velocity increases after exiting from the nozzle reaching the first maximum velocity after a distance of about one nozzle diameter, after which it reduces to a minimum just before impingement onto the kerf surface. The velocity then increases until it reaches second maximum velocity at a location very close to kerf surface, after which it decreases as flow approaches kerf exit. The standoff distance does not have significant effect of centerline velocity distribution.

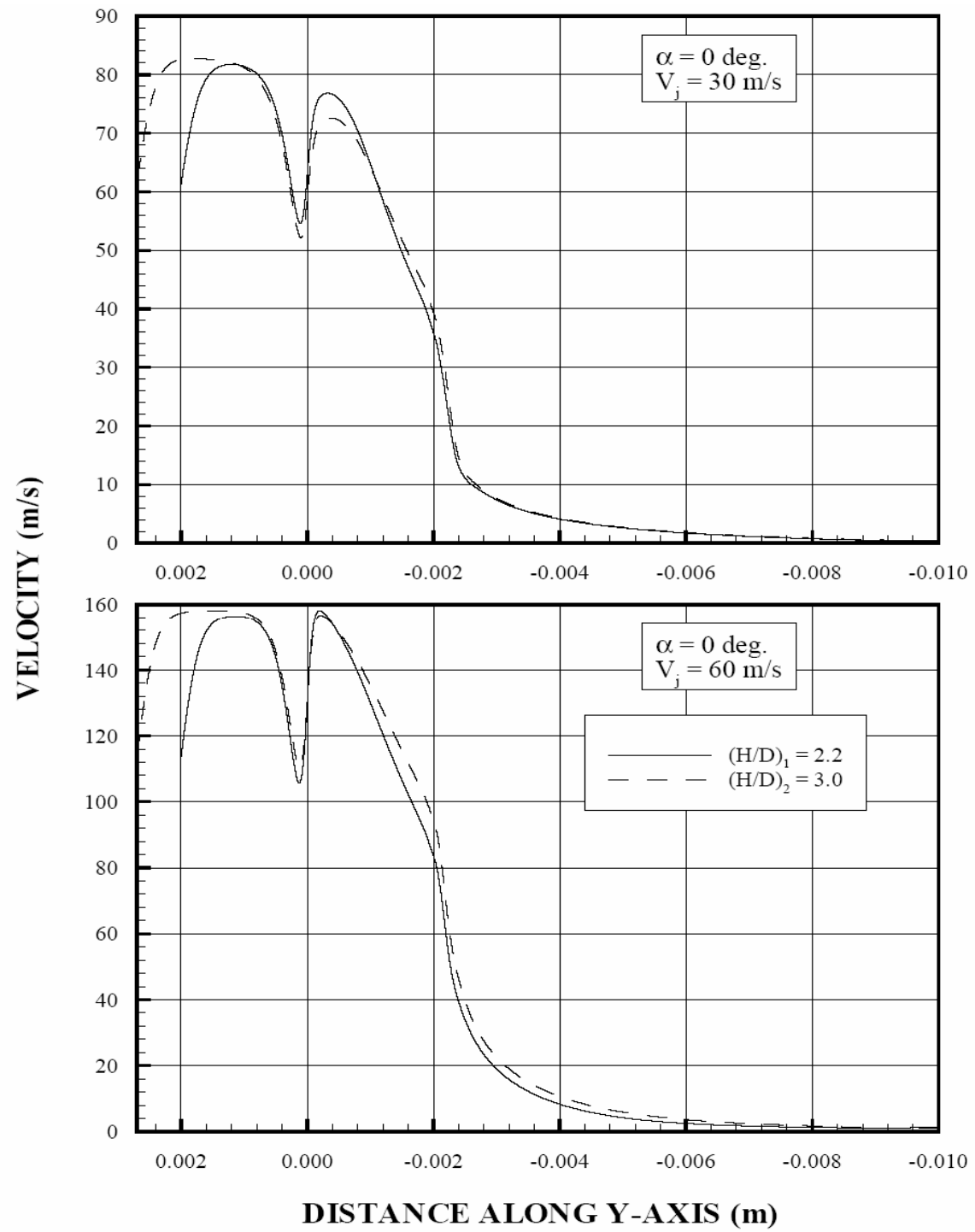

Figure 5.103 Velocity magnitude along laser beam axis for two different averaged jet velocities, kerf thickness of 2.0 mm, and two dimensionless standoff distances

Figure 5.104 shows pressure distribution along the laser beam axis for kerf thickness = 2.0 mm, two averaged jet velocities, and two dimensionless standoff distances. Static pressure reduces after exiting the nozzle because of jet expansion and then increases to a maximum at a location close to the kerf top surface because of stagnation formation and blockage effect of the kerf. Pressure drop occurs close to kerf surface and continues in the kerf because of the jet radial expansion in this region.

Figure 5.105 shows temperature distribution along the laser beam axis for kerf thickness = 2.0 mm, two averaged jet velocities, and two dimensionless standoff distances. Temperature increases onset fluid enters the kerf region until a maximum is reached close to the kerf exit. Temperature then decreases as fluid expands after exiting the kerf. The standoff distance has no significant effect on centerline temperature distribution.

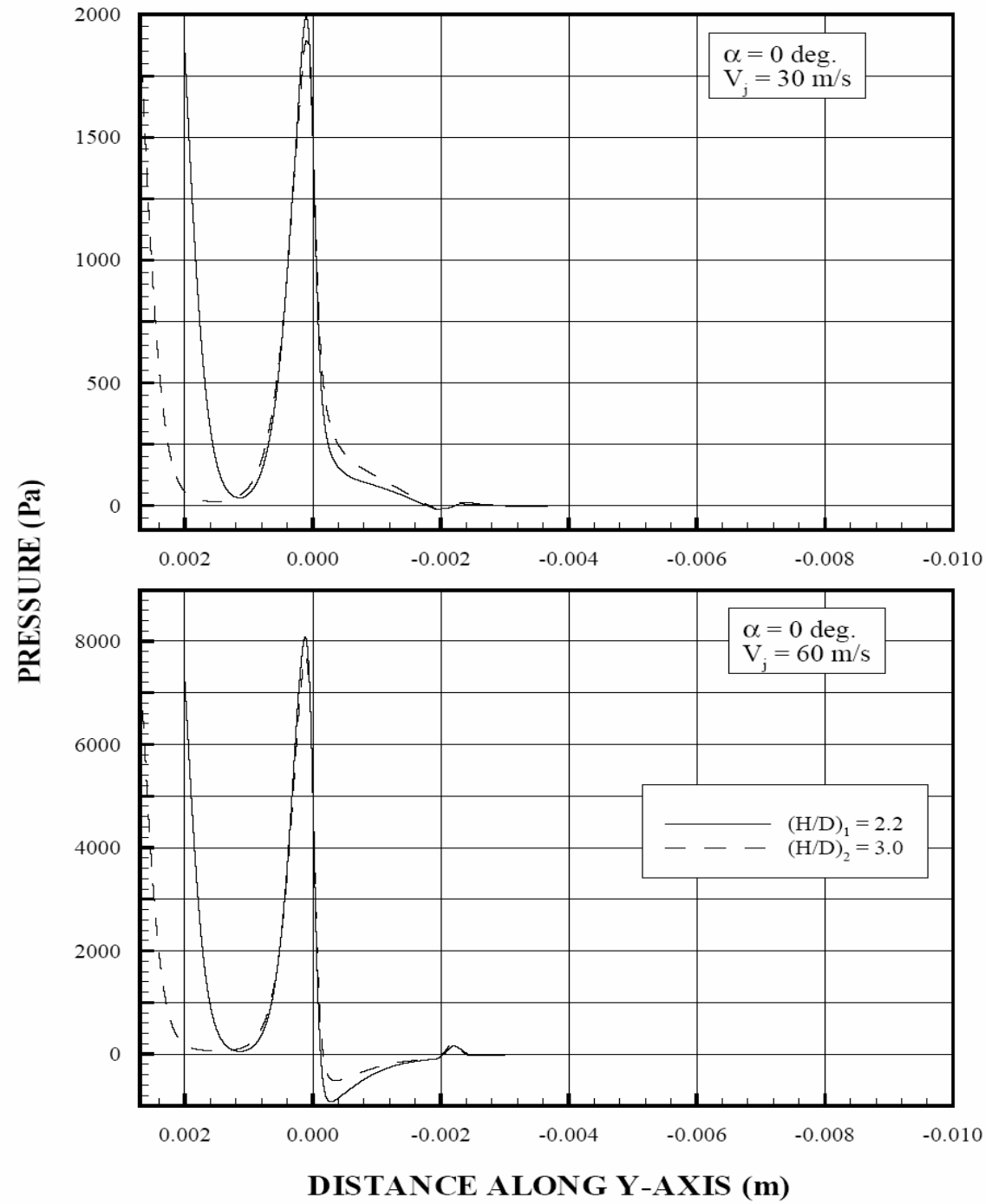

Figure 5.104 Pressure distribution along laser beam axis for two different averaged jet velocities, kerf thickness of 2.0 mm, and two dimensionless standoff distances

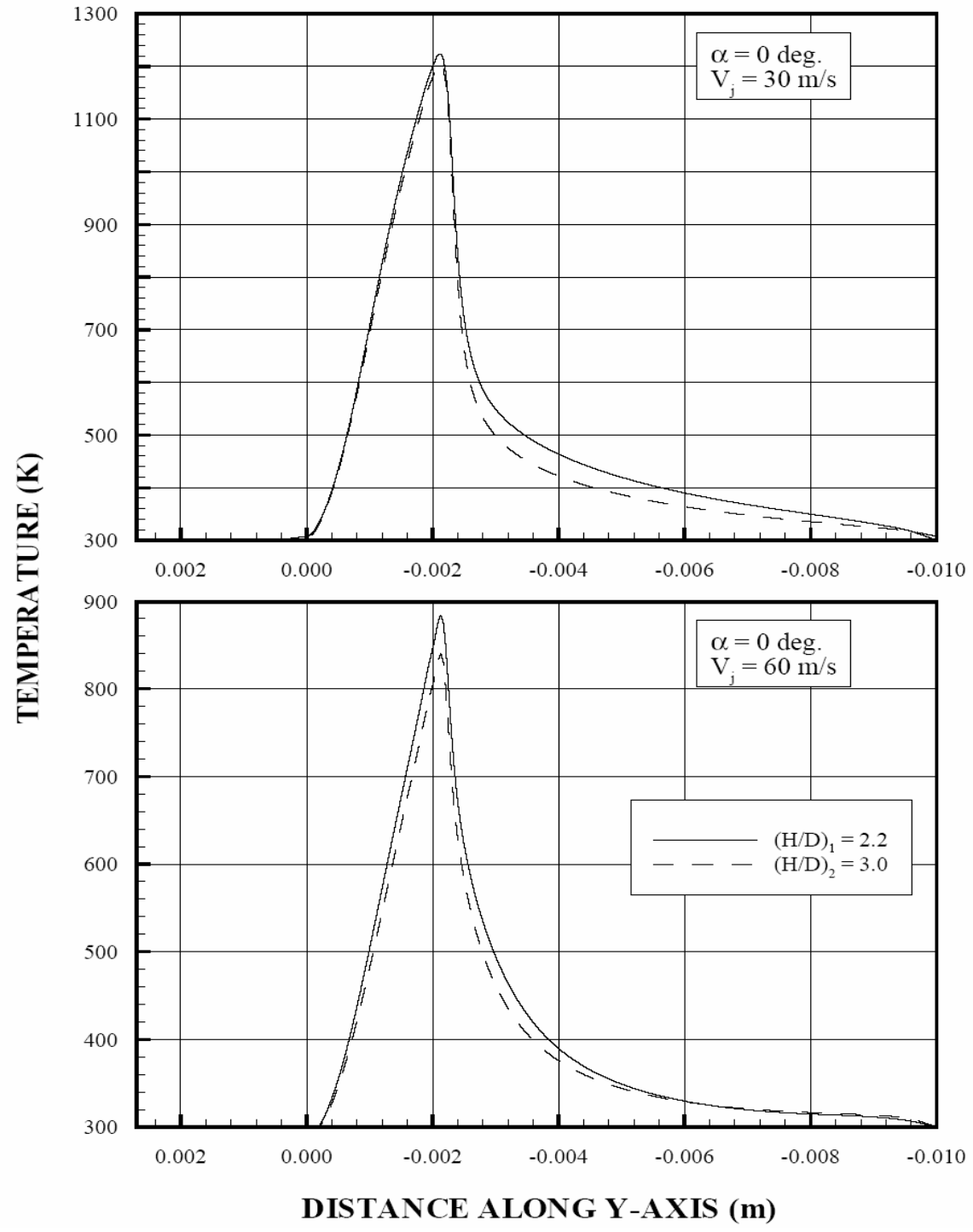

Figure 5.105 Temperature distribution along laser beam axis for two different averaged jet velocities, kerf thickness of 2.0 mm, and two dimensionless standoff distances

Figure 5.106 shows the Nusselt number distribution along the normalized kerf wall thickness for two averaged jet velocities at nozzle exit and two dimensionless standoff distances. The kerf wall thickness is normalized with the maximum thickness; i.e., normalized kerf wall thickness = 0 represents the kerf inlet and normalized kerf wall thickness = -1 is the kerf exit. The curves are plotted at a location B (x = -0.000075 m; z = 0.000129 m) where the Nusselt number attained the highest value. The Nusselt number increases sharply from the kerf edge due to convective cooling of the jet in the kerf. The Nusselt number decreases gradually in the kerf, increases slightly to attain a second maximum whose value is lower than the first maximum, and then reduces sharply towards the kerf exit. The Nusselt number is higher at the larger standoff distance, which indicates more heat transfer. This can be associated with the increase in the jet turbulence due to the larger standoff distance. The effect is slightly more pronounced at the lower averaged jet velocity at nozzle exit.

Figure 5.107 shows the skin friction distribution along the normalized kerf thickness for different averaged jet velocities at the nozzle exit and two dimensionless standoff distances. The skin friction increases sharply at the inlet of the kerf due to the flow acceleration within the kerf. As the kerf depth increases, the skin friction reduces. This is attributed to the shear layer developed within the vicinity of the kerf wall, which is influenced by high wall temperature because of the formation of high thermodynamic pressure in this region. The effect of standoff distance on skin friction distribution is almost significant although a slight increase in skin friction is observed at the higher averaged jet velocity.

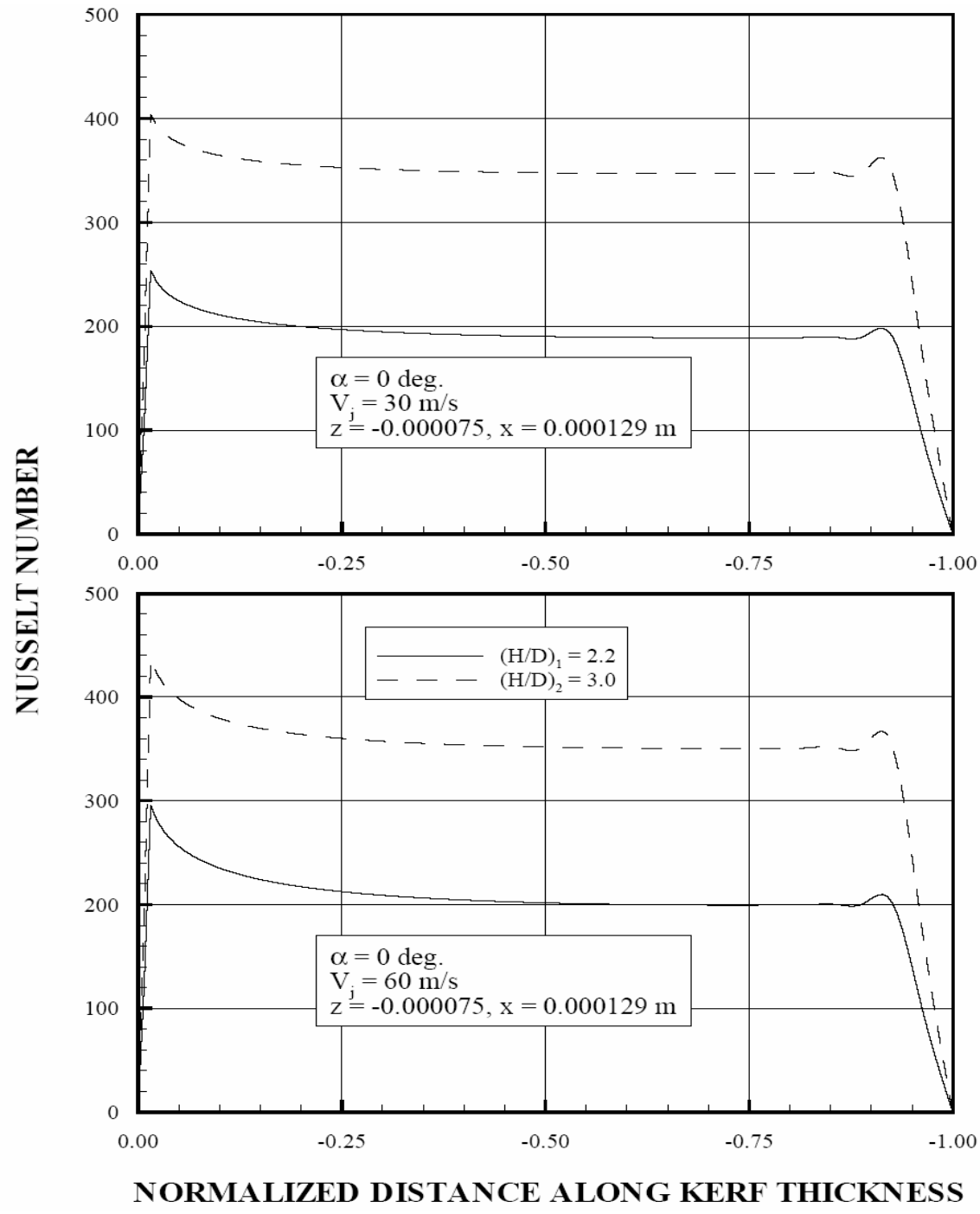

Figure 5.106 Nusselt number distribution along the normalized kerf wall thickness for two different averaged jet velocities at nozzle exit and two dimensionless standoff distances

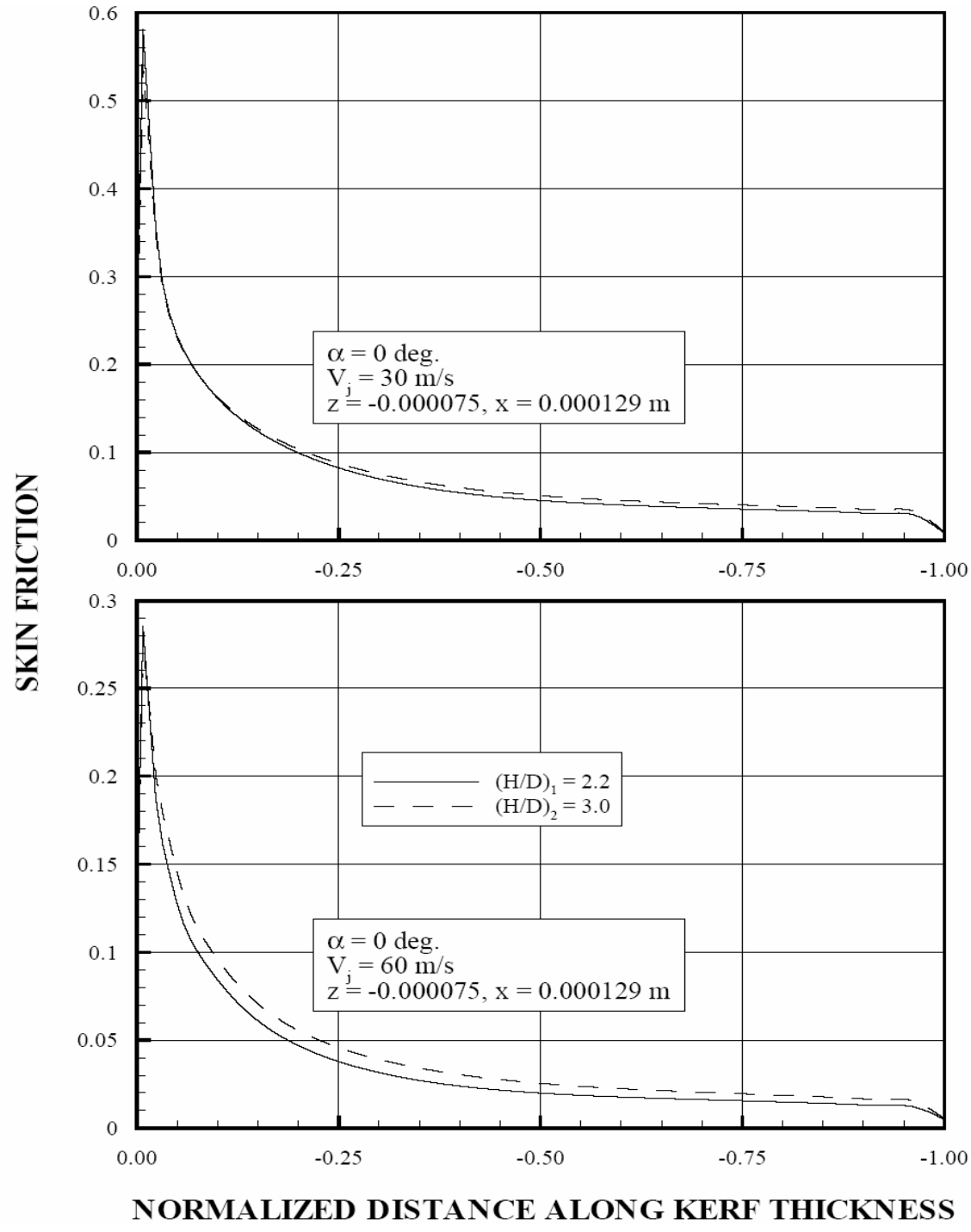

Figure 5.107 Skin Friction distribution along the normalized kerf wall thickness for two different averaged jet velocities at nozzle exit and two dimensionless standoff distances

5.5 Effect of Averaged Jet Velocity, Kerf Wedge Angle, Kerf Depth, and Standoff Distance on Exiting Mass Flow Rate Ratio, Average Nusselt Number, and Average Skin Friction

A mass flow rate factor χ is defined as the ratio of the mass flow rate ejected from the bottom of the kerf to the mass flow rate at the inlet. It is important to study the effect of the various system parameters on χ because it indicates the efficiency of the process and the effective mass entering the kerf and contributing to melt flow ejection and to cooling processes. It also gives an indication of the strength of the gas jet departing from the bottom of the kerf. Another important parameter worth of consideration is the average Nusselt number. The average Nusselt number gives an indication of the amount and rate at which heat is transferred from high temperature kerf wall. It is true that Nusselt number distribution has been determined at several locations in the above sections; however, the average Nusselt number gives a better indication of how effective the impinging gas jet is in cooling the surface. The last parameter that is studied in this section is the average heat transfer coefficient, which gives an indication of how effective the impinging gas jet is in the melt removal process.

The local heat flux q'' distribution along the kerf side wall with the imposed temperature is determined using FLUENT. The local heat flux q'' may be expressed as

$$q'' = h(T_w - T_j)$$

where h is the local convection coefficient;

T_w is the fixed wall temperature;

and T_j is the jet temperature.

T_j and T_w constitute two fixed reference temperatures for computing the wall/gas heat transfer coefficient. The corresponding local Nusselt number Nu for impinging jet configuration can be defined as follows with the characteristic length being the nozzle hydraulic diameter [93, 20]:

$$Nu = hD/\lambda_g$$

where D is nozzle diameter and λ_g is thermal conductivity of the gas.

The total heat transfer rate Q may be obtained by integrating the local flux over the entire three dimensional surface of the kerf side wall. That is,

$$Q = \int_{A_s} q'' dA_s$$

The average convective wall heat transfer coefficient is consequently defined as:

$$\bar{h} = \frac{1}{A_s} \frac{Q}{T_w - T_j}$$

where A_s is the surface area of the kerf side wall. The area associated with each configuration is reported by FLUENT and the obtained values are verified using Tecplot 360.

The corresponding average Nusselt number as:

$$\overline{Nu} = \frac{\bar{h}D}{\lambda_g}$$

The average Nusselt number is reported in the following table as Nu_{av}.

A similar procedure is followed to determine the average wall shear stress which will be divided by ($\frac{1}{2}\rho V_j^2$) to obtain the average skin friction C_{fav}.

Table A.1 provided in Appendix A gives a complete record of the abovementioned three parameters, χ, Nu_{av} , and C_{fav} for all the geometric and flow parameters considered in the present work.

In general, for kerf depth = 0.0005 m, the mass flow rate factor χ increases with increasing averaged jet velocity at nozzle exit for all kerf wall wedge angles and the two standoff distances. At a given averaged jet velocity and given standoff distance, χ decreases with increasing kerf wall wedge angle. Taking into considerations the errors that might be involved in computing the above tabulated values, we can say that at a given averaged jet velocity and given kerf wedge angle, χ increases with increasing standoff distance. However this is not true in few of the averaged jet velocity – kerf wedge angle combinations. The same trend of variation in χ are observed for the case for which kerf depth = 0.0010 m. However, it is clear that for the two cases for which kerf wedge angle = 4° and 6°, χ decreases with increasing standoff distance at a given averaged jet velocity. The same trend of variation in χ are observed for the case for which kerf depth = 0.0015 m. However, it is clear that for the two cases for which kerf wedge angle = 2° and 4°, χ decreases with increasing standoff distance at a given averaged jet velocity. The same trend of variation in χ are observed for the case for which kerf depth = 0.0020 m. However, for the case for which kerf wedge angle = 4° and 6°, χ decreases with increasing standoff distance at the two lowest averaged jet velocities and remains the same at the two highest averaged jet velocities.

In general, for kerf depth = 0.0005 m, the average Nusselt number increases with increasing averaged jet velocity at nozzle exit for kerf wall wedge angles = 0°, 2°, and 4°

and the two standoff distances. For kerf wall wedge angles = 6°, increasing averaged jet velocity from 30 m/s to 40 m/s increases average Nusselt number. However, Nusselt number reduces with further increase in averaged jet velocity. This is almost true at the two standoff distances. At a given averaged jet velocity and given standoff distance, a large increase in the average Nusselt number is observed with increasing kerf wall wedge angle. The average Nusselt number almost triples as the kerf wall wedge angle changes from 0° to 4°. Another increase of almost 50% is observed as the kerf wall wedge angle changes from 4° to 6°. This indicates that at higher kerf wall wedge angles, a low mass flow rate can achieve a significant amount of cooling as compared to cases of lower kerf wall wedge angles. For kerf wedge angle = 0° and a given velocity, average Nusselt number increases with increasing standoff distance. Mostly, it decreases with increasing standoff distance for the other kerf wall wedge angles. In general, for kerf depth = 0.0010 m, the average Nusselt number increases with increasing averaged jet velocity at nozzle exit for kerf wall wedge angle = 0° and the two standoff distances. At the other kerf wedge angles the trend of variation of average Nusselt number is difficult to identify. This can be due to numerical errors or it can be that the trend of variation is random. At a given averaged jet velocity and given standoff distance, a large increase in the average Nusselt number is observed with increasing kerf wall wedge angle. The average Nusselt number almost triples as the kerf wall wedge angle changes from 0° to 4°. Another increase of almost 50% is observed as the kerf wall wedge angle changes from 4° to 6°. At a given velocity and given kerf wall wedge angle, average Nusselt number increases with increasing standoff distance. In general, for kerf depth = 0.0015 m, the average

Nusselt number increases with increasing averaged jet velocity at nozzle exit for kerf wall wedge angle = 0° and the two standoff distances. At the other kerf wedge angles the trend of variation of average Nusselt number is difficult to identify. At a given averaged jet velocity and given standoff distance, a large increase in the average Nusselt number is observed with increasing kerf wall wedge angle. The average Nusselt number almost triples as the kerf wall wedge angle changes from 0° to 4°. For kerf wall wedge angle = 0°, 2°, and 4° and given averaged jet velocity, average Nusselt number increases with increasing standoff distance. The opposite is true for kerf wedge angle = 6°. In general, for kerf depth = 0.0020 m, the average Nusselt number increases with increasing averaged jet velocity at nozzle exit for kerf wall wedge angle = 0° and 2° and the two standoff distances. At a given averaged jet velocity and given standoff distance, a large increase in the average Nusselt number is observed with increasing kerf wall wedge angle. The average Nusselt number almost doubles as the kerf wall wedge angle changes from 0° to 2°. At a given averaged jet velocity and given kerf wall wedge angle, average Nusselt number increases with increasing standoff distance. It almost doubles for the case for which kerf wedge angle = 2°.

In general, for kerf depth = 0.0005 m, the average skin friction decreases with increasing averaged jet velocity at nozzle exit for all kerf wall wedge angles and the two standoff distances. At a given averaged jet velocity and given standoff distance, the average skin friction increases with increasing kerf wall wedge angle. At a given averaged jet velocity and given kerf wedge angle, average skin friction increases with increasing standoff distance. This is true for kerf wall wedge angles = 0° and 2°. It is also

true for the other wedge angles but only at the higher velocities. In general, for kerf depth = 0.0010 m, the average skin friction decreases with increasing averaged jet velocity at nozzle exit for all kerf wall wedge angles and the two standoff distances. At a given averaged jet velocity and given standoff distance, the average skin friction increases with increasing kerf wall wedge angle. At a given averaged jet velocity and given kerf wedge angle, average skin friction increases with increasing standoff distance. This is only true for kerf wall wedge angles = 0° and 2°. The opposite is observed at the other kerf wedge angles. For kerf depth = 0.0015 m, the average skin friction decreases with increasing averaged jet velocity at nozzle exit for all kerf wall wedge angles and the two standoff distances. At a given averaged jet velocity and given standoff distance, the average skin friction increases with increasing kerf wall wedge angle. At a given averaged jet velocity and given kerf wedge angle, average skin friction increases with increasing standoff distance. This is only true for kerf wall wedge angles = 0° and 2°. The opposite is observed at the other kerf wedge angle. For kerf depth = 0.0020 m, the average skin friction decreases with increasing averaged jet velocity at nozzle exit for all kerf wall wedge angles and the two standoff distances. At a given averaged jet velocity and given standoff distance, the average skin friction increases with increasing kerf wall wedge angle. At a given averaged jet velocity and kerf wedge angle = 0°, average skin friction increases with increasing standoff distance. The opposite is observed for the case for which kerf wedge angle = 2°.

CHAPTER 6

CONCLUSIONS AND RECOMMENDATIONS

Three-dimensional numerical simulations were conducted to study the fluid flow and heat transfer phenomena of nitrogen gas jet emerging from a conical convergent nozzle and impinging onto a laser produced kerf. This study presented numerical consideration of the three-dimensional kerf geometry generated during the laser cutting process. The kerf wall temperature is kept at 1500 K (almost the melting temperature of the substrate material) to resemble the laser cutting situation.

The fluid flow and heat transfer are governed by the Favre-averaged Navier-Stokes and energy transport equations. The renormalization group (RNG) k-ε model is used for closure of the Favre-averaged transport equations. Near wall modeling is based on the enhanced wall treatment. A finite-volume approach is employed to discretize the governing equations and the SIMPLE algorithm is used for adjusting the pressure field so as to satisfy continuity. FLUENT 6.2.16 is utilized to conduct the simulations using a segregated and implicit solver. The CFD solver is validated against a recent case study reported in the literature. Moreover, the solution is determined to be grid independent. The parameters considered in this study are four averaged jet velocities at nozzle exit, two dimensionless standoff distances, four different kerf depths, and four kerf wall wedge angles (Recall that the number of kerf wedge angles accommodated depends on

thickness). Nusselt number and skin friction distributions at the surface of the kerf wall are examined. Moreover, the mass flow rate factor, average Nusselt number at kerf wall surface, and average skin friction at kerf wall surface are estimated.

6.1 EFFECTS OF AVERAGED JET VELOCITY

- It is found that the flow first accelerates in the kerf inlet and then decelerates towards the kerf exit. This is because of the pressure buildup in the kerf.
- Increasing the mean jet velocity at the nozzle exit enhances the values of the Nusselt number, which is more pronounced for the larger kerf wall wedge angles.
- The skin friction increases sharply at the kerf inlet and decreases sharply towards the kerf exit for the kerf wall wedge angle of 0°, which is more pronounced for the low averaged jet velocity at the nozzle exit.
- The mass flow rate factor χ, defined as the ratio of the mass flow rate ejected from the bottom of the kerf to the mass flow rate at the inlet, increases with increasing averaged jet velocity at nozzle exit for a given kerf wall wedge angle, given standoff distance, and given kerf wall thickness.
- In general, the average Nusselt number at kerf wall surface increases with increasing averaged jet velocity at nozzle exit for a given kerf wall wedge angle, given standoff distance, and given kerf wall thickness.
- In general, the average skin friction decreases with increasing averaged jet velocity at nozzle exit for a given kerf wall wedge angle, given standoff distance, and given kerf wall thickness.

6.2 EFFECTS OF KERF WEDGE ANGLE

- Radial expansion of the jet in the kerf region gets more pronounced as the kerf wedge angle increases. Higher velocity magnitudes are observed in the kerf for larger kerf wedge angles.
- As the kerf wedge angle increases, the pressure coefficient in the region close to the kerf wall increases. This is partially due to the increase in thermodynamic pressure as effect of the increase in temperature as is shown later in the temperature contours. The blockage effect of the kerf wedge also contributes to this increase in pressure.
- Pressure drop occurs in the kerf because of the jet radial expansion in this region. Pressure drop is sharp in the case for which kerf wedge angle = 0° and becomes more gradual as kerf wedge angle increases.
- Fluid temperature increases as kerf wedge angle increases. Fluid temperature reaches a maximum value whose value and location depends on kerf wedge angle.
- The Nusselt number distribution for large kerf wedge angles is characterized by appearance of a secondary maximum. This maximum often exceeds the first maximum attained.
- As the wedge angle increases, Nusselt number increases. The blockage effect of the kerf leads to pressure buildup that increases the density of the fluid in the kerf while enhancing the amount of heat transfer in the kerf.

- At a given averaged jet velocity, given kerf wall thickness and given standoff distance, χ decreases with increasing kerf wall wedge angle.
- At a given averaged jet velocity, given kerf wall thickness and given standoff distance, a large increase in the average Nusselt number is observed with increasing kerf wall wedge angle.
- At a given averaged jet velocity, given kerf wall thickness and given standoff distance, the average skin friction increases with increasing kerf wall wedge angle.

6.3 EFFECTS OF KERF THICKNESS

- Deceleration along the y-axis gets more pronounced as the kerf thickness increases, such that higher velocities at the kerf exit are associated with kerfs of smaller thickness.
- As thickness increases, pressure coefficient in the kerf attains higher values. This pressure rise can be associated with increase in thermodynamic pressure resulting from higher temperatures attained as thickness increases.
- Nusselt number attained highest values at the location of maximum heat transfer in the kerf whose thickness = 0.5 mm. Nusselt number values attained at that location in the kerf whose thickness = 1.5 mm are higher than those attained in the kerf with thickness = 1.0 mm which are higher than those attained in the kerf whose thickness = 2.0 mm.
- Skin friction increases sharply at the inlet of the kerf until a maximum skin friction is attained. The value of this maximum skin friction decreases as kerf

thickness increases. Skin friction then decreases as kerf depth increases. Skin friction then increases until a second maximum skin friction is attained close to the kerf exit in all cases. The value of the second maximum attained skin friction is higher than the first maximum in the case for which kerf thickness = 1.5 mm, and averaged jet velocity at nozzle exit = 60 m/s.

6.4 EFFECTS OF STANDOFF DISTANCE

- The local Nusselt number distribution at the location of maximum heat transfer is higher at the larger standoff distance.
- The effect of standoff distance on local distribution considered in the present study is not much pronounced.
- At a given averaged jet velocity, given kerf wall thickness, and given kerf wedge angle, χ increases with increasing standoff distance. However this is not true in few of the averaged jet velocity – kerf wedge angle combinations. At large kerf wedge angles, χ decreases with increasing standoff distance at a given averaged jet velocity.
- At a given velocity and given kerf wall wedge angle, average Nusselt number typically increases with increasing standoff distance. It almost doubles for the case for which kerf wall thickness = 2.0 mm and kerf wedge angle = 2°. This is true for all averaged jet velocities considered.
- At a given averaged jet velocity, average skin friction increases with increasing standoff distance. This is true for kerf wall wedge angles = 0° and 2° associated

with kerf wall thickness = 0.5, 1.0 and 1.5 mm. The opposite is observed at the other kerf wedge angles.

- At a given averaged jet velocity, kerf wall thickness = 2.0 mm, and kerf wedge angle = 0°, average skin friction increases with increasing standoff distance. The opposite is observed for the case for which kerf wedge angle = 2°.

6.5 CLOSURE

This work provides information on the flow and heat transfer characteristics associated with an inert gas jet emerging from a conical nozzle and impinging onto a workpiece surface and penetrating into a narrow laser cut kerf. The results can be used in laser cutting applications to improve process efficiency and end product quality. It enables selection of appropriate mass flow rate at nozzle inlet and optimum parameters corresponding to particular material thickness and geometry. The predictions may be extended to include various nozzle configurations, several stand-off distances, different types of assisting gases, and other kerf widths. This work is expected to be a useful source of physical information for those working in laser cutting applications. It also offers practical help for researchers and scientists working in laser cutting field. Furthermore, knowledge of the behavior of the flow field and heat transfer provides crucial information for future numerical or experimental studies in the considered configuration.

Despite the uncertainties that can be associated with turbulence modeling of the complex flow and heat transfer phenomena associated with jet impingement, the results

obtained are expected to be valuable in identifying effects of the key parameters on the flow and heat transfer. Consequently, this can serve in the design of the impinging jet system in the laser cutting process for improved quality and performance. It can also help in identifying important parameters that can be considered in setting a simplified and cost-efficient experimental investigation of the jet impingement effects in laser cutting. Furthermore, it will serve as a starting point for evaluating turbulence models and identifying the best performing model of turbulence for impingement flows in the laser cutting process.

APPENDIX A

TABLE A.1 The Variation of the Mass Flow Rate Factor χ, and Average Nusselt number Nu_{av}, and Average Skin Friction C_f with the Variation of Averaged Jet velocity, Dimensionless Standoff Distance (H/D), Kerf Depth (t) and Kerf Wedge Angle (α)

		$(H/D)_1 = 2.2$				$(H/D)_2 = 3.0$			
		$V_j = 30$ m/s	$V_j = 40$ m/s	$V_j = 50$ m/s	$V_j = 60$ m/s	$V_j = 30$ m/s	$V_j = 40$ m/s	$V_j = 50$ m/s	$V_j = 60$ m/s
		χ Nu_{av} C_f	χ Nu_{av} C_f	χ Nu_{av} C_f	χ Nu_{av} C_f	χ Nu_{av} C_f	χ Nu_{av} C_f	χ Nu_{av} C_f	χ Nu_{av} C_f
t = 0.0005 m	$\alpha = 0°$	0.302 55.20 0.00320	0.326 59.44 0.0246	0.341 72.73 0.0203	0.350 74.73 0.0176	0.309 63.74 0.0340	0.341 76.05 0.0268	0.354 80.35 0.0217	0.367 83.43 0.0187
	$\alpha = 2°$	0.299 121.55 0.0418	0.324 124.43 0.0333	0.336 125.46 0.0275	0.345 126.79 0.0237	0.293 96.24 0.0425	0.321 100.05 0.0342	0.345 100.15 0.0289	0.354 103.09 0.0248
	$\alpha = 4°$	0.275 171.60 0.0544	0.299 152.51 0.0481	0.314 176.38 0.0364	0.323 177.35 0.0313	0.261 136.79 0.0526	0.301 148.94 0.0445	0.319 143.67 0.0376	0.329 154.97 0.0322
	$\alpha = 6°$	0.234 220.86 0.0684	0.258 231.43 0.0562	0.281 209.82 0.0486	0.295 207.47 0.0422	0.227 231.94 0.0672	0.261 227.99 0.0576	0.279 232.47 0.0488	0.291 230.74 0.0424

TABLE A.1 Continued

		$(H/D)_1 = 2.2$				$(H/D)_2 = 3.0$			
		$V_j = 30$ m/s	$V_j = 40$ m/s	$V_j = 50$ m/s	$V_j = 60$ m/s	$V_j = 30$ m/s	$V_j = 40$ m/s	$V_j = 50$ m/s	$V_j = 60$ m/s
		χ Nu_{av} C_f	χ Nu_{av} C_f	χ Nu_{av} C_f	χ Nu_{av} C_f	χ Nu_{av} C_f	χ Nu_{av} C_f	χ Nu_{av} C_f	χ Nu_{av} C_f
t = 0.0010 m	α = 0°	0.292 57.44 0.0276	0.324 59.64 0.0207	0.345 61.22 0.0168	0.356 62.88 0.0142	0.308 78.42 0.0307	0.339 80.80 0.0232	0.364 81.97 0.0192	0.369 80.37 0.0154
	α = 2°	0.255 116.74 0.0463	0.287 109.83 0.0361	0.311 105.62 0.0301	0.327 107.58 0.0257	0.245 124.82 0.0460	0.291 119.66 0.0384	0.314 123.00 0.0317	0.330 123.25 0.0270
	α = 4°	0.170 175.25 0.0748	0.202 181.06 0.0632	0.223 177.26 0.0539	0.237 194.00 0.0465	0.158 200.85 0.0712	0.196 219.96 0.0625	0.220 205.61 0.0538	0.225 224.04 0.0463
	α = 6°	0.0595 273.16 0.105	0.0740 275.17 0.0944	0.0856 275.95 0.0842	0.0949 276.18 0.0750	0.0564 306.47 0.0998	0.0709 302.72 0.0909	0.0841 294.66 0.0821	0.0947 315.96 0.0576

TABLE A.1 Continued

		$(H/D)_1 = 2.2$				$(H/D)_2 = 3.0$			
		$V_j = 30$ m/s	$V_j = 40$ m/s	$V_j = 50$ m/s	$V_j = 60$ m/s	$V_j = 30$ m/s	$V_j = 40$ m/s	$V_j = 50$ m/s	$V_j = 60$ m/s
		χ Nu_{av} C_f	χ Nu_{av} C_f	χ Nu_{av} C_f	χ Nu_{av} C_f	χ Nu_{av} C_f	χ Nu_{av} C_f	χ Nu_{av} C_f	χ Nu_{av} C_f
t = 0.0015 m	α = 0°	0.280 69.97 0.0271	0.320 71.03 0.0203	0.343 72.03 0.0163	0.362 73.37 0.0140	0.283 81.33 0.0290	0.329 84.80 0.0225	0.358 79.55 0.0183	0.377 84.29 0.0154
	α = 2°	0.196 121.94 0.0561	0.237 116.19 0.0461	0.262 117.03 0.0379	0.280 102.34 0.0324	0.188 146.70 0.0553	0.233 148.24 0.0462	0.262 147.92 0.0392	0.277 150.72 0.0325
	α = 4°	0.0514 265.58 0.0988	0.0652 262.94 0.0883	0.0768 269.57 0.0783	0.0861 266.63 0.0693	0.0484 231.24 0.0934	0.0622 229.47 0.0843	0.0751 249.69 0.0764	0.0853 248.16 0.0680
t = 0.0020 m	α = 0°	0.260 42.64 0.0274	0.306 50.00 0.0203	0.332 47.00 0.0161	0.349 46.22 0.0135	0.263 87.01 0.0288	0.312 88.05 0.0222	0.342 88.44 0.0178	0.365 89.06 0.0152
	α = 2°	0.129 82.49 0.0675	0.163 83.05 0.0568	0.187 83.67 0.0482	0.206 84.22 0.0416	0.124 169.50 0.0658	0.161 174.92 0.0563	0.187 176.34 0.0481	0.206 181.61 0.0416

NOMENCLATURE

a	speed of sound (m/s)
A_ε	constant for turbulence length scale
c_l	constant for turbulence length scale
c_p	constant pressure specific heat (KJ/Kg.K)
c_v	constant volume specific heat (KJ/Kg.K)
$C_{1\varepsilon}, C_{2\varepsilon}$	RNG turbulence model constants
$C^*_{2\varepsilon}$	RNG turbulence model modified constant
C_v, C_μ	turbulent viscosity modeling constants
G_k	generation of turbulence kinetic energy (Kg/ms^3)
G_r	Grashof number
k	turbulence kinetic energy (m^2/s^2)
k_{eff}	effective thermal conductivity (W/mK)
l_μ	length scale
M_t	turbulent Mach number
Nu	Nusselt number
p	pressure (Pa)
Pr	Prandtl number
R	gas constant (KJ/Kg.K)
RNG	renormalization group

RSTM	Reynolds Stress Turbulence Model
Re	Reynolds number
Re_y	wall-distance based Reynolds number
Ri	Richardson number
S	strain rate (s^{-1})
S_{ij}	mean rate of strain tensor (s^{-1})
S_σ	source term
t	time (s)
T	temperature (K)
U_i, U_j	arbitrary mean velocity component (m/s)
U	velocity in the x-direction (m/s)
V	velocity in the y-direction (m/s)
W	velocity in the z-direction (m/s)
$u_i^{'}, u_j^{'}$	arbitrary fluctuating velocity component (m/s)
$u_i^{'} u_j^{'}$	Reynolds stresses
$u^{'}$	fluctuating velocity in the x-direction (m/s)
$v^{'}$	fluctuating velocity in the y-direction (m/s)
$w^{'}$	fluctuating velocity in the z-direction (m/s)
x_i, x_j	arbitrary direction
x	distance along x-axis (m)
y	distance along y-axis (m)
y^+	non-dimensional wall coordinate

z	distance along z-axis (m)

Greek

α	inverse Prandtl number
α_k, α_ε	inverse effective Prandtl numbers for k and ε respectively
χ	ratio of mass flow rate at kerf exit to mass flow rate at nozzle inlet
δ_{ij}	Kronecker delta
ε	turbulence kinetic energy dissipation (m^2/s^3)
γ	specific heat ratio (c_p/c_v)
Γ	blending function for velocity laws-of-the-wall
Γ_σ	general diffusion coefficient
κ	von Karman constant (=0.4187)
λ	thermal conductivity (W/m.K)
Π	blending function for temperature laws-of-the-wall
μ	dynamic viscosity (Kg/m.s)
μ_t	turbulent (eddy) viscosity (Kg/m.s)
μ_{eff}	effective viscosity ($\mu + \mu_t$) (Kg/m.s)
ν	kinematic viscosity (m^2/s)
$\hat{\nu}$	ratio of effective to dynamic viscosity
σ	general dependent variable
φ	arbitrary scalar quantity
φ'	fluctuating component of arbitrary scalar quantity
ρ	density (kg/m^3)

τ_{ij}	arbitrary Reynolds stress (Pa)
θ'	fluctuating component of temperature (K)

Subscripts

eff	effective
ε	turbulence kinetic energy dissipation
i, j	arbitrary direction
j	jet
k	turbulence kinetic energy
t	turbulent
under-bar	vector quantity

Superscripts

over-bar	time-averaged variable
˜ tilde	density-weighted or Favre-averaged variable
y	wall distance

Bibliography

[1] M.S. Gross. On gas dynamic effects in the modeling of laser cutting processes. *Applied Mathematical Modelling*, 30:307-318, 2006.

[2] A. Kar and J. Mazumder. Two-dimensional model for material damage due to melting and vaporization during laser irradiation. *Journal of Applied Physics*, 68(8):3884-3891, 1990.

[3] E. Kannatey-Asibu. *Principles of Laser Materials Processing*. Wiley Series on Processing of Engineering Materials. John Wiley & Sons, Inc., Hoboken, New Jersey, 2009.

[4] J. Powell. *CO_2 Laser Cutting*. Springer-Verlag London Limited, Germany, 1998.

[5] J.C. Ion. *Laser Processing of Engineering Material: Principles, Procedure and Industrial Application*. Elsevier Butterworth-Heinemann, Oxford, 2005.

[6] G. Tani, L. Tomesani, and G. Campana. Prediction of melt geometry in laser cutting. *Applied Surface Science*, 208-209:142-147, 2003.

[7] M. Vicanek, G. Simon, H.M. Urbassek, I. Decker. Hydrodynamical instability of melt flow in laser cutting. *Journal of Physics D: Applied Physics*, 20 (1):140-145, 1987.

[8] S.Z. Shuja. *Simulation of Three-Dimensional Laser Gas-Assisted Heating of Solid Substance: The Fourier Heat Conduction Theory Approach*. PhD thesis, King Fahd University of Petroleum and Minerals, Dhahran, 1998.

[9] D.J. Womac, S. Ramadhyani, F.P. Incropera. Correlating equations for impingement cooling of small heat sources with single circular liquid jets. *Journal of Heat Transfer* (Transactions of the ASME), 115:106-115, 1993.

[10] S. Polat, B. Huang, A.S. Mujumdar, and W.J.M. Douglas. *Numerical flow and heat transfer under impinging jets:* A review, volume 2 of *Annual review of Numerical Fluid Mechanics and Heat Transfer,* chapter 4, pages 157-197. Hemisphere publishing corporation, New York, 1989.

[11] J.A. Fay. *Introduction to Fluid Mechanics*. MIT Press, Massachusetts, 1994.

[12] D.C. Wilcox. *Turbulence Modeling for CFD*. DCW Industries, Inc., California, 1998.

[13] G.K. Morris and S.V. Garimella. Orifice and impingement flow fields in confined jet impingement. *Journal of Electronic Packaging,* 120:68-72, 1998.

[14] Y. Shi, M.B. Ray, and A.S. Mujamdar. Computational study of impingement heat transfer under a turbulent slot jet. *Ind. Eng. Chem. Res*., 41:4643-4651, 2002.

[15] FLUENT User's Guide, Release. FLUENT Inc., Lebanon, 2005.

[16] G. K. Morris, S.V. Garimella, and R.S. Amano. Prediction of jet impingement heat transfer using a hybrid wall treatment with different turbulent Prandtl number functions. *Journal of Heat Transfer*, 118:562-569, 1996.

[17] K. Chen, Y.L Yao, and V. Modi. Gas jet-workpiece interactions in laser machining. *Journal of Manufacturing Science and Engineering*, 122:429-438, 2000.

[18] Y. Shi, M.B. Ray, and A.S. Mujamdar. Effects of Prandtl number on impinging jet heat transfer under a semi-confined turbulent slot jet. *Int. Comm. Heat Mass Transfer*, 29 (7):929-938, 2002.

[19] A. Ramezanpour, I. Mirzaee, D. Firth, and H. Shirvani. A numerical heat transfer study of slot jet impinging on an inclined plate. *International Journal of Numerical Methods for Heat and Fluid Flow*, 17 (7):661-676, 2007.

[20] B. Sagot, G. Antonini, A. Christgen, and F. Buron. Jet impingement heat transfer on a flat plate at a constant wall temperature. *International Journal of Thermal Sciences*, 47:1610-1619, 2008.

[21] A.K. Dubey and V. Yadava. Laser beam machining-A review. *International Journal of Machine Tools & Manufacture*, 48:609-628, 2008.

[22] M. Gross. Comprehensive numerical simulation of laser materials processing. In J. Dowden, editor, *The Theory of Laser Materials Processing*, pages 339-380. Springer Series in Materials Science, The Netherlands, 2009.

[23] S.-L. Chen. The effects of high-pressure assistant-gas flow on high-power CO_2 laser cutting. *Journal of Materials Processing Technology*, 88:57-66, 1999.

[24] J. Wang and W.C.K. Wong. CO2 laser cutting of metallic coated sheet steels. *Journal of Materials Processing Technology*, 95:164-168, 1999.

[25] W. O'Neill and J.T. Gabzdyl. New developments in laser-assisted oxygen cutting. *Optics and Lasers in Engineering*, 34:355-367, 2000.

[26] C. Karatas, O. Keles, I. Uslan, and Y. Usta. Laser cutting of steel sheets: Influence of workpiece thickness and beam waist position on kerf size and stria formation. *Journal of Materials Processing Technology,* 172:22-29, 2006.

[27] M. Vicanek, G. Simon, H.M. Urbassek, I. Decker. Momentum and heat transfer of an inert gas jet to the melt in laser cutting. *Journal of Physics D: Applied Physics*, 20 (9): 1191-1196, 1987.

[28] K. Farooq and A. Kar. Removal of laser-melted material with an assist gas. *Journal of Applied Physics*, 83(12):7467-7473, 1998.

[29] A.F.H. Kaplan. An analytical model of metal cutting with a laser beam. *Journal of Applied Physics*, 79(5):2198-2208, 1996.

[30] W. Schulz, V. Kostrykin, M. Nieben, J. Michel, D. Petring, E.W. Kreutz, and R. Poprawe. Dynamics of ripple formation and melt flow in laser beam cutting. *Journal of Physics D: Applied Physics*, 32:1219-1228, 1999.

[31] B.S. Yilbas. Laser cutting quality assessment and thermal efficiency analysis. *Journal of Materials Processing Technology,* 155-156:2106-2115, 2004.

[32] G. Tani, L. Tomesani, G. Campana, A. Fortunato. Quality factors assesses by analytical modeling in laser cutting. *Thin Solid Films*, 453-454:486-491, 2004.

[33] B.S. Yilbas and B.J. Abdul Aleem. Dross formation during laser cutting process. *Journal of Physics D: Applied Physics,* 39:1451-1461, 2006.

[34] B.S. Yilbas. Laser cutting of thick sheet metals: Effects of cutting parameters on kerf size variations. *Journal of Materials Processing Technology,* 201:285-290, 2008.

[35] C. Mai and J. Lin. Flow structures around an inclined substrate subjected to a supersonic impinging jet in laser cutting. *Optics and Laser Technology*, 34:479-486, 2002.

[36] W. Schulz, M. Nieben, U. Eppelt, and K. Kowalick. Simulation of Laser Cutting. In J. Dowden, editor, *The Theory of Laser Materials Processing*, pages 21-70. Springer Series in Materials Science, The Netherlands, 2009.

[37] J.W. Baughn and S. Shimizu. Heat transfer measurements from a surface with uniform heat flux and an impinging jet. *Journal of heat transfer*, Transactions of the ASME, 111:1096-1098, 1989.

[38] D. Cooper, D.C. Jackson, B.E. Launder, and G.X. Liao. Impinging jet studies for turbulence model assessment – I. Flow – field experiments. *International Journal of Heat and Mass Transfer,* 36 (10):2675-2684, 1993.

[39] A.K. Mohanty and A.A. Tawfek. Heat transfer due to a round jet impinging normal to a flat surface. *International Journal of Heat and Mass Transfer*, 36 (6):1639-1647, 1993.

[40] L. Huang and M.S. El-Genk. Heat transfer of an impinging jet on a flat surface. *International Journal of Heat and Mass Transfer*, 37(13):1915-1923, 1994.

[41] D. Lytle and B.W. Webb. Air jet impingement heat transfer at low nozzle-plate spacings. *International Journal of Heat and Mass Transfer,* 37(12):1687-1697, 1994.

[42] B. Elison and B.W. Webb. Local heat transfer to impinging liquid jets in the initially laminar, transitional, and turbulent regimes. *International Journal of Heat and Mass Transfer*, 37(8):1207-1216, 1994.

[43] D.J. Bizzak and M.K. Chyu. Use of a laser-induced fluorescence thermal imaging system for local jet impingement heat transfer measurement. *International Journal of Heat and Mass Transfer,* 38(2):267-274, 1995.

[44] D.H. Wolf, R. Viskanta, and F.P. Incropera. Turbulence dissipation in a free-surface jet of water and its effect on local impingement heat transfer from a heated surface: part 1-flow structure. *Journal of Heat Transfer* (Transactions of the ASME), 117:85-94, 1995.

[45] D.H. Wolf, R. Viskanta, and F.P. Incropera. Turbulence dissipation in a free-surface jet of water and its effect on local impingement heat transfer from a heated surface: part 2-local heat transfer. *Journal of Heat Transfer* (Transactions of the ASME), 117:95-103, 1995.

[46] S.V. Garimella and R.A. Rice. Confined and submerged liquid jet impingement heat transfer. *Journal of Heat Transfer* (Transactions of the ASME), 117:871-877, 1995.

[47] D. Lee, R. Greif, S.J. Lee, and J.H. Lee. Heat transfer from a flat plate to a fully developed axisymmetric impinging jet. *Journal of Heat Transfer* (Transactions of the ASME), 117:772-776, 1995.

[48] D.H. Lee, J. Song and M.C. Jo. The effects of nozzle diameter on impinging jet heat transfer and fluid flow. *Journal of Heat Transfer* 126:554-557, 2004.

[49] M. Fenot, J. Vullierme, and E. Dorignac. A heat transfer measurement of jet impingement with high injection temeperature. *C.R. Mecanique*, 333:778-782, 2005.

[50] B.P.E. Dano, J.A. Liburdy, and K. Kanokjaruvijit. Flow characteristics and heat transfer performance of a semi-confined impinging array of jets: effect of nozzle geometry. *International Journal of Heat and Mass Transfer*, 48:691-701, 2005.

[51] H. Eren, N. Celik, and B. Yesilata. Nonlinear flow and heat transfer dynamics of a slot jet impinging on a slightly curved concave surface. *International Communications in Heat and Mass Transfer,* 33:364-371, 2006.

[52] J.-Y. San and W.-Z. Shiao. Effects of jet plate size and plate spacing on the stagnation Nusselt number for a confined circular air jet impinging on a flat surface. *International Journal of Heat and Mass Transfer*, 49:3477-3486, 2006.

[53] D.W. Zhou and C.F. Ma. Radial heat transfer behavior of impinging submerged circular jets. *International Journal of Heat and Mass Transfer*, 49(9-10):1719-1722, 2006.

[54] Z.X. Yuan, Y.Y. Chen, J.G. Jiang, and C.F. Ma. Swirling effect of jet impingement on heat transfer from a flat surface to CO_2 stream. Experimental *Thermal and Fluid Sciences*, 31:55-60, 2006.

[55] T.S. O'Donnovan and D.B. Murray. Jet impingement heat transfer – part I: mean and root-mean-square heat transfer and velocity distributions. *International Journal of Heat and Mass Transfer,* 50:3291-3301, 2007.

[56] T.S. O'Donnovan and D.B. Murray. Jet impingement heat transfer – part II: a temporal investigation of heat transfer and local fluid velcoities. *International Journal of Heat and Mass Transfer*, 50:3302-3314, 2007.

[57] D.W. Zhou and S.-J. Lee. Forced convective heat transfer with impinging rectangular jets. *International Journal of Heat and Mass Transfer*, 50:1916:1926, 2007.

[58] J. Senter and C. Solliec. Flow filed analysis of a turbulent slot air jet impinging on a moving flat surface. *International Journal of Heat and Fluid Flow*, 28:708-719, 2007.

[59] C.H. Lee, K.B. Lim, S.H. Lee, Y.J. Yoon, and N.W. Sung. A study of the heat transfer characteristics of turbulent round jet impinging on an inclined concave surface using liquid crystal transient method. *Experimental Thermal and Fluid Sciences*, 31:559-565, 2007.

[60] K.B. Lim, C.H. Lee, N.W. Sung, and S.H. Lee. An experimental study on the characteristics of heat transfer on the turbulent round impingement jet according to the inclined angle of convex surface using the liquid crystal transient method. *Experimental Thermal and Fluid Sciences*, 31:711-710, 2007.

[61] H.C. Man, J. Duan and T.M. Yue. Analysis of the dynamic characteristics of gas flow inside a laser cut kerf under high cut-assist gas pressure. *Journal of Physics D. Applied Physics*, 32:1469-1477, 1999.

[62] R.S. Amano and H. Brandt. Numerical study of turbulent axisymmetric jets impinging on a flat plate and flowing into an axisymmetric cavity. *Journal of Fluids Engineering*, 106:410-417, 1984.

[63] X.S. Wang, Z. Dagan, and L.M. Jiji. Heat transfer between a circular free impinging jet and a solid surface with non-uniform wall temperature or wall heat flux – 1. Solution for the stagnation region. *International Journal of Heat and Mass Transfer*, 32(7):1351-1360, 1989.

[64] X.S. Wang, Z. Dagan, and L.M. Jiji. Heat transfer between a circular free impinging jet and a solid surface with non-uniform wall temperature or wall heat flux – 2. Solution for the boundary layer region. *International Journal of Heat and Mass Transfer*, 32(7):1361-1371, 1989.

[65] A. Bejan. Thermodynamics of an isothermal flow: the two-dimensional turbulent jet. *International Journal of Heat and Mass Transfer*, 34(2):407-413, 1991.

[66] Craft, T. J., Graham, J. W., Launder, B. E., 1993. Impinging jet studies for turbulence model assessment – II. An examination of the performance of four turbulence models. *International Journal of Heat and Mass Transfer* 36 (10), 2685-2697.

[67] W.C. Lasher and D.B. Taulbee. Reynolds stress model assessment using round jet experimental data. *International Journal of Heat and Fluid Flow*, 15(5):357-363, 1994.

[68] S.M. Hosseinalipour and A.S. Mujumdar. Comparative evaluation of different turbulence models for confined impinging and opposing jet flows. *Numerical Heat Transfer, Part A*, 28:647-666, 1995.

[69] M. Dianat, M. Fairweather, and W.P. Jones. Predictions of axisymmetric and two-dimensional impinging turbulent jets. *International Journal of Heat and Fluid Flow*, 17(6):530-538, 1996.

[70] S. Ashforth-Frost and K. Jambunathan. Numerical prediction of semi-confined jet impingement and comparison with experimental data. *International Journal for Numerical Methods in Fluids* 23:295-306, 1996.

[71] S.Z. Shuja and B.S Yilbas. 3-Dimensional conjugate laser heating of a moving slab. *Applied Surface Science*, 167:134-148, 2000.

[72] S.Z. Shuja, B.S. Yilbas, and M.O. Budair. Entropy generation due to jet impingement on a surface: effect of annular nozzle outer angle. *International Journal of Numerical Methods for Heat and Fluid Flow*, 17(7):677-691, 2007.

[73] B.S. Yilbas, S.Z. Shuja, and M.O. Budair. Jet impingement onto a conical hole in relation to laser machining. *Journal of Materials Processing Technology*, 155-156:2039-2044, 2004.

[74] S.Z. Shuja, B.S. Yilbas, and S.A. Khan. Jet impingement onto a conical cavity: Effects of annular nozzle outer angel and jet velocity on heat transfer and skin friction. *International Journal of Thermal Sciences*, 48:985-997, 2009.

[75] S.Z. Shuja, B.S. Yilbas, and M.O. Budair. Jet impingement on cylindrical cavity: Conical nozzle considerations. *Journal of Fluids and Structures*, 23:1106-1118, 2007.

[76] S.Z. Shuja, B.S. Yilbas, and S.M.A. Khan. Jet emerging from an annular nozzle and impinging onto cylindrical cavity: effect of jet velocity on flow structure and heat transfer rates. *Proceedings of the Institution of Mechanical Engineers, Part C: Journal of Mechanical Engineering Science*, 222(6):1021-1031, 2008.

[77] S.Z. Shuja, B.S. Yilbas, and S.M.A. Khan. Flow emerging from annular-conical nozzle combinations and impinging onto a cylindrical cavity. *International Journal of Thermal Sciences*, 48:975-984, 2009.

[78] S.Z. Shuja, B.S. Yilbas, and S.M.A. Khan. Jet impingement onto a tapered hole: influence of jet velocity and hole wall velocities on heat transfer and skin friction. *International Journal for Numerical Methods in Fluids*, 60(9):972-991, 2009.

[79] X.J. Lei, X. Zhong, and H. Shurjan. Numerical study of semi-confined slot jet impingement. *Journal of Hydrodynamics*, Ser. B, 3:14-18, 1999.

[80] T. Cziesla, E. Tandogan, and N.K. Mitra. Large-Eddy simulation of heat transfer from impinging jets. *Numerical Heat Transfer*, Part A, 32:1-17, 1997.

[81] H. Hattori and Y. Nagano. Direct numerical simulation of turbulent heat transfer in plane impinging jet. *International Journal of Heat and Fluid Flow*, 25:749-758, 2004.

[82] D. Sahoo and M.A.R. Sharif. Numerical modeling of slot-jet impingement cooling of a constant heat flux surface confined by a parallel wall. *International Journal of Thermal Sciences,* 43:877-887, 2004.

[83] X. Li, J.L. Gaddis, and T. Wang. Multiple flow patterns and heat transfer in confined jet impingement. *International Journal of Heat and Fluid Flow*, 26:746-754, 2005.

[84] I. Dagtekin and H.F. Oztop. Heat transfer due to double laminar slot jets impingement onto an isothermal wall within one side closed long duct. International *Communications in Heat and Mass Transfer*, 35:65-75, 2008.

[85] Y.C. Chen, C.F. Ma, M. Qin, and Y.X. Li. Theoretical study on impingement heat transfer with single-phase free-surface slot jets. *International Journal of Heat and Mass Transfer,* 48:3381-3386, 2005.

[86] P. Patel and S. and Roy. Study of jet impingement heat transfer for varying fluid flow characteristics, in: *Proceedings of the 2001 ASME Fluids Engineering Division Summer Meeting, Volume 2: Symposia*, pp. 197-204, 2003.

[87] S.C. Rasipuram and K.J. Nasr. A numerically-based parametric study of heat transfer off an inclined surface subject to impinging airflow. *International Journal of Heat and Mass Transfer*, 47:4967-4977, 2004.

[88] H. Chattopadhyay and S.K. Saha. Turbulent flow and heat transfer from a slot jet impinging on a moving plate. *International Journal of Heat and Fluid Flow*, 24:685-697, 2003.

[89] H. Schlichting. *Boundary-Layer Theory*, Translated by J. Kestin. Seventh Edition, . McGraw-Hill. New York, 1979.

[90] H. Herwig, H. Mocikat, T. Gurtler, and S. Goppert. Heat transfer due to unsteadily impinging jets. *International Journal of Thermal Sciences*, 43:733-741, 2004.

[91] H.K. Versteeg and W. Malalasekera. *An Introduction to Computational Fluid Dynamics: The Finite Volume Method*, 2nd Ed. Pearson Education Limited, England, 2007.

[92] J.C. Tannehill, D.A. Anderson, and R.H. Pletcher. *Computational Fluid Mechanics and Heat Transfer*, 2nd Ed. Taylor & Francis, Philadelphia, 1997.

[93] F.P. Incropera and D.P. Dewitt. *Fundamentals of Heat and Mass Transfer*, 5th Ed. John Wiley & Sons, Inc., Hoboken, 2002.

[94] S.V. Patankar. *Numerical Heat Transfer and Fluid Flow*. Hemisphere Publishing Corporation, Washington, 1980.

[95] J.D. Hoffman. *Numerical Methods for Engineers and Scientists*. McGraw-Hill, Inc., New York, 1993.

[96] M.A.R. Sharif and K.K. Mothe. Evaluation of turbulence models in the prediction of heat transfer due to slot jet impingement on plane and concave surfaces. *Numerical Heat Transfer, Part B: Fundamentals*, 55(4):273-294, 2009.

OMAR AHMAD MELHEM - VITA

King Fahd University of Petroleum and Minerals
P.O. Box: 1060, Dhahran 31261
Kingdom of Saudi Arabia
(966) 3 860 5350 – (966) 55 132 3927
omelhem@kfupm.edu.sa
melhemomar@hotmail.com

PERSONAL DETAILS:

Nationality:	Lebanese
Date of Birth:	12 August 1977
Marital Status:	Married
Languages:	Arabic, English
Permanent Address:	Issam Center Bldg., 1st floor, Jamil Adra Street (El-Mina Road), Tripoli, Lebonon, Tel: (961) 6 201 348

Omar Melhem received his Bachelor of Science in Mechanical Engineering from the University of Texas at Austin in the United States in 2000. There, he participated in designing an actuating mechanism to be used in Oil Well completion for Schlumberger, Texas. Later, he attended the University of Balamand in North Lebanon from where he earned Master of Science in Mechanical Engineering in 2003. He pursued further graduate work at the American University of Beirut in the year 2004 – 2005 aiming at Master of Engineering. He then joined King Fahd University of Petroleum and Minerals pursuing his PhD. He successfully defended his dissertation in January, 2010. He received Hariri's Foundation Scholarship for the year 1995 – 1996. His main areas of interest are Fluid Mechanics, Heat Transfer, Thermodynamics, and Combustion.